EXPERIMENTAL REALIZATION AND THEORETICAL STUDIES OF NOVEL ALL-OPTICAL DEVICES BASED ON NANO-SCALE WAVEGUIDES

CHEN YIJING

(B. Sc. (Hons.), NUS)

A THESIS SUBMITTED

FOR THE DEGREE OF DOCTOR OF PHILOSOPHY

NUS GRADUATE SCHOOL FOR INTEGRATIVE SCIENCES AND ENGINEERING

NATIONAL UNIVERSITY OF SINGAPORE

2015

DECLARATION

I hereby declare that this thesis is my original work and it has been written by me in its entirety. I have duly acknowledged all the source of information, which have been used in the thesis.

This thesis has also not been submitted for any degree in any university previously.

_____

Chen Yijing

6 April 2015

ACKNOWLEDGEMENT

Foremost, I would like to express the deepest appreciation to my supervisors, Prof Chong Tow Chong and Prof Ho Seng-Tiong, for their continuous support of my Ph. D study and research. I would especially like to thank Prof. Ho, for the patient guidance, encouragement, and advice he has provided. I have been amazingly fortunate to have an advisor who has such immense knowledge in both fundamental science and application engineering fields.

My sincere thank also goes to my co-supervisor, Dr. Lai Yicheng, who has been a good mentor as well as a good friend to me. His patience and support helped me overcome many crisis situations throughout my Ph. D study. He is also an experienced and remarkable experimental scientist. Without his help, I could not complete our photonic transistor measurement setup.

I also would like to thank Dr. Lee Chee Wei, who is my first fabrication advisor. I have learnt a great deal of fabrication skills from him. The simulation and technical discussion with Dr. Vivek Krishnamurthy has benefited me a lot in reaching a better understanding of our photonic transistor. Thank Dr. Huang Yingyan for her assistance and guidance in photonic transistor device design and fabrication process development. Dr. Doris Ng Keh Ting has helped to develop the ICP etching recipes for silicon and InP etching, which is very critical to my device realization. The direct bonding process was initially developed by Dr. Wang Yadong, and was later optimized and taught to me by Dr. Pu Jing. Their efforts and help are sincerely appreciated. The MLME-FDTD program, which I used to demonstrate the dynamic switching of our photonic transistor, was written by a very smart and passionate person, Dr. Ravi Koustuban. There are many other different people, Dr. Wang Qian,

Dr. Tang Kun, Ng Siu Kit, etc, having contributed to my research project in different ways. I would like to extend my appreciation to every one of them.

I also feel grateful with the support from Data Storage Institute and allowing me to focus on my research work throughout my Ph. D. years.

Lastly, I would like to thank my parents, for everything. You are the best parents in the world. I love you.

TABLE OF CONTENTS

SUMMARY

A novel all-optical switching device, being termed as photonic transistor (PT), which utilizes the optically induced gain and absorption change to manipulate the interference characteristics in a 2-waveguide directional coupler, was recently

proposed. Initial theoretical studies show high-speed all-optical switching with switching gain and substantially lower power than the semiconductor optical amplifier (SOA) approach can be realized based on the new switching scheme, which will benefit next-generation ultrafast and power-efficient optical network. However, systematical studies and experimental realization of PT have been lacking.

In this dissertation, first of all, the parametric analysis of the absorption-assisted energy-up photonic transistor (EUPT) switching performance is carried out based on a new analytical method developed, highlighting the important device design aspects that have never been raised before. Quantitative evaluation of the switching gain, switching speed and energy consumption is carried out based on InGaAsP bulk semiconductor, showing an absorption factor $\alpha_{H0}L$ value of greater than 30 is required to achieve switching gain and a minimum energy of ~250fJ/bit is consumed with use of bulk semiconductor, which is about 10 times higher than the 50fJ/bit required for the initially proposed 4-level system with $\alpha_{H0}L$ of about 7-10.

Secondly, the interband absorption and gain characteristics in the semiconductor quantum well is theoretically analyzed and compared with the bulk semiconductor based on the Free-Carrier theory. The results suggest the employment of quantum well in EUPT will benefit the switching gain, but will not affect the switching speed or energy consumption significantly. For QW-InGaAsP based EUPT, the $\alpha_{H0}L$ requirement to achieve switching gain >1 is reduced to 22.

Thirdly, photonic transistor is fabricated in an integrated platform for the first time with different fabrication approaches being developed, including quantum-well-intermixing (QWI) assisted approach on InP-based substrate, and III-V-on-silicon integration approach assisted by direct wafer bonding technique. Based on the evaluation of fabrication complexity and challenges, we adopt the self-aligned QW-

on-SOI architecture for final device fabrication.

Fourthly, two new PT architectures based on three-waveguide (3-WG) directional coupler and MZI are proposed to alleviate the fabrication challenges posed to the initial design, and 3-WG EUPT is shown to exhibit advantageous performance over the 2-WG and MZI EUPT.

Lastly, optical studies of the devices fabricated are performed and pump-control switching with switching gain is demonstrated in a single-waveguide structure.

LIST OF TABLES

LIST OF FIGURES

Fig. 4.10: The transmitted pump power (solid line) when a 27.5ps control pulse with 10% of pump intensity (dash line) is launched from the opposite end of the waveguide with $\alpha_{H0}L = 22.8$

Fig. 4.11: The transmitted pump power (solid line) when a 10ps control pulse with 10% of the pump intensity is launched from the opposite end of the waveguide with $\alpha_{H0}L = 22.8$.

Fig. 5.1: Switching gain of EUPT versus $1/r_{in} = \frac{P_{L-ON}}{P_{H-CW}}$ at different $\alpha_{H0}L$, with $I_{H-CW} = 15MW/cm^2$. $\lambda_L = 1.45\mu m$ and $\lambda_H = 1.35\mu m$.

Fig. 5.2: (a) Device geometry and simulation parameters for EUPT with $\alpha_{H0}L = 17.4$ and the (b) input and output signal profiles.

Fig. 5.3: (a) Device geometry and simulation parameters for EUPT with $\alpha_{H0}L = 34.8$ and the (b) input and output signal profiles.

Fig. 6.1: Optical absorption in bulk (i.e., 3D) semiconductors and in quantum wells, in the simplest model where excitonic effects are neglected.

Fig. 6.2: Absorption spectrum of a typical GaAs/AlGaAs quantum well structure at room temperature.

Fig. 6.3: Analytically calculated I_{Hsat}versus pump wavelength λ_H for quantum well (solid) and bulk (dash) InGaAsP.

Fig. 6.4: (a) $\frac{g_{L0}}{\alpha_{H0}}$ versus λ_L and (b) $\frac{I_{Lsat}}{I_{Hsat}}$ versus λ_L at different pump wavelength λ_H for bulk (black) and quantum well (red) medium.

Fig. 6.5: Switching gain of QW-InGaAsP-based EUPT versus $1/r_{in} = \frac{P_{L-ON}}{P_{H-CW}}$ at $\alpha_{H0}L = 22$ (black solid) and $\alpha_{H0}L = 30$ (black dash), and switching gain of bulk InGaAsP EUPT at $\alpha_{H0}L = 30$ (red solid). $I_{H-CW} = P_{H-CW}/A_{eff} = 15MW/cm^2$. $\lambda_L = 1.45\mu m$ and $\lambda_H = 1.35\mu m$.

Fig. 8.2: Symmetric 3-WG directional coupler with two identical passive side waveguides and one active central waveguide.

Fig. 8.3: Optical intensity along WG1, WG2 and WG3 in the symmetric 3-WG coupler when $|\Delta\beta|L_{C0}$=0, 2, 4, 6, 8 and 10.

Fig. 8.4: Transparency-state output power from WG1 in 2-WG and 3-WG coupler with different $|\Delta\beta|L_{C0}$ when the incident light is launched from WG1.

Fig. 8.5: Power transmission from WG1 of the symmetric 3-WG coupler at coupling length L_{C3} versus $\alpha_{am}L_{C3}$ at different$|\Delta\beta|L_{C0}$.

Fig. 8.6: The switching gain of 3-WG EUPT versus $\frac{P_{L-ON}}{P_{H-CW}}$ at $\Delta\beta L_{L0} = 0, 2, 4, 6, 8$.

Fig. 8.7: The maximum switching gain that can be achieved at different $\Delta\beta L_{C0}$ and $\alpha_{H0}L$.

Fig. 8.8: Relative figure of merit for bulk-InGaAsP based 3-WG EUPT at different $\Delta\beta L_{L0}$, and fixed $\alpha_{H0}L_{C3} = 30$.

Fig. 8.9: a) 3-WG coupler structure and simulation parameters for FDTD simulation of EUPT operation. $\Delta\beta L_{C0} = 6$ and $L_{C3} = 115\mu m$. b) FDTD simulation of pump supply beam propagating along the 3-WG coupler after the central waveguide is pumped to transparency.

Fig. 8.10: Input and output signal profiles for 3WG-EUPT with $\Delta\beta L_{C0} = 6$ for two different $\alpha_{H0}L$.

Fig. 8.11: Switching operation in MZI-based EUPT, which consists of two identical active arms.

Fig. 8.12: (a) The switching gain of MZI-EUPT versus $\frac{P_{L-ON}}{P_{H-CW}}$ for different $\alpha_{H0}L$. (b) the maximum switching gain that can be reached at each $\alpha_{H0}L$ in MZI-EUPT (solid), 2-WG EUPT (dotted line) and 3-WG EUPT (dash line).

LIST OF SYMBOLS

λ_H: Wavelength of light with higher photon energy

λ_L: Wavelength of light with lower photon energy

E_g: Band gap energy of semiconductor

P_{H-CW}: Optical power of incident CW pump beam at wavelength λ_H

P_{H-ON}: Optical power of output signal at switch-on state

P_{H-OFF}: Optical power of output signal at switch-off state

P_{L-ON}: Optical power of input signal at switch-on state

P_{H-OFF}: Optical power of input signal at switch-off state

r_e: Extinction ratio of signal

β_i: Propagation constant of light in waveguide i

n_{eff}: Effective propagation index of light in a waveguide

α_{am}: Absorption coefficient of field amplitude, $2\alpha_{am}$ gives the absorption coefficient of optical power

κ_{ij}: Coupled coefficient between waveguide i and waveguide j

$a_i(z)$: field amplitude of light in waveguide i

L_{C0}: Complete coupling length of 2WG directional coupler in the index-matching condition

L_{C2}: Coupling length of 2WG directional coupler in general case

A_{eff}: optical modal area in the active waveguide

h: Planck constant

c: Speed of light in free space

N_i: Carrier densities at level i

N_c: Total carrier density in the conduction band

ΔN_{ij}: Carrier density difference between level i and j

I_H: Intensity of light at wavelength λ_H

I_L: Intensity of light at wavelength λ_L

τ_{ij}: Intraband/Interband transition time from level i to level j

τ_r: Intraband-interband transition time ratio

α_H: Power absorption coefficient at wavelength λ_H

α_{H0}: Small-signal absorption coefficient at λ_H

g_L: Optical gain coefficient at wavelength λ_L

g_{L0}: Small-signal gain coefficient seen by light at λ_L when the medium is pumped to transparency at λ_H

I_H: Intensity of light at wavelength λ_H

I_{Hsat}: Saturation intensity of absorption at pump wavelength λ_H

I_{Lsat}: Saturation intensity of gain at signal wavelength λ_L

$g(\omega)$: absorption/gain coefficient at frequency ω

ω_L, ω_H: Angular frequency of light at wavelength λ_L and λ_H

ϵ_0: Susceptibility of free space

m_e, m_h: Effective mass of electron and hole

n: refractive index

m_r: Reduced mass

m_0: electron mass

q: electron charge

ε: Reduced-mass energy

$\mu(\varepsilon)$: Dipole matrix element

μ_e, μ_h: Quasi-equilibrium chemical potential of electron and hole

$f_e(\varepsilon, \mu_e)$, $f_h(\varepsilon, \mu_h)$: Fermi-Dirac distribution of electron and hole

$D(\varepsilon)$: Density of states

γ: Dipole dephasing rate

τ_{sp}: spontaneous emission time

I_{L-in}, I_{L-out}: Incident and transmitted intensity of control beam

I_{H-in}, I_{H-out}: Incident and transmitted intensity of pump beam

P_{L-in}, P_{L-out}: Incident and transmitted peak power of control pulse

P_{H-in}, P_{H-out}: Incident and transmitted power of pump beam

r_{in}: incident pump/control or pump/signal intensity ratio

T_H: Transmission of pump beam

G_{sw}: Switching gain

I_{Hsat-L}: Saturation intensity of absorption at λ_H in a thick medium

τ_{p2}: 10%-90% transmission rising time in the transmission-out stage

ξ: Pumping rate coefficient for the transmission-out stage

D_c: Duty cycle of the signal or control pulses

R_{bit}: Data bit rate

E_{bit}: Energy consumption per bit

η: Coupling efficiency of power from the incident waveguide to the adjacent waveguide

$I_{H-CW} = P_{H-CW}/A_{eff}$

$I_{H-ON} = P_{H-ON}/A_{eff}$

$I_{L-ON} = P_{L-ON}/A_{eff}$

τ_{ON}, τ_{OFF}: Switch-on and switch-off time

A_d: Device area

α_p: Propagation loss coefficient for the QW-on-SOI waveguide

T_{FP}: Transmission of Fabry Perot cavity

R_f: Waveguide end-facet reflectivity (into the fundamental mode)

A_t: Single-pass total power loss along the device waveguide

C_{fw}: Free-space-to-waveguide coupling coefficient, including the input and output coupling efficiencies

A_S: Single-pass propagation loss along the SOI waveguide region of the device waveguide

A_{QS}: Total loss along the QW-on-SOI waveguide (transparency condition), including the top-down coupling loss and the propagation loss

C_{td}: Top-down coupling coefficient between the SOI and QW-on-SOI waveguides.

P_{in}, P_{out}: Input and output optical power before the first objective lens and after the

second objective lens.

c_1: Total input coupling efficiency, i.e. the percentage of the incident laser power (before the first objective lens) being coupled into the QW-on-SOI waveguide

c_2: Total output coupling efficiency, i.e. the percentage of the exited power (before coupled out of the QW-on-SOI waveguide) being detected by the photodetector

P_{sim}: Simulated mode power

I_{sim}: Simulated mode intensity

CHAPTER I INTRODUCTION AND MOTIVATION

1.1 Backgrounds

All-optical communication network was first proposed a quarter of century ago, with the original goal of keeping the entire network connections in the optical domain to eliminate the so-called electronic bottleneck. In the past decades, optical transmission has benefitted from the continued advancements of fiber technology, including the development of low loss optical fiber, Wavelength-Division Multiplexing (WDM) technology and the invention of erbium-doped fiber amplifier (EDFA), which dramatically increased the network capacity in a cost-effective manner. However, the complementary all-optical switching breakthrough is largely absent, leading to a modified reality that electronics remains at some points along the data path for signal regeneration and switching. The resultant system involves large number of transitions between optical and electrical domains, i.e. Optical-to-Electrical (OE) and Electrical-to-Optical (EO) or OEO conversions, which poses a lot of power consumption, space occupation, and reliability issues [1].

In spite of the recent development of photonic integration circuit (PIC) technology in the core optical network [2], where the discrete components in the traditional optical system, e.g. the transponder and wavelength demultiplexer, are monolithically integrated on a chip, resulting in a significant reduction of cost, power, space and reliability burdens, PIC technology does not remove the OEO paradigm. The ‘electronic bottleneck’ regarding the speed limitation and scalability issue of electronic switch, remains in the core electronic switching [2].

With the fast growing demand for network traffic speed and capacity, the data

bitrates continue to increase and the intensive electronic processing at the transponders consumes increasingly high power. If the same techniques are used in future system, the situation will be greatly exacerbated. Therefore, continual effort has been devoted into the development of all-optical processing devices in the past decades in order to eliminate the OEO architecture and bring back the original vision of all-optical communication network.

All-optical processing has been widely studied with different material systems and various device configurations, among which semiconductor-based all-optical processing devices have substantial interests due to the capability of realizing all-optical processing and optical interconnects in an integrated platform (the photonic integration circuit), which will benefit the next-generation ultrafast and power-efficient optical network [3-4].

To realize large-scale system integration on chip requires a series of considerations on the switching device components, including high switching speed, low device power consumption, CMOS compatibility, small device footprint, as well as switching gain. Switching gain describes the ability of using small signal beam power to switch a much larger beam power, which is an important device requirement to achieve cascadability and high fan-out for the switches.

Currently, the two mainstream technologies for semiconductor-based all-optical switches include semiconductor optical amplifier (SOA) and more recently silicon photonics. Implementation of ultrafast silicon photonic switch is largely based on the weak $\chi^{(3)}$ nonlinearity, which usually requires high-Q cavity enhancement to compensate the low $\chi^{(3)}$, resulting in very narrow bandwidth [5]. SOA-based all-optical switch utilizes the higher though slower $n^{(2)}$ effect, commonly with use of the Mach-Zehnder Interferometer (MZI) configuration, which usually resulted in a

millimeter-sized device [6-7]. Apart from the large device footprint, each SOA pair requires high electrical power (~0.5W per SOA) and careful electrical biasing at the optical transparency point to operate. The spontaneous emission noise added to the output signal by the switching process is another problem with the SOA based switch. Thus, those SOA switch has been around for many years, it has yet to see much practical network deployment.

In terms of switching gain, the intensity cross modulation between the pump and signal in the fast $n^{(2)}$ or $\chi^{(3)}$ processes fundamentally makes it impossible to achieve switching gain. As a result, in the SOA-based all-optical switches, additional optical amplifier has to be employed to amplify the output signal, which consumes even more electrical power and result in higher spontaneous emission noise. Some switching devices based on the slower switching processes such as thermal optics could result in some apparent switching gain. A reported silicon-based switch that exhibits switching gain utilizes the slow thermo-optic effect in a dual-ring-resonator structure, giving less than 0.1nm switching bandwidth and switching gain up to 3dB [8].

1.2 Photonic Transistor

More recently, a new switching scheme that utilizes the optically induced gain and absorption change to manipulate the coupling characteristics in a two-waveguide (2-WG) directional coupler was proposed. Based on the new switching scheme, a highly efficient all-optical switch, being termed as photonic transistor (PT), is theoretically demonstrated. It shows that such PT device can realize high-speed all-optical switching with switching gain and substantially lower power than the SOA

approach [9]. Spontaneous emission noise that is commonly present in the SOA-based switching device can be intrinsically avoided in the proposed switching scheme. Cascading ability is further promised by the switching gain. In addition, based on high-refractive-index-contrast nano-waveguide, the device footprint of PT is much smaller than that of SOA-MZI architecture. Good input/output isolation, broad operational bandwidth and free of biasing are promised in the proposed photonic transistor. Furthermore, the implementation of PT involves a pump supply and a signal beam at different wavelengths, thus intrinsically promising the wavelength conversion functionality, which is an important functionality to overcome the traffic blocking issue associated with the wavelength continuity constraint in the WDM all-optical network [1].

The initial study of PT was carried out based on the numerical simulation via a FDTD program incorporated with a 4-level 2-electron quantum mechanical model [10-12]. With the employment of two electron governed by the Pauli exclusion principle, the 4-level 2-electron model takes into account a simple picture of electron-hole pumping dynamics from the lower valence band to the upper conduction band. However, this model is still too simple to properly encompass the complex physical effects in the medium such as the semiconductor energy band structure, band filling effect with Fermi Dirac statistics, carrier induced gain and refractive index change, and carrier relaxation to thermal equilibrium after excitation. As a result, much of the transient and nonlinear behaviors in the medium were not included. Later, a more sophisticated model capable of modeling realistic semiconductor band properties, namely multi-level multi-electron model, was proposed for photonic transistor study [9]. In that model, the semiconductor band is modeled by many pairs of levels, which can quite accurately take into account of band filling effect and interband and

intraband transition. However, introducing sufficient number of levels to cover the full Fermi-Dirac distribution is important for accurate simulation. As a result, the computational efficiency is compromised for fully exploring the operational space and fast device design. According to our best knowledge, there have been no further studies reported on this new switching device since the initial proposal. Systematic studies and experimental realization of such photonic transistor device have been lacking.

This thesis aims at carrying out the first systematic study of the photonic transistor, establishing the progress of the photonic transistor research and delivering the useful information so that future photonic transistor research work can be built on them.

1.3 Outline of Dissertation

This dissertation is the first work that details and systemizes the study of photonic transistor from both the theoretical and experimental perspectives. In the theoretical part, we developed a new analytical approach that can properly address the complex carrier dynamics and light propagation characteristics simultaneously in a realistic semiconductor waveguide structure. Efficient parametric study of the photonic transistor performance is thus promised. A series of physical insights and important device design aspects are highlighted for the first time. Furthermore, we proposed two alternative architectures of photonic transistor to address the sever fabrication challenges associated with the original version. Theoretical studies show no compromise of the switching performance in these new architectures.

As for the experimental part, the first successful fabrication of photonic

transistor based on a hybrid silicon photonic integration platform is reported in this dissertation. Different fabrication process flows are developed and evaluated, which provides useful guidelines for the future fabrication work. The important material parameters that determine the switching performance of photonic transistor are experimentally characterized in this dissertation. All-optical switching with switching gain is demonstrated for the first time in a hybrid III-V/Si nano-photonic platform.

The dissertation is presented in the following manner:

We start with an introduction of the photonic transistor in Chapter II. The new switching physics proposed, namely Gain and Absorption Manipulation of Optical Interference (GAMOI), and the two complementary types of photonic transistor, namely energy-up photonic transistor (EUPT) and energy-down photonic transistor (EDPT), will be introduced. Advantageous performance of GAMOI-based photonic transistor will be highlighted, based on the Figure of Merit calculation as proposed in [9]. Subsequently, we focus on the discussion of the computational model for active semiconductor device simulation. It is highlighted that the widely used 4-level 2-electron FDTD model has a serious drawback that is it does not take into account of the realistic semiconductor band structure, thus cannot properly address the band filling effect, interband and intraband transition, etc. An advanced quantum mechanical FDTD model, named multi-level multi-electron FDTD (MLME-FDTD), was proposed to overcome the drawbacks of 4-level 2-electron FDTD model to simulate the photonic transistor realistically [9]. The results show that utilizing semiconductor as the active medium result in a switching performance for the GAMOI PT that is worse than that given by the initial idealized 4-level 2-electron FDTD medium.

In the subsequent three chapters, Chapter III, IV and V, a new analytical model

is developed that will enable a much more efficient theoretical studies of the operating space parameters for the EUPT. Starting with the coupled mode analysis for the directional coupler with one transparent and one absorptive waveguide, the AMOI effect is analytical formulated and the switching action induced by the absorption coefficient change in the absorptive waveguide is theoretically demonstrated. Subsequently, we developed an analytical formulation for the absorption and gain coefficients seen by the two monochromatic waves at different wavelengths interacting with a semiconductor medium. The formulation is verified with MLME-FDTD simulation for the case of InGaAsP bulk semiconductor, and is shown to be consistent. Next, the absorption/gain coefficient formulation is substituted into the propagation equations of the interacting lights to first study a simple pump-control switching scheme in a single-waveguide structure. Based on that, EUPT switching analysis is continued with the employment of the coupled mode formulation developed previously. The analytical formulation highlights the key parameters that determine the switching performance of EUPT, revealing some important device design aspects that have never been raised before. Using our analytical formulation and MLME-FDTD simulation, quantitative analysis of switching performance is carried out for InGaAsP bulk semiconductor based EUPT, showing one-order worse Figure of Merit than that given by the 4-level 2-electron FDTD simulation results [9].

In Chapter VI, we will investigate the characteristics of semiconductor quantum well (QW) in comparison with the bulk medium in affecting the switching performance of EUPT.

In chapter VII, experimental realization of EUPT in an integrated platform is presented with different fabrication approaches being developed, including quantum-

well-intermixing (QWI) assisted approach on InP-based substrate, and III-V-on-silicon integration approach assisted by direct wafer bonding technique. The fabrication challenges for each approach are discussed and compared, based on which the self-aligned QW-on-SOI architecture is chosen for final device fabrication.

Due to the fabrication challenges of achieving index matching between the passive SOI waveguide and the active QW-on-SOI waveguide in the 2-waveguide (2-WG) photonic transistor, two new device architectures for EUPT operation are proposed in Chapter VIII to alleviate the index-matching constraint. The proposed structures include the symmetric three-waveguide (3-WG) directional coupler structure and Mach Zehnder Interferometer (MZI) structure, the switching performance of which are systematically analyzed and compared based on our analytical method and MLME-FDTD simulation. The results show that 3-WG EUPT exhibits advantageous performance over the 2-WG EUPT and MZI-EUPT.

Lastly in Chapter IX, measurements of the devices fabricated are performed. The saturation intensity and small signal absorption coefficient of the InGaAsP-based strained QW medium are experimentally determined. All-optical pump-control switching with switching gain is demonstrated in the single-waveguide structure. However, switching effect in 2-WG EUPT, 3-WG EUPT and MZI EUPT hasn't been observed. The initial index-matching test in 2-WG EUPT is not successful, which requires further exploration. Meanwhile, some new concerns regarding the fabrication process and device design are highlighted. The future work plan will be presented in Chapter X.

Portions of this work have appeared in journal form in (Chen et al. 2012 [70]; Chen et al. 2013 [26]; Chen et al. 2014 [29]; Chen et al. 2014 [73]; Chen et al. 2014 [74])

CHAPTER II INTRODUCTION TO PHOTONIC TRANSISTOR

2.1 Working Principle of Photonic Transistor

The original photonic transistor device proposed by Y. Huang [9] is in the form of a two-waveguide directional coupler, consisting of one passive and one active waveguide. Directional coupler is a structure of two parallel waveguides lying in proximity so that the light power entering one waveguide can be transferred into the other. When the coupler is passive, complete power transfer (complete coupling) can be achieved at certain distance (coupling length) if the effective propagation indices of the two waveguides are identical. The presence of index mismatch between two waveguides will result in incomplete coupling of optical power. Therefore, changing the refractive index of the waveguide medium to alter the optical coupling characteristics in a directional coupler has been widely utilized for optical switching operation. On the other hand, it is less commonly known that changing the imaginary part of propagation index of the waveguide, i.e. absorption or gain, can also effectively manipulate the coupling characteristics of the coupler to achieve the similar switching effect. This effect, namely Absorption or Gain Manipulation of Optical Interference (GAMOI), is the basic working principle of the photonic transistor.

With GAMOI, all-optical switching can be realized in the photonic transistor by optically manipulating the absorption and gain in the active waveguide via, for example, carrier pumping or depletion dynamics in semiconductor medium involving

two optical beams. Depending on the relative wavelengths of the switching beam (signal beam) and the switched beam (pump supply beam), the implementation of PT can be categorized into two complementary approaches, namely energy-up PT (EUPT) and energy-down PT (EDPT), which achieve opposite wavelength conversion functionalities, and can be cascaded to realize broadband wavelength conversion.

The theoretical details regarding GAMOI effect will be discussed in Chapter III. Here, we will first present the general working principles and switching operations of EUPT and EDPT.

2.1.1 Energy-up photonic transistor based on AMOI scheme

The all-optical operation of EUPT adopts the Absorption Manipulation of Optical Interference (AMOI) scheme, which is shown in Fig.2.1a. EUPT consists of one passive and one active waveguide lying in proximity in parallel. The passive waveguide has larger band gap energy than the active waveguide. Three input/output ports are labeled as PS-IN (CW pump supply in), SIG-OUT (pulsed signal out) and SIG-IN (pulsed signal in). The CW pump supply (PS) beam at wavelength λ_H, with photon energy larger than the active medium band-gap energy, is launched from PS-IN port, coupled to the active waveguide and pumps it to transparency at λ_H. For the desired operation, PS is fully coupled out of the active waveguide at switch-off state. When a signal pulse at a longer wavelength λ_L is launched into SIG-IN, it sees the gain in the active waveguide and depletes the carriers to increases the absorption coefficient seen by λ_H. The increase of absorption coefficient alters the coupling characteristics of PS beam, causing part of PS power to exit at SIG-OUT. As a consequence, the signal at a longer wavelength λ_L is converted to a signal at the

shorter wavelength λ_H. Fig. 2.1b shows the band filling condition in the active medium at the switch-OFF state and switch-ON state respectively.

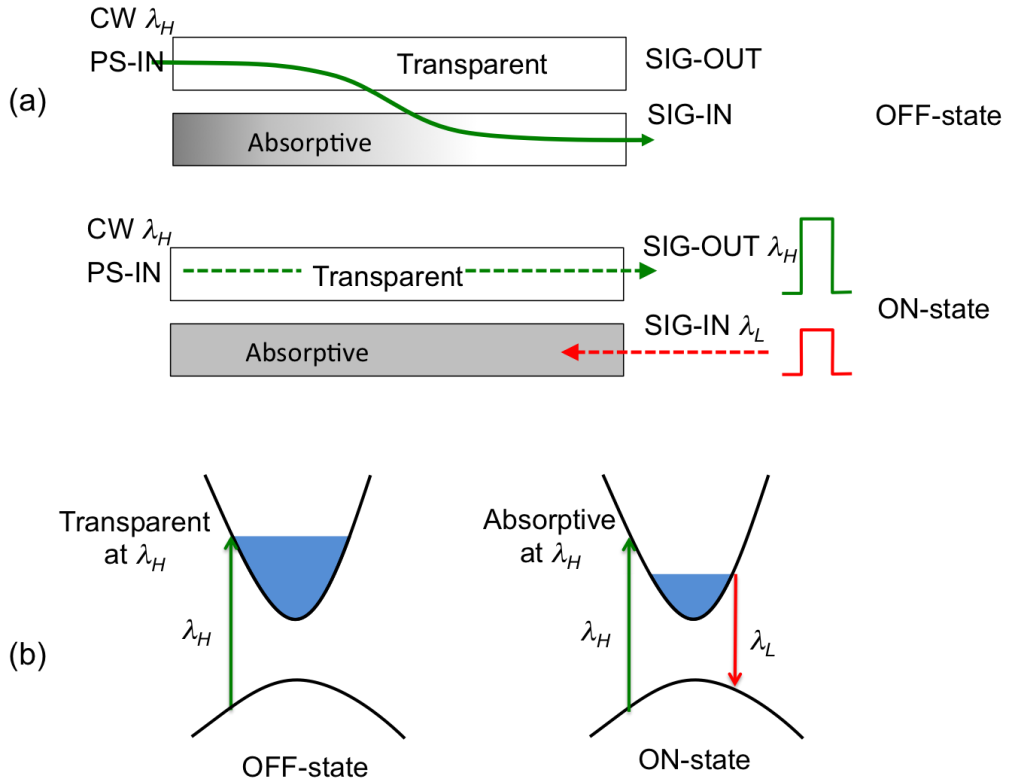

Figure 2.1: (a) switching operation diagram for energy-up photonic transistor (EUPT) based on absorption manipulation of optical interference (AMOI), (b) the carrier population change in the conduction band during the switching operation.

In comparison with refraction-based all-optical switching, such as $\chi^{(3)}$ switching or $n^{(2)}$ switching in SOA, the main advantage of AMOI scheme is the capability of achieving the switching gain. Switching gain describes the ability of using small signal beam power to switch a much larger beam power, which is an important device requirement to achieve cascadability and high fan-out for the switches. This is because in practice of $\chi^{(3)}$ and $n^{(2)}$ switching, when the weak signal beam induces π phase shift, the much stronger pump supply beam will experience self-phase modulation of multiple π, resulting in serious spectral broadening as well as

encountering multi-photon absorption. These problems make the devices not very cascadable, which is essential for complex photonic circuits. However, in AMOI scheme, as signal beam depletes the carriers in the active waveguide, it is amplified along the propagation, the carrier-depletion-induced absorption change would thus be enhanced the longer the control beam propagates along the waveguide and eventually would cause significant switch of the pump beam. In a sense, the weak signal beam gains the optical energy from the pump beam, which is then used to manipulate the strong pump beam, resulting in switching gain. Moreover, the AMOI effect causes the pump supply power to be partially switched to the passive waveguide, and therefore reduces the optical pumping at the active waveguide, which further assists in the carrier depletion process.

Since the pump supply beam can be strong, which can be several-orders higher than the saturation intensity of the active medium, the switch-OFF process governed by the saturation of the active medium can be very fast. On the other hand, the switch-ON process is governed by the ultrafast stimulated emission, thus the overall switching speed of EUPT can be ultrafast.

Furthermore, spontaneous emission noise that is commonly present in the SOA-based switching devices can be alleviated in the proposed EUPT architecture, due to the separation of the active medium and SIG-OUT port. When the signal beam is introduced, only the pump supply beam sees significant AMOI effect and is switched out of the passive waveguide. The spontaneously emitted light on the other hand will mostly remain in the active waveguide.

2.1.2 Energy-down photonic transistor based on GMOI scheme

The all-optical operation of EDPT is based on Gain Modulation of Optical

Interference (GMOI) scheme, which is shown in Fig.2.2a. The device structure is the same as EUPT, which consists of one passive and one active waveguide, with three input/output ports labeled as PS-IN, SIG-OUT and SIG-IN respectively. In EDPT, all three ports are along the active waveguide. The CW pump supply (PS) beam at a longer wavelength λ_L, with photon energy larger than the band-gap energy of the active medium, is launched from PS-IN and pumps the active waveguide to transparency, which is subsequently coupled to the passive waveguide. Without direct pumping, the remaining half of the active waveguide is either transparent or absorptive at λ_L, ensuring zero output of SIG-OUT port at switch-off state. When a signal pulse at a shorter wavelength λ_L is launched into SIG-IN port, it pumps the remaining half of the active waveguide to induce gain at λ_L. Then, part of the pump supply beam will exit SIG-OUT port, also the SIG-IN port, due to the GMOI effect. As a result, the input signal at shorter wavelength λ_H is converted to the signal at longer wavelength λ_L. Fig. 2.2b shows the band filling condition in the active medium at the switch-OFF state and switch-ON state respectively.

As we can see, ultrafast switching can also be achieved in EDPT, since the switch-ON and switch-OFF are governed by the fast optical pumping and stimulated emission process respectively. However, switching gain is absent in EDPT. The carriers excited by the incident signal beam produce optical gain seen at λ_L, resulting in the amplification of pump supply beam. Meanwhile the carrier depletion at λ_L will reduce the gain, suppressing the GMOI effect. Each input signal photon will at most result in one excited electron and each output signal photon will deplete one excited electron. Therefore, despite the pump supply beam can be very strong, the effective amount of switching is below unity quantum efficiency. As the output photon is at lower energy than the input photon, even with unity quantum efficiency, the power

gain will be less than one. Thus, there is no switching gain. In comparison to XGM-SOA, XGM-SOA requires careful electrical current biasing to achieve transparency at the signal wavelength (equivalent to the pump supply beam here), while EDPT does not require biasing operation.

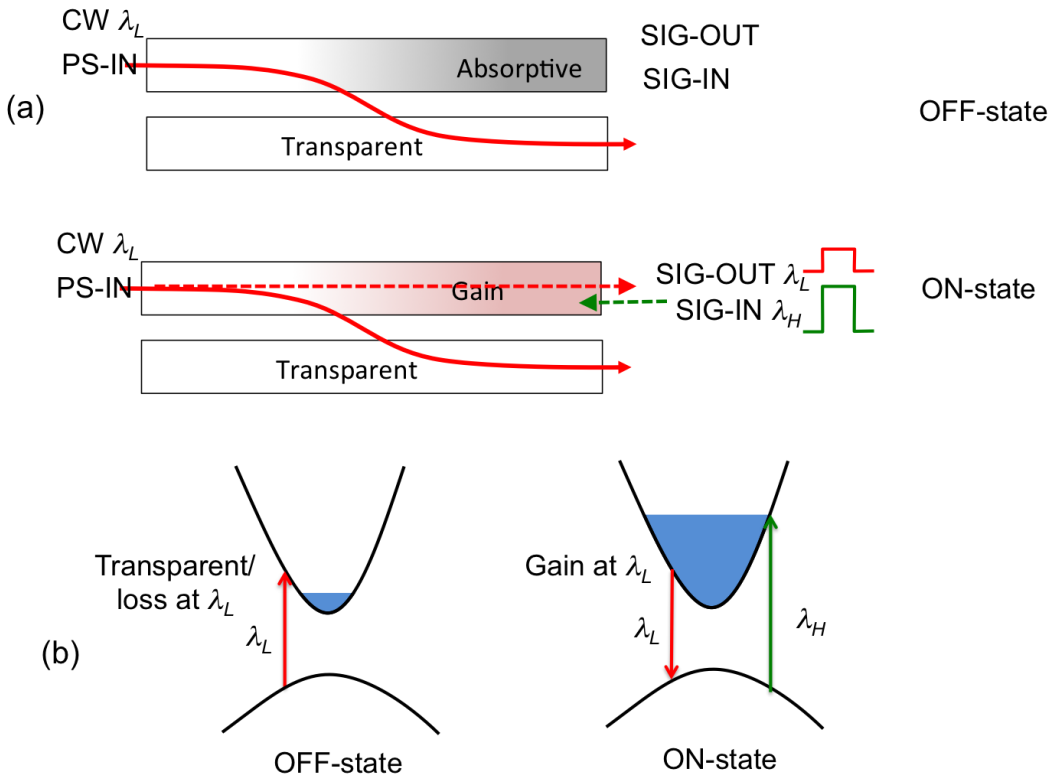

Figure 2.2: (a) switching operation diagram for energy-down photonic transistor (EDPT) based on gain manipulation of optical interference (GMOI), (b) the carrier population change in the conduction band during the switching operation.

2.1.3 Full photonic transistor (FPT)

In Fig. 2.3, EUPT and EDPT are cascaded to form a two-stage photonic transistor device, namely full photonic transistor (FPT), with broadband wavelength conversion capability and the switching gain [13]. The input signal at wavelength λ_{La} (red) is firstly converted and amplified to an intermediate pulse at a shorter

wavelength λ_H (green) through EUPT stage. Subsequently, the intermediate pulse is used to switch the pump supply beam at a longer wavelength λ_{Lb} (orange) over EDPT stage, generating the output signal pulse at λ_{Lb}. Note that λ_{Lb} can be either longer or shorter than λ_{La}, or even equal to λ_{La}. Meanwhile, switching gain can be achieved in FPT due to the EUPT stage.

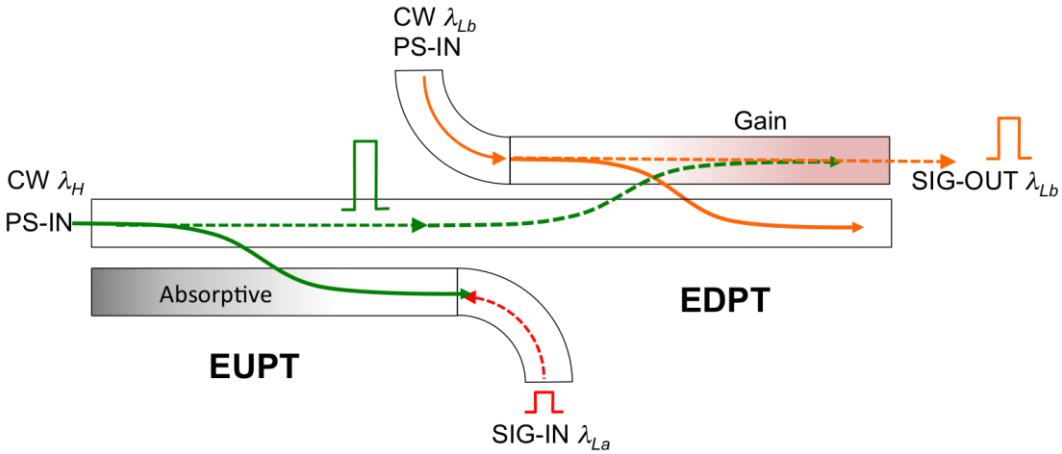

Figure 2.3: switching operation in a full photonic transistor by cascading EUPT and EDPT. $\lambda_H < \lambda_{La}, \lambda_{Lb}$.

2.2 FDTD Simulation of Photonic Transistor Switching: Review and Discussion

2.2.1 Introduction to 4-level 2-electrn FDTD model and Multi-Level Multi-Electron FDTD model

Recently, a quantum mechanical model of a 4-level 2-electron atomic system with the incorporation of the Pauli exclusion principle is introduced into the FDTD program for the simulation of complex photonic devices with active semiconductor medium [10-12]. Implementation of it has been commercially available, e.g. in Lumerical FDTD. A simple illustration of 4-level 2-electron treatment is shown in

Fig. 2.4 [14], where the electron interband and intraband dynamics in semiconductor medium under excitation of photon with photon energy above the band-gap energy is effectively represented by a 4-level 2-electron picture. At ground state, the two electrons stay at position 0 and 1. Under excitation of the photons, the electron at the corresponding photon energy will undergo interband excitation from 1 to 2, leaving a hole at the valence band. The electron at position 2 and the hole at position 1 will then undergo intraband decay to the band edge positions 3 and 0, respectively, through phonon-assisted processes. Subsequently, the electron and hole will recombine via radiative or nonradiative decay and the medium will return to the ground state. The employment of two electrons incorporates the Pauli exclusion principle, which provides a simplified model for electron-hole pumping dynamics in a semiconductor medium [14].

For the case of photonic transistor simulation that involves two monochromatic waves at different frequencies, the active medium is effectively represented by two dipoles with resonant wavelengths at the pump supply wavelength and input signal wavelength, and each dipole is homogeneously broadened by the dipole dephasing time, which is typically in the scale of 100 fsec. The detailed formulation is available in [10-12], which will not be discussed further in this dissertation.

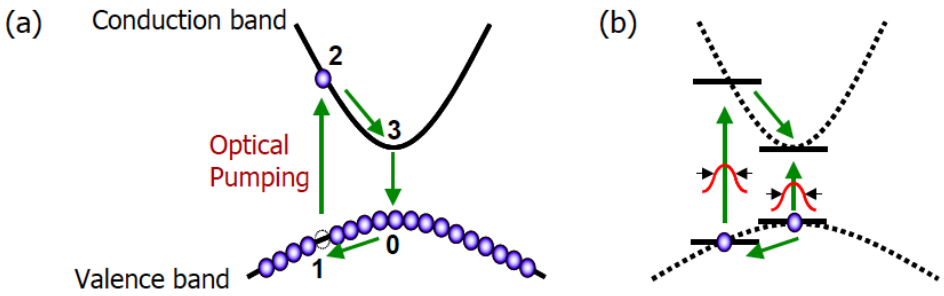

Figure 2.4: electron dynamics in 4-level 2-electron model: (a) electron interband and intraband dynamics in semiconductor medium under excitation of photon with above-bandgap energy; (b) representation by four energy levels and two electrons [14].

The 4-level 2-electron model represents an ideal medium for the device. One of its potential practical realizations would be with use of a semiconductor medium with a conduction and valence band structure having a direct energy bandgap. However, such a semiconductor medium cannot be adequately modeled by a 4-level 2-electron system as it is too simple to properly encompass the complex physical effects in the medium such as the semiconductor energy band structure, band filling effect with Fermi Dirac statistics, carrier induced gain and refractive index change, and carrier relaxation to thermal equilibrium after excitation. As a result, much of the transient and nonlinear behaviors in the medium were not included.

To more accurately model semiconductor medium dynamics, additional energy levels and electron dynamics need to be accounted. The typical approach to modeling carriers in semiconductor band structure involves solving Bloch equations at many energy states in the momentum space (k-states) [15,16]. In FDTD simulation, the structure to be simulated is first discretized spatially, then the electromagnetic field at each spatial point is updated at each time step, making FDTD an intrinsically numerically intensive method. Now if using the typical approach of semiconductor modeling, then for each grid, the carrier distribution function in many k-states has to be updated at each time step [17], making the computational time forbiddingly long [14].

Based on the 4-level 2-electron FDTD model, a more sophisticated quantum mechanical model, namely dynamical-thermal-electron quantum-medium FDTD model (DTEQM-FDTD) or simply as multi-level multi-electron FDTD (MLME-FDTD), is recently developed to address the complex carrier dynamics in a realistic semiconductor band structure with high computational efficiency [18-19]. In the MLME model, the conduction and valence band states are divided into several

groups, each of which is represented by a single dipole with broadened width, as shown in Fig. 2.5 [14]. It has been pointed out in the 4-level 2-electron model that due to the short dipole de-phasing time in semiconductor (~100fsec), comparing to the spontaneous decay lifetime of 3nsec, one can represent many spontaneous-decay-broadened k states by one effective k state, provided the electron-scattering process that affect the dipole phase is lumped into an effective dipole dephasing time. Further studies have been performed to show that carrier dynamics can then be accurately represented by a finite number of dipoles with optimal spacing, linewidth and with a parabolic distribution to represent the parabolic nature of the band structure of the semiconductor medium. As a result, complete band characteristics can be represented by only a few such dipoles. Take an example of a dipole dephasing time of ~50fsec, giving a spectral broadening of $\Delta\lambda$~50nm (FWHM) at λ=1550nm. Employment of only a few such dipoles is able to cover a wavelength range of 100-300nm, which is sufficient for various optoelectronic and photonic device application.

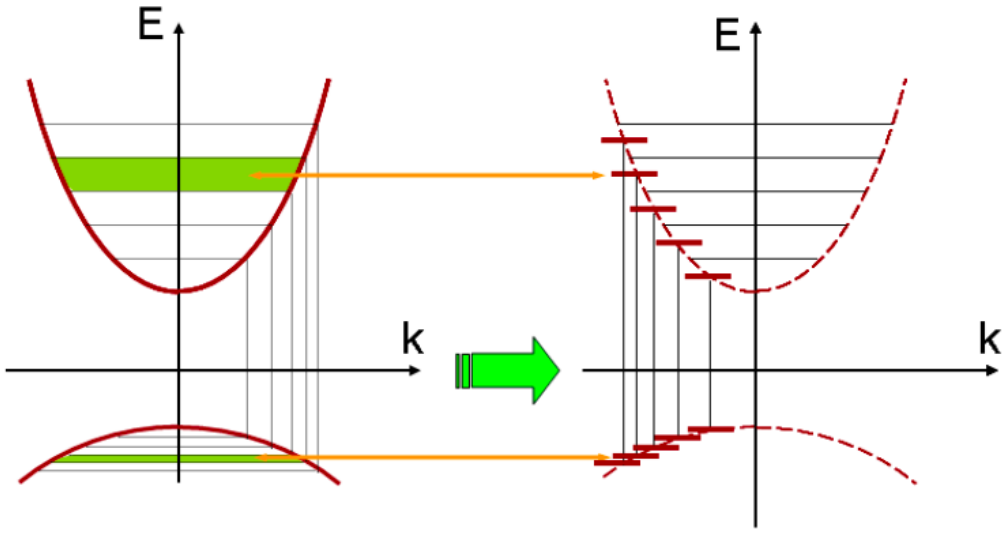

Figure 2.5: the multi-level multi-electron model for FDTD simulation of semiconductor material [14].

With MLME-FDTD, interband carrier radiative or nonradiative decays,

intraband carrier relaxation, and interband transition (gain or absorption) over a large bandwidth can be addressed. In addition, implementation of Pauli Exclusion Principle for the transitions between any two levels will result in carrier band-filling effect.

2.2.2 Compare 4-level 2-electron FDTD model and MLME FDTD model

Here we perform a single test to show the discrepancy between the two FDTD models in the simulation of the carrier-depletion induced absorption change. Consider a short active waveguide with 4μm length, as shown in Fig. 2.6a. The CW beam at $\lambda_H = 1350$nm with modal peak intensity at 5MW/cm^2 is launched into the waveguide to pump it to transparency, i.e. 100% transmission. After that, a 50ps square pulse at $\lambda_L = 1450$nm with peek intensity of 0.5MW/cm^2 is incident from the opposite end of the waveguide. Due to the carrier depletion at 1450nm, the absorption seen by 1350nm increases, thus the transmission of 1350nm reduces.

For the 4-level 2-elecdtron FDTD simulation in this case, the resonance wavelengths of two dipoles are set at 1350nm and 1450nm. For MLME-FDTD simulation, we are allowed to define the band gap wavelength and effective masses of electron and holes (m_e and m_h) to characterize the energy band structure, which are not explicitly involved in the 4-level 2-electron FDTD program. Here we set the band gap wavelength at 1562.5nm, $m_e = 0.046m_0$ and $m_h = 0.36m_0$, in which case the small-signal absorptions at 1450nm is comparable with the value from the 4-level 2-electron FDTD, i.e. ~$0.6\mu m^{-1}$. Both models adopt the same spontaneous emission time (1ns), intraband transition time (100fs) and dipole dephasing frequency (3.98x10^{13} rad/s). In addition, in this dissertation, we will utilize a universal MLME-FDTD model with a total of 20 pairs of energy levels, i.e. 40 energy levels and 20 electrons. Two adjacent dipoles have a wavelength spacing of 25nm. Thus, a total of

500nm wavelength range (given by 500nm = 20 x 25nm) is covered in the simulation, which is sufficiently broad to simulate the dynamics of the Fermi-Dirac carrier distribution under the dual-wavelength interaction situation. Take note that the MLME-FDTD program that has been used in this dissertation only simulates the bulk-semiconductor system.

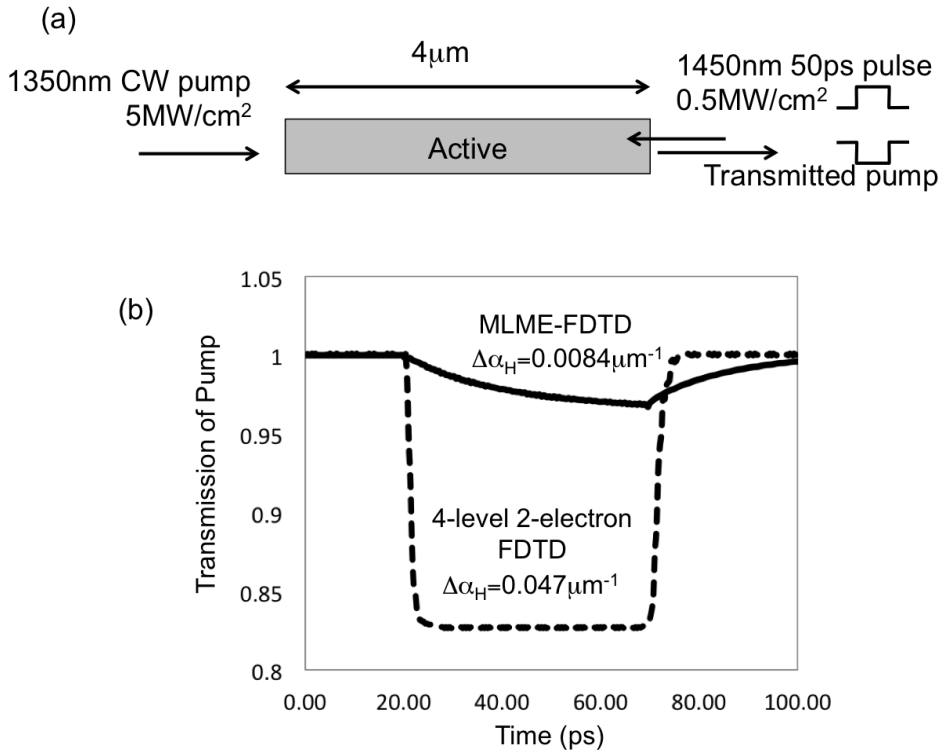

Figure 2.6: (a) 4μm single active waveguide with CW pump beam at 1350nm and square signal pulse at 1450nm launched from the opposite ends of the waveguides. (b) The transmission profile of the pump beam simulated by 4-level 2-electron FDTD (dash) and 40-level 20-electron FDTD (solid).

The transmission profiles of the 1350nm CW beam simulated by 4-level 2-electron FDTD (dash) and MLME-FDTD (solid) are plotted in Fig. 2.6b, and the induced absorption coefficients $\Delta\alpha_H$ are calculated correspondingly. As we see, with 4-level 2-electron FDTD simulation, the transmission drops by ~12% upon the incidence of the 1450nm pulse, giving $\Delta\alpha_H = 0.047\mu m^{-1}$, while with MLME-FDTD, the transmission drop is only ~3% and the induced absorption coefficient is 5

times smaller, giving $\Delta\alpha_H = 0.0084\mu m^{-1}$. Furthermore, we also notice the carrier depletion speed and the pumping speed are both much slower with the MLME-FDTD simulation due to the inclusion of band filling effect.

2.2.3 Initial studies of GAMOI photonic transistor performance

The first study of PT based on the MLME-FDTD simulation is carried out with the incorporation of 10 pairs of levels (20 levels, 10 electrons) for InGaAsP-based bulk semiconductor system [9]. With two adjacent dipoles having wavelength spacing of 25nm, simulation covers 250nm wavelength range. It shows that 100Gbps switching with switching gain of 10 can be achieved in GAMOI photonic transistor with micro-watt switching power and as low as ~2mW pump supply power. The overall switching performance of photonic transistor is further evaluated quantitatively based on a Merit Factor proposed [9,14], which is given by

$$MF = \frac{N_{ch} G_{sw} R}{(P_{PS} + P_{SIG}) A_d} \tag{2.1}$$

where P_{PS} and P_{SIG} stand for the pump-supply power and input signal power respectively. R is the bit rate and A_d represents the device area. G_{sw} is used to denote the switching gain. N_{ch} corresponds to the optical channels that the device can process, which is a measure of the operational bandwidth of the optical switching device. For the typical electronic transistor in microprocessor [20], we have R~3.8 GHz, $P_{PS} + P_{SIG}$ ~0.24mW (V~1.1Volt, I_{on}~1.38mA/μm), G_{sw} ~2, $A_d \sim 0.0256\mu m^2$ (160nm transistor pitch), and N_{ch} =1, giving for the electronic transistor an equivalent Merit Factor of $MF_{ET} = 1.2 \times 10^{27} (J^{-1} m^{-2})$. It is

subsequently used to normalize the MF of photonic transistor to give the relative Figure of Merits (FOM), i.e. $F=MF_{PT} / MF_{ET}$. An ideal photonic transistor device shall have F value approaching or exceeding 1 to be competitive with electronic transistor.

The initial study shows that the relative figure of merit F for the GAMOI photonic transistor is ~0.012, which is 10^5x higher than the for typical the $\chi^{(3)}$ and SOA based switches, as shown in Table 2.1. It is also highlighted in [9] that further engineering the active medium and waveguide geometry can improve the device power consumption and reduce the device footprint, thus can further increase the FOM of the PT to make it comparable with the electronic transistor.

Table 2.1: Relative figure of merit for various photonic switching devices (1) $\chi^{(3)}$ of semiconductor [21,22], (2) SOA BASED [23-25], (3) GAMOI

	$X^{(3)}$	SOA	GAMOI
P_{PS} (at 100Gbps)	0	~400mW	~4mW
P_{SIG} (at 100Gbps)	~1W	~0.01mW	~400μW
Switching gain G_{sw}	~0.1	~0.1	10
Device area A_d (μm^2)	~10,000	~10,000	300
Max. Data Rate $(1/T_{sig})$	~5Tb/s	~100Gbps	~100Gbps
N_{ch}	~1	~20	~20
F	~$4x10^{-8}$	~$4x10^{-7}$	~0.012

Next, with adoption of the same energy band parameters, we use the 40-level 20-electron model to repeat the EUPT switching simulation presented in [9]. The wavelengths of the CW pump supply and the 50ps input signal pulse are at λ_H =1450nm and λ_L = 1550nm respectively, and the modal peak intensities in the active waveguide are at $3MW/cm^2$ and $0.12MW/cm^2$ respectively. For semiconductor waveguide with a high refractive index core material with n=3.4

surrounded by a low refractive index cladding material with n=1.45 and a cross-sectional dimension of 250nmx350nm, which gives a mode area of $A_{eff} = 0.043\mu m^2$ at 1450nm, the corresponding pump supply power and signal pulse peak power are 1.29mW and 0.43 μW respectively. The coupling length or device length is $18\mu m$.

The resultant dynamic switching is shown in Fig. 2.7, where the instantaneous optical power of the input signal (dash line) and output signal (solid lines) is plotted against the simulation time. The blue solid curve shows output signal simulated by the 20-level-FDTD program [9], and the red curve shows the output signal simulated by the 40-level-FDTD program. We find switching effect is nearly absent in the examined EUPT structure when 40-level-FDTD simulation is adopted. The absorption coefficient change induced by the carrier depletion at the signal wavelength could have been overestimated with the 20-level model.

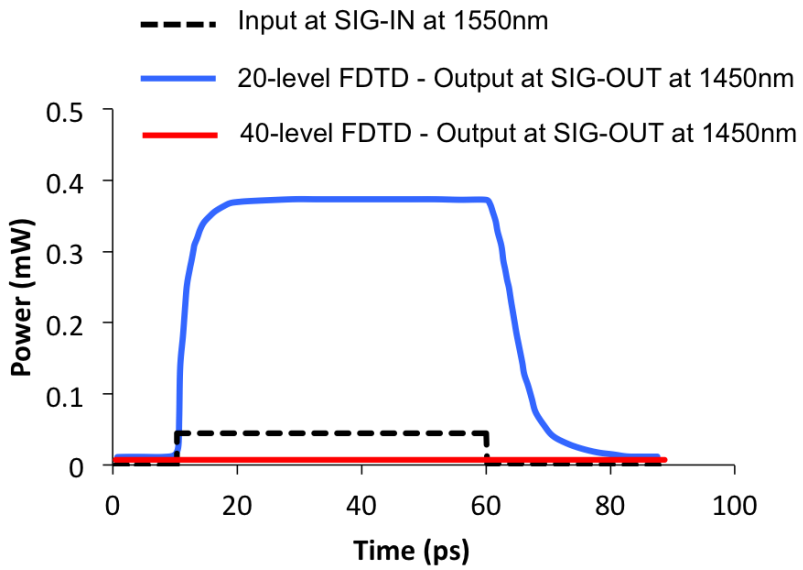

Figure 2.7: dynamic switching of bulk-InGaAsP-based EUPT with CW pump supply beam at 1450nm and 50ps input signal pulse at 1550nm wavelength (dash line). The output signal at 1450nm obtained from 20-level FDTD simulation (blue solid line) and 40-level FDTD simulation (red solid line) are compared.

The discrepancy between the two MLME-FDTD simulations could be due to insufficient number of levels adopted in [9]. Separate calculation shows the Fermi-level for the medium of interest pumped to transparency at 1450nm is at 1420nm, while the 20-level model is able to cover the wavelength range up to 1350nm. Such coverage is marginal for representing the complete Fermi-Dirac distribution. Unfortunately, further studies on PT have been lacking. Based on the above test, we can see a more systematic and in-depth discussion on the switching performance and switching physics of the photonic transistor is needed. Additional concern with the MLME-FDTD model for photonic transistor simulation is the long simulation time. It can take a minimum of 2 days for just one case simulation, which is thus not suitable for full exploration of the operational space and fast device design. Therefore, a more efficient simulation approach is required.

2.3 Conclusion

In this chapter, we reviewed the working principle of GAMOI photonic transistor device and highlighted its significantly advantageous switching performance over the current mainstream all-optical switching technologies ($\chi^{(3)}$ and SOA) [9]. We also introduced a MLME-FDTD quantum mechanical model to the overcome the main drawbacks of the widely used 4-level 2-electron FDTD model, such that to properly address the complex carrier dynamics in semiconductor medium and thus simulate the photonic transistor realistically. We also utilized the MLME-FDTD model incorporated with 20 pairs of energy levels to repeat the exemplary EUPT switching presented in [9]. It shows an overestimation of switching gain exists with the adoption of fewer energy pairs in the MLME FDTD simulation. Thus the 40-level 20-electron model will be adopted in this thesis.

Although MLME-FDTD provides a quite accurate way of evaluating the switching performance of GAMOI photonic transistor, the simulation is very time consuming, which is not suitable for parametric device studies. In the next chapter, a novel analytical method is developed, based on which parametric study of photonic transistor is performed and important device design aspects that have never been raised before will be highlighted.

The carrier transition physics in the GMOI-based EDPT switching is fundamentally similar to the conventional cross-gain modulation (XGM) based SOA, and the gain manipulation of optical interference is essentially the same as the absorption manipulation approach except for the opposite sign in the imaginary index of the active medium. Therefore, the detailed studies of GMOI-based EDPT will not be extended in this dissertation. The AMOI-based EUPT is the key stage that provides switching gain to the full photonic transistor, which will be focused on in this dissertation.

CHAPTER III THEORETICAL STUDIES OF EUPT PART I: Static Switching Studies and Development of an Efficient Effective Semiconductor 2-Beam Interaction Model with 4-Level Like Rate Equations

The PT devices can be simulated in the spatial temporal domain using the MLME-FDTD method we have. The problem of FDTD in general is that while it can give almost all the performance information for the devices with a good level of accuracy without much approximation, it is very slow. Thus, to fully investigate the performances of the PT devices, it would be very difficult to rely only on the MLME-FDTD model. To address this issue, a powerful semi-analytical method is developed that make certain simplifying assumptions and yet is able to take band-filling and saturation into account. It gives a set of 4-level like equations that can be solved semi-analytically. We have checked the reasonable accuracy of this approach against the MLME-FDTD results and found good agreements. A set of performance curves for the PT is then generated using this simplified approach. Another advantage of this approach is that it is able to produce physical insights that are hard to obtain from pure numerical method based on MLME-FDTD.

In the following three chapters, a novel analytical approach is developed to study the switching performance of EUPT, including the power consumption, switching speed and switching gain. Important design aspects, such as the pump supply and signal beam conditions, material properties and coupler dimensions, for optimizing the device performance will be discussed. Meanwhile, the analytical

calculation will be examined with the employment of the Multi-Level Multi-Electron FDTD (MLME-FDTD) model with model parameters fitted to simulate the InGaAsP bulk semiconductor system.

As the working principle of EUPT has been illustrated in Fig. 2.1, here we just want to clarify the notations of the parameters that will be involved in the later discussion. As shown in Fig. 3.1, the CW pump supply beam at wavelength λ_H, is launched from the passive waveguide, with optical power denoted by P_{H-CW}. The subscript H refers to the higher photon energy among the operating light. The signal pulse at a longer wavelength λ_L is launched into the opposite end of the active waveguide, with OFF-state power denoted by P_{L-OFF} and ON-state power denoted by P_{L-ON}. The subscript L refers to the lower photon energy compared to the pump supply. The increase of absorption coefficient alters the coupling characteristics of pump supply beam, causing part of pump supply power P_{H-CW} to exit from the passive waveguide to generate the output signal. The output signal power at switch-off state is denoted by P_{H-OFF} and at switch-ON state is P_{H-ON}. It is important to note that all the power parameters referred to here represent the instantaneous power, rather than the average power.

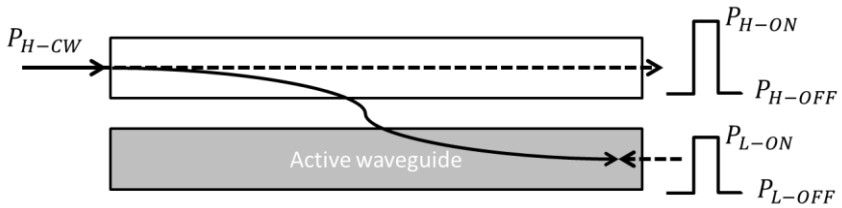

Figure 3.1: Switching action in EUPT. P_{H-CW} is the continuous pump supply power at wavelength λ_H, incident into the passive waveguide. P_{L-ON} and P_{L-OFF} denote the ON- and OFF-state input signal power at wavelength λ_L. P_{H-ON} and P_{H-OFF} denote the ON- and OFF-state output signal power at wavelength λ_H. Solid arrow shows the light propagation at switch-OFF state and dash arrows show the switch-ON state.

3.1 Static Switching Studies of Absorption Manipulation of Optical Interference - Coupled Mode Analysis

First of all, we will use the coupled mode theory to illustrate the basic working principle of EUPT, i.e. via Absorption Manipulation of Optical Interference (AMOI), which utilizes the optically induced absorption change in one constituent waveguide of a directional coupler to manipulate the coupling characteristics of light and achieve switching action. The formulation will be utilized to analyze the switching performance in the later sections.

Consider a two-waveguide (2-WG) directional coupled composed of one passive waveguide and one absorptive waveguide as shown in Fig. 3.2. The passive waveguide, waveguide 1 (WG1), has a propagation constant of β_1. The absorptive waveguide, WG2, has the propagation constant of the form $\beta_2 = \beta_{2r} + i\alpha_{am}$. The imaginary part α_{am} is the absorption coefficient of the optical field amplitude, as denoted by the subscript am. The optical field is launched from WG1 at z=0.

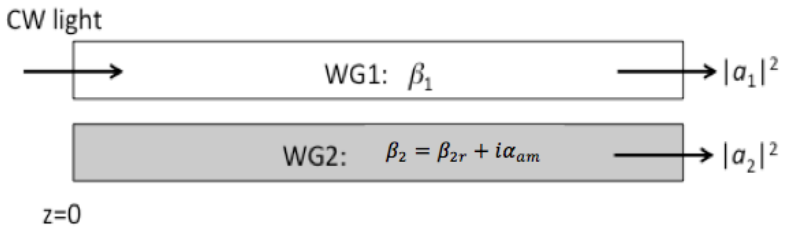

Figure 3.2: Two-waveguide coupler with a passive waveguide and an absorptive waveguide. The continuous wave is launched into the passive waveguide at z=0. The transmitted power from WG1 and WG2 are denoted by $|a_1|^2$ and $|a_2|^2$.

The coupled mode equations for this 2-WG directional coupler are given as follows.

$$-i\frac{da_1}{dz} = \beta_1 a_1 + \kappa_{12} a_2 \,, \tag{3.1a}$$

$$-i\frac{da_2}{dz} = \beta_2 a_2 + \kappa_{21} a_1 \,, \tag{3.1b}$$

where a_1 and a_2 are the normalized field amplitudes in WG1 and WG2 respectively. κ_{12} and κ_{21} are coupling coefficients between two waveguides. Substitute Eqn. (3.1) into the energy-conservation relation,

$$\frac{d(|a_1|^2 + |a_2|^2)}{dz} = -2\alpha_{am}|a_2|^2, \tag{3.2}$$

we get $\kappa_{12} = \kappa_{21}^*$. For simplicity, we write $\kappa_{21} = \kappa$ and $\kappa_{12} = \kappa^*$.

The coupled mode equations in Eqn. (3.1) can be solved analytically. The general solution of $a_1(z)$ for the initial condition $a_1(0) = 1$ and $a_2(0) = 0$ are given by

$$a_1(z) = \frac{\beta_1 - \beta^-}{\beta^+ - \beta^-} e^{i\beta^+ z} + \frac{\beta^+ - \beta_1}{\beta^+ - \beta^-} e^{i\beta^- z} \,, \tag{3.3}$$

where

$$\beta^{\pm} = \frac{\beta_1 + \beta_{2r}}{2} \pm \gamma + \frac{i}{2}(\alpha_{am} \pm b) \tag{3.4}$$

are the eigenmode propagation constants, and γ and b are given by

$$2\gamma + ib = \sqrt{\Delta\beta^2 - \alpha_{am}^2 + \frac{\pi^2}{L_{C0}^2} + 2i\alpha_{am}\Delta\beta} \,. \tag{3.5}$$

Here a length-unit parameter L_{C0} is used to represent κ through $L_{C0} = \frac{\pi}{2|\kappa|}$. The longer L_{C0} represents the weaker coupling strength. L_{C0} is equal to the complete coupling length of a 2-WG directional coupler at index matching condition. $\Delta\beta = \beta_{2r} - \beta_1$ gives the effective propagation constant difference between two waveguides, which relates to the effective propagating refractive indices (called the model indices) mismatch for the optical propagating modes in the two coupled

waveguide arms through $\Delta\beta = \Delta n_{eff}\frac{2\pi}{\lambda}$. λ is the wavelength of light. Explicit expressions of γ and b in Eqn. (3.5) are given in [26].

The optical power variation along WG1 is thus determined, which gives

$$|a_1(z)|^2 = \frac{e^{-\alpha_{am}z}}{4\gamma^2 + b^2}\left\{\left[\Delta\beta\cosh\left(\frac{bz}{2}\right) + 2\gamma\sinh\left(\frac{bz}{2}\right)\right]^2 + \left[\alpha_{am}\cosh\left(\frac{bz}{2}\right) + b\sinh\left(\frac{bz}{2}\right)\right]^2 - (\Delta\beta^2 + \alpha_{am}^2) + [2\gamma\cos(\gamma z) + \alpha_{am}\sin(\gamma z)]^2 + [b\cos(\gamma z) - \Delta\beta\sin(\gamma z)]^2\right\}. \quad (3.6)$$

Next we show how the solution of Eqn. (3.6) can be used to illustrate the switching operation in EUPT.

i. Switch-OFF state, $\alpha_{am} = 0$

At switch-off state, the active waveguide is pumped to transparency, i.e. $\alpha_{am} = 0$. Eqn.(3.6) becomes

$$|a_1(z)|^2 = 1 - \left[1 - \left(\frac{\Delta\beta}{2\gamma}\right)^2\right]\sin^2(\gamma z), \quad (3.7)$$

where $\gamma = \frac{1}{2}\sqrt{\Delta\beta^2 + \frac{\pi^2}{L_{Co}^2}}$.

The device length of EUPT is designed to be one coupling length at transparency condition, so that the output power from WG1 at switch-off state, i.e. P_{H-OFF} as denoted in Fig. 3.1, is minimized. Coupling length is defined as the minimum distance by which maximum power of incident light is coupled out of the incident waveguide. Thus when Eqn.(3.7) reaches the minimum value, the corresponding z gives the coupling length

$$L_{C2} = \frac{L_{C0}}{\sqrt{\left(\frac{\Delta\beta L_{C0}}{\pi}\right)^2 + 1}}, \tag{3.8}$$

where the subscript 2 in L_{C2} indicates the coupling length for the 2-WG coupler.

Substituting Eqn. (3.8) into Eqn.(3.7) gives the power output of WG1 normalized to the input pump supply power at switch-off state, which is given by

$$\frac{P_{H-OFF}}{P_{H-CW}} = 1 - \frac{1}{\left(\frac{\Delta\beta L_{C0}}{\pi}\right)^2 + 1} = 1 - \left(\frac{L_{C2}}{L_{C0}}\right)^2. \tag{3.9}$$

In the case of $\Delta\beta = 0$, the effective modal indices of the two coupled waveguides are equal. As a result, the incident pump power is completely coupled out of WG1, giving $P_{H-OFF} = 0$ and $L_{C2} = L_{C0}$ becomes the complete coupling length. This is the ideal operational condition for EUPT to achieve high-extinction-ratio switching.

However, it is important to note that, in real application, material asymmetry between passive and active waveguides poses fabrication complexity and challenges in achieving effective modal index matching. Fabrication discrepancies based on current technology can easily compromise coupling efficiency particularly in high-refractive-index-contrast nano-waveguide structures. Moreover, asymmetric coupler structure is particularly sensitive, as dispersion of individual constituent waveguide differs, leading to different coupling efficiency at different wavelength, which limits the operational bandwidth. Meanwhile, pumping up the active medium will change the refractive index of it, which further increases the uncertainty in achieving effective modal index matching. From Eqn. (3.8) and Eqn. (3.9), we can see that the

sensitivity of coupling length and coupling efficiency to the model index mismatch $\Delta\beta$ is dependent on the complete coupling length L_{C0}. The longer L_{C0} we target, the more sensitive the coupler is to the undesired model index mismatch. Therefore, with the aim of reducing the fabrication challenge, it is referred to have a shorter device.

ii. Switch-ON state $\alpha_{am} > 0$

At switch-ON state, the input signal entering the active waveguide depletes the carriers and increases the absorption coefficient seen by the pump supply beam. The output signal power at switch-ON state, which is normalized to the input pump supply power, i.e. $\frac{P_{H-ON}}{P_{H-CW}}$, can be obtained from Eqn. (3.6) with $z = L_{C2}$ substituted in, where L_{C2} is given by Eqn. (3.8). The resultant expression depends on two parameters only, which are $|\Delta\beta|L_{C0}$ and $\alpha_{am}L_{C2}$. In Fig. 3.3, $\frac{P_{H-ON}}{P_{H-CW}}$ is plotted versus $\alpha_{am}L_{C2}$ at different $|\Delta\beta|L_{C0}$. The points at $\alpha_{am}L_{C2} = 0$ corresponds to $\frac{P_{H-OFF}}{P_{H-CW}}$. As we can see, with the increase of absorption in WG2, the incident power is partially switched out of WG1, resulting in the increase of P_{H-ON}. Meanwhile, by increasing L_{C2}, i.e. employing longer device, P_{H-ON} can be further increased.

On the other hand, as effective modal index mismatch increases, P_{H-OFF} increases, and the optical modulation amplitude $\Delta P_H = P_{H-ON} - P_{H-OFF}$ induced by a fixed $\alpha_{am}L_{C2}$ decreases. As a result, the extinction ratio of the output signal $r_e = P_{H-ON}/P_{H-OFF}$ drops significantly.

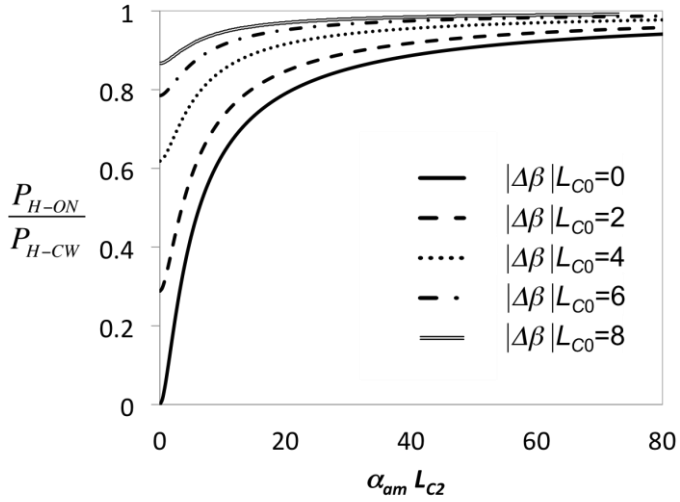

Figure 3.3: $\frac{P_{H-ON}}{P_{H-CW}}$, represented by the power transmission from WG1 at $z = L_{C2}$versus $\alpha_{am}L_{C2}$ at different $|\Delta\beta|L_{C0}$. $|\Delta\beta|L_{C0}$.varies from 0 to 8 corresponds to the effective modal index mismatch Δn_{eff} from 0 to 0.02 with $L_{C0} = 100\mu m$ and 1550nm light wavelength.

3.2 Development of an Efficient Effective Semiconductor 2-Beam Interaction Model with 4-Level Like Rate Equations

In the last section, the absorption induced switching action in EUPT is analytically formulated with a uniform and arbitrary value of absorption coefficient along the active waveguide. However, in the actual switching operation, as shown in Fig. 2.1, the absorption coefficient, seen at the pump supply wavelength at λ_H induced by the carrier depletion at the signal wavelength λ_L, is a complicated function of the operating wavelengths λ_H and λ_L, the corresponding intensities, as well as the energy band structure of the active medium. Furthermore, since the absorption coefficient varies with the light intensities and at the same time attenuates the pump intensity, it should be coupled with the propagation characteristics of the operating beams and vary spatially.

The available approaches that can self-consistently deal with the optical field propagation and light-matter interaction in a semiconductor waveguide include the MLME FDTD simulation [10-13, 18,19] and the Bloch-equation-based semi-analytical model [27]. FDTD simulation incorporated with carrier dynamics calculation is typically time consuming, thus not suitable for parametric study of complex optical device. The Bloch-equation-based semi-analytical model, that utilizes the planewave-based eigenmode expansion technique and mode-matching analysis, is computationally more efficient than FDTD, but still requires intensive computation associated with iterative mode solving and mode-matching analysis. Moreover, due to the assumption of the quasi-equilibrium carrier distribution, Bloch-equation-based semi-analytical model cannot properly deal with the high input power cases when deviation from Fermi-Dirac statistics occurs.

In this section, we will derive a simple analytical expression for the absorption coefficient and gain coefficient seen by the two interacting optical fields at different wavelengths in a semiconductor medium. The formulation is developed based on a 4-level like picture, which provides a dynamic picture for the interband and itraband transition of carriers with the presence of two monochromatic fields at different wavelengths. The realistic semiconductor energy band features, on the other hand, can be preserved through the employment of the generic parameter – saturation intensity. With the Free-carrier formulation, the saturation of interband absorption and gain takes into account of the density of states of the semiconductor energy band and characterize the band filling effect with the Fermi-Dirac statistics. At the end, our analytical formulation is shown to be consistent with the MLME-FDTD simulation.

3.2.1 4-level 1-electron picture

We first consider a 4-level system as shown in Fig. 3.4. The energy difference between level 0 and 3 is equal to the photon energy of pump supply beam hc/λ_H, and the energy difference between level 1 and 2 is equal to the photon energy of signal beam hc/λ_L, where h is the Planck's constant, c denotes the speed of light. The carrier densities at these four levels are denoted by N_0, N_1, N_2 and N_3 respectively. Suppose the intensities of pump supply beam and signal beam are I_H and I_L. The rate equations in this 4-level system are given as follows.

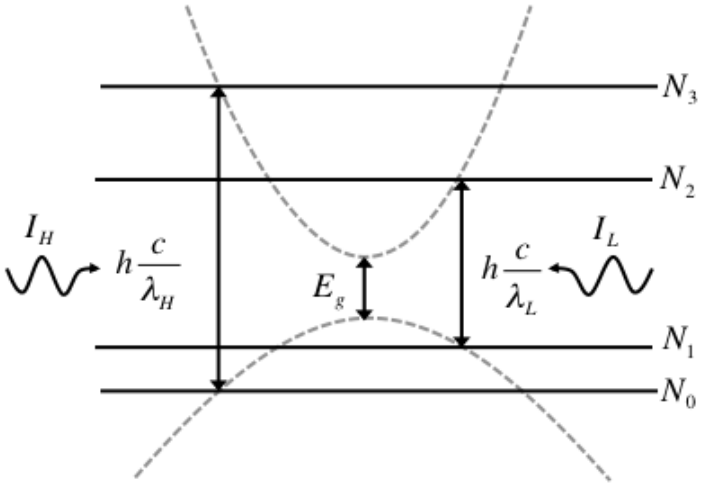

Figure 3.4: Simplified 4-level system is used to represent the semiconductor band structure (dash curves). The energy difference between level 0 and 3 is equal to the photon energy of pump supply beam at λ_H, and the energy difference between level 1 and 2 is equal to the photon energy of the signal beam at λ_L. The stimulated carrier transition is promoted by the incidence of pump supply beam and signal beam with intensities of I_H and I_L respectively.

$$\frac{dN_0}{dt} = \frac{N_3}{\tau_{30}} + \frac{N_1}{\tau_{10}} + (N_3 - N_0)B_{30}\, I_H, \tag{3.10a}$$

$$\frac{dN_3}{dt} = -\frac{N_3}{\tau_{30}} - \frac{N_3}{\tau_{32}} - (N_3 - N_0)B_{30}\, I_H, \tag{3.10b}$$

$$\frac{dN_1}{dt} = \frac{N_2}{\tau_{21}} - \frac{N_1}{\tau_{10}} + (N_2 - N_1)B_{21}\, I_L, \tag{3.10c}$$

$$\frac{dN_2}{dt} = -\frac{N_2}{\tau_{21}} + \frac{N_3}{\tau_{32}} - (N_2 - N_1)B_{21}\, I_L, \qquad (3.10d)$$

where τ_{30} and τ_{21} represent the inter-band spontaneous decay time for transition energies of hc/λ_H and hc/λ_L respectively. τ_{10} and τ_{32} correspond to the intraband transition time in valence band and condition band. τ_{30} and τ_{21} are typically in the nano-second scale, while τ_{10} and τ_{32} are in the 10-100fs scale. $(N_3 - N_0)B_{30}\, I_H$ and $(N_2 - N_1)B_{21}\, I_L$ gives the stimulated emission rate between level 3 and 0 and between level 2 and 1.

To make the 4-level 1-electron model feasible to represent the actual carrier dynamics in the semiconductor medium, the following constraints or conditions have to be met. First of all, the 4-level 1-electron model does not incorporate the Pauli exclusion principle, which leads to N_1=0 at the ground state. The direct consequence is that the population inversion between level 2 and 1 is present upon any pumping rate at λ_H i.e. the signal beam at λ_L always sees gain. Therefore, 4-level 1-electron picture is applicable only when the pump supply intensity is sufficiently high to introduce gain at the signal wavelength. Secondly, the off-resonance dipole-field interaction is neglected in our formulation, i.e. the pump supply at λ_H does not contribute to the carrier transition between level 2 and 1, and the signal beam at λ_L does not contribute to the transition between level 3 and 0. This is valid when the wavelength separation λ_L -λ_H is larger than the spectral broadening line width, which is typically ~50nm. In the actual EUPT operation, the above two conditions are typically satisfied or even desired. The gain at the signal wavelength implies fast carrier depletion, which is the cause of the absorption increase at the pump supply wavelength. On the other hand, large wavelength separation between the pump

supply and the input signal is desired to prevent the direct interband transition competition between the two wavelengths, which is to say we do not want the carrier excitation at pump wavelength to directly compete with the carrier depletion at the control wavelength and vise versa. Thus, the formulation based on the 4-level 1-electron model will be generally applicable for our EUPT analysis.

Eqn. (3.10) are solved at steady state, i.e. $\frac{dN_0}{dt} = \frac{dN_1}{dt} = \frac{dN_2}{dt} = \frac{dN_3}{dt} = 0$. By introducing the total carrier density $N_{tot} = N_0 + N_1 + N_2 + N_3$, the difference of carrier density between level 0 and 3, $\Delta N_{30} = N_3 - N_0$, can be derived

$$\Delta N_{30} = -\frac{N_{tot}}{1 + 2\frac{\tau_{32} + \tau_{10}}{\tau_{32} + \tau_{30}}\tau_{30}B_{30}\, I_H + \frac{\tau_{21} - \tau_{10}}{\tau_{32} + \tau_{30}}\frac{\tau_{30}B_{30}\, I_H}{1 + \tau_{21}B_{21}\, I_L}}. \tag{3.11}$$

As we see, when $I_L = 0$, Eqn. (3.11) is reduced to

$$\Delta N_{30} = -\frac{N_{tot}}{1 + \left(\frac{2\tau_{32} + \tau_{10} + \tau_{21}}{\tau_{32} + \tau_{30}}\right)\tau_{30}B_{30}\, I_H}\ , \tag{3.12}$$

which leads to the absorption coefficient at λ_H

$$\alpha_H(I_L{\sim}0) = \frac{\alpha_{H0}}{1 + {I_H}/{I_{Hsat}}}, \tag{3.13}$$

where $\alpha_H = \sigma_{30}|\Delta N_{30}|$, $\alpha_{H0} = \sigma_{30}N_{tot}$ is the small-signal absorption coefficient, and $I_{Hsat} = \left[\left(\frac{2\tau_{32}+\tau_{10}+\tau_{21}}{\tau_{32}+\tau_{30}}\right)\tau_{30}B_{30}\right]^{-1}$ is the saturation intensity at λ_H, defined as the intensity required to reduce the absorption coefficient by half.

On the other hand, we derived the relationship between $\Delta N_{21} = N_2 - N_1$ and ΔN_{30} at the steady state, which is given by

$$\frac{\Delta N_{21}}{\Delta N_{30}} = -\frac{\tau_{30} B_{30}\, I_H}{1 + \tau_{21} B_{21}\, I_L}\, \frac{\tau_{21} - \tau_{10}}{\tau_{32} + \tau_{30}}. \tag{3.14}$$

With the substitution of Eqn. (3.12), Eqn. (3.14) gives

$$\Delta N_{21} = \frac{1}{1 + \tau_{21} B_{21}\, I_L}\, \frac{N_{tot}}{\left(\frac{I_{Hsat}}{I_H} + 1\right) \frac{2\tau_{32} + \tau_{10} + \tau_{21}}{\tau_{21} - \tau_{10}}}\ , \tag{3.15}$$

which leads to the expression of the gain coefficient seen by λ_L as the medium is pumped at λ_H with intensity I_H,

$$g_L(I_L \sim 0) = \frac{g_{L0}(I_H)}{1 + {I_L}/{I_{Lsat}}}\ , \tag{3.16}$$

where $g_L = \sigma_{21} \Delta N_{21}$ and $I_{Lsat} = (\tau_{21} B_{21})^{-1}$ is the saturation intensity at λ_L. $g_{L0}(I_H) = \frac{\sigma_{21} N_{tot}}{\left(\frac{I_{Hsat}}{I_H}+1\right)\left(2\frac{\tau_{32}+\tau_{10}}{\tau_{21}-\tau_{10}}+1\right)}$ is the small-signal gain coefficient, which is dependent on the pump intensity I_H. When $I_H \gg I_{Hsat}$ such that the medium is pump up to transparency at λ_H, $g_{L0}(I_H)$ reaches the maximum value $\sigma_{21} N_{tot} \frac{\tau_{21}-\tau_{10}}{2\tau_{32}+\tau_{10}+\tau_{21}}$, denoted by g_{L0} here.

Therefore, with the substitution of I_{Lsat} and I_{Hsat} into Eqn. (3.11), the absorption coefficient at λ_H induced by carrier depletion at λ_L is written as

$$\alpha_H = \frac{\alpha_{H0}}{1 + \frac{2\tau_{32} + 2\tau_{10}}{2\tau_{32} + \tau_{10} + \tau_{21}} \frac{I_H}{I_{Hsat}} + \frac{\tau_{21} - \tau_{10}}{2\tau_{32} + \tau_{10} + \tau_{21}} \frac{I_H / I_{Hsat}}{1 + I_L / I_{Lsat}}}. \tag{3.17}$$

If we consider $\tau_{10} = \tau_{32} = 100fs$ and $\tau_{30} = \tau_{21} = 1ns$, $\frac{2\tau_{32}+2\tau_{10}}{2\tau_{32}+\tau_{10}+\tau_{21}} \sim 4 \times 10^{-4}$ and $\frac{\tau_{21}-\tau_{10}}{2\tau_{32}+\tau_{10}+\tau_{21}} \sim 1$. Although $\frac{2\tau_{32}+2\tau_{10}}{2\tau_{32}+\tau_{10}+\tau_{21}}$ is small, the product of $\frac{2\tau_{32}+2\tau_{10}}{2\tau_{32}+\tau_{10}+\tau_{21}} \frac{I_H}{I_{Hsat}}$ is not negligible when $I_H > 10^3 I_{Hsat}$. And in EUPT operation, the pump supply intensity is typically that high in order to pump the active waveguide to transparency (section 4.3.1). The role of $\frac{2\tau_{32}+2\tau_{10}}{2\tau_{32}+\tau_{10}+\tau_{21}} \frac{I_H}{I_{Hsat}}$ in affecting the value of α_H can be interpreted as follows. With $\tau_{32} \sim \tau_{10} \ll \tau_{21}$, we noticed $\frac{2\tau_{32}+2\tau_{10}}{2\tau_{32}+\tau_{10}+\tau_{21}} \sim 4\frac{\tau_{32}}{\tau_{21}}$ represents the ratio of spontaneous emission rate over the intraband transition rate, while I_H/I_{Hsat} can be interpreted as the ratio of stimulated pumping rate over the spontaneous emission rate. Thus $\frac{2\tau_{32}+2\tau_{10}}{2\tau_{32}+\tau_{10}+\tau_{21}} \frac{I_H}{I_{Hsat}}$ effectively tells the relative rate between the stimulated pumping and the intraband transition, or equivalently the states filling rate at level 3. That means, despite of the fast intraband decaying from 3 to 2, the empty states left over at 3 can be quickly re-filled at high I_H, resulting in reduced empty states and thus the reduced absorption coefficient seen at λ_H.

Simplifying the expression of Eqn. (3.17), it is written as

$$\alpha_H = \frac{\alpha_{H0}}{1 + \tau_r \frac{I_H}{I_{Hsat}} + \frac{I_H/I_{Hsat}}{1 + I_L/I_{Lsat}}} \quad , \tag{3.18}$$

where $\tau_r = \frac{2\tau_{32}+2\tau_{10}}{2\tau_{32}+\tau_{10}+\tau_{21}}$ denotes the transition time ratio between the intraband transition and spontaneous emission.

Subsequently, the gain coefficient seen by λ_L can be obtained by substituting Eqn. (3.11) into Eqn. (3.14), and with the substitution of I_{Lsat} and I_{Hsat}, we get

$$g_L = \frac{g_{L0}}{1 + \tau_r \frac{I_L}{I_{Lsat}} + \frac{1 + I_L/I_{Lsat}}{I_H/I_{Hsat}}} = \frac{g_{L0}}{\alpha_{H0}} \frac{I_H/I_{Hsat}}{1 + I_L/I_{Lsat}} \alpha_H \ . \qquad (3.19)$$

For the case of $I_L \gg I_{Lsat}$, Eqn. (3.18) and Eqn. (3.19) are reduced to

$$\alpha_H = \frac{\alpha_{H0}}{1 + \ \tau_r \frac{I_H}{I_{Hsat}} + \frac{I_{Lsat}}{I_{Hsat}} \frac{I_H}{I_L}} \ , \qquad (3.20)$$

$$\frac{g_L}{\alpha_H} = \frac{g_{L0}}{\alpha_{H0}} \frac{I_{Lsat}}{I_{Hsat}} \frac{I_H}{I_L} \ . \qquad (3.21)$$

Eqn.(3.20) and Eqn. (3.21) tell us that $\frac{\alpha_{H0}}{\alpha_H}$ is linearly dependent on I_H and $\frac{I_H}{I_L}$, and the ratio of g_L/α_H is proportional to the intensity ratio $\frac{I_H}{I_L}$. Furthermore, reducing $\frac{I_H}{I_L}$ and reducing I_H will increase the induced absorption coefficient α_H. These characteristics will be examined by MLME-FDTD simulation in the later section.

3.2.2 Analytical formulation of $\frac{g_{L0}}{\alpha_{H0}}$ and $\frac{I_{Lsat}}{I_{Hsat}}$ for bulk semiconductor based on free carrier theory and quasi equilibrium approximation

To verify the accuracy of the absorption and gain formulation developed, we first consider the bulk semiconductor system, where $\frac{g_{L0}}{\alpha_{H0}}$ and $\frac{I_{Lsat}}{I_{Hsat}}$ can be formulated analytically. The calculation will be subsequently compared with the MLME-FDTD simulation.

Free-carrier theory and quasi-equilibrium approximation are adopted to derive the expressions of I_{Lsat}, I_{Hsat} and $\frac{g_{L0}}{\alpha_{H0}}$, and because of that, band filling effects with Fermi-Dirac statistics in a realistic semiconductor band structure are taken into account in our absorption and gain formulation [28].

The gain coefficient at wavelength λ is expressed by

$$g(\omega) = \frac{\omega}{\epsilon_0 nc\hbar\gamma}\int_0^{\infty} d\varepsilon \; D(\varepsilon)|\mu(\varepsilon)|^2 \frac{f_e(\varepsilon,\mu_e) + f_h(\varepsilon,\mu_h) - 1}{1 + \left(\frac{\varepsilon + E_g - \hbar\omega}{\hbar\gamma}\right)^2}, \qquad (3.22)$$

where $\omega = \frac{2\pi c}{\lambda}$ is the angular frequency of light, γ is the polarization dephasing rate, ϵ_0 is susceptibility of free space, n is the refractive index of the material and c is the speed of light. $\varepsilon = \frac{\hbar^2 k^2}{2m_r}$ is the reduced-mass energy, with reduced mass $m_r = \left(\frac{1}{m_e} + \frac{1}{m_h}\right)^{-1}$ and wave vector k of the corresponding state. The integration is performed over the entire energy band for ε from zero to infinity. $\mu(\varepsilon)$ is the dipole matrix element between conduction and valence, which is be represented by $|\mu(\varepsilon)|^2 = \frac{q^2\hbar^2}{6m_0\left(E_g+\varepsilon\right)^2}E_p$, where E_g is the band gap energy and $E_p = 25eV$ for InGaAsP. q and m_0 are electron charge and mass. $D(\varepsilon)$ represents the joint density of states. $f_e(\varepsilon,\mu_e)$ and $f_h(\varepsilon,\mu_h)$ are the Fermi-Dirac distribution for electron and hole respectively, which are given by

$$f_e(\varepsilon,\mu_e) = \frac{1}{e^{\beta\left(\varepsilon\frac{m_r}{m_e}-\mu_e\right)}+1}, \qquad (3.23)$$

$$f_h(\varepsilon,\mu_h) = \frac{1}{e^{\beta\left(\varepsilon\frac{m_r}{m_h}-\mu_h\right)}+1}, \qquad (3.24)$$

where $\beta = \frac{1}{k_B T} \sim 1/(25meV)$ at room temperature. μ_e and μ_h are the quasi-equilibrium chemical potential of electron or holes. When $f_e(\varepsilon) + f_h(\varepsilon) < 1$, $g(\omega) < 0$, which becomes the absorption coefficient.

i. Formulation for g_{L0}/α_{H0}

α_{H0} is the small-signal absorption coefficient at λ_H, when the carriers are mostly in the valence band, giving $f_e(\varepsilon, \mu_e) \sim 0$ and $f_h(\varepsilon, \mu_h) \sim 0$. Therefore α_{H0} is given by

$$\alpha_{H0} = \frac{\omega_H}{\epsilon_0 nc\hbar\gamma} \int_0^\infty d\varepsilon \; D(\varepsilon) |\mu(\varepsilon)|^2 \frac{1}{1 + \left(\frac{\varepsilon + E_g - \hbar\omega_H}{\hbar\gamma}\right)^2}. \quad (3.25)$$

g_{L0} is the small-signal gain coefficient at λ_L, when the medium is pumped to transparency at λ_H, i.e. $g(\omega_H) = 0$, from which the chemical potentials μ_e and μ_h are calculated. Since there are two variables, a second equation is required to relate μ_e and μ_h. Here we utilize the carrier conservation relation based on low-temperature condition, from which we have $\mu_e m_e = \mu_h m_h$. By defining $\mu = \mu_e + \mu_h$, it gives $\mu_e = \mu \frac{m_r}{m_e}$ and $\mu_h = \mu \frac{m_r}{m_h}$. The solution μ from $g(\omega_H) = 0$ is denoted by $\mu_{\alpha_H \to 0}$. The subscript $\alpha_H \to 0$ represents the chemical potential at which the absorption coefficient of λ_H is zero. So g_{L0} is given by

$$g_{L0} = \frac{\omega_L}{\epsilon_0 nc\hbar\gamma} \int_0^\infty d\varepsilon \; D(\varepsilon) \; |\mu(\varepsilon)|^2 \frac{f_e\left(\varepsilon, \mu_{\alpha_H \to 0} \frac{m_r}{m_e}\right) + f_h\left(\varepsilon, \mu_{\alpha_H \to 0} \frac{m_r}{m_h}\right) - 1}{1 + \left(\frac{\varepsilon + E_g - \hbar\omega_L}{\hbar\gamma}\right)^2} \quad (3.26)$$

Therefore, we have

$$\frac{g_{L0}}{\alpha_{H0}} = \frac{\omega_L \int_0^\infty d\varepsilon \, \frac{D(\varepsilon)}{\left(E_g+\varepsilon\right)^2} \frac{f_e\left(\varepsilon, \mu_{\alpha_H \to 0}\frac{m_r}{m_e}\right) + f_h\left(\varepsilon, \mu_{\alpha_H \to 0}\frac{m_r}{m_h}\right) - 1}{1+\left(\frac{\varepsilon + E_g - \hbar\omega_L}{\hbar\gamma}\right)^2}}{\omega_H \int_0^\infty d\varepsilon \, \frac{D(\varepsilon)}{\left(E_g+\varepsilon\right)^2} \frac{1}{1+\left(\frac{\varepsilon + E_g - \hbar\omega_H}{\hbar\gamma}\right)^2}} . \quad (3.27)$$

ii. Formulation for I_{Lsat} / I_{Hsat}

Refer to the derivation from Eqn. (3.13) to Eqn. (3.16), it is important to note that I_{Lsat} and I_{Hsat} are defined under different contexts, thus do not share a universal expression.

I_{Hsat} is defined for the pumping process, i.e. the pump intensity at which the absorption coefficient at pump supply wavelength is reduced by half. Thus we start with the rate equation of carrier density as follows

$$\frac{dN_c}{dt} = -\frac{g(\omega_H) I_H}{\hbar\omega_H} - \int_0^\infty d\varepsilon \frac{D(\varepsilon) f_e(\varepsilon, \mu_e) f_h(\varepsilon, \mu_h)}{\tau_{sp}(\varepsilon)} \quad , \quad (3.28)$$

where N_c is the total carrier density in the conduction band. The first term at right hand side represents the rate of stimulated carrier generation by absorbing the incident light at λ_H with intensity I_H, and $g(\omega_H) = -\alpha_H$. The second term represents the spontaneous decay rate, with the interband transition time $\tau_{sp}(\varepsilon) = \frac{\pi\hbar c^3 \epsilon_0}{n\omega^3 \, |\mu(\varepsilon)|^2}$ and $\hbar\omega = \varepsilon + E_g$. At steady state, these two rates are balanced, so that $\frac{dN_c}{dt} = 0$ and gives

$$I_H = \frac{\hbar\omega_H}{\alpha_H} \int_0^\infty d\varepsilon \frac{D(\varepsilon) f_e(\varepsilon, \mu_e) f_h(\varepsilon, \mu_h)}{\tau_{sp}(\varepsilon)} . \quad (3.29)$$

The definition of I_{Hsat} tells that $\alpha_H = \frac{1}{2}\alpha_{H0}$, when $I_H = I_{Hsat}$. Thus Eqn. (3.29)

becomes

$$I_{Hsat} = \frac{2\hbar\omega_H}{\alpha_{H0}} \int_0^\infty d\varepsilon \frac{D(\varepsilon) f_e\left(\varepsilon, \mu_{\alpha_H \to 1/2} \frac{m_r}{m_e}\right) f_h\left(\varepsilon, \mu_{\alpha_H \to 1/2} \frac{m_r}{m_h}\right)}{\tau_{sp}(\varepsilon)}, \qquad (3.30)$$

where the subscript $\alpha_H \to 1/2$ denotes the chemical potentials at witch the absorption coefficient at λ_H is equal to half of the small-signal absorption coefficient and α_{H0} is given by Eqn. (3.25).

As for the depletion process, where I_{Lsat} is defined, the rate equation of carrier density is given by

$$\frac{dN_c}{dt} = -\frac{g(\omega_L) I_L}{\hbar\omega_L} - \frac{g(\omega_H) I_H}{\hbar\omega_H} - \int_0^\infty d\varepsilon \frac{D(\varepsilon) f_e(\varepsilon, \mu_e) f_h(\varepsilon, \mu_h)}{\tau_{sp}(\varepsilon)} , \qquad (3.31)$$

where $g(\omega_L) = g_L > 0$, corresponding to the gain coefficient at λ_L. The rest of the parameters are defined similarly as in Eqn. (3.28). At steady state, i.e. $\frac{dN_c}{dt} = 0$, Eqn.(3.31) gives

$$I_L = \frac{\omega_L}{\omega_H} \frac{\alpha_H}{g_L} I_H - \frac{\hbar\omega_L}{g_L} \int_0^\infty d\varepsilon \frac{D(\varepsilon) f_e(\varepsilon, \mu_e) f_h(\varepsilon, \mu_h)}{\tau_{sp}(\varepsilon)} . \qquad (3.32)$$

Consider the case of $I_L = I_{Lsat}$ and $g_L = g_{L0}/2$ in Eqn. (3.19), we get

$$\alpha_H = \alpha_{H0} \frac{I_{Hsat}}{I_H} . \qquad (3.33)$$

Eqn. (3.33) is then substituted into Eqn. (3.32) with $I_L = I_{Lsat}$ and $g_L = g_{L0}/2$, giving that

$$I_{Lsat} = 2\frac{\omega_L}{\omega_H}\frac{\alpha_{H0}}{g_{L0}}I_{Hsat} - 2\frac{\hbar\omega_L}{g_{L0}}\int_0^\infty d\varepsilon \frac{D(\varepsilon)f_e\left(\varepsilon,\mu_{g_L\to\frac{1}{2}}\frac{m_r}{m_e}\right)f_h\left(\varepsilon,\mu_{g_L\to\frac{1}{2}}\frac{m_r}{m_h}\right)}{\tau_{sp}(\varepsilon)} \tag{3.34}$$

The subscript $g_L \to 1/2$ denotes the chemical potentials at witch the gain coefficient at λ_L is equal to half of the small-signal gain coefficient g_{L0} when the medium is pump to transparency at λ_H. With the substitution of Eqn. (3.30), Eqn. (3.34) becomes

$$I_{Lsat} = 2\frac{\hbar\omega_L}{g_{L0}}\left[\begin{aligned} &2\int_0^\infty d\varepsilon \frac{D(\varepsilon)f_e\left(\varepsilon,\mu_{\alpha_H\to\frac{1}{2}}\frac{m_r}{m_e}\right)f_h\left(\varepsilon,\mu_{\alpha_H\to\frac{1}{2}}\frac{m_r}{m_h}\right)}{\tau_{sp}(\varepsilon)} \\ &-\int_0^\infty d\varepsilon \frac{D(\varepsilon)f_e\left(\varepsilon,\mu_{g_L\to\frac{1}{2}}\frac{m_r}{m_e}\right)f_h\left(\varepsilon,\mu_{g_L\to\frac{1}{2}}\frac{m_r}{m_h}\right)}{\tau_{sp}(\varepsilon)}\end{aligned}\right]. \tag{3.35}$$

3.2.3 Verification with MLME-FDTD simulation

With the explicit expressions of I_{Lsat}, I_{Hsat} and $\frac{g_{L0}}{\alpha_{H0}}$, the absorption and gain coefficients in Eqn. (3.20) and Eqn.(3.21) can be analytically calculated for varied band structures and interacting light properties. In this section, MLME-FDTD simulation will be adopted to verify our formulation, based on the energy band parameters in Table 3.1 for the InGaAsP bulk semiconductor.

Table 3.1: Energy band parameters of InGaAsP bulk semiconductor

Parameters	Values
Energy band (in wavelength)	1.5625 μm
Background refractive index (n)	3.4
Electron effective mass (m_e)	$0.046m_0$
Hole effective mass (m_h)	$0.36m_0$
Dipole dephasing rate (γ)	4×10^{13}rad/s
Intraband transition time	50fs

The FDTD simulation is carried out for a single waveguide with short length of 4μm. The CW pump supply beam at $\lambda_H = 1350nm$ is launched into the waveguide at intensity $I_H \gg I_{Hsat}$ and the signal beam at $\lambda_L = 1450nm$ is launched from the opposite end of the waveguide with intensity $I_L \gg I_{Lsat}$. Based on our calculation, $I_{Hsat} = 17.8kW/cm^2$ and $I_{Lsat} = 82kW/cm^2$. FDTD simulation shows the small-signal absorption coefficient of the waveguide at 1350nm is equal to $\alpha_{H0} = 0.57\mu m^{-1}$. Subsequently, the transmissions of the pump supply and signal beams are monitored at different incident I_H and I_L, based on which α_H and g_L can be calculated.

3.2.3.1 Verification of the absorption coefficient expression α_H

To verify the absorption coefficient expression α_H in Eqn. (3.20), we first plot α_{H0}/α_H versus the intensity ratio I_H/I_L at different I_H, as shown in Fig. 3.5. We find α_{H0}/α_H is linearly dependent on I_H/I_L, the linear curve filling of which is shown by the solid lines. As we can see, the slope of it is generally a constant that does not vary with the pump intensity, while the intercept increases with the pump intensity, which is consistent with our formulation.

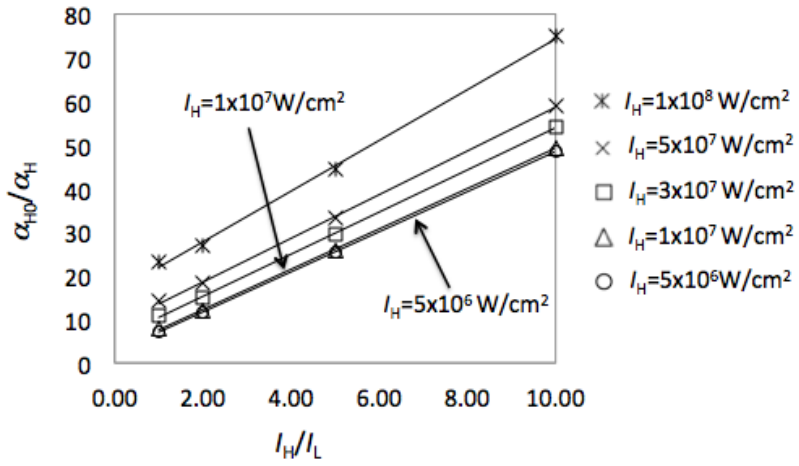

Figure 3.5: $\frac{\alpha_{H0}}{\alpha_H}$ versus $\frac{I_H}{I_L}$ at different I_H, simulated using 40-level 20-electron FDTD. $\lambda_H = 1.35\mu m$ and $\lambda_L = 1.45\mu m$. $\alpha_{H0} = 0.12\mu m^{-1}$ is the small-signal absorption coefficient at $\lambda_H = 1.35\mu m$. The solid lines correspond to the linear curve fitting for each data set.

Next, to compare the slopes in Fig. 3.5 with the coefficient I_{Lsat}/I_{Hsat} in Eqn. (3.20), we consider fixed $\lambda_H = 1350nm$ and varied λ_L from 1425nm to 1520nm. In Fig. 3.6a, the slopes of 'α_{H0}/α_H vs I_H/I_L' plots are plotted against I_H for different λ_L, which we find are constant at $I_H < 3 \times 10^7 W/cm^2$, and start to increase as $I_H > 3 \times 10^7 W/cm^2$. The increasing behavior cannot be interpreted by our formulation, which requires further investigation. In the following discussion, we focus on the cases of $I_H < 3 \times 10^7 W/cm^2$, which is also the practical range for many device applications. Subsequently, I_{Lsat}/I_{Hsat} is calculated using Eqn. (3.30) and Eqn. (3.35) for the corresponding λ_H and λ_L, and compared with the slope values in the constant range (i.e. $I_H < 3 \times 10^7 W/cm^2$) in Fig. 3.6a, which is shown in Fig. 3.6b. As we can see, our analytical calculation is generally consistent with the FDTD simulation, with a percentage error <5%.

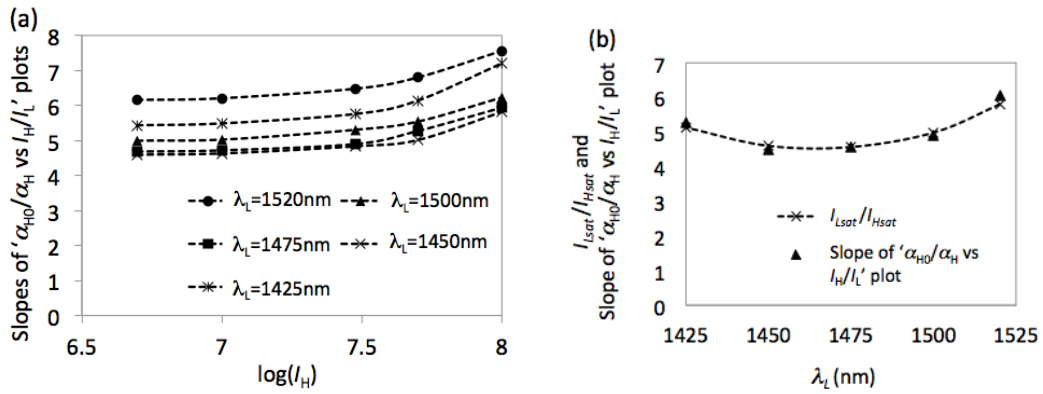

Figure 3.6: a) slopes of 'α_{H0}/α_Hvs I_H/I_L' plots are plotted against I_H at different λ_L. b) Analytically calculated $\frac{I_{Lsat}}{I_{Hsat}}$ (cross dot with dash line) and the slope values in a) that are obtained from FDTD simulation (triangle dots) versus the signal wavelength λ_L. $\lambda_H = 1350nm$.

Then to verify the term of $1 + \tau_r I_H/I_{Hsat}$ in Eqn. (3.20), we first plot the intercepts of the α_{H0}/α_H vs I_H/I_L' plots in Fig 3.5 with respect to I_H for fixed $\lambda_H = 1350nm$ and varied λ_L from 1425nm to 1520nm, which is shown in Fig. 3.7a. We find it is linearly dependent on I_H with intercepts close to 1 and are generally independent of λ_L, which are all consistent with the behavior of $1 + \tau_r I_H/I_{Hsat}$.

Subsequently, to further verify the coefficient τ_r/I_{Hsat} in $1 + \tau_r I_H/I_{Hsat}$, we consider fixed signal wavelength $\lambda_L = 1450nm$ and varied pump supply wavelength λ_H from 1300nm to 1375nm. In Fig. 3.7b, α_{H0}/α_H is plotted versus I_H with $I_H/I_L = 1$ for different λ_H, the slopes of which are then multiplied by the corresponding I_{Hsat}, calculated using Eqn. (3.30), to get the intraband-interband transition ratio τ_r. The results are listed in Table 3.2. As we can see, τ_r is generally constant at $\tau_r \sim 3 \times 10^{-3}$. In the actual semiconductor band structure, the intraband transition is a process of thermalizing the optically excited carriers into a quasi-equilibrium distribution through carrier-carrier and carrier-phonon scattering, which is slower than the inter-state transition time, i.e. 50ps we used in our FDTD simulation. The typical timescale for the intraband process lies between a few picoseconds and a few hundred

picoseconds, depending upon the detailed condition. In our case, the spontaneous emission time by calculation is ~1ns, thus the $\tau_r = 3 \times 10^{-3}$ implies an intraband transition time of ~3ps, which is within a reasonable range.

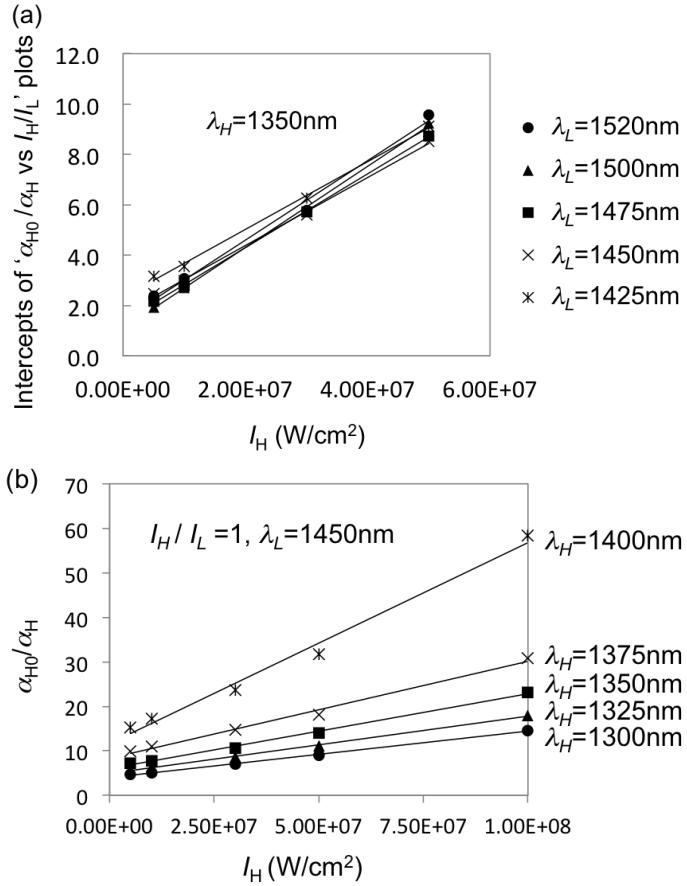

Figure 3.7: (a) the intercepts of 'α_{H0}/α_H vs I_H/I_L' plots are plotted against I_H at different λ_L. $\lambda_H = 1350nm$. (b) α_{H0}/α_H vs I_H at different λ_H, with $\lambda_L = 1450nm$ and $I_H/I_L = 1$.

Table 3.2: Intraband-interband transition time ratio τ_r determined from FDTD simulation in Fig. 3.7b

λ_H (nm)	Slopes of Fig.3.7b	I_{Hsat} (kW/cm²)	τ_r
1375	2.18×10^{-7}	13.6	2.96×10^{-3}
1350	1.68×10^{-7}	17.8	2.99×10^{-3}
1325	1.29×10^{-7}	22.6	2.92×10^{-3}
1300	1.04×10^{-7}	29.0	3.02×10^{-3}

3.2.3.2 Verification of the gain coefficient expression g_L

Next, we continue to examine the gain coefficient g_L in Eqn. (3.21) by plotting α_H/g_L against I_H/I_L at different I_H, which is shown in Fig. 3.8a. $\lambda_H = 1350nm$ and $\lambda_L = 1450nm$. We find α_H/g_L is linearly proportional to I_H/I_L , and the proportionality is independent of I_H, which is consistent with Eqn. (3.21).

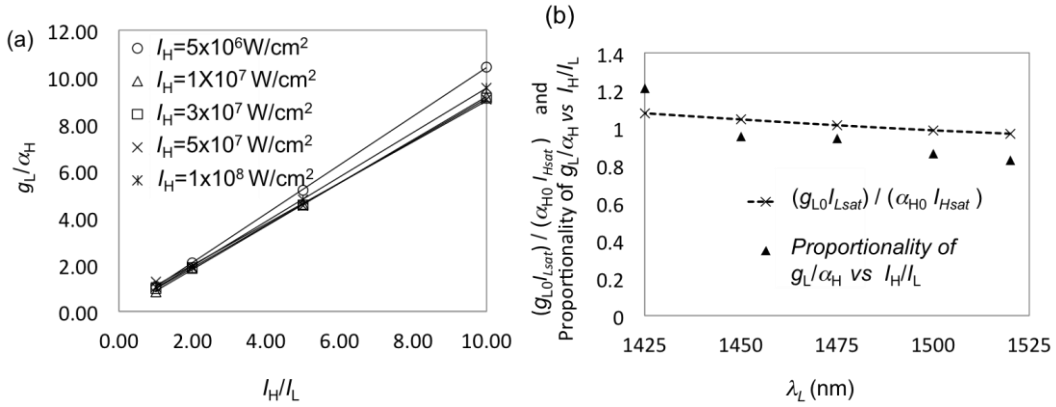

Figure 3.8: (a) g_L/α_H is plotted versus I_H/I_L at different I_H. $\lambda_H = 1.35\mu m$ and $\lambda_L = 1.45\mu m$. The solid lines show the linear curve fitting for each data set. (b) Analytically calculated $\frac{g_{L0}}{\alpha_{H0}}\frac{I_{Lsat}}{I_{Hsat}}$ (cross dot dash line) and the proportionality of g_L/α_H over I_H/I_L (triangle dots) versus the signal wavelength λ_L, with $\lambda_H = 1350nm$.

The proportionality is subsequently examined at fixed $\lambda_H = 1350nm$ and varied λ_L from 1425nm to 1520nm, and compared with the analytically calculated $\frac{g_{L0}}{\alpha_{H0}}\frac{I_{Lsat}}{I_{Hsat}}$ using Eqn. (3.27), (3.30) and (3.35), which is shown in Fig. 3.8b. We find they are generally consistent with each other with an error <10%.

To summarize, an analytical formulation for absorption and gain coefficients seen by two interacting monochromatic fields of different wavelengths in a semiconductor material is derived to analyze the case of high-intensity operation in the bulk semiconductor system. Starting with a simplified 4-level 1-electron picture, our analytical model gives a first-order estimation of up to 90% accuracy to the actual situation as verified by MLME-FDTD simulation. One of the main causes to the 10%

error could be from the saturation intensity expressions given by Eqn. (3.16) and Eqn. (3.13). We note that higher-order saturation behaviors due to multi-photon absorptions in semiconductor that can be important at sufficiently high intensity were not included. They could have affected the accuracy of our formulation, though at our main operating intensity level of interest, we expected these effects to be relatively small (they become important at above a few GW/cm^2 intensity). In addition, we note that both the MLME-FDTD model we used and our analytical model neglected many-body effects that are also higher-order effects, e.g. many-body Coulomb interaction, carrier heating and cooling, etc. These many body effects can come in at relatively low intensity. They usually will add additional features to the response, typically ultrafast features at turn on/off. Such many-body effects have been incorporated into MLME-FDTD model very recently [19], and may be used to study the impacts of these many-body effects on changing the switching performances of the photonic transistor in the future.

CHAPTER IV THEORETICAL STUDIES OF EUPT PART II: Applications of the Efficient Effective Semiconductor 2-Beam Model to All Optical Switching in a Single Semiconductor Waveguide

Before we look at the EUPT switching, let us first study a simple pump vs control switching operation in a single waveguide structure, which will benefit the parametric study of EUPT later. This is because the basic switching mechanism in EUPT is based on the medium saturation by the pump beam at a high energy level, which creates optical gain for the signal beam at a lower energy level than the pump beam's photon energy. The signal beam then gain optical energy as it propagates and simultaneously de-excite the medium, causing the pump to see loss. This same process can also occur in a pump-signal interaction situation within a single waveguide, also causing all-optical switching in that the pump.energy gets absorbed, causing a "downward pulse" when the signal beam enters the waveguide.

The device geometry and operating parameters are shown in Fig. 4.1. A continuous wave pump beam at a wavelength λ_H, with the photon energy above the semiconductor bandgap energy E_g, is lunched into a single semiconductor waveguide of length L. The incident intensity of the pump I_{H-in} is higher than the saturation intensity of the waveguide medium so that it can pump the waveguide to transparency at wavelength λ_H. After that, an input control beam (or input-signal beam as named in EUPT operation) at a wavelength λ_L longer than λ_H and with a photon energy above

the band gap energy E_g, is launched into the waveguide at intensity I_{L-in} from the waveguide end opposite to that of the pump beam's entrance. The pump beam will output at the entrance of the input control or input signal beam, giving the "output signal beam", with intensity I_{H-out}. As the input control beam would see optical gain, it would de-excite the excited carriers in the conduction band, resulting in the depletion of the carriers at λ_H, which then induces an increase in the optical absorption at λ_H. This consequently reduces the transmission of the pump beam. Since the control beam sees the optical gain, it would be amplified along its propagation direction towards the pump's input end. Thus, the carrier-depletion-induced absorption change would be enhanced the longer the control beam propagates along the waveguide and eventually would cause significant switch-off of the pump beam. In a sense, the weak control beam gains the optical energy from the pump beam, which is then used to shut off the pump beam [29].

For consistency, we name the transmission drop of the pump beam upon the incidence of control beam as the switch-on process, and the pump pumping back the waveguide to transparency after the control beam exits as the switch-off process.

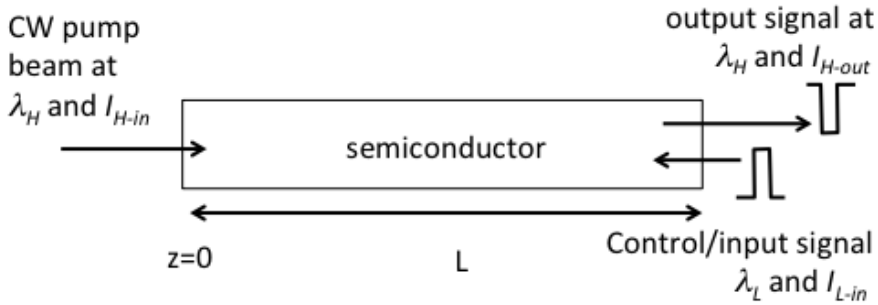

Figure 4.1: Single active waveguide with continuous pump at λ_H and intensity $I_H(z)$ incident from z=0. The signal beam at λ_L with intensity $I_L(z)$ is launched in the opposite direction from z=*L*. The wavelength length is *L*.

Analytical formulation for the switching gain, switching speed and switching energy of the proposed single-waveguide switch will be derived in the following

sections, based on which parametric study of the pump-control switching will be carried out. At the end, dynamic switching with ultrafast switching speed and high switching gain will be demonstrated in a bulk-InGaAsP single waveguide structure based on MLME-FDTD simulation.

4.1 Propagation Equations of Pump and Control Beams

As shown in Fig. 4.1, the pump beam with intensity I_{H-in} is launched at z=0 and propagating along +z direction, while the control beam with intensity I_{L-in} is launched at z=L and propagates along –z direction. At the steady state, the propagation equations for the pump supply and signal beams with Eqn. (3.20) and (3.21) substituted in are given by

$$\frac{dI_H(z)}{dz} = -\frac{\alpha_{H0}}{1+\frac{\tau_r}{I_{Hsat}}I_H(z)+\frac{I_{Lsat}}{I_{Hsat}}\frac{I_H(z)}{I_L(z)}}I_H(z) \tag{4.1}$$

$$\frac{dI_L(z)}{dz} = -\frac{g_{L0}}{\alpha_{H0}}\frac{I_{Lsat}}{I_{Hsat}}\frac{I_H(z)}{I_L(z)}\frac{\alpha_{H0}}{1+\frac{\tau_r}{I_{Hsat}}I_H(z)+\frac{I_{Lsat}}{I_{Hsat}}\frac{I_H(z)}{I_L(z)}}I_L(z) \tag{4.2}$$

where $\tau_r = 3\times10^{-3}$. The negative sign in Eqn. (4.2) indicates the negative propagation direction of signal beam.

First of all, it is straightforward to find that

$$\frac{dI_L(z)}{dz} = \frac{g_{L0}}{\alpha_{H0}}\frac{I_{Lsat}}{I_{Hsat}}\frac{dI_H(z)}{dz} \tag{4.3}$$

Take integration from z to L, it gives

$$I_L(z) = I_{L-in} - \frac{g_{L0}}{\alpha_{H0}} \frac{I_{Lsat}}{I_{Hsat}} [I_{H-out} - I_H(z)] \tag{4.4}$$

where $I_{L-in} = I_L(L)$ and $I_{H-out} = I_H(L)$. Then Eqn. (4.4) is substituted into Eqn. (4.1), followed by the integration from z=0 to L, which leads to

$$-ln(T_H) + \frac{\alpha_{H0}}{g_{L0}} ln\left[1 + \frac{g_{L0}}{\alpha_{H0}} \frac{I_{Lsat}}{I_{Hsat}} (1 - T_H) r_{in}\right] + (1 - T_H) \frac{\tau_r}{I_{Hsat}} I_{H-in} = \alpha_{H0} L \tag{4.5}$$

where $T_H = I_{H-out}/I_{H-in}$ denotes the transmission of pump beam and $r_{in} = I_{H-in}/I_{L-in}$ represents the incident intensity ratio of the incident pump supply and signal beam. As a reminder, g_{L0} refers to the small signal coefficient at λ_L when the material is pumped to transparency at λ_H.

After I_{H-out} is determined, Eqn. (4.4) and Eqn. (3.27) can be used to solve for the pump intensity variation along the waveguide $I_H(z)$, which is given by

$$-lnT_H(z) + \frac{\alpha_{H0}}{g_{L0}} ln\left[\frac{1 + \frac{g_{L0}}{\alpha_{H0}} \frac{I_{Lsat}}{I_{Hsat}} (1 - T_H) r_{in}}{1 + \frac{g_{L0}}{\alpha_{H0}} \frac{I_{Lsat}}{I_{Hsat}} (T_H(z) - T_H) r_{in}}\right] + \left(1 - T_H(z)\right) \frac{\tau_r}{I_{Hsat}} I_{H-in} = \alpha_{H0} z \tag{4.6}$$

where $T_H(z) = I_H(z)/I_{H-in}$. Subsequently, the intensity profile of the signal beam $I_L(z)$ can be calculated using Eqn. (4.4), and the absorption and gain coefficient profiles are determined using Eqn. (3.20) and (3.21).

4.2 Switching gain characteristics versus material properties, light properties and device geometry

First of all, we need to define the switching gain for the single waveguide switching, in which case the output signal is inverted. Consider the amount of change in the strong pump power at the pump's output end can be viewed as the "output signal", which is denoted as $\Delta P_{H-out} = \Delta I_{H-out} A_{eff}$. A_{eff} is the effective modal area of the waveguide. Let the pulse height of the control beam power be $\Delta P_{L-in} = I_{L-in} A_{eff}$. The all-optical switching gain is defined to be $G_{sw} = \frac{\Delta P_{H-out}}{\Delta P_{L-in}} = \frac{\Delta I_{H-out}}{I_{L-in}}$. Therefore, with the transmission of the pump beam ($T_H = \frac{I_{H-out}}{I_{H-in}}$) determined with Eqn. (4.5) and varied incident intensity ratio $r_{in} = \frac{I_{H-in}}{I_{L-in}}$, the switching gain can be calculated by $G_{sw} = (1 - T_H) r_{in}$.

As shown in Eqn. (4.5), four key parameters are involved in the switching gain calculation, which include $\frac{g_{L0}}{\alpha_{H0}}$, $\frac{I_{Lsat}}{I_{Hsat}}$, I_{Hsat} and $\alpha_{H0} L$. By considering the bulk InGaAsP as the waveguide core medium (Table 3.1), each parameter's role in determining the switching gain characteristics will be examined as follows.

Here we first consider the cases in which the pump conditions are fixed. Let the pump wavelength at $\lambda_H = 1350nm$, with which $I_{Hsat} = 17.8kW/cm^2$, and let $\alpha_{H0} L = 10$ and $I_{H-in} = 10MW/cm^2$. Assuming $\frac{g_{L0}}{\alpha_{H0}}$ and $\frac{I_{Lsat}}{I_{Hsat}}$ can vary arbitrarily, G_{sw} is calculated at different $\frac{g_{L0}}{\alpha_{H0}}$ and $\frac{I_{Lsat}}{I_{Hsat}}$ with varied $1/r_{in}$, which are plotted in Fig. 4.2. (As a reference, for the bulk InGaAsP, $\frac{I_{Lsat}}{I_{Hsat}} = 4.6$ and $\frac{g_{L0}}{\alpha_{H0}} = 0.22$ when $\lambda_L = 1450nm$.) In Fig. 4.2a, $\frac{I_{Lsat}}{I_{Hsat}} = 5$ is fixed and $\frac{g_{L0}}{\alpha_{H0}} = 0.1, 0.2$ and 0.3 is varied. We can see that increasing $\frac{g_{L0}}{\alpha_{H0}}$, or equivalently increasing $g_{L0} L$ seen by the control beam, can

significantly enhance the switching gain. In Fig. 4.2b, with $\frac{g_{L0}}{\alpha_{H0}} = 0.2$ being fixed, $\frac{I_{Lsat}}{I_{Hsat}}$ is varied from 4 to 8. It shows G_{sw} becomes significantly higher when $\frac{I_{Lsat}}{I_{Hsat}}$ is reduced. It is also noticed G_{sw} increases as the input control intensity $(1/r_{in})$ reduces. The enhancement of G_{sw} with the increase of $\frac{g_{L0}}{\alpha_{H0}}$ and reduce of $\frac{I_{Lsat}}{I_{Hsat}}$ is more significant when $1/r_{in}$<40%.

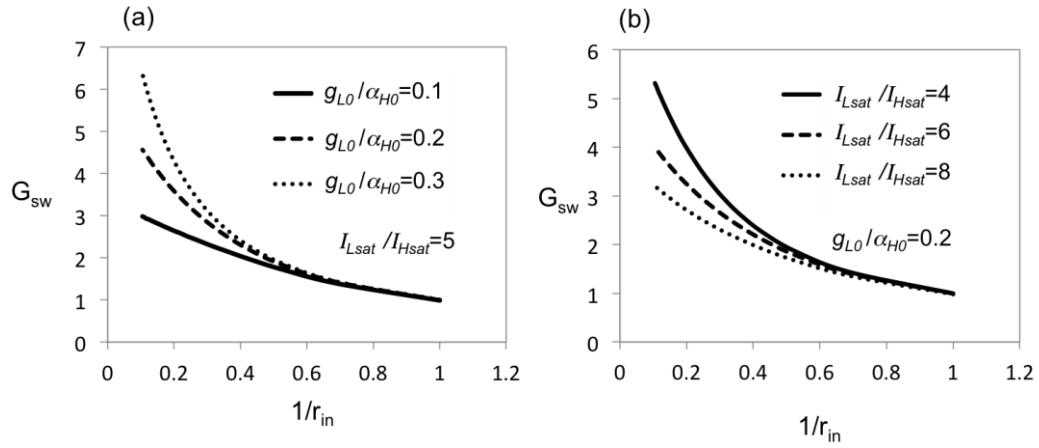

Figure 4.2: Switching gain G_{sw} versus $1/r_{in} = \frac{I_{L-in}}{I_{H-in}}$ for (a) varied $\frac{g_{L0}}{\alpha_{H0}}$ (b) varied $\frac{I_{Lsat}}{I_{Hsat}}$, where $\alpha_{H0}L = 10$, $I_{Hsat} = 17.8kW/cm^2$ and $I_{H-in} = 10MW/cm^2$ are fixed.

Next we use Eqn. (3.27), (3.30) and (3.35) to examine the characteristics of $\frac{g_{L0}}{\alpha_{H0}}$ and $\frac{I_{Lsat}}{I_{Hsat}}$, which are plotted versus the control beam wavelength λ_L at three different pump wavelength λ_H in Fig. 4.3. We find reducing pump wavelength will lead to the higher $\frac{g_{L0}}{\alpha_{H0}}$ and the lower $\frac{I_{Lsat}}{I_{Hsat}}$, which will increase the switching gain. It is also noticed that, at fixed λ_H, the λ_L to give the maximum $\frac{g_{L0}}{\alpha_{H0}}$ also gives the close-to-minimum value of $\frac{I_{Lsat}}{I_{Hsat}}$. Therefore, the maximum-gain λ_L can be the optimal control wavelength for high-switching-gain operation.

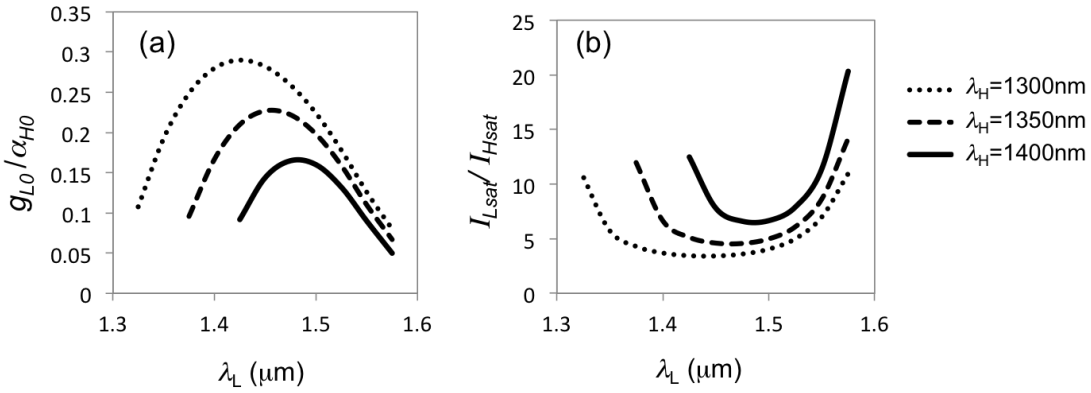

Figure 4.3: (a) $\frac{g_{L0}}{\alpha_{H0}}$ versus λ_L and (b) $\frac{I_{Lsat}}{I_{Hsat}}$ versus λ_L at different pump wavelength λ_H for InGaAsP bulk medium.

To examine the roles of $\alpha_{H0}L$ and I_{Hsat}, we fix $g_{L0}L$ and I_{Lsat} instead of $\frac{g_{L0}}{\alpha_{H0}}$ and $\frac{I_{Lsat}}{I_{Hsat}}$. Considering $g_{L0}L = 2$, $I_{Lsat} = 82kW/cm^2$ and $I_{H-in} = 10MW/cm^2$, G_{sw} is plotted against $1/r_{in}$ at varied $\alpha_{H0}L$ and I_{Hsat}. In Fig. 4.4a, with $I_{Hsat} = 17.8kW/cm^2$, $\alpha_{H0}L$ increases from 5 to 20. As we see, despite of $\frac{g_{L0}}{\alpha_{H0}}$ being reduced from 0.4 to 0.1, the switching gain is still significantly increased with the increase of $\alpha_{H0}L$, which implies $\alpha_{H0}L$ plays more significant roles than $g_{L0}L$ in determining the switching gain. In Fig. 4.4b, we let $\alpha_{H0}L = 10$ and I_{Hsat} increase from $10.5kW/cm^2$ to $29kW/cm^2$. We can see the switching gain is increased at the higher I_{Hsat}. This could be partially due to the reduced $\frac{I_{Lsat}}{I_{Hsat}}$ value, as shown in Fig. 4.2b.

Since α_{H0} and I_{Hsat} are typically larger at the shorter wavelength, we are led to the same conclusion as from Fig. 4.3 that reducing the pump wavelength will enhance the switching gain.

To summarize the analysis above, the switching gain of single-waveguide pump-control switch can be effectively improved with the higher $\alpha_{H0}L$, $g_{L0}L$, I_{Hsat} and the lower I_{Lsat}, by reducing the pump wavelength, setting the control wavelength at the maximum-gain point, and increasing the waveguide length.

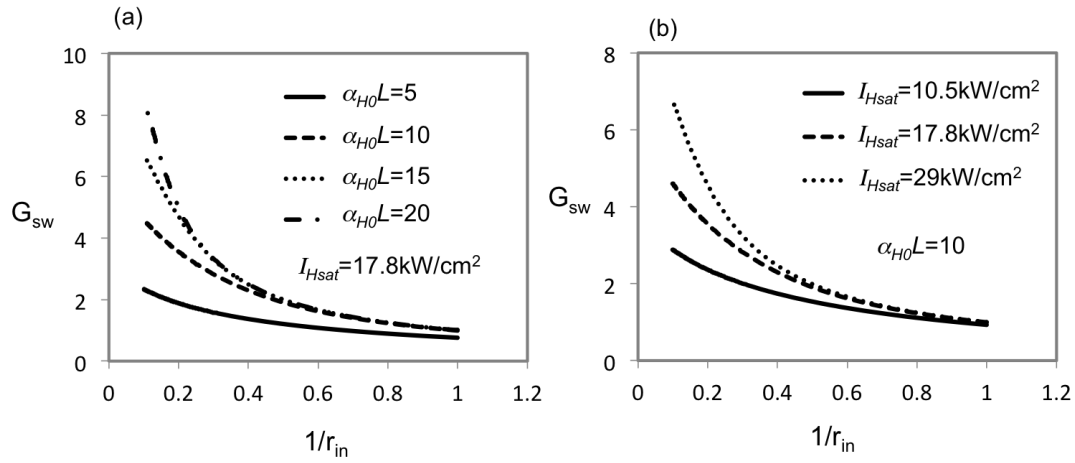

Figure 4.4: Switching gain G_{sw} versus $1/r_{in} = \frac{I_{L-in}}{I_{H-in}}$ with varied (a) $\alpha_{H0}L$ and (b) I_{Hsat}. $I_{H-in} = 10MW/cm^2, g_{L0}L = 2, I_{Lsat} = 82kW/cm^2$.

4.3 Switching Speed and Switching Energy

In this section, we start with proposing a new saturation intensity for describing the optical pumping and saturation behavior in a thick medium. Then with assistance of MLME-FDTD simulation, the co-directional optical pumping rate is studied in a bulk InGaAsP waveguide, based on which the switching speed and the switching energy of pump-control switching scheme are expressed analytically.

4.3.1 Saturation intensity of thick medium

Part of the Phsyics in EUPT or the single-wavegudie switching case is the saturation of the medium by the pump. While the saturation behavior by a pump in a thin medium has been well studied, the saturation behavior by a pump in a thick medium has not. Here we make a study of the medium saturation for the case of a thick medium and discuss the physics involved.

Previously, we introduced the saturation intensity for the absorption coefficient,

which is defined as the intensity at which the absorption coefficient drops to exactly half of the small-signal absorption.

$$\alpha_H = \frac{\alpha_{H0}}{1 + {I_H}/{I_{Hsat}}} \tag{4.7}$$

where α_{H0} is the small-signal absorption coefficient and I_{Hsat} is the saturation intensity. *H* denotes the wavelength of light at λ_H.

However, when an optical field propagates through a thick active medium, such as an active waveguide with a finite length, the optical power is attenuated as it propagates due to the absorption, causing stronger pumping at input region than the output region. As a result, the absorption coefficient along the propagation direction is not uniform. Here we propose a new definition of saturation intensity for the thick medium with thickness of *L*, which is denoted by I_{Hsat-L} to be distinguished from the material saturation intensity I_{Hsat}. It is defined as the input optical intensity required to reduce the absorption coefficient at the output end of the medium by half.

Consider the active waveguide lies along z axis. The pump supply beam at λ_H is incident at z=0 and exits at z=*L*. With Eqn.(3.13), the intensity variation along the waveguide is given by

$$\frac{dI_H(z)}{dz} = -\frac{\alpha_{H0}}{1 + {I_H(z)}/{I_{Hsat}}} I_H(z) \tag{4.8}$$

With the integration from z=0 to z=*L*, Eqn. (4.8) becomes

$$ln\frac{I_H(L)}{I_H(0)} + \frac{I_H(L) - I_H(0)}{I_{Hsat}} = -\alpha_{H0}L \tag{4.9}$$

i. Saturation

The definition of I_{Hsat-L} tells that when $I(0) = I_{Hsat-L}$, the absorption coefficient at z=L is reduced to half, i.e. $I(L) = I_{Hsat}$. Thus Eqn.(4.9) at saturation condition becomes

$$ln\frac{I_{Hsat-L}}{I_{Hsat}} + \frac{I_{Hsat-L}}{I_{Hsat}} = 1 + \alpha_{H0}L \tag{4.10}$$

$\frac{I_{Hsat-L}}{I_{Hsat}}$ is plotted versus $\alpha_0 L$ in Fig. 4.5. When the waveguide length is significantly small, i.e. $\alpha_{H0}L \to 0$, the solution is $\frac{I_{Hsat-L}}{I_{Hsat}} = 1$, giving $I_{Hsat-L} = I_{Hsat}$.

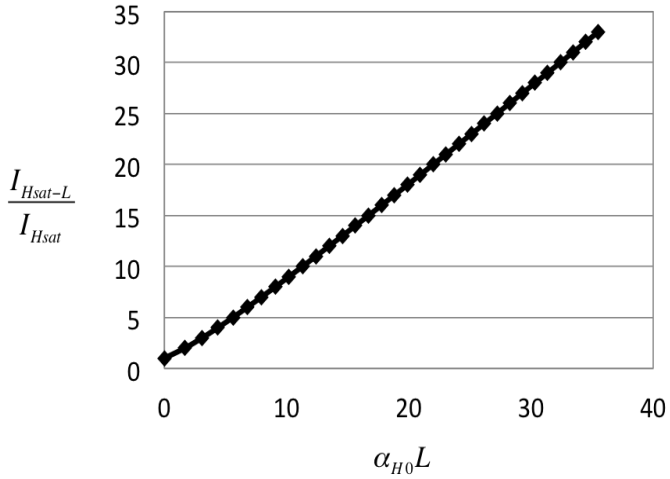

Figure 4.5: I_{Hsat-L}/I_{Hsat} vs $\alpha_{H0}L$.

ii. Transparency

To achieve the transparency condition, it requires the transmission $T_H = \frac{I_H(L)}{I_H(0)} \sim 1$. Substitute $T_H = \frac{I_H(L)}{I_H(0)}$ into Eqn. (4.10), it gives

$$\frac{I_H(0)}{I_{Hsat}} = \frac{\alpha_{H0}L + lnT_H}{1 - T_H} \tag{4.11}$$

As $T_H \to 1$, Eqn. (4.11) is reduced to $\frac{I_H(0)}{I_{Hsat}} = \frac{\alpha_{H0}L}{1-T_H} - 1$. Therefore to achieve 99% transmission for example, the required incident intensity is in the order of ~ $100\alpha_{H0}LI_{Hsat}$ and to achieve 99.9% transmission, it requires ~ $1000\alpha_{H0}LI_{Hsat}$. Take an example of $\alpha_{H0}L = 10$ and $I_{Hsat} = 17.8kW/cm^2$, the incident pump intensity to achieve 99% transmission is $17.8MW/cm^2$, which corresponds to the pump power of 7.7mW in a waveguide with modal area $A_{eff} = 0.043\mu m^2$. However, to further increase the transmission to 99.9%, the required pump power will be increase by one order to be 77mW. Apparently, it is impractical to pump the waveguide to high transparency. Therefore, we consider 95% transparency as an acceptable transparency level for our EUPT operation. The corresponding pump intensity requirement is ~$20\alpha_{H0}LI_{Hsat}$.

It is also noted that, to reduce the pump power requirement for the transparency state, we need to reduce $\alpha_{H0}L$ or I_{Hsat}, which however will compromise the switching gain. In other words, we cannot infinitely increase $\alpha_{H0}L$ or I_{Hsat} to achieve high switching gain without compromising the power consumption.

4.3.2 Co-directional optical pumping rate of a waveguide

The maximum switching speed of the pump-control switching operation is mainly determined by the switch-off speed, i.e. the speed of pumping the waveguide back to transparency, since the switch-on process dominated by the stimulated emission is ultrafast. In the last section, we have studied the saturation characteristics of a co-directionally pumped waveguide structure in the steady state, the dynamic behavior of which will be analyzed here based on MLME-FDTD simulation.

In the co-directional pumping process, the optical pumping is initially stronger

at the entrance end than the transmitted end, due to the absorption of the waveguide. As the pumping continues, the saturation effect reduces the absorption coefficient and allows more of the light to travel to the transmitted end. As a result, the carrier-pumping rate at the transmitted end is increased, which speeds up the transmission increase of the pump. Therefore, the whole pumping process will take more time if the waveguide is longer and the small-signal absorption coefficient is higher. Based on the steady-state saturation characteristics formulated in the last section, we expect the co-directional pumping rate of a waveguide structure will also be $\alpha_{H0}L$ dependent.

The MLME-FDTD simulation is carried out for the bulk InGaAsP waveguide (Table 3.1) pumped by the continuous wave light at 1350nm. We first consider two waveguides with the same $\alpha_{H0}L$, but different individual values of α_{H0} and L. A vertical optical confinement factor is introduced in our MLME-FDTD program, which allows us to linearly adjust the value of α_{H0} without changing the material properties. Here we let one waveguide have $L = 4\ \mu m$ and $\alpha_{H0} = 0.573\mu m^{-1}$ with optical confinement factor equal to 1 and the other waveguide have $L = 20\ \mu m$ and $\alpha_{H0} = 0.115\mu m^{-1}$ with optical confinement factor equal to 0.2. The two waveguides are pumped at $\lambda_H = 1350nm$ with the same input intensity $I_{H-in} = 15MW/cm^2$. Note that $15MW/cm^2 > 100\alpha_{H0}LI_{Hsat}$, thus the waveguide will be pumped to transparency eventually. The transmission of the two waveguide are plotted with respect to the simulation time in Fig. 4.6, showing the co-directional pumping rate of the waveguide is related with the product parameter $\alpha_{H0}L$, instead of individual values of α_{H0} and L.

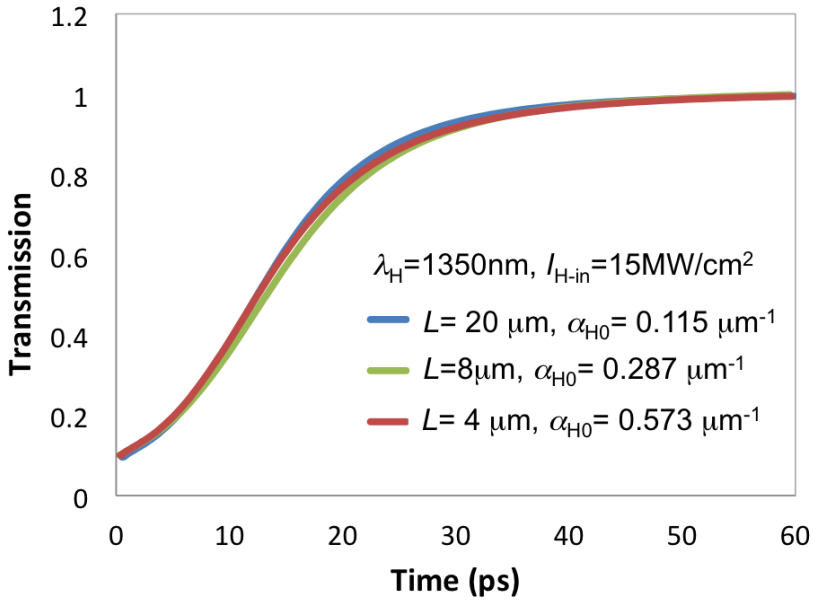

Figure 4.6: single waveguide pumping at the same $\alpha_{H0}L = 2.3$, but different individual values of α_{H0} and L. Transmission of pump beam through waveguide with $L = 20\,\mu m$ and $\alpha_{H0} = 0.115\mu m^{-1}$ (blue), waveguide with $L = 8\,\mu m$ and $\alpha_{H0} = 0.287\mu m^{-1}$, and waveguide with $L = 4\,\mu m$ and $\alpha_{H0} = 0.573\mu m^{-1}$ (red). Pump wavelength is 1350nm, intensity is $I_{H-in} = 15MW/cm^2$.

Next, with the same material properties and incident pump beam condition, the co-directional pumping rate is examined at varied $\alpha_{H0}L$. The transmission of the pump beam versus the simulation time is plotted in Fig. 4.7 for $\alpha_{H0}L$ ranging from 0.46 to 11.5. As we see, it takes longer time to pump the waveguide to the transparency state when $\alpha_{H0}L$ is larger. We also notice that for $\alpha_{H0}L \geq 5.7$, the transmission of the pump stays ~0 for a certain period before it gets significant increase, and the zero-transmission period increases with $\alpha_{H0}L$. While for $\alpha_{H0}L \leq 2.3$, the initial transmission at t~0 is high enough to promote significant carrier pumping at the output end, thus the zero-transmission stage is absent. It is also important to note that the increasing slope of the pump transmission does not differ significantly among varied $\alpha_{H0}L$.

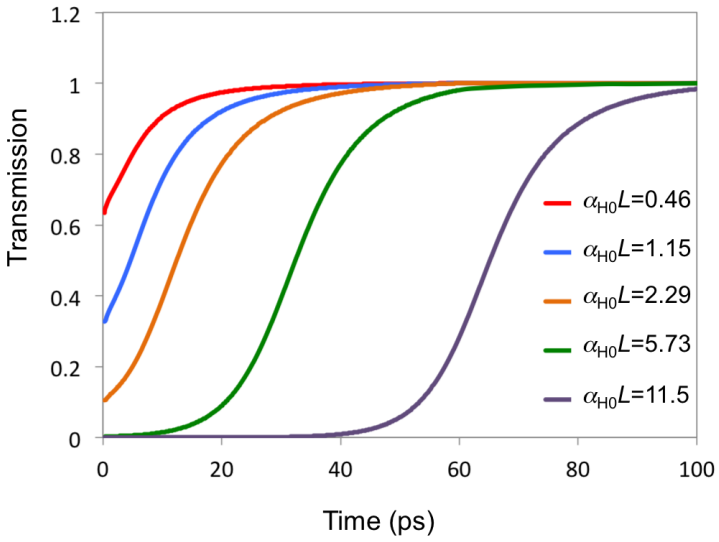

Figure 4.7: The transmitted pump (1350nm) versus simulation time through bulk InGaAsP (Table 3.1) waveguides with varied $\alpha_{H0}L$.

Based on the results in Fig. 4.7, the co-directional pumping process in the waveguide structure can be categorized into two stages. The first stage refers to the zero-transmission stage, in which the pump beam saturates the waveguide to get transmit out. This stage gets longer when $\alpha_{H0}L$ is larger. In the second stage, namely transmission-out stage, the output end of the waveguide is pumped up and the transmission of pump beam significantly increases, the increasing slope of which as we demonstrated is independent of $\alpha_{H0}L$. In the pump-control switching operation, depending on the carrier depletion strength during the switch-on process, the switch-off pumping process can start with either the zero-transmission stage or the transmission-out stage. However, to achieve high-speed switching, it is desirable to operate at the transmission-out stage, i.e. to prevent complete shut-off of the output signal.

Next, the speed of the transmission-out stage is examined with different incident pump intensity. Consider the waveguides with $\alpha_{H0}L = 2.3$ pumped at $\lambda_H = 1350nm$, with the input pump intensity I_{H-in} varying from $5MW/cm^2$ to $20MW/cm^2$. The transmission variation with time at different I_{H-in} is shown in Fig.

4.8a. Define time period of the transmission-out stage as the time taken to increase the pump transmission from 10% to 90%, which is denoted by τ_{p2}. The subscript p2 stands for the second pumping stage. In Fig. 4.8b, the pumping rate $1/\tau_{ps}$ is plotted against I_{H-in}. As we see, they are proportional to each other, which is similar to the thin-medium pumping behavior. The interpolation function is displayed in Fig. 4.8b, giving that

$$1/\tau_{p2} = \xi I_{H-in} \tag{4.12}$$

where $\xi = 0.24\ (m^2 J^{-1})$.

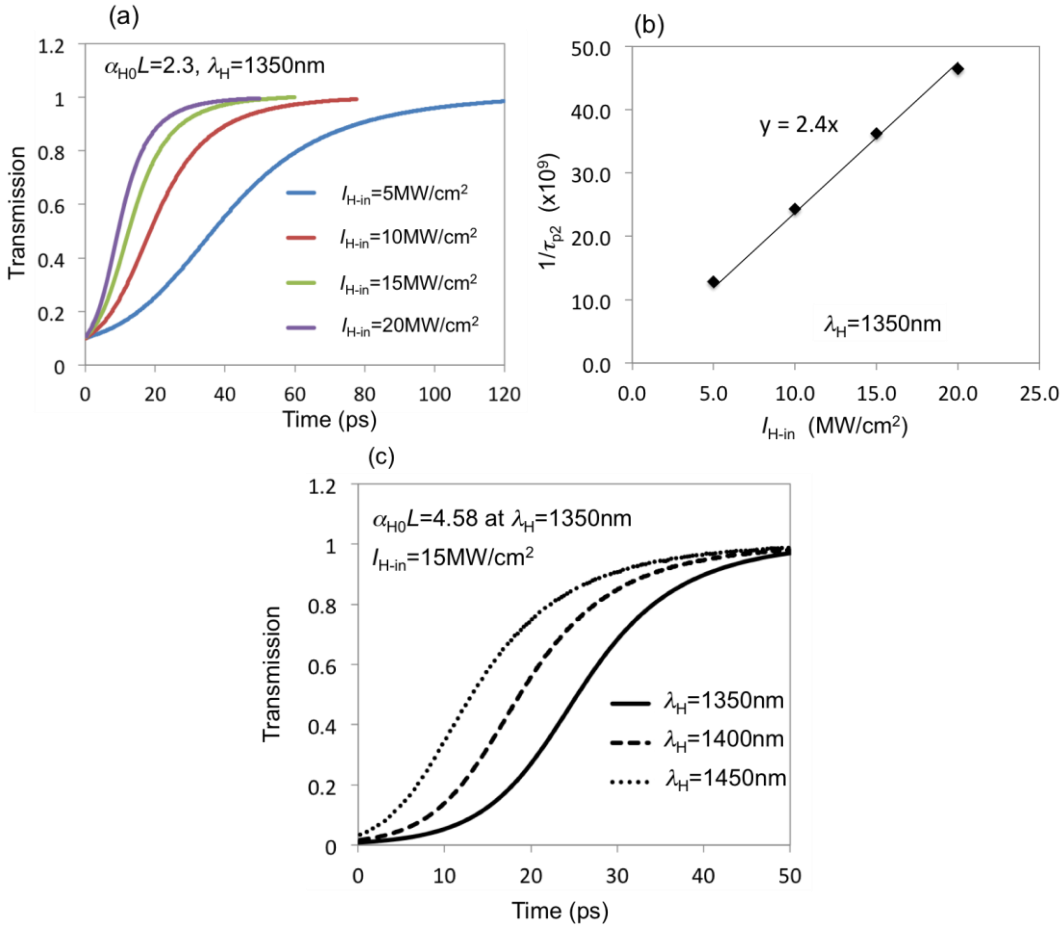

Figure 4.8: (a) Transmission of pump (1350nm) versus simulation time at different incident intensity. $\alpha_{H0}L = 2.3$. (b) the stage-two pumping rate in (a) versus input pump (1350nm) intensity (dots) and the linear interpolation (solid line). (c) Transmission of pump at 1350nm (solid), 1400nm (dash) and 1450nm (dotted) versus simulation time, with $\alpha_{H0}L = 4.58$ for $\lambda_H = 1350nm$ and $I_{H-in} = 15MW/cm^2$. L is fixed.

Subsequently, τ_{p2} is examined at different pump wavelengths $\lambda_H = 1400nm$ and $\lambda_H = 1450nm$. Consider $\alpha_{H0}L = 4.58$ for $\lambda_H = 1350nm$. The incident pump intensity $I_{H-in} = 15MW/cm^2$, the waveguide length L and the optical confinement factor are fixed. The transmission of the pump beam versus the simulation time is shown in Fig. 4.8c. As we can see, the pumping rate of the transmission-out stage is not strongly dependent on the pumping wavelength. We also examine the value of ξ for $\lambda_H = 1400nm$ and $\lambda_H = 1450nm$, which turns out to be the same value as that for the $\lambda_H = 1350nm$ case.

4.3.3 Analytical estimation of switching energy

The energy consumption E_{bit} (energy per bit) of the single waveguide switch is estimated by

$$E_{bit} = \frac{(I_{H-in} + D_c I_{L-in}) \cdot A_{eff}}{R_{bit}} \tag{4.13}$$

where D_c refers to the duty cycle of the control pulse sequence, R_{bit} represents the bit rate of the input control pulses. Consider the highest switching speed $R_{bit} \sim 1/\tau_{p2}$, we have

$$E_{bit} = \frac{A_{eff}}{\xi}\left(1 + D_c \frac{1}{r_{in}}\right) \tag{4.14}$$

where $r_{in} = I_{H-in}/I_{L-in}$. Since $\frac{1}{r_{in}} \ll 1$ is typically required to achieve high switching gain and $D_c < 1$, the switching energy of single waveguide switching is more of a constant determined by the waveguide geometry and material property, i.e. $\frac{A_{eff}}{\xi}$. For example of $\xi = 0.24\ (m^2J^{-1})$ and $A_{eff} = 0.043\mu m^2$, we have $E_{bit} \sim 180fJ/bit$, which stands for the minimum energy requirement for the single-waveguide switch operated at the highest switching speed. This is much higher than

the 10fJ/bit criteria for optical devices to offer sufficient energy advantage for optics over the electrical system in the coming 10 years [30]. $A_{eff} = 0.043\mu m^2$ corresponds to the mode size of 1450nm light in a 250nmx350nm silicon waveguide surrounded by a cladding of silicon dioxide, which is difficult to be further reduced. Therefore, the only way to significantly improve the energy efficiency of the pump-control switching scheme is adopting a "faster" medium with higher value of ξ.

4.4 MLME-FDTD Simulation of Single Waveguide Switching Based on InGaAsP Bulk Semiconductor

The analytical formulation developed for the switching gain and the switching speed of the single-waveguide switch will be examined by MLME-FDTD simulation in this section. Meanwhile, a 50Gbps and 0.5pJ per bit switching operation with switching gain of around 10 is demonstrated for a 40μm-long bulk-InGaAsP-based waveguide.

First of all, consider the pump-control switching operation in a $20\mu m$-length 400nm-width bulk-InGaAsP-based (Table 3.1) single waveguide. Let $\lambda_H = 1350nm$, $\lambda_L = 1450nm$ and $I_{H-in} = 15MW/cm^2$ be fixed, and I_{L-in} varies. MLME-FDTD simulation gives $\alpha_{H0} = 0.57\mu m^{-1}$, thus $\alpha_{H0}L = 11.4$. The transmission of pump beam T_H versus $1/r_{in}$ is plotted in Fig. 4.9, where the triangular dots show the MLME-FDTD results and the solid line shows the analytical calculation result. As we see, the analytical calculation is generally consistent with the FDTD simulation with a slight underestimation of T_H, or an overestimation of the switching gain by ~10%, which is of the same order of error with our absorption/gain formulation (Fig. 3.8).

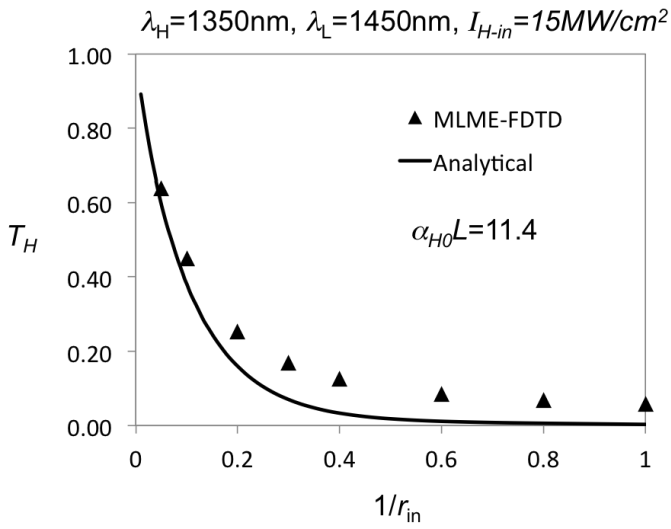

Figure 4.9: The transmission of pump beam versus $1/r_{in} = \frac{I_{L-in}}{I_{H-in}}$ for $\alpha_{H0}L = 11.4$, calculated by our analytical formulation (solid line) and MLME-FDTD simulation. $\lambda_H = 1350nm$ and $\lambda_L = 1450nm$. $I_{H-in} = 15MW/cm^2$.

Next, MLME-FDTD is utilized to demonstrate the dynamic switching in a $L = 40\mu m$ bulk-InGaAsP waveguide operated at $\lambda_H = 1350nm$, $\lambda_L = 1450nm$, $I_{H-in} = 15MW/cm^2$ and $I_{H-in} = 1.5MW/cm^2$. With $\alpha_{H0} = 0.57\mu m^{-1}$, it gives $\alpha_{H0}L = 22.8$. Consider $A_{eff} = 0.043\mu m^2$, the pump power and the control pulse peak power are equal to 6.45mW and 0.645mW respectively. The temporal profiles of the input and output signal powers are shown in Fig. 4.10. As we can see, the waveguide is initially pumped to transparency, with 100% of the pump power transmitted through. As a 27.5ps-width square control pulse is launched from the opposite end of the waveguide, the transmission of pump is rapidly reduced to ~0 within ~10ps. After the control pulse exits, the pump beam re-pumps the waveguide to transparency within ~50ps. The 10% - 90% transmission rising time, i.e. τ_{p2}, is consistent with our analytical calculation using Eqn. (4.12), which gives $\tau_{p2} = 28ps$. Hence, a 20Gbps switching operation with switching gain of 10 is demonstrated in a 40 μm long bulk-InGaAsP waveguide. The energy consumption per bit calculated by

Eqn. (4.13) is around 0.34pJ/bit.

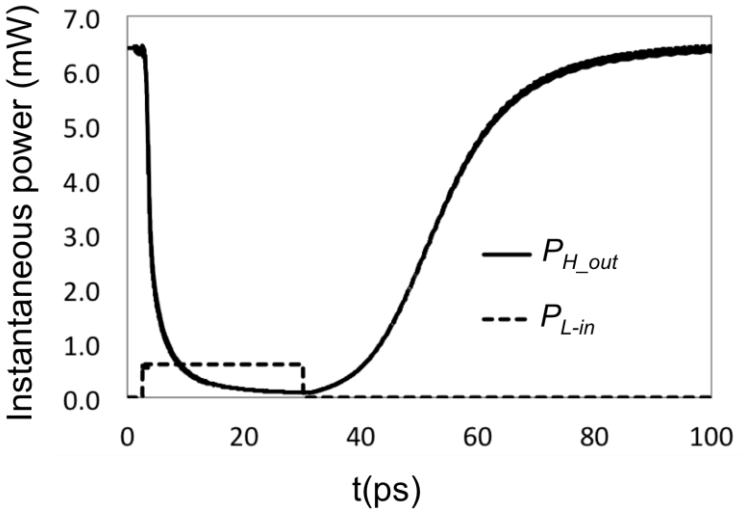

Figure 4.10: The transmitted pump power (solid line) when a 27.5ps control pulse with 10% of the pump intensity (dash line) is launched from the opposite end of the waveguide. $\lambda_H = 1350nm$ and $\lambda_L = 1450nm$. $I_{H-in} = 15MW/cm^2$. The waveguide length L=40 m and $\alpha_{H0}L$=22.8. Assume $A_{eff} = 0.043\mu m^2$.

To further increase the switching speed, we simultaneously increase the pump and control intensities by 4 times. At the same time, the control pulse width is reduced to 10ps. The resultant signal profiles are shown in Fig. 4.11. As we see, the switching gain is slightly reduced, giving $G_{sw} = 9$. The switch-on speed governed by the carrier depletion at the control wavelength does not exhibit significant increase, remaining at ~10ps, despite of the increase in control intensity. While the switch-off speed is significantly increased, giving a time scale of ~10ps. Thus 50Gbps switching is achieved. With $A_{eff} = 0.043\mu m^2$, the pump power and control peak power are equal to 25.8mW and 2.58mW respectively, giving the total switching energy of 0.54pJ/bit.

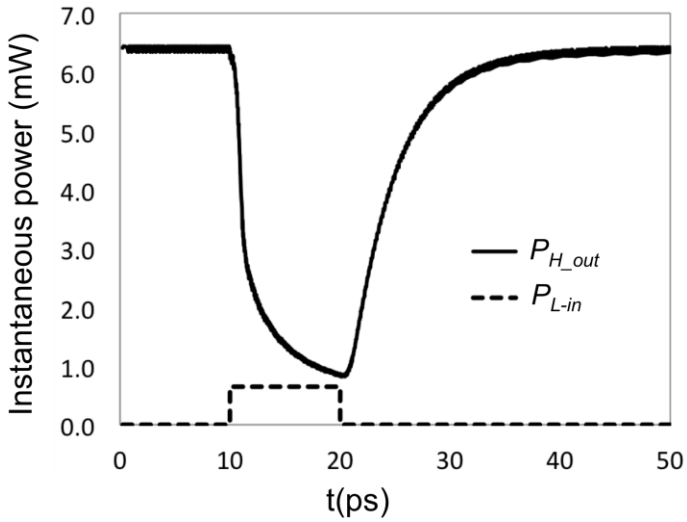

Figure 4.11: The transmitted pump power (solid line) when a 10ps control pulse with 10% of the pump intensity (dash line) is launched from the opposite end of the waveguide. $\lambda_H = 1350nm$ and $\lambda_L = 1450nm$. $I_{H-in} = 60MW/cm^2$. The waveguide length L=40μm and $\alpha_{H0}L$=22.8. The mode area is $A_{eff} = 0.043\mu m^2$.

4.5 Conclusion

Based on the analysis above, several main switching parameters and their roles in affecting the switching performance of single waveguide switch are summarized as follows:

1) Pump wavelength λ_H: reducing the pump wavelength benefits the switching gain performance in the way of increasing $\frac{g_{L0}}{\alpha_{H0}}$, $\alpha_{H0}L$ and I_{Hsat}, and reducing $\frac{I_{Lsat}}{I_{Hsat}}$. However, the power efficiency of the device will drop with the adoption of the shorter wavelength pump, due to the increased pump power requirement for achieving the transparency state with the larger $\alpha_{H0}L$ and I_{Hsat}.

2) Pump intensity I_{H-in}: $I_{H-in} > 20\alpha_{H0}LI_{Hsat}$ is required to ensure 95% transparency at switch-off state. Meanwhile, it is the main parameter that determines the switching speed. The higher I_{H-in}, the faster the device is switched off.

3) Control wavelength λ_L: to increase the switching gain, choose the

wavelength that gives the maximum optical gain as the waveguide medium is pumped up at λ_H.

4) Control intensity I_{L-in}: Reduce to increase the switching gain.

5) $\alpha_{H0}L$: It is a parameter dependent on the material property, pump wavelength choice as well as the device geometry, and also the most important parameter that determines the switching performance of the single waveguide switch. Increasing $\alpha_{H0}L$ can effectively increase the switching gain, but it will also increase the pump power requirement to achieve transparency state.

6) Waveguide modal area A_{eff}: Reducing the modal area can reduce the energy consumption, therefore strongly guiding nano-waveguide is important for low-power all-optical switching.

In the following section, the switching performance of EUPT will be systematically analyzed based on the analytical technique developed in this section.

CHAPTER V THEORETICAL STUDIES OF EUPT PART III: Performance Study and Optimization of EUPT

5.1 Analytical Analysis of Switching Gain in EUPT

Consider the ideal operational condition in EUPT, i.e. the pump supply beam is completely coupled into the active waveguide at the switch-OFF condition. Refer to the notations defined in Fig. 3.1, P_{H-OFF} and P_{L-OFF} are thus equal to zero. The switching gain of EUPT is given by $G_{sw} = P_{H-ON}/P_{L-ON}$.

The accurate way of calculating P_{H-ON} is substituting the absorption/gain formulation into the coupled mode equations of pump supply and input signal beams and solving them self-consistently, which however will not be explored here. Instead, an approximation method is developed, by utilizing the single-waveguide formulation in Eqn. (4.5) to calculate the effective absorption coefficient α_{eff} induced in the active waveguide by the carrier depletion, which is then substituted into the coupled mode formulation in section 3.1 to determine the output signal power P_{H-ON}. It is important to note that, in the EUPT operation, as the signal beam is launched into active waveguide of the coupler, it experiences efficient coupling into the passive waveguide, resulting in reduced interaction distance along the active waveguide. To take this factor into account, we assume the coupling effect simply reduces the interaction length by half. Subsequently, Eqn. (4.5) is modified as follows

$$-ln(T_H) + \frac{\alpha_{H0}}{g_{L0}} ln\left[1 + \frac{g_{L0}}{\alpha_{H0}} \frac{I_{Lsat}}{I_{Hsat}} (1 - T_H) r_{in}\right] + (1 - T_H) \frac{\tau_r}{I_{Hsat}} I_{H-CW}$$

$$= \frac{1}{2} \alpha_{H0} L \quad (5.1)$$

where T_H can be written as $e^{-\alpha_{eff} L}$ to calculate the effective absorption coefficient α_{eff} induced in the active waveguide. Here the incident intensity ratio r_{in} is denoted by $\frac{I_{H-CW}}{I_{L-ON}}$, where $I_{H-CW} = P_{H-CW}/A_{eff}$, $I_{L-ON} = P_{L-ON}/A_{eff}$, and A_{eff} is the effective modal area in the active waveguide. Thus r_{in} can also been written as $\frac{P_{H-CW}}{P_{L-ON}}$.

Next, refer to Eqn. (3.6) in section 3.1. With $\Delta\beta = 0$ and $z = L_{C2} = L_{C0}$, it gives the output signal power normalized to the input pump supply power at different absorption coefficient in the active waveguide, which is given by

$$\frac{P_{H-ON}}{P_{H-CW}} = |a_1(\alpha_{am} L_{C2})|^2 =$$

$$e^{-\alpha_{am} L_{C2}} \left[\cos\left(\frac{\sqrt{\pi^2 - (\alpha_{am} L_{C2})^2}}{2}\right) + \frac{\sin\left(\frac{\sqrt{\pi^2 - (\alpha_{am} L_{C2})^2}}{2}\right)}{\sqrt{\frac{\pi^2}{(\alpha_{am} L_{C2})^2} - 1}}\right]^2 \text{ for } \alpha_{am} L_{C2} < \pi \quad (5.2a)$$

$$e^{-\alpha_{am} L_{C2}} \left[\cosh\left(\frac{\sqrt{(\alpha_{am} L_{C2})^2 - \pi^2}}{2}\right) + \frac{\sinh\left(\frac{\sqrt{(\alpha_{am} L_{C2})^2 - \pi^2}}{2}\right)}{\sqrt{1 - \frac{\pi^2}{(\alpha_{am} L_{C2})^2}}}\right]^2 \text{ for } \alpha_{am} L_{C2} > \pi \quad (5.2b)$$

With $\alpha_{am} = \frac{\alpha_{eff}}{2}$ and $r_{in} = \frac{P_{H-CW}}{P_{L-ON}}$ substituted in, the switching gain factor is given by

$$G_{sw} = r_{in} \left| a_1 \left(\frac{\alpha_{eff} L}{2}\right)\right|^2 \quad (5.3)$$

where $\alpha_{eff} L$ is determined from Eqn. (5.1).

We note that $\left|a_1\left(\frac{\alpha_{eff}L}{2}\right)\right|^2$ in Eqn. (5.3) is a monotonically increasing function of $\alpha_{eff}L$ as shown in Fig. 3.3. Equivalently, G_{sw} monotonically decreases with the increase of T_H, which is same as the single-waveguide case given by $G_{sw} = (1 - T_H)r_{in}$. Since Eqn. (4.5) and Eqn. (5.3) for the T_H determination are similar to each other, we will expect the switching gain of EUPT to exhibit the same characteristics as in the single waveguide switch, i.e. the switching gain increases with the $\frac{g_{L0}}{\alpha_{H0}}$, I_{Hsat}, $\alpha_{H0}L$ and decreases with $\frac{I_{Lsat}}{I_{Hsat}}$. As a result, the conclusions we draw from the single-waveguide switch analysis in section 4.5 will generally apply to the EUPT switch.

Subsequently, the quantitative analysis for the switching gain of EUPT is carried out with the active waveguide material specified, i.e. the bulk InGaAsP semiconductor given in Table 3.1. With the pump supply wavelength fixed at $\lambda_H = 1.35\mu m$, the input signal wavelength is chosen at $\lambda_L = 1.45\mu m$ for the G_{sw} maximization. With that, the analytical calculation gives $\frac{g_{L0}}{\alpha_{H0}} = 0.23$, $\frac{I_{Lsat}}{I_{Hsat}} = 4.6$ and $I_{Hsat} = 17.8kW/cm^2$. The pump supply intensity $I_{H-CW} = \frac{P_{H-CW}}{A_{eff}}$ is decided by the switching speed targeted, which can be estimated by Eqn. (4.12). Here we let $I_{H-CW} = 15MW/cm^2$ to give τ_{p2}~$28ps$. Note that, $I_{H-CW} > 20\frac{\alpha_{H0}L}{2}I_{Hsat}$ is required to achieve 95% transparency at switch-off state, where $\alpha_{H0}L$ is divided by 2 since only half of the active waveguide is effectively pumped up. Therefore, we have $\alpha_{H0}L$ <84, which means with pump supply intensity at $I_{H-CW} = 15MW/cm^2$, we need to keep $\alpha_{H0}L$ <84 to ensure >95% transparency state in the active waveguide thus high coupling efficiency of pump supply beam during the switch-off state.

Next, G_{sw} is analytically calculated with different input signal intensity and

different $\alpha_{H0}L$. In Fig. 5.1, G_{sw} is plotted against $1/r_{in} = \frac{P_{L-ON}}{P_{H-CW}}$ at varied $\alpha_{H0}L$. It shows $\alpha_{H0}L$ needs to be >30 to achieve the switching gain, i.e. $G_{sw} > 1$, and switching gain of 2 can be achieved with $\alpha_{H0}L > 35$. If we increase $\alpha_{H0}L$ to 55 for example, G_{sw} will be increased to ~20. In addition, for each $\alpha_{H0}L$, there is a maximum switching gain associated with an optimal input signal power, and the optimal input signal power generally decreases with the increase of $\alpha_{H0}L$. When $\alpha_{H0}L = 55$, the optimal $\frac{P_{L-ON}}{P_{H-CW}}$ ratio is ~0.01.

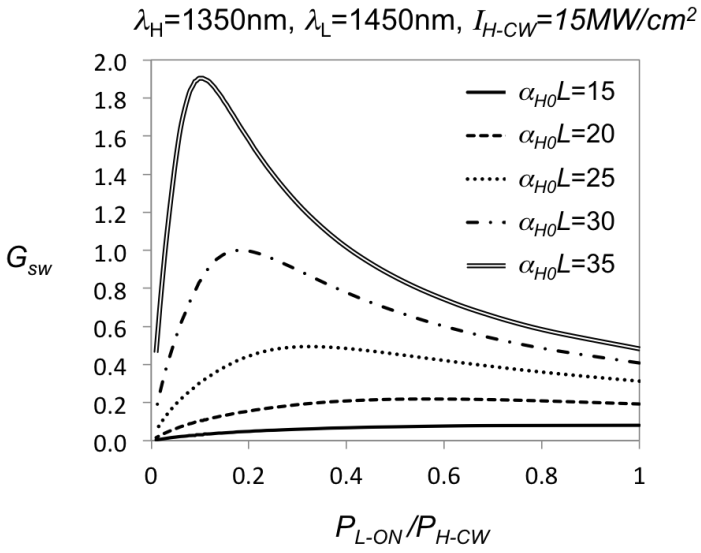

Figure 5.1: Switching gain of EUPT versus $1/r_{in} = \frac{P_{L-ON}}{P_{H-CW}}$ at different $\alpha_{H0}L$, with $I_{H-CW} = P_{H-CW}/A_{eff} = 15MW/cm^2$. $\lambda_L = 1.45\mu m$ and $\lambda_H = 1.35\mu m$.

5.2 Switching Speed and Figure of Merit of Bulk-InGaAsP-based EUPT

In section 4.3.2, we derived Eqn. (4.12) to estimate the co-directional pumping rate of a single waveguide structure at the transmission-out stage, which is

proportional to the incident pump intensity. However, for the case of EUPT in the directional-coupler structure, the pump supply power is partially switched out of the active waveguide during the switch-on state, thus the overall pumping rate will be slower than the direct pumping of the single waveguide structure. With this fact taken into account, the switch-off time of EUPT is estimated by

$$1/\tau_{OFF} = \xi\left[1 - \left|a_1\left(\frac{\alpha_{eff}L}{2}\right)\right|^2\right] \; I_{H-CW} = \xi(I_{H-CW} - I_{L-ON}G_{sw}) \qquad (5.4)$$

where $\xi = 0.24m^2J^{-1}$ for the bulk InGaAsP.

Next, the relative Figure of Merit of bulk-InGaAsP EUPT is calculated based on our analytical model, and compared with value presented in Huang's work [9]. With the substitution of our new notations, the Merit Factor as defined in Eqn. (2.1) is written as

$$MF = \frac{N_{ch}G_{sw}R_{bit}}{(P_{PS} + P_{SIG})T_{sig}A_d} = \frac{N_{ch}G_{sw}}{(I_{H-CW} + I_{L-ON})A_{eff}(\tau_{OFF} + \tau_{ON})A_d} \qquad (5.5)$$

where the signal pulse repetition time $1/R_{bit}$ is equal to the sum of switch-on time and switch-off time to represent the maximum-switching-speed case. Based on the previous single-waveguide FDTD simulation, the switch-on time is assigned with a fixed value of $\tau_{ON} = 10^{-11}sec$. The switch-off time τ_{OFF} is given by Eqn. (5.4). $(I_{H-CW} + I_{L-ON})A_{eff}(\tau_{OFF} + \tau_{ON})$ gives the energy per bit E_{bit} of the EUPT.

Consider the $\alpha_{H0}L = 55$ case for the bulk-InGaAsP-based EUPT, we have $G_{sw} = 20$, $I_{L-ON} = 0.01I_{H-CW} = 0.15MW/cm^2$, and using Eqn. (5.4), it gives $\tau_{OFF} = 28.8ps$. To make a fair comparison, the same A_{eff} and N_{ch} values as in Huang's work are adopted here, giving $A_{eff} = 0.043\mu m^2$ and $N_{ch} = 20$. In addition, Huang's calculation considered EUPT operated at $\alpha_{H0}L = 7.5$ has a device

area of $A_d = 150\mu m^2$, thus $\alpha_{H0}L = 55$ in our case leads to a device area of $A_d = 1100\mu m^2$.

The resultant Merit Factor for EUPT is $1.4 \times 10^{24} J^{-1}m^{-2}$, which is then normalized to the Merit Factor for the electronic transistor ($1.2 \times 10^{27} J^{-1}m^{-2}$) to obtain the relative figure of merits (FOM) for the EUPT. It shows FOM=1.2×10^{-3}, which is one order lower than the FOM for the GAMOI photonic transistor obtained from the 4-level 2-electron FDTD simulation (Table 2.1). In addition, the energy consumption of EUPT based on our calculation is ~250fJ/bit, which is about 5 times higher than the previous calculation in [9] given by ~44fJ/bit.

We also need to note that our MF calculation only involves EUTP. Once EDPT is included, additional power consumption and device area will be added on, and the switching gain will be reduced. As a result, the FOM for the full photonic transistor will be lower than 1.2×10^{-3}.

5.3 Dynamic Switching of EUPT Simulated by MLME-FDTD

The dynamic switching of InGaAsP-based EUPT will be demonstrated by MLME-FDTD simulation in this section, with one case of $\alpha_{H0}L < 30$ and one case of $\alpha_{H0}L > 30$. The pump supply and signal wavelengths are fixed at $\lambda_H = 1350nm$ and $\lambda_L = 1450nm$.

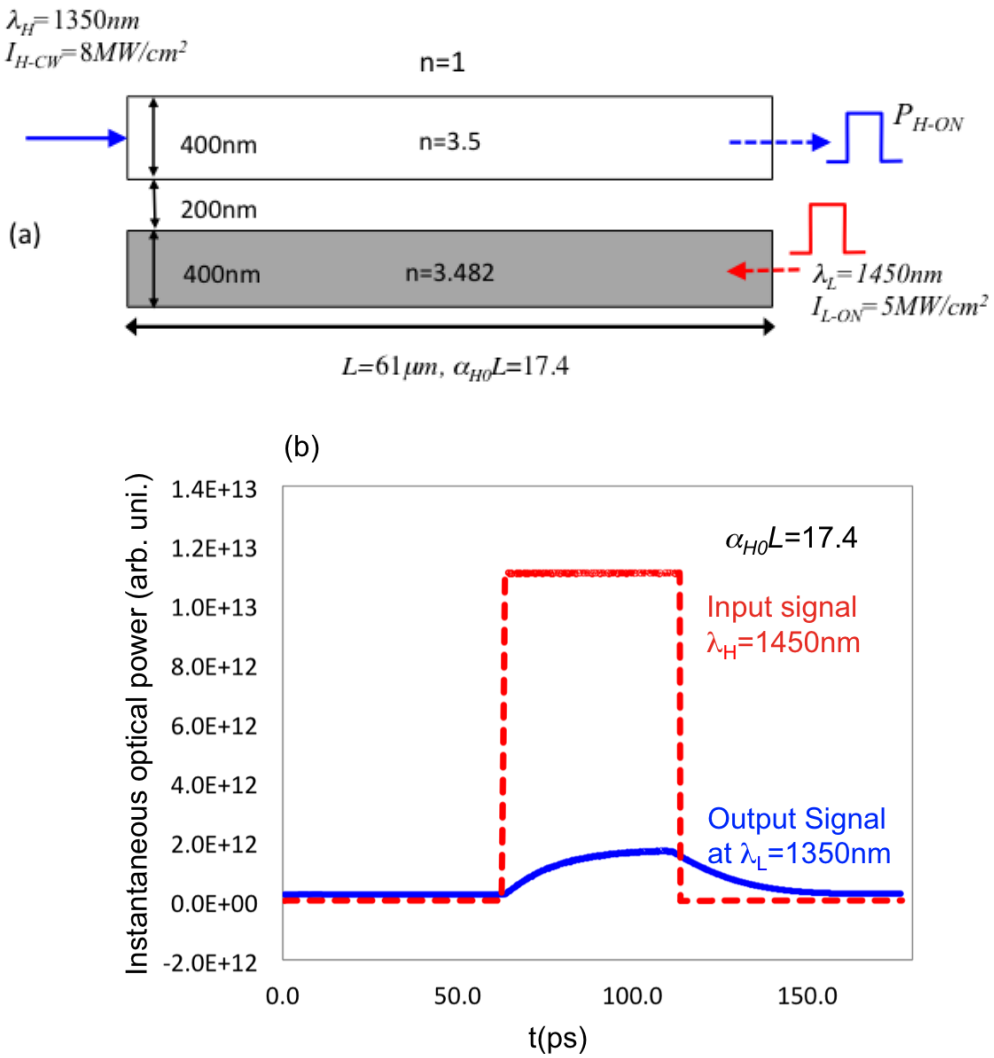

Figure 5.2: (a) EUPT with $\alpha_{H0}L = 17.4$. n is the background material refractive index. The pump supply beam at $\lambda_H = 1350nm$ and $I_{H-CW} = 8MW/cm^2$ is incident from the passive waveguide, and the square signal at $\lambda_L = 1450nm$ with $I_{L-ON} = 5MW/cm^2$ and $I_{L-OFF} = 0$ is launched from the opposite end of the active waveguide after the active waveguide is pumped to transparency. (b) The input signal (red dash) and output signal (blue solid) intensity profiles.

For the first case in Fig. 5.2, the directional coupler consisting of two 400nm-width waveguides separated by 200nm has the coupling length of 61 μm. With the vertical optical confinement factor equal to 0.5, we have $\alpha_{H0} = 0.285\mu m^{-1}$ for the active waveguide, which gives $\alpha_{H0}L = 17.4$. The background refractive index of the active medium is 3.482, so that it can be index matched to the passive waveguide with n=3.5 when the active waveguide is pumped to transparency at $\lambda_H = 1350nm$.

The pump supply beam at input intensity of $I_{H-CW} = 8MW/cm^2$ is launched from the passive waveguide, and the 50ps signal pulse with peak intensity at $I_{L-ON} = 5MW/cm^2$ is launched from the opposite end of the active waveguide after the active waveguide is pumped to transparency. The temporal profiles of input signal (red dash line) and output signal (blue solid line) power are plotted in Fig. 5.2b. The analytically calculated switching gain for this case is $G_{sw} = 0.2$, which is close to the FDTD simulation results. The switch-on and switch-off time are ~10ps and ~40ps respectively. With A_{eff} =0.043μm^2, the pump power P_{H-CW} is equal to 3.44mW, and the peak power of the input signal P_{L-ON} is equal 2.15mW. Therefore, Fig. 5.2 shows a 20Gbps switching with switching gain of 0.18 and switching energy of 0.28pJ/bit.

For the second case, as shown in Fig. 5.3, without changing the geometry of the coupler, the small-signal absorption coefficient is increased to $\alpha_{H0} = 0.57\mu m^{-1}$ by setting the optical confinement factor at 1. As a result, we have $\alpha_{H0}L = 34.8$. The background refractive index of the active medium in this case is 3.464 to promise index matching when the active waveguide is pumped to transparency. The incident pump intensity and the peak intensity of the 50ps signal pulse are equal to $I_{H-CW} = 17MW/cm^2$ and $I_{L-ON} = 2MW/cm^2$s respectively.

Fig. 5.3b shows the temporal profiles of the input signal (red dash line) and output signal (green solid line) power. The switching gain is equal to 2.2, which is close to the analytical calculation result of $G_{sw} = 1.8$. The switch-off time ~40ps is consistent with the analytical calculation using Eqn. (5.4), which gives $\tau_{OFF} = 33ps$. Therefore, with A_{eff} =0.043μm^2, the pump power P_{H-CW} is equal to 7.31mW, and the peak power of the input signal P_{L-ON} is equal 0.86mW, giving the total switching energy of 0.4pJ/bit.

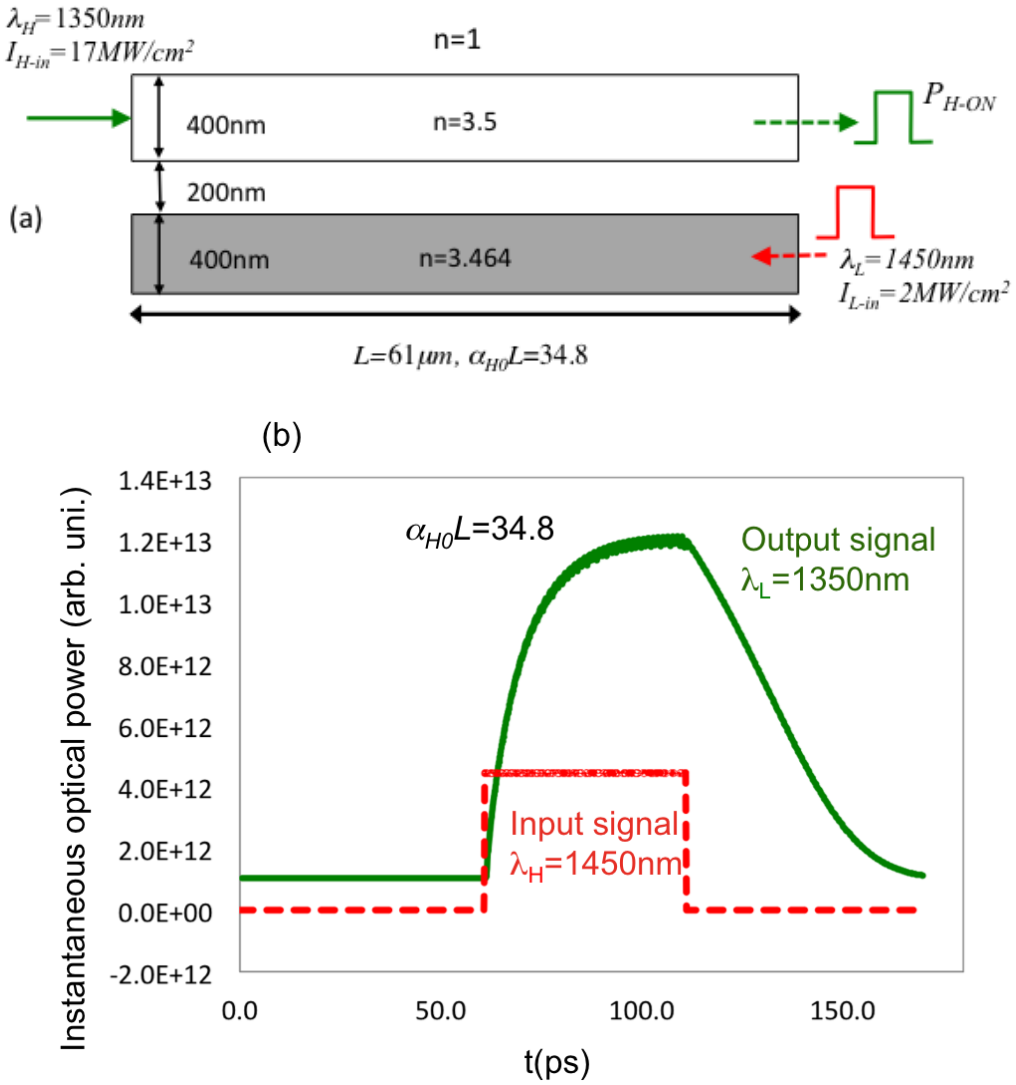

Figure 5.3: a) EUPT with $\alpha_{H0}L = 34.8$. n is the background material refractive index. The pump supply beam at $\lambda_H = 1350nm$ and $I_{H-CW} = 17MW/cm^2$ is incident from the passive waveguide, and the square signal at $\lambda_L = 1450nm$ with $I_{L-ON} = 2MW/cm^2$ and $I_{L-OFF} = 0$ is launched from the opposite end of the active waveguide after the active waveguide is pumped to transparency. (b) The input signal (red dash) and output signal (green solid) intensity profiles.

5.4 Conclusion

To conclude Chapter III, IV and V, a new analytical formulation is developed for calculating the absorption and gain coefficients seen by two monochromatic fields of different wavelengths interacting with a semiconductor medium. Based on that, the

switching performance of 2-WG EUPT is analytically formulated and systematically studied. It shows $\frac{g_{L0}}{\alpha_{H0}}$, $\frac{I_{Lsat}}{I_{Hsat}}$, I_{Hsat} and $\alpha_{H0}L$ are the four key parameters that effectively determine the switching gain of 2-WG EUPT. Increasing $\frac{g_{L0}}{\alpha_{H0}}$, $\alpha_{H0}L$ and I_{Hsat}, or effectively reducing $\frac{I_{Lsat}}{I_{Hsat}}$ will lead to the higher switching gain. On the other hand, increasing $\alpha_{H0}LI_{Hsat}$ will compromise the power efficiency of EUPT in the way that more pump power is required to pump the active waveguide to transparency. Therefore, in the real application, the switching gain and power consumption needs to be balanced with appropriate choices of active material, pump supply wavelength and device length.

Furthermore, with the assistance of MLME-FDTD, the co-directional pumping rate in a waveguide is analyzed, and two pumping stages are identified: the zero-transmission stage and transmission-out stage. We suggested the switch-off process of EUPT should be constrained to the transmission-out stage to maximize the switching speed. Meanwhile, the transmission-out-stage pumping rate expression is deduced for the InGaAsP bulk medium (Eqn. (4.12)), which is shown proportional to the input pump intensity with a proportionality constant of $\xi = 0.24\ (m^2J^{-1})$ and has little dependence on the pumping wavelength.

With the employment of InGaAsP-based bulk semiconductor in Table 3.1, the switching performance of EUPT is quantitatively analyzed. Compared with the previous analysis based on 4-level 2-electron FDTD simulation in [9], our calculation shows a larger $\alpha_{H0}L$ ($\alpha_{H0}L > 30$) is required to achieve switching gain, the energy consumption is at least 5 times higher (~250fJ/bit) and the Figure of Merit is more than one-order worse. But the overall performance is still significantly advantageous over the $\chi^{(3)}$ and SOA based switches.

At the end, 20Gbps switching operation with switching gain of ~2 and switching energy of 0.4pJ/bit is demonstrated in a bulk-InGaAsP-based EUPT switch with the employment of MLME-FDTD simulation. Simulation results are shown consistent with our analytical calculation.

CHAPTER VI: QUANTUM WELL SEMICONDUCTOR FOR EUPT APPLICATION

In the last chapter, the switching performance of EUPT is theoretically studied based on InGaAsP bulk semiconductor. The calculation shows a $\alpha_{H0}L$ value of at least 30 is required to promise switching gain and a minimum of 250fJ/bit energy is consumed, which result in a relative Figure of Merit in the order of 10^{-3}. According to the roadmap of optical network power consumption illustrated in D. A. B. Miller's article in 2009 [30], an energy target of ~10fJ/bit (or power target of 10μW/Gbps) is suggested for the optical devices to offer sufficient energy advantage over the electrical system in the coming 10 years. Thus a power reduction of at least 10 times is required for the current EUPT based on bulk InGaAsP. On the other hand, the device footprint, or equivalently the requirement of $\alpha_{H0}L$ to achieve switching gain, also needs to be reduced to further improve the Figure of Merit. These can be only done with the employment of new active medium.

In this chapter, we will investigate the characteristics of semiconductor quantum well (QW) in comparison with the bulk medium in affecting the switching performance of EUPT. We will start with a brief introduction to the semiconductor quantum well to highlight the main energy band features and some basic interband absorption behaviors in the QW. The key parameters that have been shown to determine the switching performance of EUPT are then calculated for the bulk InGaAsP and QW InGaAsP based on the free-carrier theory. At the end, a conclusion will be given.

6.1 Introduction to Semiconductor Quantum Wells

6.1.1 Band structures

Quantum well in semiconductors is formed by having a thin layer of a material with narrower bandgap (well) sandwiched between two layers of a material with a wider bandgap (barriers). The electrons and holes are confined in the lower-energy well layer, and when the well layer is sufficiently thin, the wave natures of electrons and holes respond to form standing waves, resulting in the quantized energy system.

With the energy quantization, a selection rule applies for the interband carrier transition, which states that only transitions between states of the same quantum number in the valence and conduction bands are allowed. Since quantum well has only one-dimensional confinement, this rule only applies to the momentum space perpendicular to the layers, while in the directions parallel to the layers, electron and holes are still free to move as in the bulk system. As a result, we do not really have discrete energy states for electrons and holes in quantum wells, we have instead "subbands" that form above the energies calculated for the confined states. The electron in a given confined state can gain additional kinetic energy from the in-plane motion in quantum well.

6.1.2 Interband optical absorption

The direct consequence of such energy subband structure is the modified density of states that distinguishes the quantum well from the bulk system in many optical properties. In a bulk semiconductor (3D) system, the density of states rises with square root of energy from the band gap edge, while in the semiconductor

quantum well, the density of states for a given subband turns out to be a constant with energy, thus the density of states over the entire energy band is a series of steps with each step starting at the appropriate confinement energy (Fig. 6.1). If we consider the simplest model for the interband absorption that an electron is raised "vertically" (no change of momentum) from the valence band to the conduction band by absorbing a photon, and we presume such transitions have identical strength over different photon energies, the absorption spectrum of semiconductor will follow directly from the density of states, as shown in Fig. 6.1.

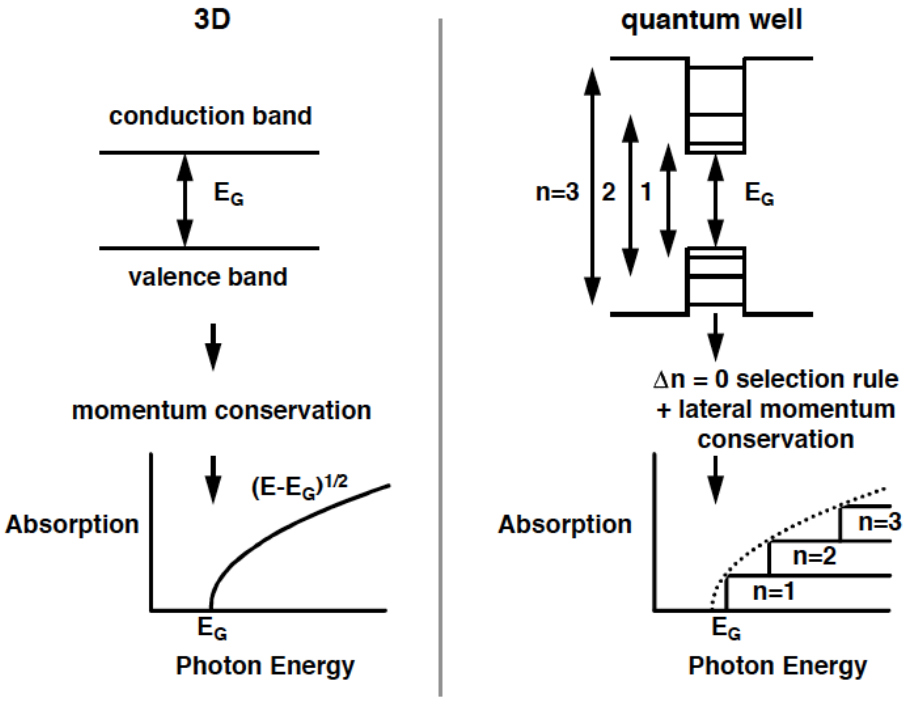

Figure 6.1: Optical absorption in bulk (i.e., 3D) semiconductors and in quantum wells, in the simplest model where excitonic effects are neglected.[31]

On the other hand, the quantum confinement results in the heavy-hole-light-hole splitting in the valence band. The heavy and light holes with different effective masses have energy quantization at different levels. Therefore, the light hole and heavy hole subbands are coupled with the electron subbands individually, leading to

separate set of interband transitions. If we consider a waveguide with light propagating along the quantum well layers, there are two distinct optical polarization directions: one with polarization parallel to the quantum well layers, called TE polarization, and the other with the polarization perpendicular to the quantum well layers, called TM polarization. Because of some microscopic selection rules associated with the unit cell wavefunctions, the heavy-hole-to-conduction band transition is forbidden for TM polarization. Thus, the absorption strength or gain at TM polarization is typically smaller than those for TE polarization. This is why quantum well waveguide lasers essentially always run in the TE polarization. For our EUPT application, we also keep the pump supply and signal beam at TE polarization.

Furthermore, the quantum confinement enhances the excitonic effect in the quantum well medium. Exciton refers to electron-hole pair in a bound hydrogenic state formed due to the Coulomb attraction between the negatively charged electron and positively charged hole. It has slightly lower energy (binding energy) than the free carrier states, thus optical excitation of valence band carriers into the excitonic state introduces an absorption peak near and below the band gap edge or subband edge. Excitonic absorption is difficult to resolve in the room-temperature bulk semiconductor, since the excitons are rapidly ionized via collisions with optical phonons. However, the quantum confinement in the quantum well confines the electron and hole closer together than in the three-dimensional case, making the absorption strength to create an exciton larger [32]. An actual absorption spectrum of a quantum well sample is shown in Fig. 6.2. The absorption in a series of steps agrees with the single-carrier picture discussed above, while the strong absorption peaks at the subband edges require the concept of excitons to interpret.

The large optical nonlinearity of the excitons has been investigated and utilized

widely in many applications, such as laser mode locking [33], optical processing [34], etc. However, the excitonic effect is not applicable in our EUPT case since our device is strongly pumped at a wavelength far above the band gap edge. The large population of the excited carriers will significantly saturate the formulation of the excitons. Therefore, we may ignore the excitonic effect in our discussion. The energy subband picture will be sufficient to analyze the characteristics of semiconductor quantum well for our EUPT application.

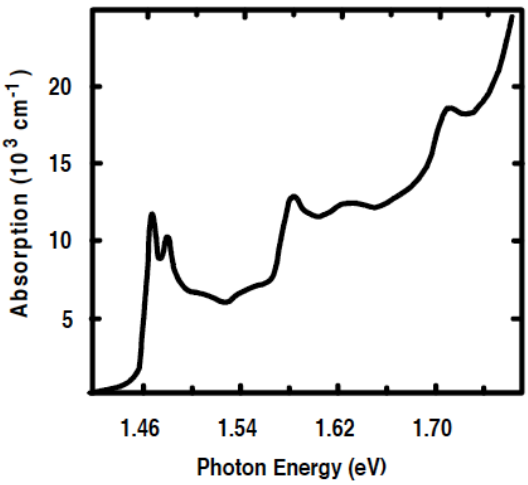

Figure 6.2: Absorption spectrum of a typical GaAs/AlGaAs quantum well structure at room temperature. [31]

6.2 Bulk-vs-QW Comparison Based on Free-Carrier Theory

In this dissertation, the interband absorption, saturation, and transition dynamics in a semiconductor medium is studied based on the free-carrier theory. The free-carrier model treats the carriers as ideal Fermi gases, and assumes the charged particle interactions are sufficiently fast compared to the field transition, such that intraband thermodynamic quasi-equilibrium Fermi-Dirac carrier distributions can be established. Although the realistic picture contains more effects, such as many-body Coulomb interaction, which renormalizes the bandgap energy and electric-dipole

interaction energy, the free-carrier model is reasonably accurate for comparing the interband transition characteristics between the bulk semiconductor and quantum well semiconductor.

In section 3.2.2, we derived the formulation for α_{H0}, g_{L0}, I_{Lsat}, and I_{Hsat} based on the free carrier theory, and the calculation results for these parameters for the bulk semiconductor is shown consistent with the MLME FDTD simulation. These formulations are also applicable to the quantum well system with the substitution of 2D density of state expression. To make a fair comparison, we consider the same InGaAsP band parameters as in Table 3.1, and consider the lowest confinement energy of the quantum well to be equal to the band gap energy of the bulk InGaAsP. Meanwhile, we assume the second-order confinement energy in the QW is sufficiently high such that the states there will not be excited.

6.2.1 Pump power requirement

First of all, with Eqn. (3.30) and Eqn. (3.25), the saturation intensity I_{Hsat} are calculated for the bulk and quantum well InGaAsP at different pump wavelength λ_H, which is shown in Fig. 6.3. We can see I_{Hsat} significantly increases with the decrease in the value of λ_H, and is up to 50% higher in the QW than in the bulk. It lies in the range of 10~100kW/cm^2, which is of the same order as the experimental results for the GaAs-based system [35]. Since the pump power requirement to achieve transparency state in the active waveguide increases with I_{Hsat} (section 4.3.1), the adoption of quantum well in our EUPT device will compromise the power efficiency to certain extend.

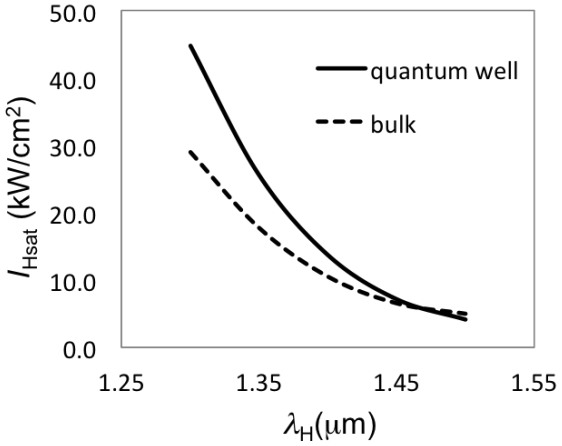

Figure 6.3: Analytically calculated I_{Hsat} versus pump wavelength λ_H for quantum well (solid) and bulk (dash) InGaAsP.

6.2.2 Switching gain

In section 4.2, we highlighted the significance of increasing $\frac{g_{L0}}{\alpha_{H0}}$ and reducing $\frac{I_{Lsat}}{I_{Hsat}}$ in enhancing the switching gain of EUPT and examined the characteristics of $\frac{g_{L0}}{\alpha_{H0}}$ and $\frac{I_{Lsat}}{I_{Hsat}}$ in the InGaAsP-based bulk semiconductor, as shown in Fig. 3.11. Here we use Eqn. (3.27), (3.30) and (3.35) to perform the calculation for InGaAsP-based quantum well medium with the same band parameters as given by Table 3.1. In Fig. 6.4, the $\frac{g_{L0}}{\alpha_{H0}}$ and $\frac{I_{Lsat}}{I_{Hsat}}$ are plotted versus the signal wavelength λ_L at three different pump supply wavelengths λ_H, where the red plots correspond to the quantum well cases and the black plots show the bulk cases. We find with 2D carrier confinement, quantum well medium generally gives the higher $\frac{g_{L0}}{\alpha_{H0}}$ and the lower $\frac{I_{Lsat}}{I_{Hsat}}$ than bulk medium, which is thus favorable for enhancing the switching gain. It is also noticed for the quantum well medium, reducing pump wavelength will lead to higher $\frac{g_{L0}}{\alpha_{H0}}$ and lower $\frac{I_{Lsat}}{I_{Hsat}}$, and the λ_L to give the maximum $\frac{g_{L0}}{\alpha_{H0}}$ also gives the close-to-minimum value of $\frac{I_{Lsat}}{I_{Hsat}}$, which are the same as the bulk case.

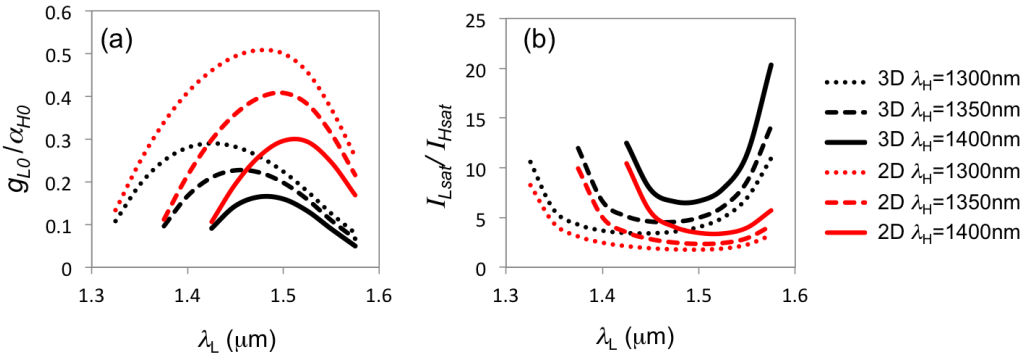

Figure 6.4: (a) $\frac{g_{L0}}{\alpha_{H0}}$ versus λ_L and (b) $\frac{I_{Lsat}}{I_{Hsat}}$ versus λ_L at different pump wavelength λ_H for bulk (black) and quantum well (red) medium.

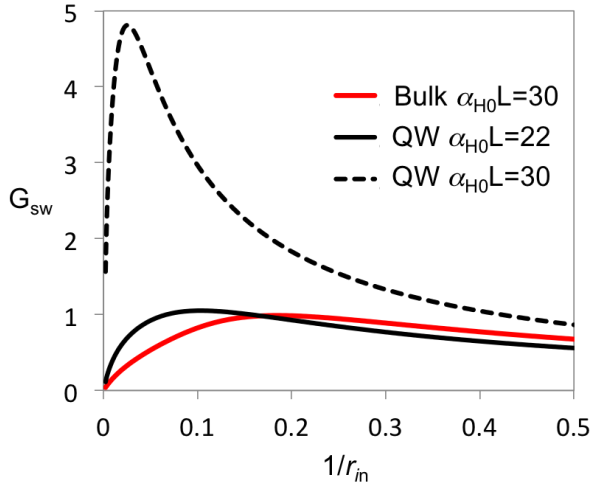

Figure 6.5: Switching gain of QW-InGaAsP-based EUPT versus $1/r_{in} = \frac{P_{L-ON}}{P_{H-CW}}$ at $\alpha_{H0}L = 22$ (black solid) and $\alpha_{H0}L = 30$ (black dash), and switching gain of bulk InGaAsP EUPT at $\alpha_{H0}L = 30$ (red solid). $I_{H-CW} = P_{H-CW}/A_{eff} = 15MW/cm^2$. $\lambda_L = 1.45\mu m$ and $\lambda_H = 1.35\mu m$.

Next, we perform the switching gain calculation for the QW-InGaAsP-based EUPT, using the same switching parameters as in Fig. 3.20, i.e. $\lambda_H = 1.35\mu m$, $\lambda_L = 1.45\mu m$ and $I_{H-CW} = 15MW/cm^2$. With $\alpha_{H0}L = 22$ and $\alpha_{H0}L = 30$, the switching gain of QW-InGaAsP-based EUPT is plotted versus $1/r_{in}$, as shown in Fig. 3.5. Meanwhile, the switching gain plot for the bulk-InGaAsP EUPT at $\alpha_{H0}L = 30$ is included for comparison. We can see, with the adoption of QW medium, the

$\alpha_{H0}L$ requirement for achieving switching gain is reduced to 22, which means the device footprint can be reduced by ~27%.

6.2.3 Switching speed

In section 4.3.2, we investigated the co-directional optical pumping rate of a waveguide, and identified two pumping stages: the zero-transmission stage and transmission-out stage. It was highlighted that the switch-off process of EUPT should be constrained to the transmission-out stage to maximize the switching speed. Meanwhile, the transmission-out-stage pumping rate expression is deduced based on MLME-FDTD simulation for the InGaAsP bulk medium (Eqn. (4.12)), which is shown proportional to the input pump intensity with a proportionality constant of $\xi = 0.24\ (m^2 J^{-1})$. ξ plays the significant role in determining the energy consumption of EUPT. By increasing ξ , one can further reduce the energy consumption.

To compare the ξ value between the bulk and quantum well medium, we consider the thin-medium pumping rate and take the simple estimation that

$$pumping\ rate \sim \frac{a_{H0} I_H}{\hbar\omega_H \int_0^{\varepsilon_H} d\varepsilon\ D(\varepsilon)} \sim \frac{|\mu(\varepsilon_H)|^2 D(\varepsilon_H)}{\int_0^{\varepsilon_H} D(\varepsilon) d\varepsilon}\ I_H \tag{6.1}$$

where we assume the absorption coefficient is constant with time, and the spontaneous decay rate is neglected since the pump intensity of interest is significantly higher than the saturation intensity in the EUPT operation. The integral $\int_0^{\varepsilon_H} D(\varepsilon) d\varepsilon$ calculates the total number of states up to the energy level where the medium is pumped, i.e. $\varepsilon_H = \hbar\omega_H - E_g$, and $\frac{a_{H0} I_H}{\hbar\omega_H}$ gives the number of carriers optically excited per second. The term $|\mu(\varepsilon_H)|^2$ is the transition dipole matrix

element at $\hbar\omega_H$. The density of state expressions for the bulk and quantum well are given by $D_{3D}(\varepsilon) = \frac{1}{2\pi^2}\left(\frac{2m_r}{\hbar^2}\right)^{\frac{3}{2}}\sqrt{\varepsilon}$ and $D_{2D}(\varepsilon) = \frac{m_r}{\pi\hbar^2}$, respectively. Subsequently, we can use Eqn. (6.1) to analytically estimate the pumping rate ratio between bulk and quantum well, which is

$$\frac{pumping\ rate\ in\ bulk}{pumping\ rate\ in\ QW} \sim \frac{\frac{3}{2}|\mu_{3D}(\varepsilon_H)|^2 \frac{1}{\varepsilon_H} I_H}{|\mu_{2D}(\varepsilon_H)|^2 \frac{1}{\varepsilon_H} I_H} \sim \frac{3}{2}\frac{|\mu_{3D}(\varepsilon_H)|^2}{|\mu_{2D}(\varepsilon_H)|^2} \tag{6.2}$$

Studies have shown that the transition dipole matrix element becomes polarization dependent in the quantum well, and a transition strength enhancement can be observed for TE polarization. Calculation also shows that the strongest enhancement is observed for the e-hh transition at the subband edge, with an enhancement factor of 3/2 [36]. In that case, the pumping rate in the bulk and QW become comparable. Therefore, employing QW will not benefit the switching speed of our EUPT.

6.2.4 Conclusion

Based on the free-carrier analysis above, we can see QW is advantageous over the bulk medium in terms of improving the switching gain of EUPT. However, compared with the bulk medium, QW requires a higher pump power to achieve the equivalent transparency state and poses little change to the switching speed of EUPT. We need to take note that the increased pump power requirement for achieving the transparency state does not necessarily increase the energy consumption of the device. Since the energy per bit is defined as the total power consumption divided by bit rate (Eqn. (4.13)) and the bit rate (mainly determined by the pumping rate) is

proportional to the pump supply intensity through a constant ξ, it turns out the energy consumption per bit has little dependence on the pump supply power.

6.3 Strained Quantum Well

More recently, extensive interests have been devoted to a new class of semiconductor quantum well structures, namely strained quantum well [37-38]. They are made of thin lattice mismatched layers where the mismatch is accompanied by a uniform elastic strain that modifies the energy band structure of semiconductors and thus changes the electronic and optical properties of the quantum well. Their applications in semiconductor lasers have been studied extensively and great improvement of the lasing characteristics has been demonstrated theoretically and experimentally. Stained quantum well can also benefit our photonic transistor in terms of increasing the switching gain and reducing the energy consumption of the device.

Two types of strain can be accommodated in the quantum well, as illustrated in Fig. 6.6. The quantum well layer with larger lattice constant experiences compressive strain, while with the smaller lattice constant, it experiences tensile strain. A critical thickness h_c exists such that the formation of dislocation and defects resulting from the misfit strain can be avoided when the layer thickness is smaller than h_c. It has been shown that the stain has a pronounced effect on the valence band structure of III-V materials. It removes the degeneracy in the valence band and removes the symmetry of the semiconductor lattice. Under a biaxial compressive strain, the heavy hole band is raised above the light hole band, resulting in reduced the density of states. On the other hand, a tensile strain raises the light-hole band above the heavy-hole band, which can change the dominant mode polarization from TE to TM and

affect the resulting optical spectrum significantly [39].

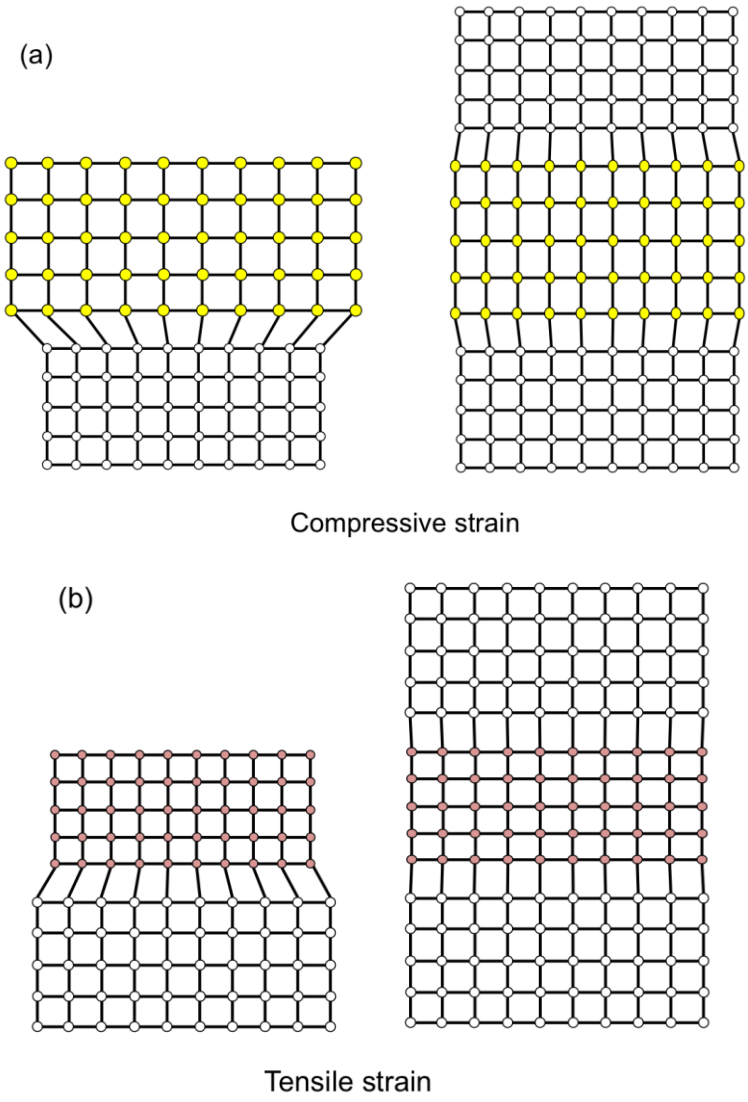

Figure 6.6: illustration of compressive strain and tensile strain in the quantum well layers. The atomic layer quantity does not represent the actual case.

One of the main applications of strained layer quantum well structures is quantum well lasers. It has been shown theoretically and experimentally that strained QW can lead to dramatic reductions in threshold current and improvement in terms of modulation bandwidth of laser linewidth [40]. Under compressive strain, the effective mass of hole is reduced due to the raise of heavy-hole band, which leads to a reduced density of states. As a result, semiconductor laser will achieve the population inversion condition at a smaller carrier density, thus has lower threshold current than

the non-strained one [41-42]. On the other hand, a tensile strain would raise the light hole band above the heavy hole band and cause the crossover between the energy bands of light hole and heavy hole at certain point. This affect can change the dominant mode from TE polarization to TM polarization and affect the optical spectrum significantly. [43]

Compressively strained quantum well is particularly interested for our photonic transistor application. The enhanced optical gain and differential gain imply more carrier depletion and the larger absorption change induced by the same amount of carrier depletion at switch-ON state, which will thus improve the switching gain characteristics of EUPT. The reduced carrier density will also benefit the EUPT operation in terms of reducing the pump power requirement to achieve transparency state. Therefore, in this dissertation, compressively strained quantum well will be adopted in the actual photonic transistor device. More details regarding the strained quantum well wafer design and the device fabrication process will be presented in the next chapter.

CHAPTER VII FABRICATION APPROACHES OF EUPT

The theoretical analysis of EUPT in the last chapter poses several basic requirements for the actual device structure of EUPT to meet the desired switching performance. First of all, high-index-contrast nano-waveguide structure is required to enhance the optical confinement, so as to increase the power efficiency of the device. The calculation in Section 5.2 shows with $A_{eff} = 0.043\mu m^2$ the energy consumption of bulk-InGaAsP EUPT is in the order of 200fJ/bit, which is 20 times of the 10fJ/bit criteria for the future optical devices [30]. Increasing A_{eff} will further exacerbate the situation. The mode size of a dielectric waveguide can be estimated by $D = \lambda/(2dn)$, where $dn = \sqrt{{n_{core}}^2 - {n_{clad}}^2}$, n_{core} and n_{clad} are the refractive index of the core and cladding respectively. For the case of InGaAsP as the core medium with n_{core} ~3.4, it requires $n_{clad} < 1.8$ to achieve modal area <0.043 μm^2 at $\lambda = 1350nm$. Therefore the conventional as-grown InP cladding (n~3.2) cannot provide sufficient refractive index contrast to achieve strong optical confinement. We need a cladding material with a lower refractive index, such as silicon dioxide and air.

Secondly, to achieve high $\frac{g_{L0}}{\alpha_{H0}}$ and prevent direct competition of interband carrier transition between the pump supply and signal beam, it is desired to have short pump supply wavelength and large wavelength separation (>50nm) between the pump and signal. As a result, the pump and signal wavelengths are typically 100-200nm shorter than the band gap wavelength of the active medium. Therefore, we need the band gap difference between the passive waveguide and active waveguide to be sufficiently large (>200nm) so that the pump supply and signal beam will see only

one waveguide active.

Furthermore, with the adoption of strongly-guiding nano-waveguide structure, the spatial gap between the active and passive waveguides for efficient optical coupling is typically in the sub-micrometer scale, which means the conventional passive-active integration techniques, such as selective-area epitaxy [44], re-growth [45], quantum well intermixing [46], which have spatial resolution in the several-micrometer scale, are not feasible for our application.

In this chapter, we will introduce two fabrication approaches for realizing the photonic transistor. One approach utilizes the ion-implantation induced quantum well intermixing (QWI) technique with assistance of diffusion-stop gap to achieve high-resolution passive-active integration, and utilizes adhesive bonding technique (BCB bonding) for high-refractive-index-contrast waveguide structure. The other approach is based on direct wafer bonding of III-V active medium on silicon-on-insulator (SOI) platform. The fabrication steps for each approach have been developed, and the pros and cons of which will be highlighted.

7.1 EUPT Based on Quantum-Well Intermixing With InGaAsP/InGaAs Multi-Quantum-Well Thin-Film Structure

The first configuration of our photonic transistor is based on III-V platform, which utilizes the ion-implantation induced quantum well intermixing (QWI) technique with assistance of diffusion-stop gap to achieve high-resolution passive-active integration. A thin-film structure obtained by BCB-bonding process is adopted to achieve high-refractive-index contrast, thus strong optical confinement in the waveguides.

7.1.1 Introduction to quantum well intermixing

Over the years many approaches have been investigated to realize different bandgap structure on the same wafer. The first representative approach is selective-area epitaxy growth [45], which is achieved by either opening a dielectric window through lithography followed by epitaxy growth or etching away the epitaxy layer in selective area followed by regrowth of quantum structure with a different energy bandgap. Those approaches have the advantage of flexibility in choosing structures for different area, leading to high material quality. However, multiple epitaxy growth leads to high cost. In addition, the joints between adjacent areas are typically discontinuous, over which is a transition region of typically ~100μm with varied and undesired energy bandgap structures. Thus, regrowth is not suitable for our application, which requires passive-active integration with high spatial resolution.

The second approach is based on post-growth modification on quantum wells, a representative example of which is quantum well intermixing (QWI) techniques. QWI utilizes the inter-diffusion effect between the quantum well and the barriers to alter the quantum well bandgap energy. Since there will not be repeated use of epitaxial growth system, the cost of it is low. Furthermore, the joints between different areas will be smoother, and the transition region is typically of a few micrometers.

The most important methods that have been used to realize QWI include the following. (1) Impurity free vacancy diffusion (IFVD), which commonly uses a SiO_2 layer to promote the outer diffusion of Ga. This method requires quite high annealing temperature compared to other approaches. (2) Impurity induced disordering (IID), in which impurities such as dopants are used to enhance the III-V material self-diffusion in the crystal and promote intermixing. However, the dopants will also change the

electrical characteristic of the structure dramatically, thus limits the application of this method. (3) Photo-absorption induced disordering (PAID), in which high power laser pulses is used to produce transient heating in the crystal. The resulting thermal expansion will then cause bond breaking and lattice disruption that lead to a localized increase in the density of point defects. This method has been shown to give good spatial resolution and high material quality. The drawback lays in the fact that in complex device geometry, it will be time consuming to scan the laser beam through the wafer. (4) Ion implantation assisted QWI, which relies on the diffusion of point defects created during ion implantation.

In our application, we will employ the low-energy ion-implantation assisted QWI to achieve passive-active integration. An exemplary process of low-energy ion-implantation induced quantum-well intermixing process is shown in Fig. 7.1. We start with a sample of InGaAs/InGaAsP quantum well grown on InP substrate and capped by a several hundred nanometers thick InP layer. SiO_2 is patterned as the ion implantation mask at selective areas, and phosphorus ions are implanted at the energy of several hundred keV. The thickness of implantation mask and the implantation energy are chosen so that implanted ions will be stopped within the mask at the covered areas to prevent introducing ions into the epitaxy wafer, and within the InP cap layer in the open areas to avoid direct implantation damage in the quantum well region. Subsequently, SiO_2 mask is removed and rapid thermal annealing is carried out, causing the defects in the InP cap layer, which are generated by ion implantation, to diffuse through the quantum well region. These defects, mostly vacancies, promote the inter-diffusion of atoms over the quantum-well and barrier interface to make it to be smeared, leading to an increase in quantized energy level in the well. As a result, the bandgap energy of the implanted region will undergo a blue-shift. Specifically,

the well is InGaAs and phosphorus ions are diffused from the InGaAsP barrier into the well, causing the well to be effectively narrower, resulting in a blue shift of the bandgap energy.

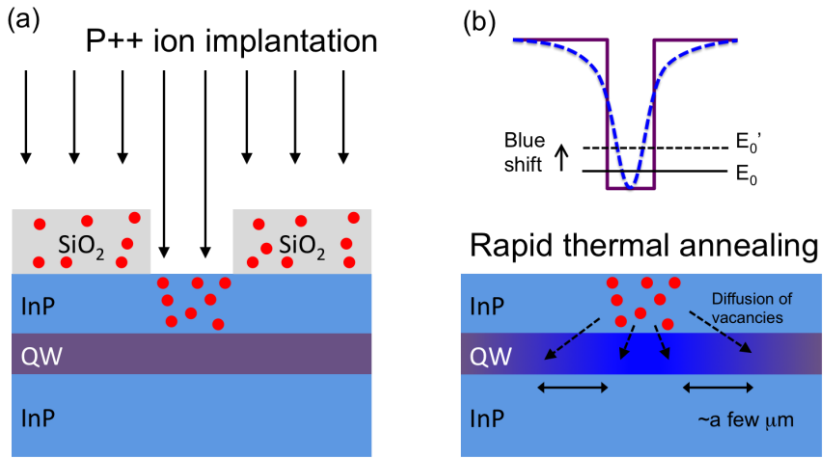

Figure 7.1: Ion-implantation induced quantum well intermixing. QW refers to the InGaAs/InGaAsP quantum well. (a) Ion implantation process, where implanted ions stops at SiO_2 mask layer and InP cap layer. (b) Annealing process to promote the vacancies at InP cap layer into QW region. The top insertion shows the quantum well potential before (solid) and after (dash) QWI and the increase of energy level due to the change of quantum well potential profile.

The lateral resolution of the ion-implantation induced quantum well intermixing is limited by two main factors. The first factor comes from the ion implantation process. The high-energy ions entering the wafer structure will collide with the atoms in the wafer and undergo a Monte Carlo process. The final distribution of the ions is influenced by many factors, including the implanted ion types, the energy of implanted ions, the wafer structure (materials, thickness, etc.), and the implantation condition such as temperature and tilting. As the wafer structure is fixed, and the type of implantation ion is typically chosen among the neutral species in the wafer system to eliminate free carrier absorption, which is thus fixed too. The next main parameter that can be adjusted is the implantation ion energy. It is known that both the depth and lateral range of ion increase with higher implantation energy. In order to

minimize the lateral range of the implanted ion, it is necessary to minimize the implantation energy.

The second factor that limits the lateral resolution of QWI is from the diffusion of vacancies during the rapid thermal annealing process. As the vacancies diffuse downwards through the QW region, the vacancies also undergo lateral diffusion over a distance that depends on the annealing time and temperature. Increasing annealing temperature and annealing time will both have the vacancies to smear out more, resulting in reduced lateral resolution of QWI. To minimize the defect diffusion length, ion implantation to very close proximity of the quantum well is needed, which however is usually avoided by conventional ion-implantation assisted QWI, because the ions will induce excessive free carrier absorption loss to the light.

Experimental results to date indicate that the resolution based on ion-implantation-induced intermixing remains on the order of $2\mu m$, which is not small enough for our application.

7.1.2 Diffusion-stop gap for increasing the lateral resolution of QWI

To further improve the resolution of QWI, we propose a diffusion-stop gap method, which refers to etching a narrow gap through the QW region prior to the QWI process to constraint the lateral traveling of both implanted ions and vacancies.

The process of diffusion-stop-gap assisted ion-implantation induced QWI is illustrated in Fig. 7.2. First of all, a narrow gap of about 100nm width is patterned using electron beam lithography (EBL) technique and etched down through the QW region using Inductively Coupled Plasma (ICP) etching technique. Subsequently, the ion implantation mask is patterned to protect area that does not require QWI. The mask can cross over the diffusion-stop gap and partially cover the region requiring

QWI to compensate the EBL overlay alignment error. With our EBL system (Elionix 100kV), the overlay alignment error is typically ~100nm, thus the mask edge is let ~500nm away from the diffusion-stop gap, which is short enough to allow the ion-implantation induced vacancies to diffuse over. After ion implantation, the sample is annealed and the vacancies diffuse into the QW region. Since the vacancies cannot diffuse across the diffusion-stop gap, the QW at other side is not affected. The lateral resolution of such QWI process is thus determined by the width of diffusion-stop gap.

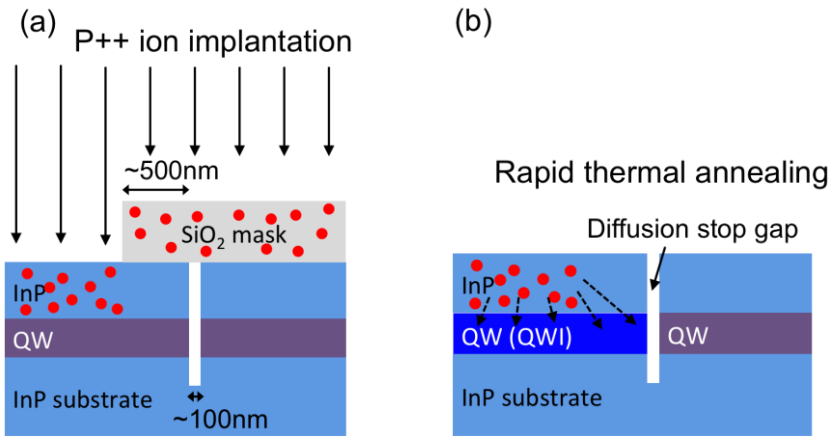

Figure 7.2: Ion implantation induced quantum well intermixing with assistance of diffusion-stop gap. QW stands for InGaAs/InGaAsP quantum well. (a) Ion implantation process: 100nm-width diffusion stop gap is etched through the QW region. SiO_2 ion implantation mask covers one side of the diffusion-stop gap. (b) Rapid thermal annealing process: the defects diffuse into the QW region and stop at the gap in the lateral direction, leaving region at the other side of the gap unaffected.

The workability of diffusion-stop gap is subsequently demonstrated with the following experiment. Commercially grown epitaxial InP-InGaAsP-InGaAs quantum well wafer with ten 5.5nm unstrained InGaAs quantum well separated by 12nm thick InGaAsP barriers, capped by 500nm InP bulk layer, is adopted. The as-grown photoluminescence peak wavelength of the QW is at 1510nm. For the first sample, as shown in Fig. 7.3a, parallel and periodic diffusion-stop gaps with 100nm width are patterned. The gaps are separated by 500nm and etched though the QW region. 500nm SiO_2 is subsequently deposited by Plasma Enhanced Chemical Vapor

Deposition (PECVD) technique as the ion implantation mask, with ion implantation windows open at alternative stripe. The reference sample, as shown in Fig. 7.3b is patterned with the same ion implantation mask, but without diffusion-stop gap. Phosphorous ions are implanted at 100keV with dosage of $10^{15} cm^{-3}$ at substrate temperature of 200°C for both samples. The defect implantation depth was about 300nm from the QW region. The SiO_2 mask is then removed and the samples are both annealed in a rapid thermal processor at 625°C for 2min.

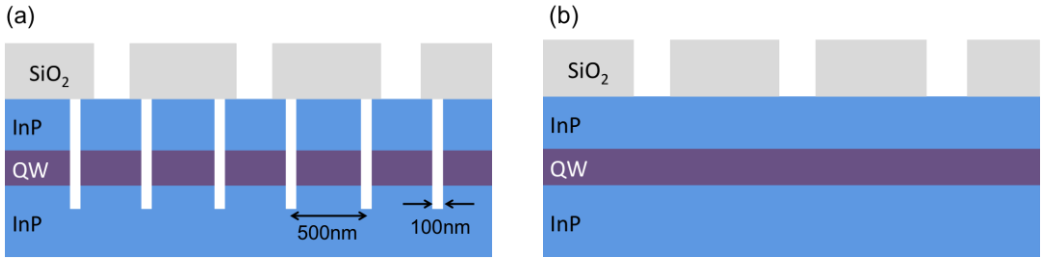

Figure 7.3: (a) InGaAs/InGaAsP quantum well wafer with a series of parallel diffusion-stop gaps etched and separated by 500nm. SiO_2 ion implantation mask covers alternative stripes. (b) InGaAs/InGaAsP quantum well wafer without diffusion-stop gap. The ion implantation mask is the same as in (a).

Figure 7.4 shows the PL spectrum of diffusion-stop-gap sample and reference sample after annealing. As we see, the reference sample without diffusion-stop gaps (Fig. 7.3b) has single PL peak at 1348nm, showing a ~160nm blue shift of bandgap energy over the sample. Although the implantation regions are well separated, the subsequent annealing has the defects smear out, resulting in uniform band gap shift across the un-implanted regions. However, the diffusion-stop-gap sample (Fig. 7.3a) exhibits two PL peaks separated by 70nm with similar peak intensities. One peak appears at the same wavelength as reference sample, showing the PL spectrum of the regions implanted with ions. The other peak at 1418nm shows the PL spectrum of regions without ion implantation, which experiences a 90nm blue shift. This shift is

caused by the QWI induced by thermal annealing process. As we can see, with adoption of diffusion-stop gap, regions with 70nm band gap difference can be patterned at a spatial resolution of 100nm. The band gap difference can be further increased by optimizing the ion implantation and annealing conditions.

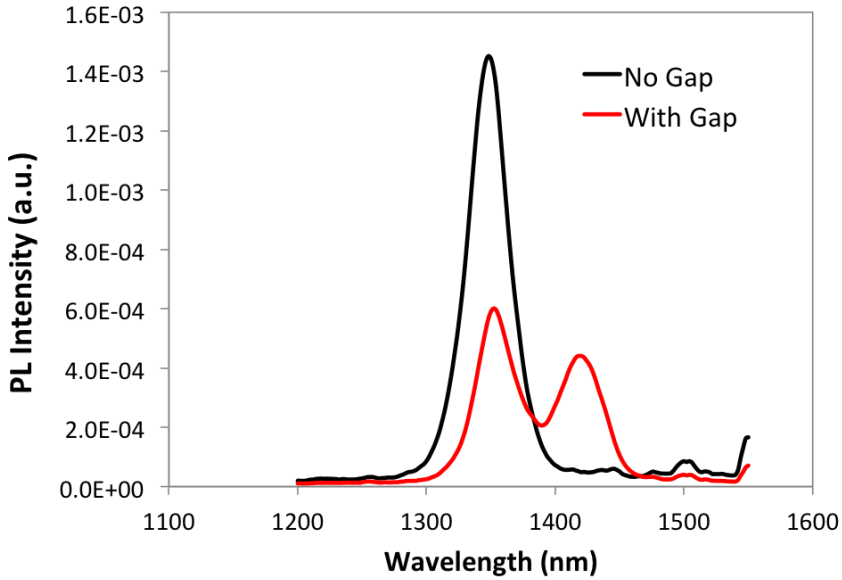

Figure 7.4: PL spectrum of diffusion-stop-gap sample in Fig. 7.3a (red) and the reference sample in Fig. 7.3b (black) after ion implantation and rapid thermal annealing.

7.1.3. Thin-film structure realized via BCB bonding

To enhance the optical confinement in the photonic transistor waveguide, and thus to increase the modal intensity and reduce the power consumption, it is necessary to have high refractive index contrast in both the lateral and vertical directions of the waveguides. The tall structure created by single etching step can provide high index contrast in the lateral direction, while the vertical contrast provided by latticed matched III-V materials， which are InP and InGaAs/InGaAsP in our case, is typically very small (dn~0.1). One way to achieve high refractive index contrast in both directions is to have the structure suspended in air, such as in the case

of micro disk [47, 48] or photonic band-gap structure [49]. Another way is to utilize certain polymer (BCB, n~1.56) [50] or dielectric material (SiO_2, n~1.45) with a refractive index low compared to the high refractive index of III-V semiconductor material (n~3.2). In this work, we will take the second approach and use the BCB bonding technique to fabricate the thin-film photonic transistor.

The detailed process steps are shown in Fig. 7.5. Following the diffusion-stop-gap assisted QWI process in Fig 7.2, we start with the InGaAsP/InGaAs quantum well wafer with patterned active and passive regions. First of all, InP cap layer is removed by chemical etching with HCl:H_2O (1:1) solution. The wafer is subsequently deposited with 300nm SiO_2 etching mask layer using PECVD technique, and coated with 300nm positive resist PMMA950-5A. After 15min hotplate baking at 170^oC, the sample is coated with a think layer of E-spacer to reduce the charging effect during the electron-beam exposure. The device structures (EUPT coupler structure) are then patterned on the PMMA layer using Electron Beam Lithography (EBL) technique followed by resist developing in MIBK:IPA (1:3) for 70s. Reactive Ion Etching (RIE) based on CHF_3/Ar chemistry is employed to transfer the EBL patterns into the PECVD-deposited SiO_2 layer. Subsequently, Inductively Coupled Plasma (ICP) etching based on Cl_2/N_2 chemistry is adopted to transfer the device patterns into the epi-wafer with SiO_2 as etching mask. Then the SiO_2 etching mask is removed with HF chemical etching, and a thin layer of PECVD SiO_2 is deposited on both the QW sample and a GaAs carrier wafer. This is to increase the surface adhesion of the QW sample and GaAs carrier wafer to BCB. After spin coating of BCB 3022-35 onto them, the device wafer is carefully flipped onto the GaAs carrier wafer. The whole assembly is placed onto a hotplate (~120^oC) and force is applied onto the top wafer. After that, the whole assembly is put into a nitrogen oven to cure the BCB. The

temperature cycle should follow the recommendation of the BCB manufacturer. After curing, the top InP substrate is chemically removed by hydrochloric acid solution ($HCl:H_2O=2:1$) and the thin-film structure is formed.

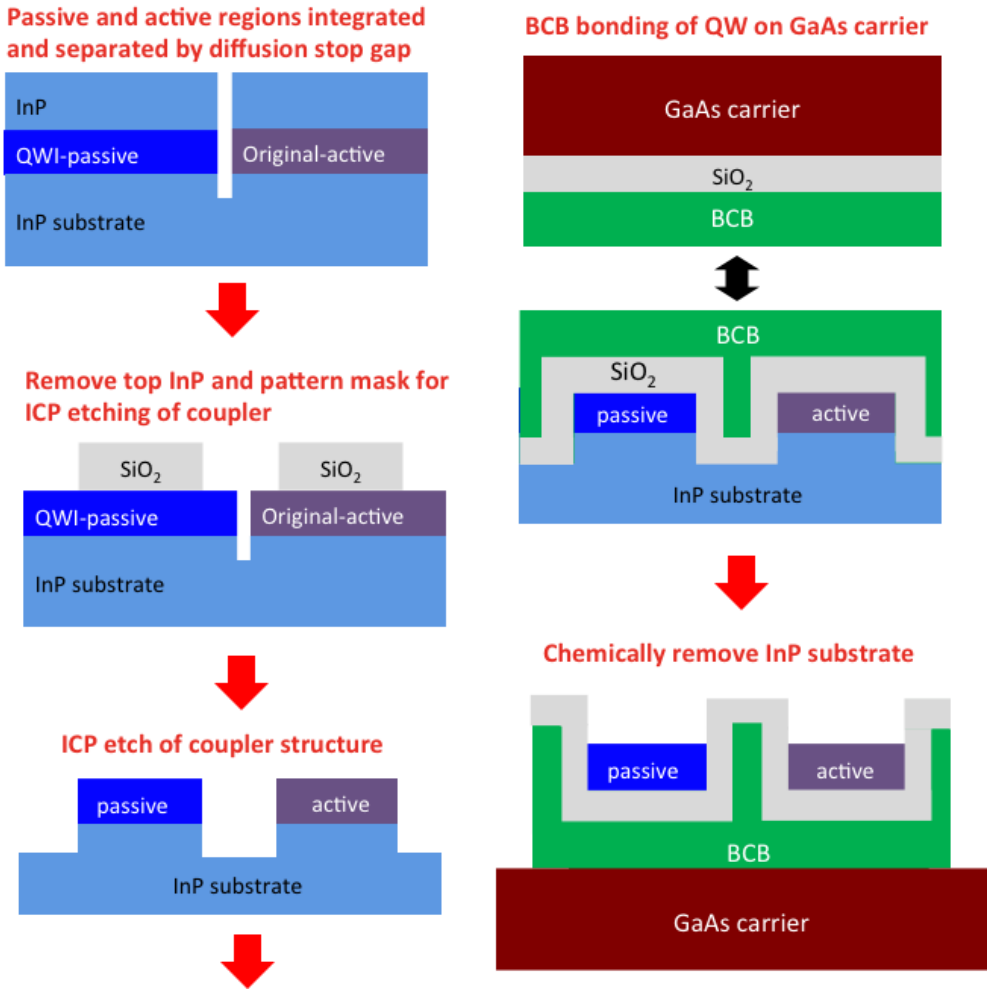

Figure 7.5: Fabrication process of BCB-based thin-film EUPT.

Fig. 7.6 shows the SEM image of resultant thin-film photonic transistor. Fig. 7.6a is the cleaved end facet of 3μm-width thin-film waveguide extended to the sample edge for free-space coupling of light. The thickness of the QW thin film is 256nm. The lateral confinement is achieved by two trenches etched on the QW wafer, which are filled with SiO_2 and BCB. Fig. 7.6b is the top image of photonic transistor coupler, with waveguides width at 305nm and gap size at 455nm.

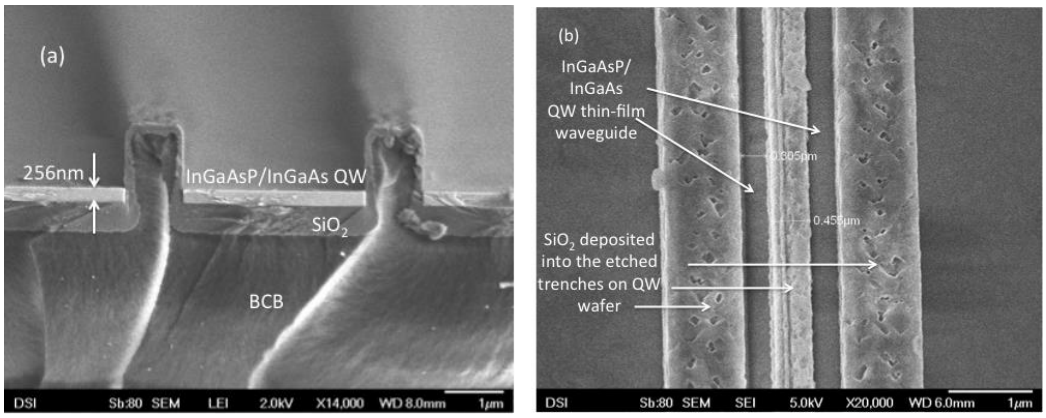

Figure 7.6: SEM images of BCB-based thin-film EUPT. a) Cross section of single thin-film QW waveguide bonded on BCB. The two stand-up structures are the etched trenches on the QW wafer filled with SiO_2 and BCB for high lateral index contrast. b) Top view of thin-film photonic transistor.

7.1.4. Pros and Cons with thin-film EUPT based on QWI approach

The main advantage of the thin-film EUPT based on QWI approach is that the active and passive waveguides are made of the same material, thus having the same material refractive index. Effective refractive index matching condition between active and passive waveguides can be achieved by simply fabricating the symmetric coupler structure, without the need of carefully tuning the waveguide widths. Otherwise, if the active and passive waveguides are composed of different materials, critical control of waveguide widths will be needed to achieve effective refractive index matching, which will increase the fabrication challenges and the complexity of device design. Thin-film structure also maximizes the optical mode confinement, compared with the other structures as to be presented in the later sections, thus potentially is the most power-efficient approach for realizing EUPT.

However, the energy band gap shift induced by QWI, as we achieved here, is not adequate for the EUPT applications. Measurement shows the passive waveguide

obtained in our QWI process is still highly absorptive to the pump and supply beams. Increasing the bandgap difference between the active and passive waveguides to up-to 150nm is possible by further optimizing the QWI recipe. However, optimization of QWI recipe is not cost effective and the fabrication process of thin-film EUPT is very complicated, which leads to high difficulty in process optimization and trouble shootings. Furthermore, 150nm bandgap difference is not ideally large for our EUPT operation. Therefore, in this dissertation, we will not continue with this approach. Separate studies could be carried out in the future to investigate the feasibility of the QWI approach for the EUPT application.

Next, we will present the second fabrication approach developed that can alleviate the above drawbacks: hybrid III-V/silicon integrated platform. This is also the approach we adopted for the actual device realization.

7.2 EUPT Based on III-V-on-Silicon Integrated Platform

The second EUPT device configuration we will propose here is based on a hybrid III-V/silicon integrated platform. The active waveguide consists of a III-V quantum well (InGaAsP/InGaAs quantum well is adopted) nano-waveguide directly bonded on the silicon on insulator (SOI) nanowaveguide, while the SOI waveguide without QW bonded on top forms the passive waveguide in EUPT. Due to the different material compositions of the two waveguides, fine control of each individual waveguide width is required to achieve effective model index matching condition. Compared with the QWI approach, much larger band-gap difference can be achieved between the passive and active waveguides. Furthermore, the buried oxide in SOI wafer provides the high refractive index contrast required for the waveguide.

It is important to highlight that fabrication of such device configuration that involves highly compact integration of passive/active nano-scale features with sub-micrometer separation on a III-V/Si integration platform has never been reported before. Requirement of high-precision dimension control for the constituent nano-waveguides further increases the fabrication challenges.

Here I propose two different fabrication process flows to realize the EUPT device on the hybrid silicon nano-photonic platform. Different process flows result in different EUPT device structures, namely T-structure and self-aligned structure. The detailed fabrication steps will be presented in the following sections. The pros and cons for each device structure will also be discussed.

7.2.1 Introduction to direct wafer bonding

The hybrid III-V/Si integration in our device fabrication relies on the direct wafer bonding technique. Direct wafer bonding refers to the process of connecting two wafer surfaces without any adhesive or additional materials to promote the adhesion between the two surfaces. It allows different materials to be stacked together without the concern for the crystalline relationship between them, leading to more innovative device architectures and many new applications. Compared with the adhesive bonding, like the BCB bonding we adopted for thin-film structure, direct bonding can withstand subsequent high temperature processes. Additionally, most direct bonded structures can subsequently be processed using standard micro-technologies and microelectronics manufacturing tools, which is a key point for CMOS Front End compatibility and developing new stacked structures.

A variety of stacking structures have been achieved with various materials, such as Si, SiO_2, SiGe, Ge, III-V, SiC, nitride, sapphire, diamond, glass, quartz,

metal, etc. [51]. According to the material similarity at the bonding interface, it can be categorized into homogenous bonding (thin film and substrate of the same material) and heterogeneous bonding (thin film and substrate of different materials). A well-known application is the mass production of silicon-on-insulator (SOI) bonded structures, which belongs to the heterogeneous bonding category. III-V to Si direct bonding is another important type of heterogeneous bonding, which has attracted a lot of interest and been widely used for photonic integration application. In this dissertation, we will focus on the III-V (in particular InP) to silicon direct wafer bonding technique.

A key challenge for direct bonding of III-V to silicon is the thermal expansion coefficient mismatch. Conventional direct bonding involves a high-temperature (>600°C) annealing step, which is detrimental when bonding dissimilar materials [52]. More recently, the O_2 plasma-assisted wafer bonding has been developed and widely used for low temperature (<400°C) bonding [53]. The bonding process is described as follows. After a rigorous sample-cleaning procedure, native oxides on Si and III-V compound semiconductors are removed in HF and NH_4OH solutions, respectively. Subsequently, sample surfaces are exposed to O_2 plasma to convert the hydrophobic surfaces to hydrophilic ones by growing a thin layer of highly reactive native oxide, which then form high density of −OH groups (i.e. hydroxyl groups) after contacting with H_2O-based solutions or even H_2O in the air. The two substrates can then be weakly bonded to each other at room temperature via Van der Waals forces or hydrogen bonds. During the following anneal process at elevated temperature (220°C in this work), the well-know chemical reactions in Si-based hydrophilic bonding given in Eqn. (7.1) and (7.2) takes place and forms strong covalent bonds,

$$Si - OH + M - OH \rightarrow Si - O - M + H_2O(g), \quad (7.1)$$

$$Si + 2H_2O \rightarrow SiO_2 + 2H_2(g), \quad (7.2)$$

where M stands for a metal with high electronegativity, i.e. group III and group V elements in our case.

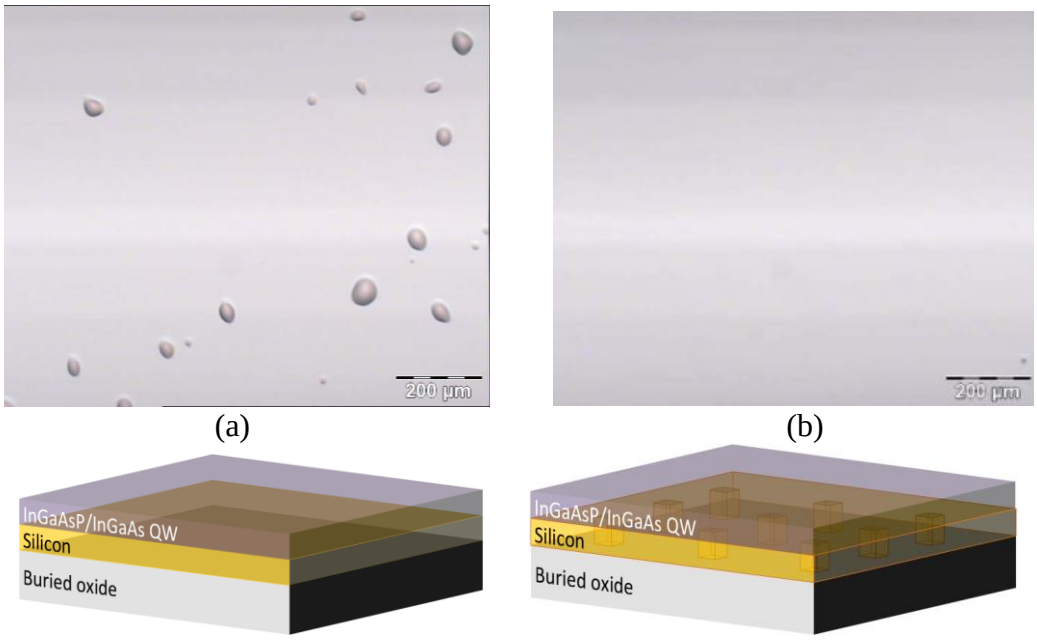

Figure 7.7: Optical microscope image of the top surface of InGaAsP/InGaAs thin film directly bonded on SOI wafer. (a) Without interfacial amorphous or outgassing channels (b) With 5µmx5µm square outgassing channels patterned on SOI prior to direct bonding process. Channel-to-channel separation is 50µm.

7.2.2 Vertical outgasing channel for void-free direct wafer bonding of III-V on SOI

The gas byproducts of H_2O and H_2 from the reactions in Eqns. (7.1) and (7.2) can accumulate and cause a large number of interfacial voids at the bonding interface as shown in Fig. 7.7a, which can even cause de-bonding. Thus to obtain high-quality bonding interface, it is critical to remove the gas byproduct efficiently.

There are two main approaches that have been widely adopted to eliminate the interfacial voids formulation. The first approach is to utilize a layer of interfacial amorphous dielectric to absorb the gas byproducts. The common interfacial amorphous dielectric is thermal or PECVD SiO_2 or SiN_x, whose thickness is typically less than 100nm in order to maintain good optical and thermal coupling between a III-V epilayer and Si [53]. However, in our application, the presence of low-refractive-index dielectric interfacial layer can cause the optical mode distortion in our QW-on-SOI nano-waveguide and complicate the coupler design, thus we will adopt the second approach, which is deploying vertical outgassing channels (VOC) on SOI prior to the wafer bonding process [54-55]. The vertical outgassing channels are basically an array of holes that are etched through the silicon layer to the buried oxide layer. During the annealing process, the gas byproducts and other forms of gaseous molecules can migrate to the closest outgassing channel, getting trapped and absorbed by the buried oxide, instead of accumulating at bonding interface to form voids. As shown in Fig. 7.7b, with VOC patterned on SOI, the voids are completely eliminated, compared to the sample without VOC in Fig. 7.7a.

Table 7.1: Process flow for direct bonding of InGaAsP/InGaAs quantum well on SOI with vertical outgassing channels employed.

<table>
<tr><th>Process steps for SOI</th><th>Process steps for QW wafer</th></tr>
<tr><td>Step 1: Pattern vertical outgassing channels and device pattern if applicable
1. Pattern VOC and alignment markers using photolithography followed by ICP etching through silicon layer
2. Pattern device features using EBL followed by ICP etching of silicon (PECVD SiO_2 is used as ICP etching mask in our process</td><td></td></tr>
<tr><td colspan="2">Step 2: Solvent cleaning:
1. Acetone + ultrasonic for 5min
2. IPA + ultrasonic for 5min
3. DI water + ultrasonic for 5min</td></tr>
<tr><td>Step 3: Piranha cleaning:
H_2SO_4+H_2O_2 (7:3), heated at 140Cdeg on hotplate for 15min to completely remove any organic residues off the sample surface
Step 4: HF cleaning:
BHF (7:1) for 1min to remove the surface oxide from ambient oxidation or deposited SiO_2 left over from the previous process.
Step 5: O_2 plasma exposure:
Pressure=200mTorr, RF = 100W, O_2=10sccm for 100s.
Step 6: Repeat Step 3
Step 7: Repeat Step 3 for 5s.</td><td>Step 8: Removing the top InP cap layer:
HCl:H_2O (1:1) for 2min
Step 9: Ammonium (NH_4OH) cleaning:
25% NH_4OH solution for 1min to remove the native oxide on the sample surface.</td></tr>
<tr><td colspan="2">Step 10: O_2 plasma exposure:
Pressure=200mTorr, RF = 50W, O_2=20sccm for 60s.
Step 11: Manual bonding
Flip over QW wafer and quickly press it onto the SOI substrate. Apply force over the bonding area, staring from the center region and gradually moving to the surrounding area.
Step 12: Annealing
The bonded sample is put into the vacuum oven with a piece of metal weight pressing on top for overnight annealing (~20hr) at 220degC.
Step 13: Remove InP substrate
The annealed sample is put into HCl:H_2O (2:1) solution to remove the InP substrate.</td></tr>
</table>

The effectiveness of the vertical outgassing channels is a function of the

channel size as well as the spacing between channels. Separate studies have shown that reducing the channel spacing can effectively reduce the number of interfacial voids, and eventually, void-free bonding is achieved when the spacing is equal to or less than $50\mu m$ [55]. On the other hand, the size of channel plays less significant roles in reducing the interfacial voids. In our process, we use $5\mu m \times 5\mu m$ square VOCs separated by $50\mu m$.

Our process flow for O_2 plasma-assisted QW-to-Si bonding with adoption of VOC is illustrated in Table 7.1. Commercially grown epitaxial InP-InGaAsP-InGaAs quantum well wafer with ten 5.5nm unstrained InGaAs quantum well separated by 12nm thick InGaAsP barriers, capped by 500nm InP bulk layer, is adopted. The InP cap layer is chemically removed before the bonding process. Fig. 7.8 shows the top surface of QW thin film bonded on SOI wafer. The smooth area has VOC patterned in SOI. 1.4cm x 1.4cm void-free bonding is achieved.

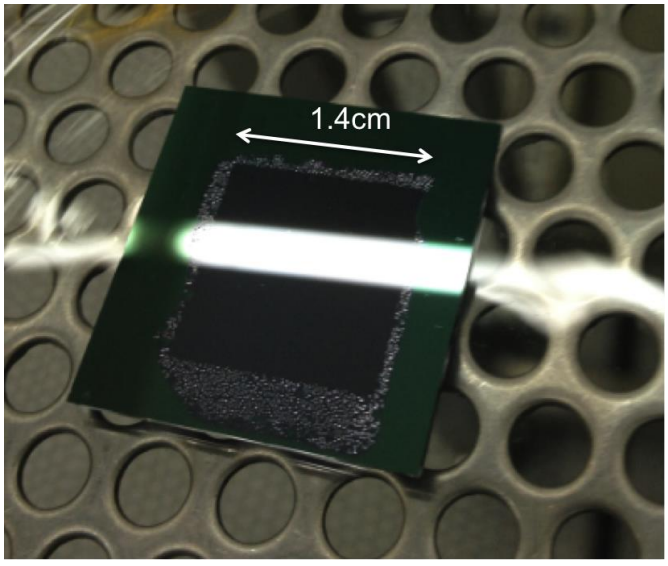

Figure 7.8: InGaAsP/InGaAs QW thin film boned on SOI patterned with VOC.

The device structures can either be patterned on SOI prior to the bonding or on the QW thin film after bonding, depending on the particular application.

7.2.3 Photonic transistor with T-structure QW-on-SOI active waveguide

Two different QW-on-SOI waveguide structures, namely T-structure and self-aligned structure, are proposed here to form the active waveguide in our EUPT device. The fabrication procedures for the corresponding EUPT will also be different. Here we start with the T-structure based EUPT.

The T-structure EUPT coupler is shown in Fig. 7.9a. The QW-on-SOI active waveguide has a wider QW waveguide on top and a narrow SOI waveguide at the bottom. The optical mode power will be mainly confined mainly in the QW region to maximize the light-matter interaction, thus to enhance effectiveness of the absorption-induced switching. Fig. 7.9b shows intensity distribution of the coupled mode in the T-structure photonic transistor.

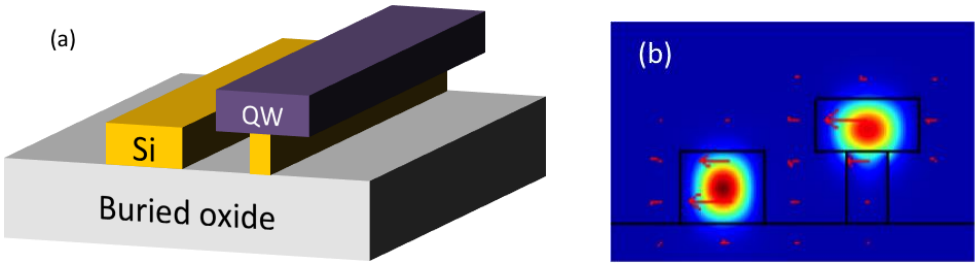

Figure 7.9: (a) T-structure EUPT, where the active waveguide is comprised of a wider QW waveguide bonded on a narrower SOI waveguide. (b) Mode solution of the index-matched T-structure photonic transistor, solved by COMSOL. The red arrows show the polarization of optical field of this mode.

The fabrication process of T-structure-based photonic transistor is shown in Fig. 7.10. The SOI waveguides are patterned together with the vertical outgassing channel prior to the bonding process. It is important to note that we should not use negative EBL resist to pattern SOI waveguide, otherwise there will be lack of sufficient bonding area to support the QW thin film. Therefore, the positive EBL resist PMMA is adopted here. Following the PECVD SiO_2 (etching mask) deposition on the SOI wafer and then PMMA coating, the device patterns and VOCs are written

on PMMA using EBL technique. After resist developing, the patterns are transferred into 300nm SiO_2 layer through RIE technique. Using the SiO_2 layer as the hard mask, Si is then etched using ICP technique based on BCl_3/HBr chemistry. Next, QW wafer is bonded on the device-patterned SOI wafer following the procedures given in Table 7.1. After chemically removing the InP substrate, 300nm PECVD SiO_2 is deposited on the bonded sample, followed by spin coating of PMMA and EBL overlay patterning of QW waveguides. After resist developing, CHF_3/Ar-based RIE etching and Cl_2/N_2-based ICP etching are performed in sequence to transfer the patterns into the SiO_2 layer first and then into the QW layer.

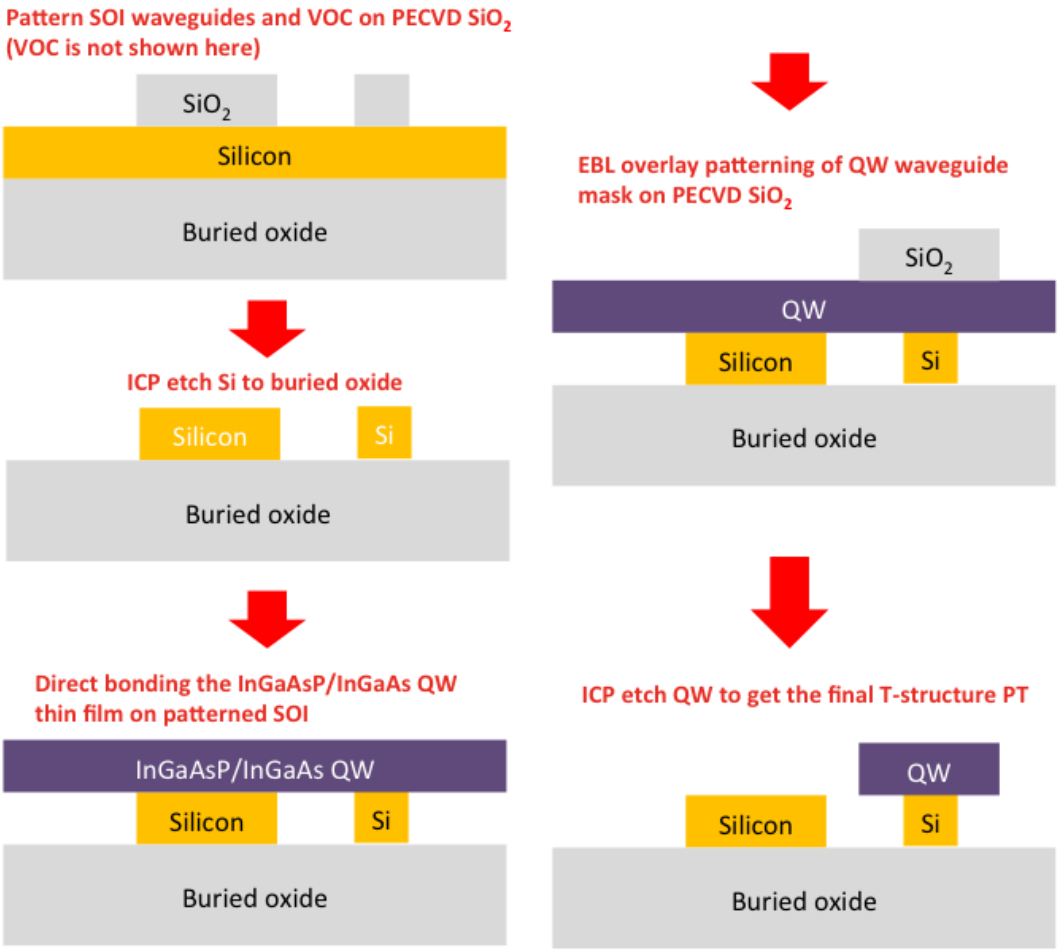

Figure 7.10: Process flow for fabricating T-structure based EUPT

Fig. 7.11 shows the SEM image of the resultant T-structure photonic transistor. The structures in Fig. 7.11a and Fig. 7.11b are from the same wafer. We find the alignment accuracy with the EBL overlay patterning of QW waveguide is not consistent over the wafer and a misalignment of as high as 150nm could happen.

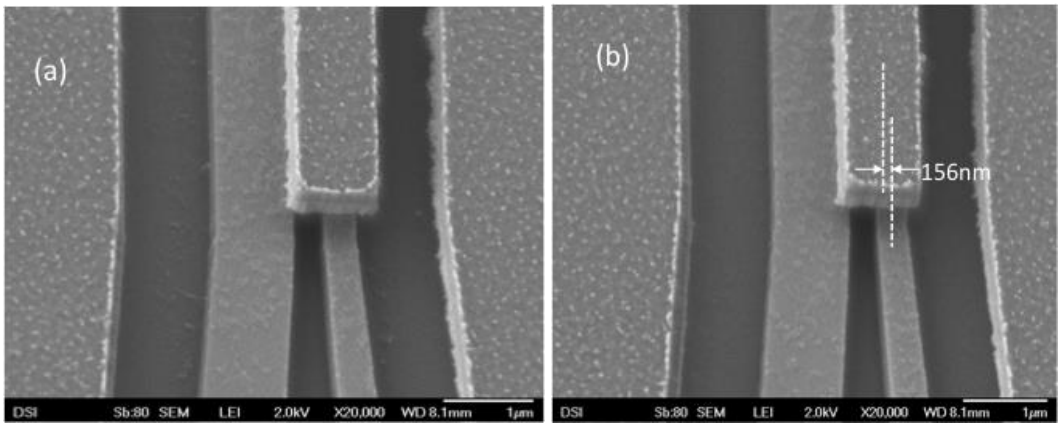

Figure 7.11: SEM image of T-structure EUPT, where the SiO_2 mask for ICP etching of QW has not been removed. (a) Good alignment (b) poor alignment between QW and bottom SOI waveguide.

The fabrication complexity is greatly reduced with T-structure QW-on-SOI approach compared with the QWI-based thin film structure. Strong optical confinement is achieved, and at the same time large band gap difference between passive and active waveguides is promised. However, T-structure QW-on-SOI faces a new fabrication challenge - the misalignment of QW and SOI in the active waveguide, caused by the EBL overlay error, may lead to significant change in the coupling condition. First of all, the misalignment will induce effective modal refractive index change in QW-on-SOI waveguide, introducing uncertainties in achieving the refractive index-matching condition. Secondly, the misalignment also effectively changes the separation between the passive and active waveguide, which will lead to great change in the coupling length. Thirdly, the angular misalignment destructs the parallel nature between the two waveguides, which further complicates

the coupling conditions.

Fig 7.12 shows the mode simulation for 1350nm light in the T-structure coupler when the QW and the bottom SOI is aligned or misaligned by 40nm. The thickness of Si and QW is 340nm and 250nm respectively. The refractive index of Si is 3.5 and the refractive index of QW is 3.45. The coupler stands on top of a buried oxide layer with n=1.47 and surrounded by air with n=1. The lateral dimensions of SOI and QW-on-SOI waveguides are adjusted such that they are refractive index matched in the aligned situation shown in Fig. 7.12a. The eigenmode with similar power in two waveguides represents the refractive index matching condition, while the eigenmode with much higher power in one waveguide than the other corresponds to the refractive index-mismatched condition. As we can see, the coupling efficiency is greatly reduced with the presence of 40nm misalignment.

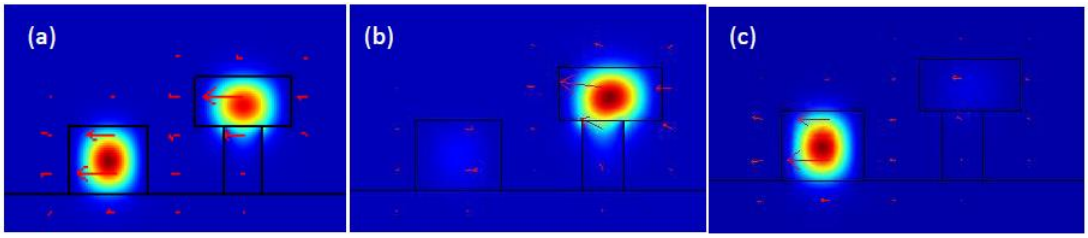

Figure 7.12: Mode simulation by COMSOL. (a) The symmetric eigenmodes in T-structure photonic transistor with QW aligned to the bottom SOI (b) The anti-symmetric eigenmode and (c) the symmetric compound mode as QW is shifted to right by 40nm.

In addition, T-structure EUPT involves three width variables, including the width of passive SOI waveguide, the width of SOI in QW-on-SOI waveguide and the width of QW, which could introduce different amount of errors into the final photonic transistor device. The effective index matching condition thus becomes highly uncertain, which poses great challenges on the device design.

7.2.4 Photonic transistor based on self-aligned QW-on-SOI waveguide

To eliminate the EBL overlay misalignment issue, the self-aligned QW-on-SOI waveguide structure is proposed, in which the QW and SOI waveguides are etched down together with the same etching mask. Since the widths of QW and SOI in the QW-on-SOI waveguide are the same, the number of variables involved in coupler design is further reduced.

The self-aligned photonic transistor structure is shown in Fig. 7.13a, and the eigenmode solution for the effective index matching case is shown in Fig. 7.13b. Unlike the T-structure where the optical mode is mostly confined in the QW thin film, the self-aligned structure has great amount of mode power stay in the Si region. Thus the effective absorption or gain change in the self-aligned QW-on-SOI waveguide will be less than that in the T-structure one. However, we can properly design the thickness of QW and SOI to increase the confinement of optical power in the QW, which will be discussed section 7.3.

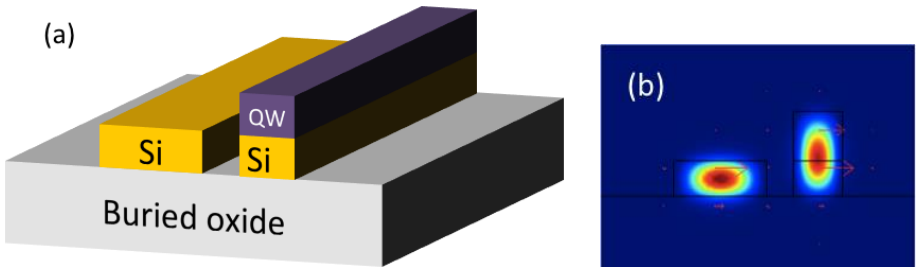

Figure 7.13: (a) Self-aligned photonic transistor, where the QW and SOI in the active waveguide are of the same width. (b) Symmetric compound mode of the index-matched self-aligned photonic transistor solved by COMSOL. The red arrows show the polarization of optical field of this mode.

The fabrication procedure of self-aligned QW-on-SOI architecture is illustrated in Fig. 7.14. The vertical outgassing channels are first patterned on the SOI wafer. The QW thin film is subsequently bonded on top following the procedure in Table

7.1. Next, 200nm thick HSQ (a negative EBL resist) is coated on the bonded sample and baked at 180°C on the hotplate for 2min. With EBL technique, the coupler structures are patterned on the HSQ layer and developed in TMAH for 30s. Subsequently, the device structures are transferred into the QW layer by ICP etching with Cl_2/N_2-chemistry and then into silicon layer by ICP etching with CHF_3/SF_6 chemistry. Then the HSQ mask residue is removed with HF wet etching and a new HSQ layer of 800nm thick is coated to cover the ~600nm-hight QW-on-SOI waveguides. Next, EBL is adopted to pattern the protection mask over the active waveguide. After EBL resist developing, the QW over the unprotected (passive) area are etched away using Cl_2/N_2-based ICP technique. The resultant device structure is shown in Fig. 7.15.

The entire fabrication process and the process parameters for the self-aligned-structure-based EUPT are tabulated at the end of the thesis (Appendix).

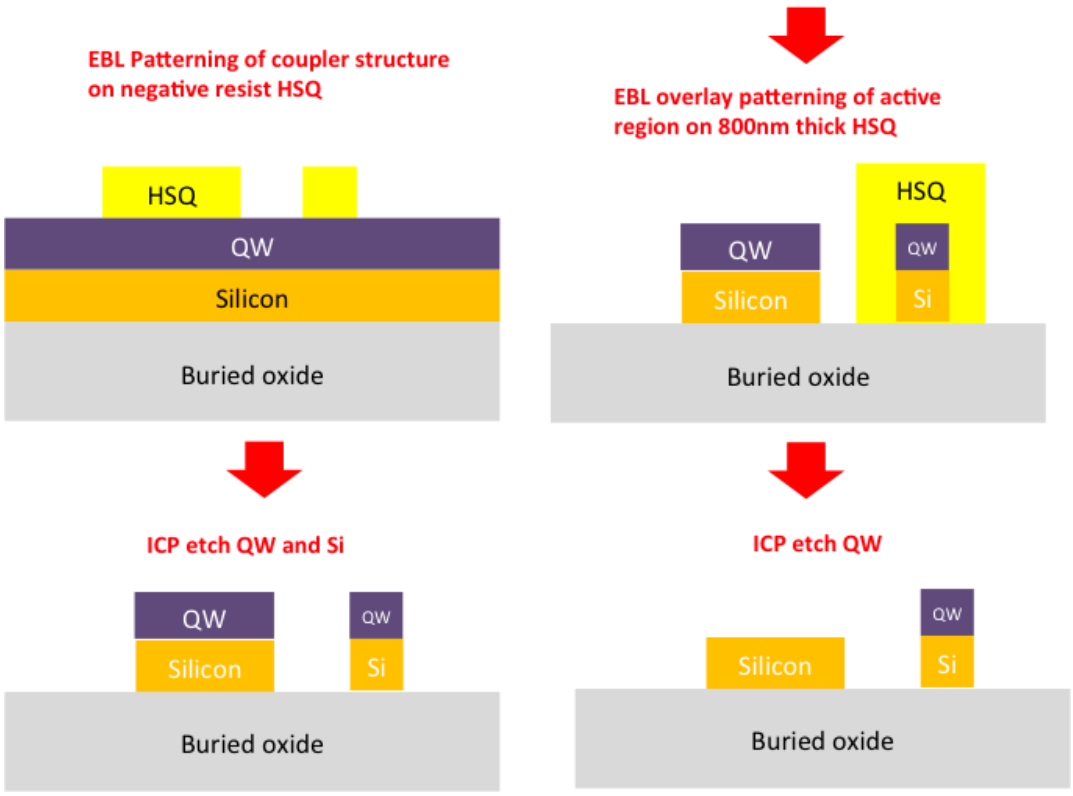

Figure 7.14: Process flow for fabricating self-aligned photonic transistor.

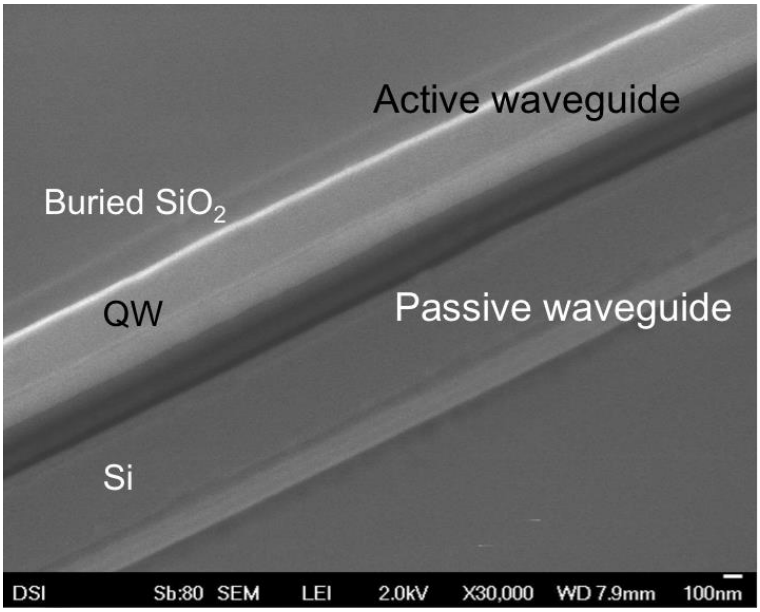

Figure 7.15: SEM image of self-aligned-structure based EUPT

7.3 Wafer Design and Device Design for Self-Aligned EUPT

Due to the advantages of self-aligned structure over the T-structure in terms of eliminating the EBL misalignment issue and reducing the number of waveguide width variables in the coupler design, the self-aligned QW-on-SOI approach will be adopted to realize our photonic transistor. On the other hand, the thin-film structure based on BCB bonding and QW-on-SOI T-structure could be promising candidates for other device configurations which do not require accurate control of the propagating refractive index of the waveguiding mode, but requires strong optical confinement such as for the case of single-waveguide or Mach Zehnder Interferometer (MZI) based structures, etc.

7.3.1 Strained InGaAsP quantum well wafer design

In Chapter VI, we have theoretically shown the significant improvement of

switching performance in our EUPT with the employment of quantum well semiconductor medium, due to the increase of $\frac{g_{L0}}{\alpha_{H0}}$ and reduction of $\frac{I_{Lsat}}{I_{Hsat}}$. In the actual wafer design, multi-layer quantum well is adopted to increase the optical confinement in the QW region thus enhancing the effective absorption and gain experienced by the propagating modes in the waveguides. Furthermore, introduction of strains into quantum well has been shown to further enhance the gain and achieve high-speed modulation [56-57], which will be employed in our wafer design.

The wafer structure is shown in Fig. 7.16, where the layers highlighted by purple color constitute the final QW thin film bonded on the SOI waveguide. The strained InGaAsP quantum well consists of seven 5.5nm-thick $In_{0.719}Ga_{0.281}As_{0.914}P_{0.086}$ wells with 1% compressive strain separated by 8nm-thick $In_{0.63}Ga_{0.37}As_{0.601}P_{0.399}$ barriers with 0.65% tensile strain. Due to the presence of strain, we cannot infinitely increase the number of wells. Thus we intentionally increased the thickness of InGaAsP cladding layer below the quantum well layers (on top of QW after bonding) to pull the mode peak to the quantum well region till the intensity for the mode within the QW layers is maximized. The simulation is carried out at wavelength of 1.342μm (given by the laser wavelength we will use for the device measurement) for the case of a QW-on-SOI waveguide with width of 400nm and height of 250nm for the SOI part of the waveguide. The mode simulation at the optimal thickness of InGaAsP cladding layer is shown in Fig. 7.16. Furthermore, a two-period InP/InGaAs superlattice is introduced near the bonding surface to prevent the defects generated at the bonding interface from diffusing into the QW [58].

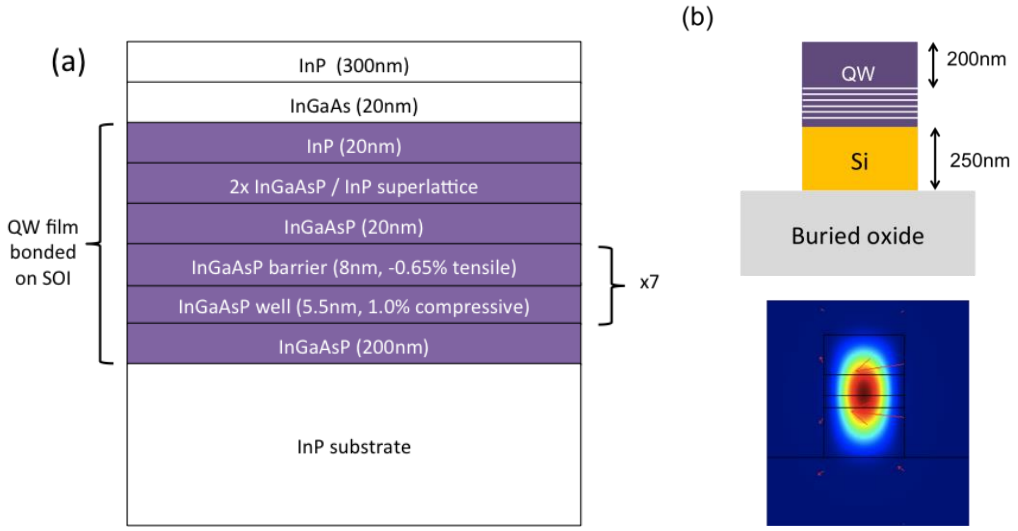

Figure 7.16: (a) Strained InGaAsP multi-quantum-well wafer structure. (b) The QW-on-SOI waveguide cross section and the optical mode profile at wavelength of 1.342μm and waveguide width of 400nm.

7.3.2 Refractive index of InGaAsP quantum well thin film

To design a propagating refractive index-matched coupler structure, the refractive indices of the constituent waveguide materials need to be known. The quantum well thin film consists of complex layer structures and is highly absorptive at the pump supply wavelength, which makes measurement of the real part of the refractive index very challenging. Here we take the theoretical approach that calculating the refractive indices of the QW layers based on different models and identifying a refractive index range for the QW thin film. This refractive index range is taken into account during the coupler design by introducing certain variation of the waveguide width accordingly to search for the index matching condition.

The material and layer composition of the QW thin film is given in Table 7.2. It mainly consists of the quaternary semiconductor $In_xGa_{1-x}As_yP_{1-y}$. A variety of theoretical models are available for calculating the refractive index of $In_xGa_{1-x}As_yP_{1-y}$ with different composition. They match the experimental results to different extents,

depending on the optical wavelength range of interest. Some reported formulae for the semiconductor refractive index calculation break down in the wavelength range close to the bandgap. In our case, the PL peak of the cladding layer $In_{0.741}Ga_{0.259}As_{0.563}P_{0.437}$, which occupies 63% of total thickness, is 1.26 μm (0.984eV), and the bandgap wavelength by calculation is 1.3 μm (0.954eV). The optical pump wavelength for our EUPT operation was chosen to be 1342nm (0.924eV), which is only 0.03eV (~$1.15k_BT$ at room temperature) below the band gap of the cladding layers. Therefore, some models, like Sellmeier formula [59] and Single oscillator model (SOM) [59], which have neglected the optical absorption, are not well applicable.

Table 7.2: The layer structure of InGaAsP multi-quantum well thin film bonded on SOI wafer.

Material		Thickness	Strain	PL peak
		200nm	0	1.26μm
$In_{0.63}Ga_{0.37}As_{0.601}P_{0.399}$	x 7	8nm	-0.65%	1.26μm
$In_{0.719}Ga_{0.281}As_{0.914}P_{0.086}$		5.5nm	1%	1.55μm
$In_{0.63}Ga_{0.37}As_{0.601}P_{0.399}$		8nm	-0.65%	1.26μm
$In_{0.741}Ga_{0.259}As_{0.563}P_{0.437}$		20nm	0	1.26μm
InP	x 2	7.5nm	0	
$In_{0.851}Ga_{0.149}As_{0.327}P_{0.673}$		7.5nm	0	1.1μm
InP		7.5nm	0	

Here we choose the following four published methods for near-bandgap calculation. Burkhard et al.'s method [60] based on interpolation of polarizabilities has shown good consistency with experimental data for the range of -0.3eV<$hv - E_g$<0.2eV, where hv is the photon energy. Modified single-oscillator model (MSOM) [61], compared with conventional SOM, uses a more realistic approach for absorption, leading to a better fit for the light close to bandgap. Adachi's approach

[62], starting from calculating the imaginary part of the complex dielectric function, followed by exploiting Kramers-Kronig relation to derive the refractive index n, is also applicable to near bandgap case. Charles et al.'s two-oscillator model [63] is not composition x, y dependent. The formula is obtained by fitting to the experimental results and involves only photon energy, material PL energy and some fitting parameters.

The formulae mentioned above are developed for $In_xGa_{1-x}As_yP_{1-y}$ lattice matched to InP, which in our case are applicable to $In_{0.741}Ga_{0.259}As_{0.563}P_{0.437}$ and $In_{0.851}Ga_{0.149}As_{0.327}P_{0.673}$ layers only. To calculate the QW barrier $In_{0.63}Ga_{0.37}As_{0.601}P_{0.399}$ and well $In_{0.719}Ga_{0.281}As_{0.914}P_{0.086}$, which are lattice mismatched to InP, we adopt Vegard's rule in Eqn. (7.3), where the quantity $X = (\epsilon - 1)/(\epsilon + 2)$ is related to the dielectric constant ϵ and thus the refractive index through $n = \epsilon^{\frac{1}{2}}$.

$$X\left(\mathrm{In}_{1-x}\mathrm{Ga}_x\mathrm{As}_y\mathrm{P}_{1-y}\right) = (1-x)(1-y)X(\mathrm{InP}) + (1-x)yX(\mathrm{InAs}) + x(1-y)X(\mathrm{GaP}) + xyX(\mathrm{GaAs}) \quad (7.3)$$

Table 7.3 shows the refractive indices of the constituent layers at wavelength 1342nm, calculated using the above methods. The refractive index of the entire structure is a weighted average based on the layers' thicknesses. As we can see, the refractive index of the QW thin film is in the range of 3.4-3.46. Furthermore, the carrier induced refractive index change due to the optical pumping is typically in the order of 0.01, which is smaller than this range. Thus, it will be not be separetly analyzed in our design.

Table 7.3: Theoretically calculated refractive index of InGaAsP at different composition and averaged refractive index of QW thin film.

	Interpolation of polarizabilities	MSOM	Dielectric function	Two-oscillator model
$In_{0.741}Ga_{0.259}As_{0.563}P_{0.437}$	3.512	3.446	3.536	3.448
$In_{0.63}Ga_{0.37}As_{0.601}P_{0.399}$	3.334 (Vegard's rule)			
$In_{0.719}Ga_{0.281}As_{0.914}P_{0.086}$	3.452 (Vegard's rule)			
$In_{0.851}Ga_{0.149}As_{0.327}P_{0.673}$	3.372	3.330	3.333	3.317
InP	3.196			
Averaged refractive index of QW thin film	3.448	3.406	3.461	3.407

7.3.3 Discussion on fabrication errors and device tolerance

In practice, the physical dimension of the final device deviates from the initial design due to the fabrication errors. The dimension error in the vertical direction is usually small, since wafer growth is typically highly precise. While the dimension error in the horizontal direction, which is mainly originated from the EBL step, is a function of many factors, including the EBL dot map, electron beam current, exposure time, the property of resist (e.g. thickness, sensitivity, conductivity, etc.), the wafer material, size of pattern, resist developing time and temperature and so on. Thus keeping the process condition consistent is important for improving the fabrication repeatability. In our case, negative resist HSQ is utilized for EBL patterning of the coupler structure. A series of dimension tests show the run-to-run and device-to-device dimension errors are typically in the order of 10nm.

According to the coupled mode theory, the coupling efficiency and coupling length in a passive directional coupler versus the index mismatch are give as follows.

$$\eta = \frac{1}{1 + (\Delta\beta L_{C0})^2/\pi^2} \tag{7.4}$$

$$L_{C2} = \sqrt{\eta} L_{C0} \tag{7.5}$$

where $\Delta\beta = dn_{eff}\frac{2\pi}{\lambda}$ is the propagation constant difference between two waveguides, dn_{eff} is the effective modal refractive index difference. $L_{C0} = \frac{\pi}{2\kappa}$ is the complete coupling length and κ is the coupling coefficient. So L_{C0} is basically the desired or designed device length in the complete coupling condition and $\Delta\beta$ represents the dimension errors due to the fabrication errors.

Table 7.4: coupling efficiency and coupling length change in the presence of effective refractive index mismatch in the 2-waveguide directional coupler.

$dn_{eff}L_{C0}$	η	$(L_{C2} - L_{C0})/L_{C0}$
0.0000	100.00%	0.00%
0.2224	90.00%	-5.13%
0.3357	80.00%	-10.56%
0.4383	70.00%	-16.33%
0.5473	60.00%	-22.54%
0.6713	50.00%	-29.29%
0.8210	40.00%	-36.75%
1.0241	30.00%	-45.23%
1.3405	20.00%	-55.28%
2.0076	10.00%	-68.38%

From Eqn. (7.5), we can obtain Table 7.4, which gives a quantitative presentation on how much the coupling efficiency and coupling length will change in the presence of effective refractive index mismatch dn_{eff}. $(L_{C2} - L_{C0})/L_{C0}$ represents the percentage of change in the coupling length. The wavelength of our interest is the pump supply wavelength 1.342 μm. As an example, if we need L_{C0}=100 μm and the fabrication error introduces an effective refractive index mismatch dn_{eff}= 0.0067, the coupling efficiency would drop by half and the coupling length would be

decreased by 29.29%. If we design a L_{C0}=200 μm index-matched coupler, with the same index mismatch, the coupling efficiency would be dropped by 80% and the coupling length would be reduced by half.

Next, we use the commercial mode solver COMSOL to examine the effective modal refractive indices of the self-aligned QW-on-SOI waveguide and the solo-SOI waveguide as the waveguide widths are varied. In our simulation, the wavelength of light is 1342nm, with polarization in the horizontal direction. We let the thicknesses of silicon and QW thin film be fixed, which according to the wafer design are 250nm and 349nm respectively. The refractive index of silicon is 3.5, and the refractive index of SiO_2 is 1.45. Our photonic transistor will be eventually covered by a thick layer of PECVD SiO_2 for protection. Thus the refractive index of the entire cladding region would be 1.45. It is also important to note that the refractive index of QW is not precisely known, which will be considered as a variable in our simulation.

As shown in Fig. 7.17, the effective modal refractive indices n_{eff} with respect to the waveguide widths are plotted for QW-on-SOI waveguide (red and blue) and SOI waveguide (black). Based on the QW refractive index (denoted as n(QW)) calculation in Table 7.3, here we consider the two extreme cases, i.e. n(QW)=3.4 and 3.47, which are plotted in red and blue color respectively. As we can see, to achieve effective index-matching condition, the QW-on-SOI waveguide width should not be >400nm and QW-on-SOI waveguide is generally more sensitive to the waveguide width change than SOI waveguide. Thus we fix the QW-on-SOI waveguide width at 380nm, and the index-matched SOI waveguide has a width in the range of 650nm to 750nm depending on the refractive index of QW, as shown by the green arrow. By taking into account of dimension error +/-10nm, the width of SOI waveguide needs to vary from 650nm to 900nm in the actual fabrication in order to hit the effective-index

matching condition.

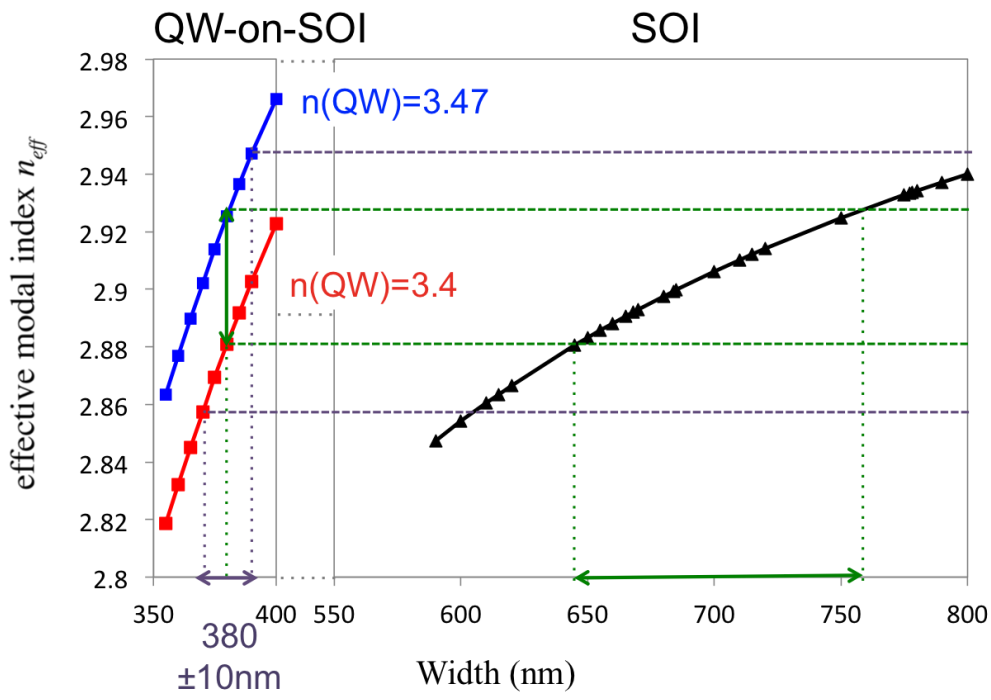

Figure 7.17: Effective modal index of self aligned QW-on-SOI waveguide with n(QW)=3.47 (blue) and n(QW)=3.4 (red), and 250nm-height SOI waveguide (black) versus the waveguide width.

It is also important to highlight that, even with the optimal SOI width being found, the 10nm dimension error induced by EBL error could leads to an effective refractive index mismatch of ~0.026 maximally, in the subsequent fabrication rounds. This will result in <10% coupling efficiency and >70% coupling length change for the coupler of L_{C0}=100 μm. Thus the device tolerance to fabrication error is very low.

CHAPTER VIII NEW ARCHITECTURES FOR EUPT

The coupling efficiency of the asymmetric 2-WG EUPT is extremely sensitive to the fabrication errors. The direct consequence of incomplete coupling in the presence of effective-model-refractive-index mismatching (termed as index mismatching for short in the following discussion) is the reduction of the switching extinction ratio, which is an important parameter that measures the signal quality, affecting the bit error rate (BER) in optical links [64]. Fabrication discrepancies based on current technology can easily compromise coupling efficiency particularly in high-refractive-index-contrast nano-waveguide structures. Moreover, asymmetric coupler structure is particularly sensitive, as dispersion of individual constituent waveguide differs, leading to different coupling efficiency at different wavelength, which limits the operational bandwidth. Meanwhile, pumping up the active medium will change the refractive index of it, which further increases the uncertainty in achieving effective modal refractive index matching.

In this chapter, we will propose two new architectures for EUPT, which can greatly alleviate the fabrication challenges without compromising the switching performance.

The first architecture is based on a symmetric three-waveguide (3-WG) directional coupler, which consists of one active central waveguide and two passive side waveguides. The symmetric nature of the structure promises efficient coupling, thus high extinction ratio switching, without stringent effective modal refractive index-matching requirement between the coupled waveguides. The absorption manipulation-based switching performance is not compromised by the presence of effective model refractive index mismatch and thus enhances the device tolerance to

fabrication errors [26,65].

The second architecture adopts the Mach-Zehnder Interferometry geometry, which consists of two identical active arms. Without the direct coupling between the passive and active waveguides, the fabrication process is much easier. Instead of using phase modulation in the conventional MZI-based switching device, amplitude modulation induced by absorption change in one of the arm is the dominant mechanism that promotes the switching. Since the carrier induced absorption is typically larger than the refraction change, the device length can be greatly shorter than the refraction-based MZI switch, such as the conventional MZI-based SOA switch [66].

In this chapter, the switching mechanism and switching performance of 3-WG EUPT and MZI-EUPT will be theoretically studied and compared with 2-WG EUPT. The pros and cons for the three architectures will be highlighted at the end of the chapter.

8.1 EUPT Based on Symmetric Three-Waveguide (3-WG) Coupler

The proposed device architecture is shown in Fig. 8.1, which consists of an active waveguide placed between two identical passive waveguides at equal distance, forming a configuration similar to a 3-WG directional coupler. The optically-induced absorption change in the central waveguide controls the optical coupling between two side waveguides, which is analogous to an electronic transistor gate using resistance to control the current flow. The same all-optical switching operation in the 2-WG EUPT can be applied to the 3-WG structure, as shown in Fig. 8.1.

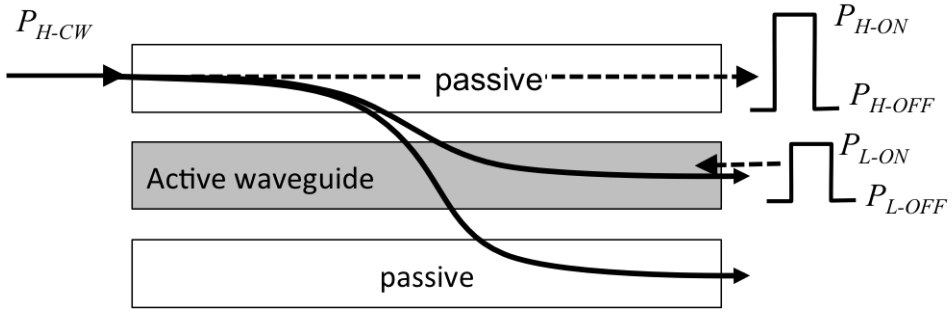

Figure 8.1: Switching action in 3-WG EUPT based on a symmetric three-waveguide coupler with central waveguide being absorptive. P_{H-CW} is the continuous pump supply power at wavelength λ_H, incident into the passive waveguide. P_{L-ON} and P_{L-OFF} denote the ON- and OFF-state input signal power at wavelength λ_L. P_{H-ON} and P_{H-OFF} denote the ON- and OFF-state output signal power at wavelength λ_H. Solid arrow shows the light propagation at switch-OFF state and dash arrows show the switch-ON state.

8.1.1 Coupled mode analysis of 3-WG EUPT

We first use the coupled mode theory to formulate the absorption-induced switching action. Consider a symmetric three-waveguide coupler as shown in Fig. 8.2. It consists of three equidistant parallel single-mode waveguides where passive waveguides 1 and 3 are identical with propagation constant β_1. The central waveguide, waveguide 2, is absorptive, with propagation constant β_2, where $\beta_2 = \beta_{2r} + i\alpha_{am}$. The imaginary part α_{am} is the absorption coefficient for the optical field amplitude. The optical field is launched into WG1. All the parameters are defined similarly as in the 2-WG case.

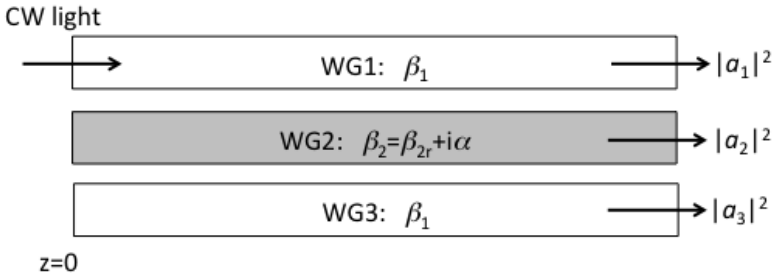

Figure 8.2: Symmetric three-waveguide coupler with absorptive central waveguide and two side waveguide, which are passive and identical. Continuous wave light is launched from the side waveguide WG1.

For strongly guiding nano-waveguide structure presented here, direct coupling between waveguide 1 and 3 can be considered to be negligible as compared to the coupling between adjacent waveguides. The coupled mode equations can hence be written as

$$-i\frac{da_1}{dz} = \beta_1 a_1 + \kappa_{12} a_2, \tag{8.1a}$$

$$-i\frac{da_2}{dz} = \beta_2 a_2 + \kappa_{21} a_1 + \kappa_{23} a_3\,, \tag{8.1b}$$

$$-i\frac{da_3}{dz} = \beta_1 a_3 + \kappa_{32} a_2. \tag{8.1c}$$

Due to the symmetric nature of the structure, $\kappa_{12} = \kappa_{32}$ and $\kappa_{21} = \kappa_{23}$. Use the energy-conservation relation $\frac{d(|a_1|^2+|a_2|^2+|a_2|^2)}{dz} = -2\alpha_{am}|a_2|^2$, it further gives$\kappa_{12} = \kappa_{32} = {\kappa_{21}}^* = {\kappa_{23}}^*$. Thus for simplicity, we have $\kappa_{12} = \kappa_{32} = \kappa^*$ and $\kappa_{21} = \kappa_{23} = \kappa$.

The following derivation is similar to the 2-WG case as shown in section 3.1, thus will not be presented. The solution of $|a_1(z)|^2$, $|a_2(z)|^2$ and $|a_3(z)|^2$ for initial condition $a_1(0) = 1$ and $a_2(0) = a_3(0) = 0$ are given by

$$\begin{aligned}
&|a_1(z)|^2 \\
&= \frac{1}{4}\frac{e^{-\alpha_{am}z}}{4\gamma^2 + b^2}\begin{Bmatrix} \left[\Delta\beta\cosh\left(\frac{bz}{2}\right) + 2\gamma\sinh\left(\frac{bz}{2}\right)\right]^2 + \left[\alpha_{am}\cosh\left(\frac{bz}{2}\right) + b\sinh\left(\frac{bz}{2}\right)\right]^2 \\ -(\Delta\beta^2 + {\alpha_{am}}^2) + [2\gamma\cos(\gamma z) + \alpha_{am}\sin(\gamma z)]^2 + [b\cos(\gamma z) - \Delta\beta\sin(\gamma z)]^2 \end{Bmatrix} \\
&+ \frac{1}{2}\frac{e^{-\alpha_{am}z}}{4\gamma^2 + b^2}\begin{Bmatrix} \left[-\left(\Delta\beta\gamma - 2\gamma^2 + \frac{\alpha_{am}b}{2} - \frac{b^2}{2}\right)\cos\left(\frac{\Delta\beta}{2} + \gamma\right)z + \left(\alpha_{am}\gamma - \frac{\Delta\beta b}{2}\right)\sin\left(\frac{\Delta\beta}{2} + \gamma\right)z\right]e^{-\frac{bz}{2}} \\ + \left[\left(\Delta\beta\gamma + 2\gamma^2 + \frac{\alpha_{am}b}{2} + \frac{b^2}{2}\right)\cos\left(\frac{\Delta\beta}{2} - \gamma\right)z - \left(\alpha_{am}\gamma - \frac{\Delta\beta b}{2}\right)\sin\left(\frac{\Delta\beta}{2} - \gamma\right)z\right]e^{\frac{bz}{2}} \end{Bmatrix} \\
&+ \frac{1}{4},
\end{aligned} \tag{8.2a}$$

$$|a_2(z)|^2 = \frac{|\kappa|^2 e^{-\alpha_{am} z}}{4\gamma^2 + b^2}\left[e^{bz} + e^{-bz} - 2\cos(2\gamma z)\right], \tag{8.2b}$$

$|a_3(z)|^2$

$$= \frac{1}{4}\frac{e^{-\alpha_{am} z}}{4\gamma^2 + b^2}\left\{\begin{matrix}\left[\Delta\beta\cosh\left(\frac{bz}{2}\right) + 2\gamma\sinh\left(\frac{bz}{2}\right)\right]^2 + \left[\alpha_{am}\cosh\left(\frac{bz}{2}\right) + b\sinh\left(\frac{bz}{2}\right)\right]^2 \\ -(\Delta\beta^2 + {\alpha_{am}}^2) + [2\gamma\cos(\gamma z) + \alpha_{am}\sin(\gamma z)]^2 + [b\cos(\gamma z) - \Delta\beta\sin(\gamma z)]^2\end{matrix}\right\}$$

$$-\frac{1}{2}\frac{e^{-\alpha_{am} z}}{4\gamma^2 + b^2}\left\{\begin{matrix}\left[-\left(\Delta\beta\gamma - 2\gamma^2 + \frac{\alpha_{am} b}{2} - \frac{b^2}{2}\right)\cos\left(\frac{\Delta\beta}{2} + \gamma\right)z + \left(\alpha_{am}\gamma - \frac{\Delta\beta b}{2}\right)\sin\left(\frac{\Delta\beta}{2} + \gamma\right)z\right]e^{-\frac{bz}{2}} \\ + \left[\left(\Delta\beta\gamma + 2\gamma^2 + \frac{\alpha_{am} b}{2} + \frac{b^2}{2}\right)\cos\left(\frac{\Delta\beta}{2} - \gamma\right)z - \left(\alpha_{am}\gamma - \frac{\Delta\beta b}{2}\right)\sin\left(\frac{\Delta\beta}{2} - \gamma\right)z\right]e^{\frac{bz}{2}}\end{matrix}\right\}$$

$$+\frac{1}{4}, \tag{8.2c}$$

where γ and b are given by $2\gamma + ib = \sqrt{\Delta\beta^2 - \alpha_{am}^2 + 2\frac{\pi^2}{L_{C0}^2} + 2i\alpha_{am}\Delta\beta}$ with $L_{C0} = \frac{\pi}{2|\kappa|}$.

i. Switch-OFF state, $\alpha_{am} = 0$

When the central waveguide is pumped to transparency, i.e. $\alpha_{am} = 0$, Eqn. (8.2) is reduced to

$$|a_1(z)|^2 = \frac{1}{4}\left[\frac{\Delta\beta}{2\gamma}\sin(\gamma z) + \sin\left(\frac{\Delta\beta}{2}z\right)\right]^2 + \frac{1}{4}\left[\cos(\gamma z) + \cos\left(\frac{\Delta\beta}{2}z\right)\right]^2, \tag{8.3a}$$

$$|a_2(z)|^2 = \frac{\pi^2}{4\gamma^2 L_{C0}^2}\sin^2(\gamma z), \tag{8.3b}$$

$$|a_3(z)|^2 = \frac{1}{4}\left[\frac{\Delta\beta}{2\gamma}\sin(\gamma z) - \sin\left(\frac{\Delta\beta}{2}z\right)\right]^2 + \frac{1}{4}\left[\cos(\gamma z) - \cos\left(\frac{\Delta\beta}{2}z\right)\right]^2, \tag{8.3c}$$

where $\gamma = \frac{1}{2}\sqrt{\Delta\beta^2 + 2\frac{\pi^2}{L_{C0}^2}}$.

We plot out Eqn. (8.3) for direct visualization of the coupling characteristics in

the symmetric three-waveguide coupler. By writing z as $L_{C0}\frac{z}{L_{C0}}$ and expanding γ explicitly, Eqn. (8.3) can be reduced to a function of two parameters only, i.e. the product $|\Delta\beta|L_{C0}$ and the ratio z/L_{C0}. The optical power variation along three waveguides in the transparency case is plotted versus z/L_{C0} at different $|\Delta\beta|L_{C0}$ as shown in Fig. 8.3.

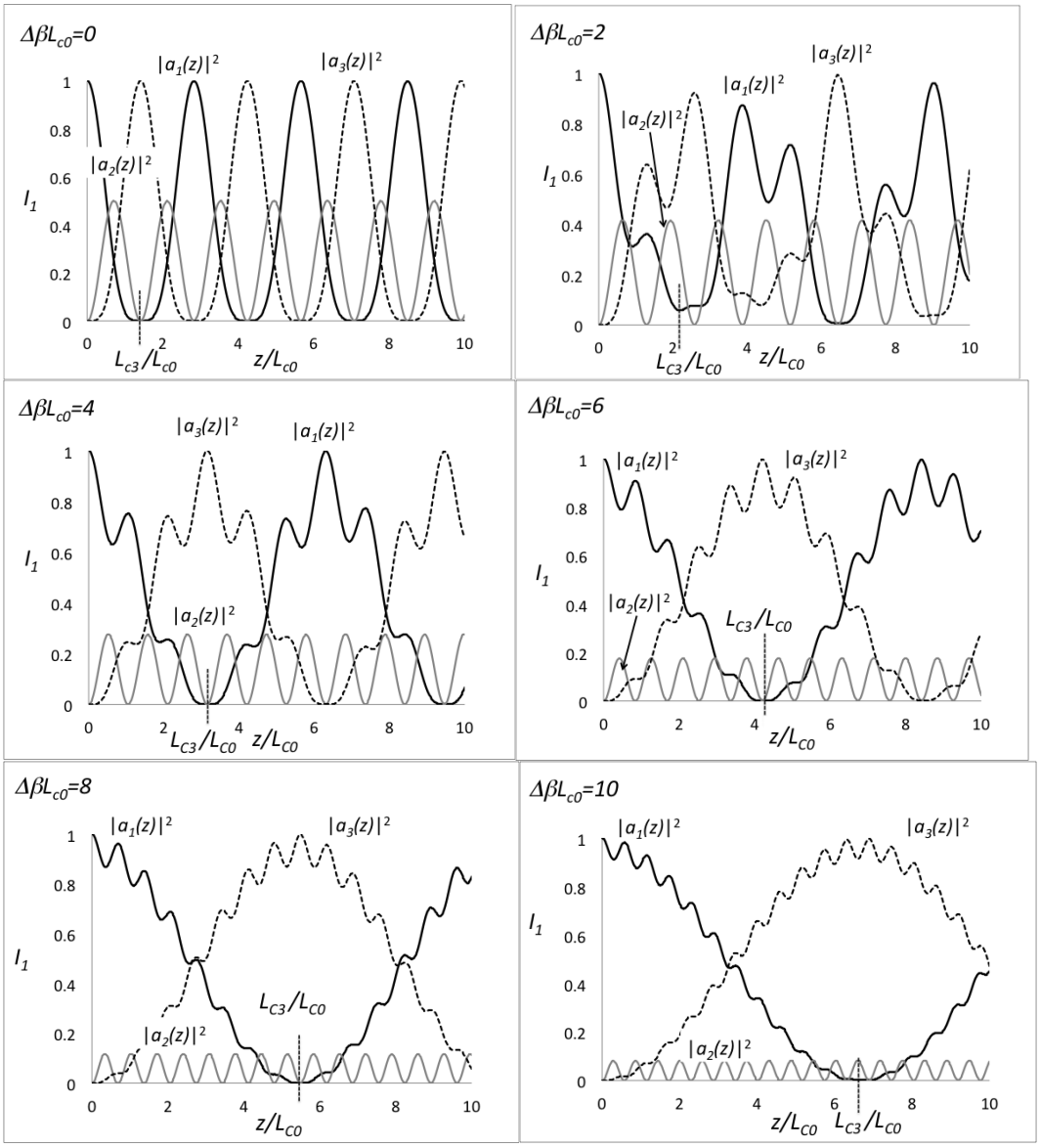

Figure 8.3: Optical intensity along WG1 (black solid line), WG2 (gray solid line), WG3 (black dash line) in the 3-WG coupler shown in Fig. 8.2, when $|\Delta\beta|L_{C0}$=0, 2, 4, 6, 8 and 10, corresponding to Δn_{eff}=0, 0.005, 0.01, 0.015, 0.02, and 0.025, with $L_{C0} = 100$. The coupling length is labeled by L_{C3}/L_{C0}.

It is important to see that >90% of light launched into WG1 can be coupled out, in spite of the index mismatch. As $|\Delta\beta|L_{C0}$ increases, the coupling between the central waveguide and side waveguides weakens and the power transfer from WG1 to WG3 becomes slower, resulting in an increase of coupling length L_{C3}. Meanwhile the maximum intensity in WG2 reduces at high $|\Delta\beta|L_{C0}$ value. If $|\Delta\beta|L_{C0}$ becomes very large, L_{C3} tends to be infinity, and the optical power in WG2 is zero, i.e. the light remains in WG1 without any coupling.

The 3-WG photonic transistor is operated at one coupling length to minimize the OFF-state output power from WG1, similar to the 2-WG EUPT. The coupling length of 3-WG coupler L_{C3}, defined as the minimum distance by which maximum power of incident light is coupled out of the incident waveguide, can be derived by finding the minimum point of $|a_1(z)|^2$ in Eqn. (8.3a), which is given by

$$L_{C3} = \frac{2\pi}{\sqrt{(\Delta\beta L_{C0})^2 + 2\pi^2} - |\Delta\beta| L_{C0}} L_{C0} \,. \tag{8.4}$$

Thus substitute Eqn. (8.4) into Eqn. (8.3a), we get the OFF-state power output of WG1 normalized to the input pump supply power, which is given by

$$\frac{P_{H-OFF}}{P_{H-CW}} = \frac{2\pi}{\sqrt{(\Delta\beta L_{C0})^2 + 2\pi^2} - |\Delta\beta| L_{C0}} \,. \tag{8.5}$$

Recall Eqn. (3.9) for the OFF-state power output normalized by the input pump supply power in the 2-WG EUPT as a function of $\Delta\beta$ between constituent waveguides

$$\frac{P_{H-OFF}}{P_{H-CW}} = 1 - \frac{1}{\left(\frac{\Delta\beta L_{C0}}{\pi}\right)^2 + 1} = 1 - \left(\frac{L_{C2}}{L_{C0}}\right)^2 \,. \tag{3.9}$$

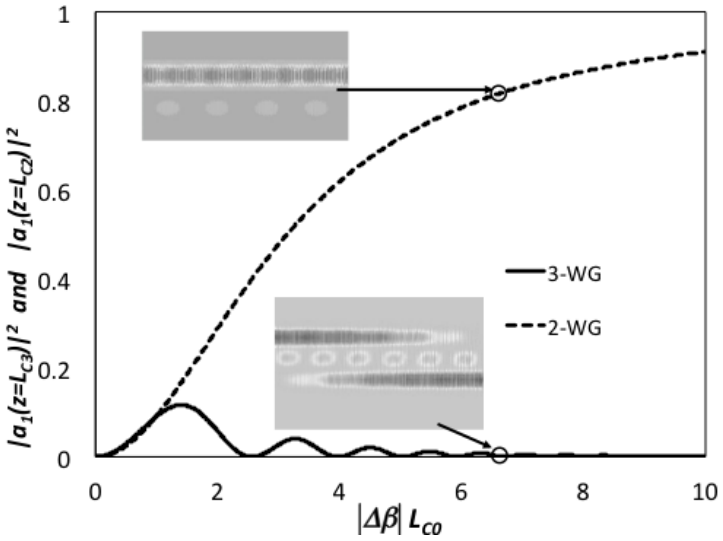

Figure 8.4: Transparency-state output power from WG1 in 2-WG coupler (dash line) and 3-WG coupler (solid line) with different $|\Delta\beta|L_{C0}$ when the incident light is launched from WG1. The inserted graphs show the FDTD simulation of light coupling in the 2-WG and 3-WG with Δn_{eff}=0.052.

To make comparison, Eqn. (8.5) and Eqn. (3.9) are plotted versus $|\Delta\beta|L_{C0}$ in Fig. 8.4. It is evident that the OFF-state output power from 3-WG photonic transistor remains at a very low value, in spite of the index mismatch between the central active waveguide and the side passive waveguides. However, in 2-WG EUPT, $\frac{P_{H-OFF}}{P_{H-CW}}$ increases with $|\Delta\beta|L_{C0}$, and quickly gets close to 1. The inserted graphs show the FDTD simulation of 1.319μm light propagating in 2-WG and 3-WG couplers with $|\Delta\beta|L_{C0}$ =6.36. The simulated couplers have $L_{C0} = 25.38\,\mu m$ and $\Delta\beta = 0.2506\mu m^{-1}$, which corresponds to an effective index mismatch of 0.0526. As we can see, the light is completely coupled out of the incident waveguide in the 3-WG coupler. However, in the 2-WG coupler, most of the light remains in the incident waveguide without coupling.

ii. Switch-ON state, $\alpha_{am} > 0$

At switch-ON state, as shown in Fig. 8.1, the input signal depletes the carriers

in the central waveguide and introduces the absorption seen by the power supply beam, i.e. $\alpha_{am} > 0$. The ON-state output power normalized to the incident pump supply power $\frac{P_{H-ON}}{P_{H-CW}}$ is given by Eqn. (8.2a) with z=L_{C3} (Eqn. (8.4)). The resultant expression, similar to the 2-WG case, is dependent on two parameters, namely $|\Delta\beta|L_{C0}$ and $\alpha_{am}L_{C3}$. $\frac{P_{H-ON}}{P_{H-CW}}$ is plotted with respect to $\alpha_{am}L_{C3}$ at different $|\Delta\beta|L_{C0}$ in Fig. 8.5. With increase of absorption in WG2, the incident pump supply power is partially switched out of WG1. Increasing the device length L_{C3} can further increase $\frac{P_{H-ON}}{P_{H-CW}}$. On the other hand, the optical modulation amplitude $\Delta P = P_{H-ON} - P_{H-OFF}$ decreases as index mismatch increases for fixed $\alpha_{am}L_{C3}$. However, $\frac{P_{H-ON}}{P_{H-CW}}$ remains at a very low value, promising a high extinction ratio $r_e = P_{H-ON}/P_{H-OFF}$ despite P_{H-ON} decreases with $|\Delta\beta|L_{C0}$.

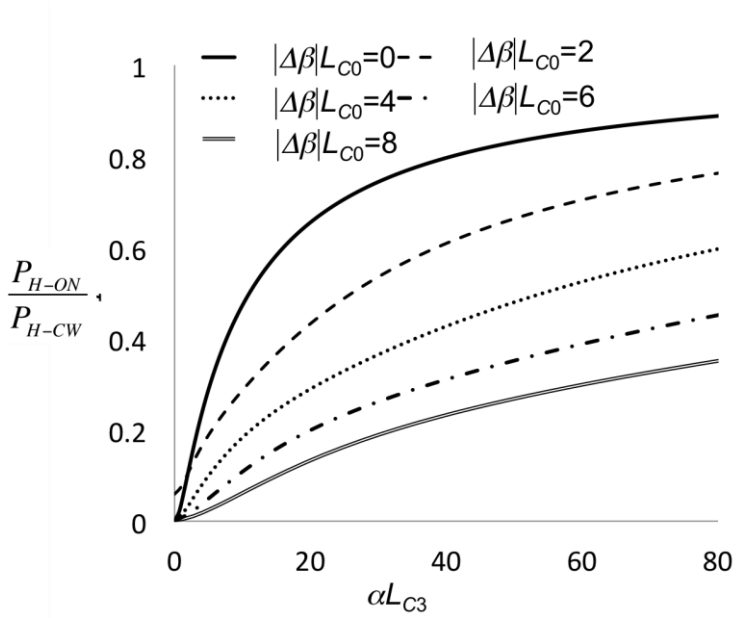

Figure 8.5: Power transmission from WG1 of the symmetric 3-WG coupler at coupling length L_{C3} versus $\alpha_{am}L_{C3}$ at different $|\Delta\beta|L_{C0}$. $|\Delta\beta|L_{C0}$ from 0 to 8 corresponds to the effective modal refractive index mismatch Δn_{eff} from 0 to 0.02 with $L_{C0} = 100$ and 1.55μm light wavelength.

8.1.2 Analytical analysis of switching gain in bulk-InGaAsP-based 3-WG EUPT

The switching gain of 3-WG EUPT will be examined in this section, following the same procedures as we adopted for the 2-WG EUPT switching gain analysis in section 5.1.

First of all, Eqn. (4.5) is modified to calculate the effective absorption coefficient α_{eff} of the central active waveguide induced by the carrier depletion at the switch-on state. Differing from the 2-WG configuration, 3-WG EUPT allows switching operation in the presence of phase mismatch between the active and passive waveguides. Only part of the incident pump power is coupled into the central active waveguide to pump the medium, and the amount of which decreases as the index mismatching increases. With Eqn. (8.3b), we can get the maximum percentage of input pump supply power coupled in to the active waveguide

$$|a_2(\Delta\beta L_{C0})|^2 = \frac{\pi^2}{\Delta\beta^2 {L_{C0}}^2 + 2\pi^2}, \tag{8.6}$$

which is equal to 50% at the index matching condition.

In addition, with the higher effective-model-refractive-index mismatch, the input signal beam launched into the central waveguide sees less coupling into the side waveguides, resulting in longer effective interacting distance or more carrier depletion in the active waveguide. Thus we introduce an interaction factor $1 - \frac{1}{2}\eta$ to the term of $\alpha_{H0}L$ in Eqn. (4.5). The term $\eta = \frac{2\pi^2}{2\pi^2 + \Delta\beta^2 {L_{C0}}^2}$ gives the coupling efficiency of signal beam launched from the central waveguide. As we can see, the interaction factor is equal to ½ when $\Delta\beta = 0$ and becomes 1 when $\Delta\beta$ increases to infinity.

With the above two factors taken into account, Eqn. (4.5) is written as

$$ln(T_H) + \frac{\alpha_{H0}}{g_{L0}} ln\left[1 + \frac{g_{L0}}{\alpha_{H0}} \frac{I_{Lsat}}{I_{Hsat}} (1 - T_H) \frac{\pi^2}{\Delta\beta^2 {L_{C0}}^2 + 2\pi^2} r_{in}\right]$$

$$+(1 - T_H) \frac{\tau_r}{I_{Hsat}} \frac{\pi^2}{\Delta\beta^2 {L_{C0}}^2 + 2\pi^2} I_{H-CW} = \frac{\pi^2 + \Delta\beta^2 {L_{C0}}^2}{2\pi^2 + \Delta\beta^2 {L_{C0}}^2} \alpha_{H0} L_{C3}, \quad (8.7)$$

where $r_{in} = \frac{I_{H-CW}}{I_{L-ON}}$, $I_{H-CW} = P_{H-CW}/A_{eff}$ and $I_{L-ON} = P_{L-ON}/A_{eff}$, with A_{eff} representing the effective modal area in the active waveguide. The effective absorption induced in the active waveguide is subsequently determined with $T_H = e^{-\alpha_{eff} L_{C3}}$.

The second step is to substitute the effective absorption $\alpha_{eff} L_{C3}$ calculated from Eqn. (8.7) into the coupled mode formulation in the last section. With Eqn. (8.4) substituted into Eqn. (8.2a), we have the output signal power normalized to the incident pump supply power, i.e. $\frac{P_{H-ON}}{P_{H-CW}}$, which is denoted by $|a_1(\alpha_{am} L_{C3}, \Delta\beta L_{C0})|^2$. The switching gain factor of 3-WG EUPT is thus given by

$$G_{sw} = r_{in} \left| a_1 \left(\frac{\alpha_{eff} L_{C3}}{2}, \Delta\beta L_{C0} \right) \right|^2 . \quad (8.8)$$

The quantitative analysis of switching gain in 3-WG EUPT is carried out based on the same InGaAsP bulk semiconductor given in Table 3.1. The pump supply and signal wavelengths are at $\lambda_H = 1.35\mu m$ and $\lambda_L = 1.45\mu m$, and $I_{H-CW} = 15 MW/cm^2$. To compare with 2-WG EUPT, we first examine the case of $\alpha_{H0} L_{C3} = 30$, at which the maximum switching gain that can be achieved in 2-WG EUPT is equal to 1. In Fig. 8.6, the switching gain G_{sw} of 3-WG EUPT is plotted versus $\frac{P_{L-ON}}{P_{H-CW}}$

at different $\Delta\beta L_{C0}$. We find under the index matching condition, i.e. $\Delta\beta L_{C0} = 0$, 3-WG EUPT achieves the higher switching gain than the 2-WG EUPT. Meanwhile, a maximum switching gain associated with an optimal input signal power is observed for each $\Delta\beta L_{C0}$, and the maximum G_{sw} generally increases with $\Delta\beta L_{C0}$.

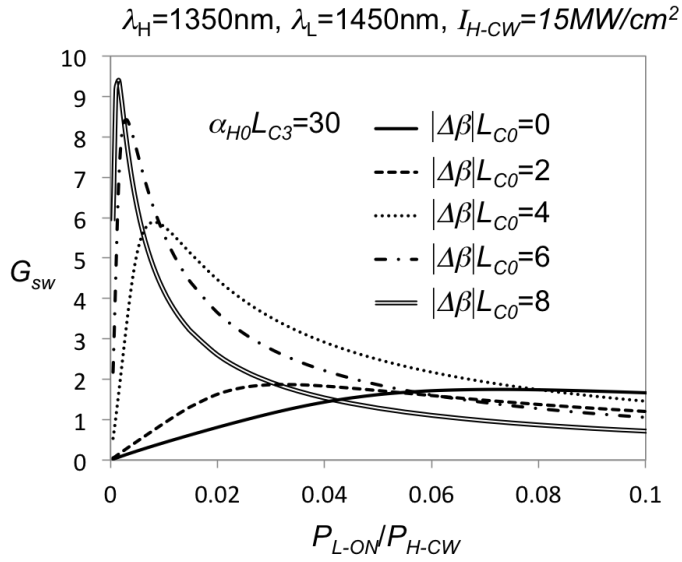

Figure 8.6: The switching gain of 3-WG EUPT versus $\frac{P_{L-ON}}{P_{H-CW}}$ at $\Delta\beta L_{L0} = 0, 2, 4, 6, 8$. $\lambda_H = 1.35\mu m$ and $\lambda_L = 1.45\mu m$. $I_{H-CW} = 15MW/cm^2$. $\alpha_{H0}L_{C3} = 30$.

Next, consider other $\alpha_{H0}L_{C3}$ with $\Delta\beta L_{C0}$ varying from 0 to 8, the maximum G_{sw} that can be achieved at each $\Delta\beta L_{C0}$ and $\alpha_{H0}L_{C3}$ are plotted in Fig. 8.7. As expected, the switching gain becomes higher when $\alpha_{H0}L_{C3}$ increases. We also find there is a significant increase of switching gain as $\Delta\beta L_{C0}$ is increased from 2 to 4, which corresponds to a refractive index change of ~0.004, if $L_{C0} = 100\mu m$. Since the carrier depletion process is always accompanied by the refractive index change, we may utilize this effect to further enhance the switching gain of 3-WG EUPT.

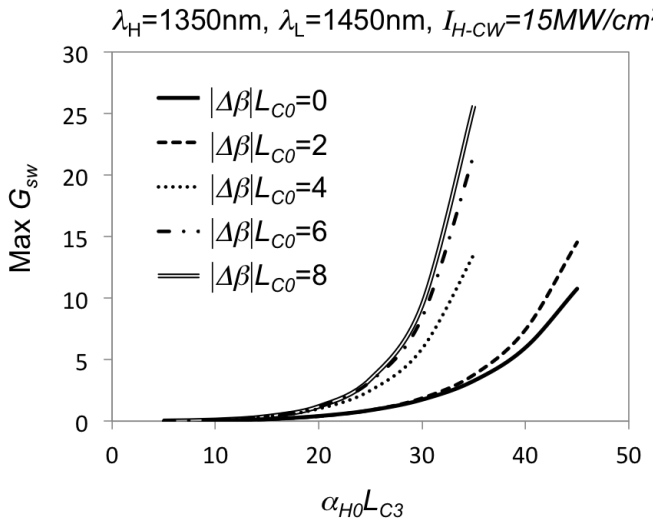

Figure 8.7: The maximum switching gain that can be achieved at different $\Delta\beta L_{C0}$ and $\alpha_{H0}L_{C3}$. $\lambda_H = 1.35\mu m$ and $\lambda_L = 1.45\mu m$. $I_{H-CW} = 15MW/cm^2$.

8.1.3 Switching speed and Figure of Merit for Bulk InGaAsP-based 3-WG EUPT

The switching speed of 3-WG EUPT is formulated differently from the 2-WG case. Refer to the inserted figure in Fig. 8.4 that shows the FDTD simulation of optical coupling in the 3-WG directional coupler with $\Delta\beta L_{C0} = 6.36$. We see the incident light experiences multiple couplings along the central waveguide, which can be considered as multiple pumping processes going in parallel at different locations, thus will speed up the overall pumping process. Therefore, depending on the number of coupling N_{cp} present along one device length L_{C3}, the switch-off speed of 3-WG EUPT with multiple-coupling situation can be written as

$$1/\tau_{OFF} = \xi\, I_{H-CW}\left|a_2\left(\alpha_{eff} = 0, \Delta\beta L_{C0}\right)\right|^2\left[1 - \left|a_1\left(\frac{\alpha_{eff}L_{C3}}{2}, \Delta\beta L_{C0}\right)\right|^2\right]N_{cp}, \quad (8.9)$$

where $\left|a_2\left(\alpha_{eff} = 0, \Delta\beta L_{C0}\right)\right|^2 = \frac{\pi^2}{\Delta\beta^2 L_{C0}^2 + 2\pi^2}$ is the maximum value of Eqn. (8.3b) giving the percentage of incident pump power that can be coupled into the central waveguide. $1 - \left|a_1\left(\frac{\alpha_{eff}L_{C3}}{2}, \Delta\beta L_{C0}\right)\right|^2$ takes into account of the switching-induced

pump-power reduction in the active waveguide. N_{cp} is a function of $\Delta\beta L_{C0}$, which can be derived from Eqn. (8.3b) and Eqn. (8.4), giving that

$$N_{cp} = \left[1 - \frac{|\Delta\beta| L_{C0}}{\sqrt{(\Delta\beta L_{C0})^2 + 2\pi^2}}\right]^{-1}. \tag{8.10}$$

As a result, Eqn. (8.9) can be written as

$$1/\tau_{OFF} = \xi(I_{H-CW} - I_{L-ON} G_{sw}) S_{3WG}(\Delta\beta L_{C0}), \tag{8.11}$$

with $S_{3WG}(\Delta\beta L_{C0}) = \frac{\pi^2}{\Delta\beta^2 L_{C0}^2 + 2\pi^2}\left[1 - \frac{|\Delta\beta| L_{C0}}{\sqrt{(\Delta\beta L_{C0})^2 + 2\pi^2}}\right]^{-1}$. $S_{3WG}(\Delta\beta L_{C0})$ increases with $\Delta\beta L_{C0}$, but is always <1, which suggests the switch-off speed of 3-WG EUPT is always slower than 2-WG EUPT if they are operated at the same optical power and the same switching gain. $\Delta\beta L_{C0}$ =0 corresponds to the slowest case, giving $S_{3WG}(\Delta\beta L_{C0}) = 0.5$, which suggests the switch-off speed of index-matched 3-WG EUPT is half of the speed in 2-WG EUPT under equivalent operating conditions. When $\Delta\beta L_{C0}$ increases to 6, $S_{3WG}(\Delta\beta L_{C0})$ increases 0.9. The validity of Eqn. (8.11) will be examined in the exemplary switching cases in the next section by MLME-FDTD simulation.

Next, the Merit Factor are calculated using Eqn. (5.5) for the bulk-InGaAsP-based 3-WG EUPT with $\alpha_{H0} L_{C3} = 30$ in Fig. 8.6, where $\lambda_H = 1.35\mu m$, $\lambda_L = 1.45\mu m$ and $I_{H-CW} = 15 MW/cm^2$. $\Delta\beta L_{L0}$ varies from 0 to 8. For each $\Delta\beta L_{L0}$, we use the maximum switching gain and the corresponding I_{L-ON} for the MF calculation. τ_{OFF} is determined using Eqn. (8.11) and let $\tau_{ON} = 10ps$. Consider $A_{eff} = 0.043\mu m^2$, $N_{ch} = 20$ and $A_d = 600\mu m^2 (150\mu m^2 \times 30/7.5)$. The resultant Merit Factors are subsequently normalized by the Merit Factor of electronic transistor to obtain the relative Figure of Merit, which are plotted versus $\Delta\beta L_{L0}$ in Fig. 8.8. As we

can see, it generally increases with $\Delta\beta L_{L0}$ and tends to saturate when $\Delta\beta L_{L0} > 6$. For the comparison, we calculate FOM for 2-WG EUPT with $\alpha_{H0}L_{C3} = 30$ in Fig. 5.1, which has $I_{H-CW} = 15MW/cm^2$, $I_{L-ON} = 3MW/cm^2$ $G_{sw} = 1$, A_d ~$600\mu m^2$, $A_{eff} = 0.043\mu m^2$, $\tau_{OFF} = 35ps$ and $N_{ch} = 20$. The result is ~5×10^{-5}, which is plotted in dash line in Fig. 8.8. As we see, with the same $\alpha_{H0}L_{C3}$, 3-WG EUPT exhibits the higher Figure of Merit than 2-WG EUPT. The FOM of 3-WG EUPT can be potentially further improved by increasing $\alpha_{H0}L_{C3}$.

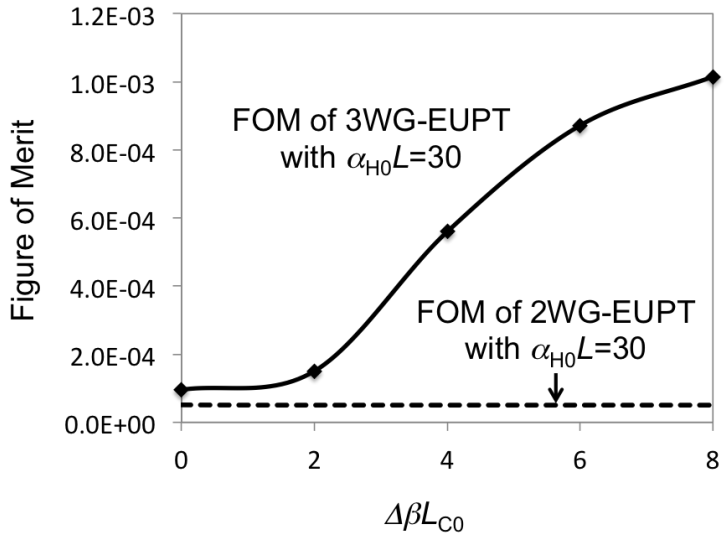

Figure 8.8: Figure of Merit for bulk-InGaAsP-based 3-WG EUPT with $\alpha_{H0}L_{C3} = 30$ at different $\Delta\beta L_{L0}$ (solid line) and for bulk-InGaAsP-based 2-WG EUPT with $\alpha_{H0}L_{C3} = 30$ (dash line). $\lambda_H = 1.35\mu m$, $\lambda_L = 1.45\mu m$, $I_{H-CW} = 15MW/cm^2$ and. $\Delta\beta L_{L0}$ varies from 0 to 8.

Note that in spite of the increasing switching gain, switching speed and the Figure of Merit with $\Delta\beta L_{L0}$, it is not favored to infinitely increase $\Delta\beta L_{L0}$ for the 3-WG EUPT operation. One of the reasons is the device will become significantly long at large $\Delta\beta L_{L0}$, making it infeasible for large-scale photonic integration. On the other hand, increasing $\Delta\beta L_{L0}$ will reduce the coupling efficiency of the input pump suppler power into the central waveguide, thus will pose higher pump power requirement to achieve transparency state in the active waveguide. Based on all the analysis above,

we consider $\Delta\beta L_{L0} < 8$ as an appropriate range for 3-WG EUPT operation.

8.1.4 Dynamic switching of index-mismatched bulk-InGaAsP 3-WG EUPT simulated by MLME-FDTD

Next, MLME-FDTD simulation is adopted to demonstrate the switching action in an index mismatched 3-WG EUPT based on InGaAsP bulk semiconductor medium (Table 3.1). The pump supply and the input signal wavelengths are $\lambda_H = 1.35\mu m$ and $\lambda_L = 1.45\mu m$ respectively. The input intensities of the two beams are also fixed, giving $I_{H-CW} = 80MW/cm^2$ and $I_{L-ON} = 0.65MW/cm^2$. We arbitrarily choose the case of $\Delta\beta L_{C0} = 6$. The device geometry is shown in Fig. 8.9a. Note that n=3.436 is the background refractive of the active medium without optical pumping, while $\Delta\beta L_{C0}$ is calculated when the central waveguide is optically pumped to transparency at the pump supply wavelength. In addition, we have purposely made the side waveguides to be multi-mode waveguides and the widths of the side waveguides wider than the central waveguide to let the simulation more consistent with the real device. Fig. 8.9b shows the FDTD simulation of pump supply beam propagating along this 3-WG coupler after the central waveguide is pumped to transparency. We can see there are 5 intensity peaks along the active waveguide, which is consistent with the analytical plot in Fig. 8.3 for $\Delta\beta L_{C0} = 6$.

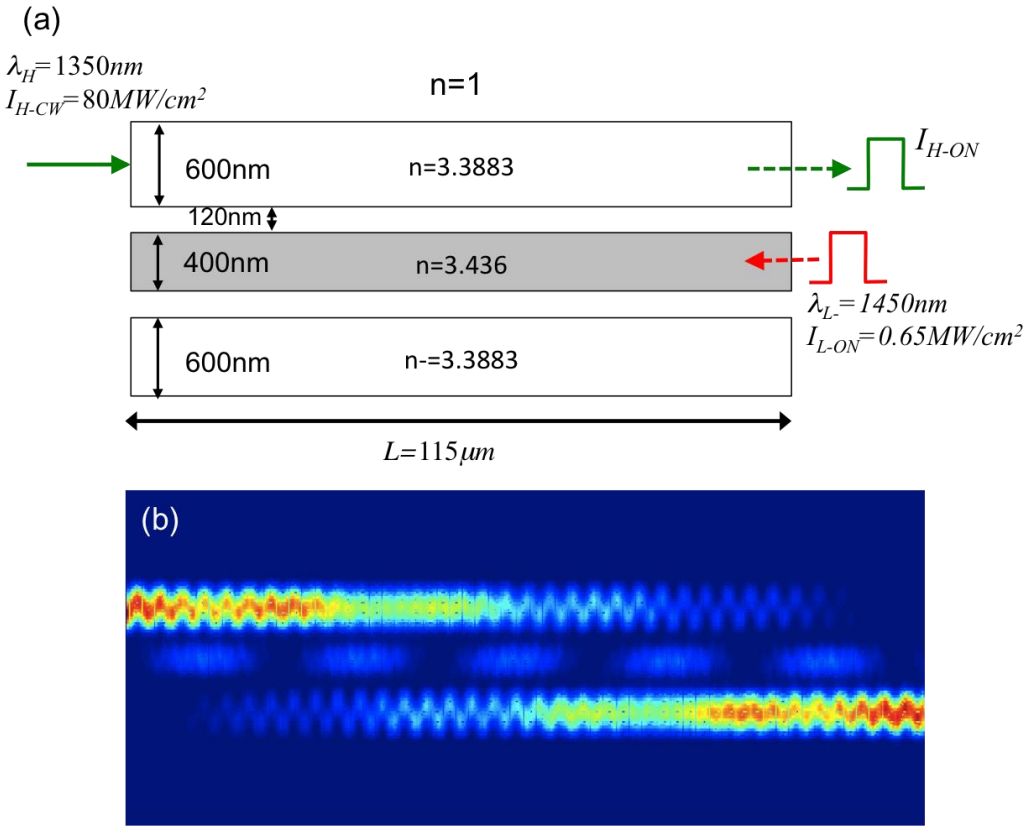

Figure 8.9: a) 3-WG coupler structure and simulation parameters for FDTD simulation of EUPT operation. $\Delta\beta L_{C0} = 6$ and $L_{C3} = 115\mu m$. b) FDTD simulation of pump supply beam propagating along the 3-WG coupler after the central waveguide is pumped to transparency.

Here we consider two different $\alpha_{H0}L_{C3}$ values, (1) $\alpha_{H0}L_{C3} = 25.1$ ($\alpha_{H0} = 0.218\mu m^{-1}$) and (2) $\alpha_{H0}L_{C3} = 28.3$ ($\alpha_{H0} = 0.246\mu m^{-1}$), where $L_{C3} = 115\mu m$ is fixed and α_{H0} is varied by adjusting the vertical optical confinement factor of the active waveguide. The MLME-FDTD simulation results are shown in Fig. 8.10, where the red plot shows the 50ps input signal pulse, and green and blue plots correspond to the output signals for the cases of $\alpha_{H0}L_{C3} = 25.1$ and $\alpha_{H0}L_{C3} = 28.3$ respectively. Based on the analytical calculation, the switching gains for theses two cases are equal to 1.7 and 3.4 respectively, which are higher than the FDTD results. This could be due to the refraction-induced switching that is not taken into account of our formulation. As we can see from Fig. 8.6, the switching gain at fixed $\alpha_{H0}L_{C3}$ could be very sensitive to the effective model refractive index shift, especially when

$\Delta\beta L_{C0}$ is around 4~6. On the other hand, the switch-off time calculated using Eqn. (8.11) is ~6ps, which is close to the simulation results.

As a result, 50Gbps switching with switching gain ~2 is demonstrated in an index-mismatched bulk-InGaAsP-based 3-WG EUPT. With $A_{eff} = 0.043\mu m^2$, the pump supply power is 34.4mW and the signal peak power is 0.28mW, which corresponds to an energy consumption of 0.56pJ/bit.

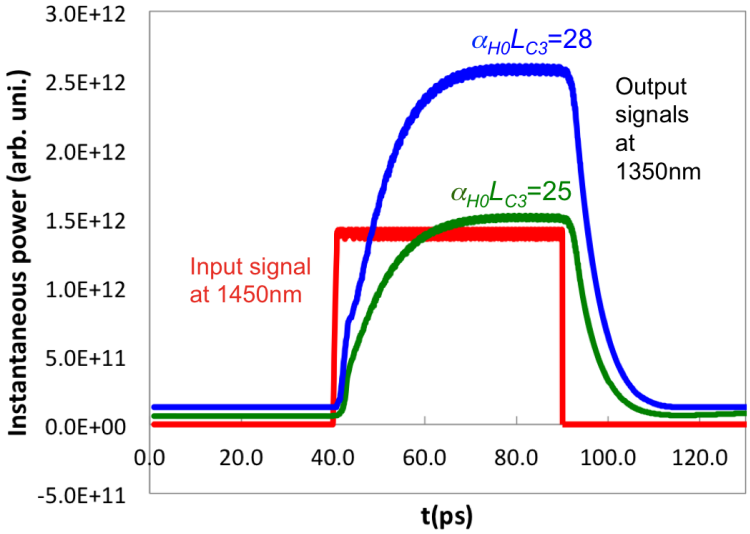

Figure 8.10: Input and output signal profiles for 3WG-EUPT with $\Delta\beta L_{C0} = 6$. Simulation parameters are given in Fig. 8.8 The three plots show the temporal profiles of incident signal (red) at 1450nm and output signal at 1350nm when $\alpha_{H0}L_{C3} = 25$ (green) and $\alpha_{H0}L_{C3} = 28$ (blue).

8.2 EUPT based on Mach–Zehnder interferometer (MZI-EUPT)

The involvement of direct coupling between passive and active waveguide poses great fabrication complexity and challenges. An alternative approach to eliminate the passive-active coupling scheme is based on the Mach-Zehnder interferometric configuration, which will be studied in the following sections.

8.2.1 Working principle of MZI-EUPT

The Mach-Zehnder-based EUPT (MZI-EUPT) structure and the switching process are shown in Fig. 8.11. To ease the fabrication and device design, we consider the symmetric MZI configuration with two identical active arms. The incident pump supply power P_{H-CW} splits into two arms by a 3-dB directional coupler, pumping the two arms to transparency. When they meet at another 3-dB coupler, all of the power exits from one arm, due to the $\pi/2$ phase difference induced in the first 3-dB coupler. When the signal at a longer wavelength is launched into one arm, it depletes carriers and introduces absorption to the pump supply beam. As a result, the pump supply in that arm is attenuated, and the coupling condition at the second 3-dB coupler changes, so that the pump supply power is partially coupled into the output port.

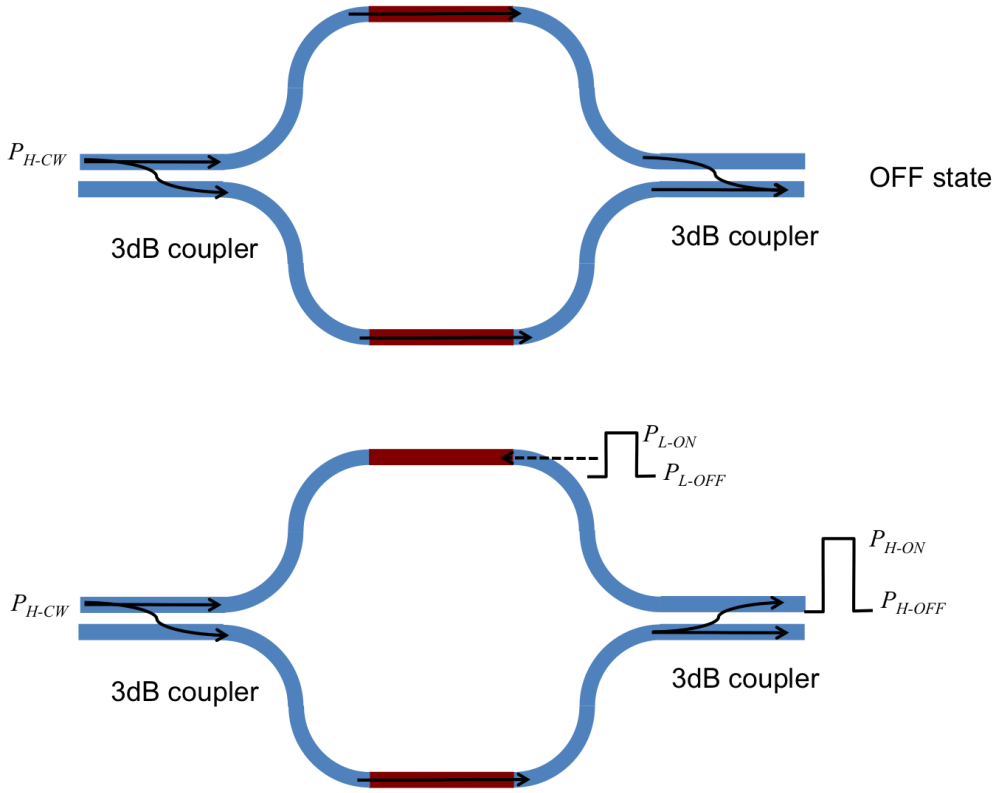

Figure 8.11: Switching operation in MZI-based EUPT, which consists of two identical active arms.

8.2.2 Analytical analysis of switching gain for MZI-EUPT

Since the input pump supply power splits to half at the first 3-dB coupler, Eqn. (4.5) is modified as follows to calculate the transmission T_H of the pump beam through the active waveguide with input signal launched in.

$$-ln(T_H) + \frac{\alpha_{H0}}{g_{L0}} ln\left[1 + \frac{g_{L0}}{\alpha_{H0}} \frac{I_{Lsat}}{I_{Hsat}} (1 - T_H) \frac{r_{in}}{2}\right] + (1 - T_H) \frac{\tau_r}{I_{Hsat}} \frac{I_{H-CW}}{2} = \alpha_{H0} L \,, \tag{8.12}$$

where $I_{H-CW} = P_{H-CW}/A_{eff}$, with A_{eff} being the modal area of the active waveguide, and $r_{in} = \frac{P_{H-CW}}{P_{L-ON}}$. At the second 3-dB coupler, two pump supply beams with different powers, i.e. $P_{H-CW}/2$ and $T_H P_{H-CW}/2$, meet and interfere with each other. The power exiting the output port can be derived from coupled mode theory, which is given by $(P_{H-CW}/2)\left(1 - \sqrt{T_H}\right)^2$. Thus the gain factor for MZI-EUPT is given by

$$G_{sw} = \frac{1}{2} r_{in} \left(1 - \sqrt{T_H}\right)^2 . \tag{8.13}$$

Next, quantitative analysis of switching gain is carried out for bulk-InGaAsP-based MZI-EUPT with different $\alpha_{H0}L$. Using the same simulation parameters as adopted for 2-WG and 3-WG EUPT analysis, we have $\lambda_H = 1.35\mu m$, $\lambda_L = 1.45\mu m$ and $I_{H-CW} = 15 MW/cm^2$. Fig. 8.12a shows the switching gain G_{sw} plotted versus $1/r_{in}$ at different $\alpha_{H0}L$. Similar to the 2-WG and 3-WG EUPT, G_{sw} of MZI-EUPT generally increases with $\alpha_{H0}L$, and there is an optimal P_{L-ON}/P_{H-CW} ratio associated

with the maximum switching gain G_{sw} for each $\alpha_{H0}L$ value. The condition $G_{sw} > 1$ is achieved when $\alpha_{H0}L > 10.5$.

Subsequently, the maximum G_{sw} that can be achieved at each $\alpha_{H0}L$ is plotted in Fig. 8.12b, and compared with the 2-WG EUPT and index-matched 3-WG EUPT working at the same λ_H, λ_L and I_{H-CW}. Note that for MZI-EUPT, the maximum G_{sw} is plotted against $2\alpha_{H0}L$, due to the presence of two active waveguides. As we can see, MZI-EUPT exhibit the highest switching gain at a given $\alpha_{H0}L$, followed by 3WG-EUPT and 2-WG EUPT.

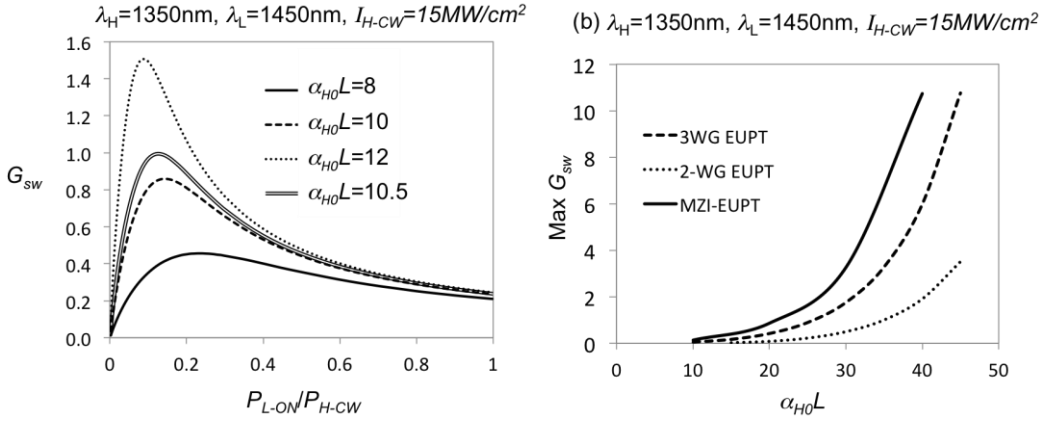

Figure 8.12: (a) The switching gain of MZI-EUPT versus $\frac{P_{L-ON}}{P_{H-CW}}$ for different $\alpha_{H0}L$. (b) the maximum switching gain that can be reached at each $\alpha_{H0}L$ plotted against $2\alpha_{H0}L$ for MZI-EUPT (solid), and against $\alpha_{H0}L$ for 2-WG EUPT (dotted line) and index-matched 3-WG EUPT (dash line). $\lambda_H = 1.35\mu m$ and $\lambda_L = 1.45\mu m$. $I_{H-CW} = 15MW/cm^2$.

8.2.3 Switching speed and Figure of Merit of bulk InGaAsP-based MZI-EUPT

The switching speed of MZI-EUPT can be estimated using the single-waveguide formulation in Eqn. (4.12), which gives

$$\frac{1}{\tau_{OFF}} = \frac{\xi I_{H-CW}}{2}, \tag{8.14}$$

where $\xi = 0.24\ (m^2J^{-1})$ for the bulk InGaAsP semiconductor in Table 3.1.

Subsequently, with Eqn. (5.5), the Figure of Merit of bulk-InGaAsP-based MZI-EUPT is calculated for the case of $2\alpha_{H0}L = 30$ in Fig. 8.12a to compare with that for the 3-WG EUPT and 2-WG EUPT. The device area of MZI-EUPT is estimated with $A_d = 6000\mu m^2$ $(150\mu m^2 \times 15/7.5 \times 20)$, where we assume the width of the MZI device is 20 times of the coupler structure. The maximum switching gain with $\alpha_{H0}L = 15$ is equal to 3.2, at which, $I_{L-ON} = 0.1I_{H-CW} = 1.5MW/cm^2$. The switch-off time is calculated from Eqn. (8.14), giving $\tau_{OFF} = 55ps$. Then with $A_{eff} = 0.043\mu m^2$ and $N_{ch} = 20$, we get the relative Figure of Merit for InGaAsP-based MZI-EUPT with $2\alpha_{H0}L = 30$ is $\sim 2 \times 10^{-5}$, which is lower than *FOM*=5×10^{-5} for the 2-WG EUPT with $\alpha_{H0}L_{C2} = 30$ and *FOM*=$1 \times 10^{-4} \sim 1 \times 10^{-3}$ for 3-WG EUPT with $\alpha_{H0}L_{C3} = 30$. The main disadvantage of MZI EUPT is the large device size.

8.2.4 Dynamic switching in Bulk-InGaAsP-based MZI-EUPT simulated by MLME-FDTD

The MLME-FDTD simulation of switching operation in bulk-InGaAsP-based MZI-EUPT is carried out for $\alpha_{H0}L = 14$ ($\alpha_{H0} = 0.57\mu m^{-1}$ and $L = 25\mu m$), as shown in Fig. 8.13. The pump supply and input signal wavelengths are $\lambda_H = 1.35\mu m$ and $\lambda_L = 1.45\mu m$. The input pump intensity is $I_{H-CW} = 13MW/cm^2$ and the input signal peak intensity is $I_{L-ON} = 0.65MW/cm^2$.

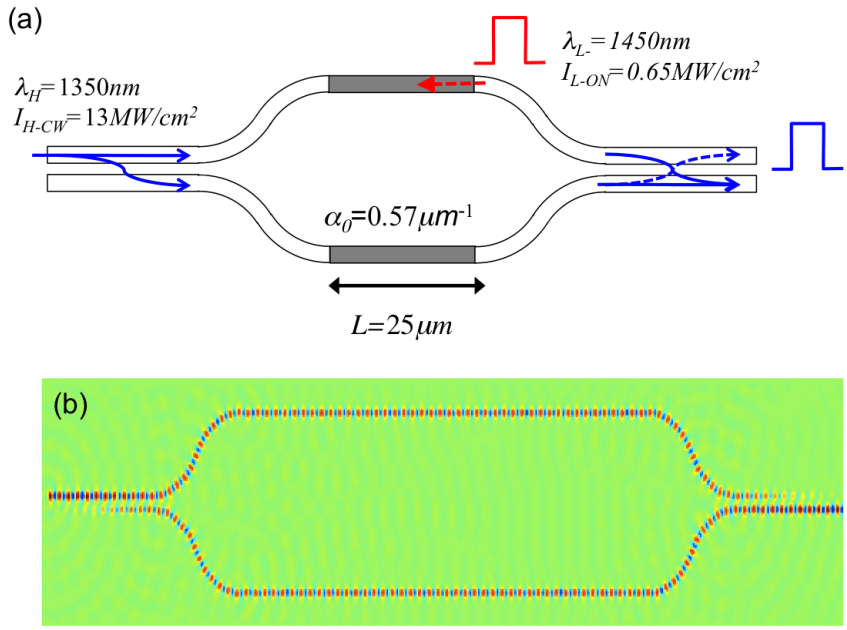

Figure 8.13: a) MZI structure with two 3dB couplers at input and output, and FDTD simulation parameters for EUPT operation. Solid arrows and dash arrows correspond to the switch-off state and switch-on state respectively. b) The intensity profile of pump supply beam at switch-off state when the two active arms are pumped to transparency.

The temporal profiles of input and out signals are shown in Fig. 8.13. The switching gain from FDTD simulation is ~2.5, which is close to the analytical calculation given by 2.9. The switch-on speed is slower than the single-waveguide case, which is because the output signal power responds to the transmission change of the active waveguide differently. The output signal of single waveguide switch responds to $1 - T_H$, while the output signal of MZI EUPT responds to $\left(1 - \sqrt{T_H}\right)^2$, which increases slowly as T_H reduces from 1. On the other hand, the switch-off time from MLME-FDTD simulation is ~30ps, which is shorter than the analytical calculation given by ~60ps. This is mainly because the pump transmission through the signal-in waveguide is only partially shut off, which takes shorter than 10%-to-90% rising time τ_{p2} to pump it to transparency.

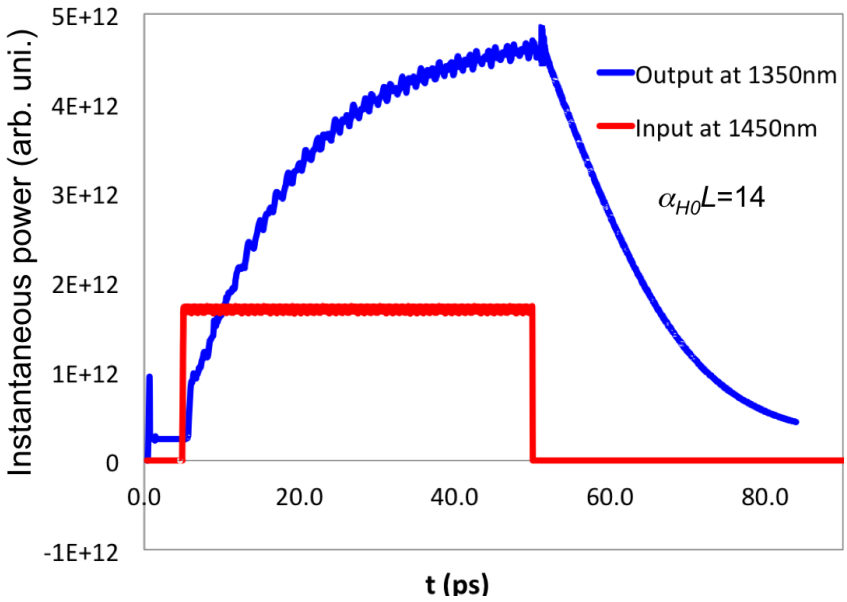

Figure 8.13: temporal profiles of input signal at 1450nm (red) and output signal at 1350nm (blue) of the MZI-EUPT in Fig. 8.13a simulated by MLME-FDTD. The band structure of active medium is given by Table 3.1.

8.3 Conclusion

To alleviate the fabrication challenges for achieving effective-model-refractive-index matching in 2WG-EUPT, we proposed two new EUPT architectures in this chapter, including 3-WG EUPT and MZI-EUPT. In the 3WG configuration, the nature of symmetry promises complete coupling thus high-extinction-ratio switching even with the presence of effective-model-refractive-index mismatching. MZI configuration eliminates the passive-active coupling mechanism, and the symmetric structure of which further reduces the fabrication challenges.

The switching performance of bulk-InGaAsP 3-WG EUPT and MZI-EUPT are systematically analyzed based on our analytical approach developed in Chapter III-V. It shows 3-WG EUPT is generally slower but has higher switching gain than 2-WG EUPT under the same operational conditions. The switching gain of MZI EUPT is higher than the 3-WG EUPT and 2-WG EUPT when they have the same $\alpha_{H0}L$, but the switching speed of MZI EUPT is slower than 2-WG EUPT since the incident

pump power splits into half before it pumps the active arms. The Figure of Merit for 3-WG EUPT is shown higher than the 2-WG EUPT and the MZI EUPT with the same $\alpha_{H0}L$. Increasing the effective-model-refractive-index mismatching factor $\Delta\beta L_{C0}$ in 3-WG EUPT can further improve the FOM due to the increase of switching gain. However, the pump supply power coupled into the central waveguide decreases with the increase of $\Delta\beta L_{L0}$, which poses the higher pump power requirement for achieving the transparency state at the switch-off state. Thus $\Delta\beta L_{L0} < 8$ is suggested for high-performance operation with 3-WG EUPT.

In the end, the optimal operational parameters for the three EUPT configurations to achieve 20Gbps switching speed and switching gain of 2 are tabulated in Table 8.1. Calculation is based on the energy band parameters of InGaAsP bulk semiconductor in Table 3.1. The pump supply and input signal wavelengths are 1.35 μm and 1.45 μm respectively. MLME-FDTD simulation shows 20Gbps is generally promised among the three EUPT device structures with the pump supply intensity of $I_{H-CW} = 15MW/cm^2$, which is fixed here. $E_{bit}$is calculated using mode area of $A_{eff} = 0.043\mu m^2$.

Table 8.1: Optimal operational parameters for bulk-InGaAsP-based 2-WG, 3-WG and MZI-EUPT to achieve 20Gbps switching speed and switching gain of 2.

$\lambda_H = 1.35\mu m$ $\lambda_L = 1.45\mu m$ $I_{H-CW} = 15MW/cm^2$	$\alpha_{H0}L$	I_{L-ON} (MW/cm^2)	E_{bit} (fJ/bit)
2-WG EUPT	35.5	1.47	354
3-WG EUPT ($\Delta\beta = 0$)	31.2	0.96	343
MZI-EUPT	13.1	1.02	344

CHAPTER IX Experimental Investigation

Experimental investigation of the proposed photonic transistor switching scheme has never been reported before. The lack of existing knowledge calls for tremendous amount of characterization and optimization work, typically requiring multiple rounds of device design, fabrication, testing and optimization process. Unfortunately, it is hardly possible to accomplish all the work within the Ph.D candidature period. Thus, my effort has been devoted to the first-stage measurement work, including material parameter characterization and demonstration of all-optical switching with switching gain in the single-waveguide structure.

The material parameter characterization, in particular the saturation intensity I_{Hsat} and small-absorption coefficient α_{H0}measurement, is important to the first-stage actual device design. With the known saturation intensities and small absorption coefficient, we are able to estimate the minimum device length L required for switching gain, and deduce the pump power requirement, switching energy, device sensitivity, fabrication feasibility and so on.

Meanwhile, all-optical switching with switching gain is demonstrated for the first time in single nanowaveguide structure based on the hybrid III-V/Silicon integration platform [74]. This single-waveguide switch features 6nm broadband operation, small device footprint and low sensitivity to fabrication error. More importantly, it experimentally demonstrated the self-enhanced carrier-depletion-induced-absorption effect, which is the key mechanism in the switching scheme we proposed that leads to the switching gain in our EUPT devices.

The 2-WG EUPT, 3-WG EUPT and MZI EUPT based on self-aligned QW-on-SOI integration are fabricated. The first batch of EUPT devices are designed to be

long enough to fulfill the $\alpha_{H0}L$ requirement for switching gain. However, the maximum pump supply power that can be delivered in our set up is not sufficient to pump up such long QW-on-SOI waveguides. Therefore, the initial tests for achieving the desired OFF-state pumping characteristics in 2-WG, 3-WG and MZI-EUPT are not successful. A series of improvements are desired for the future device design and fabrication, which will be discussed in this chapter.

9.1 Saturation Intensity and Small Absorption Coefficient Measurement

It has been shown in the previous chapters that saturation intensity I_{Hsat} and the small-signal absorption coefficient (α_{H0}) of the active waveguide at the pump supply wavelength play the determining roles in affecting the AMOI-based EUPT performance. Experimental characterization of I_{Hsat} and α_{H0} is thus very important to the actual device design. With the knowledge of I_{Hsat} and α_{H0}, the minimum device length *L* required for switching gain can be estimated, and the pump power requirement, switching energy, device sensitivity, fabrication feasibility and so on can also be subsequently deduced.

Here we propose a new measurement methodology to determine the values of I_{Hsat} and α_{H0}. The measurement is carried out in a single self-aligned QW-on-Si hybrid waveguide with the in-house-built free-space coupling station. The pump beam is launched into the waveguide and the transmitted optical power is monitored under varied experimental conditions. Analytical formulation is developed to simulate the propagation characteristics of light through the waveguide and the values of I_{Hsat} and α_{H0} are obtained from fitting the theoretical calculation to the

experimental data.

Section 9.1 is organized as follows. First of all, to formulate the propagation characteristics of light, we start with the simplest case, in which the coupling efficiency and propagation loss of the waveguide are eliminated. The basic methodology of this measurement is thus illustrated. After that, the full device structure and the measurement set up are introduced in detail. Several parameters involved in the actual measurement situation, i.e. coupling efficiencies, are subsequently taken into account to form the complete formulation. Then the measurement procedure and the data analysis are presented in detail at the end.

9.1.1 Basic methodology

Upon the launch of the pump beam into a single active QW-on-SOI waveguide, the propagation characteristics of the pump beam can be formulated with Eqn. (4.9) in Section 4.3.1

$$ln\frac{I_H(L)}{I_H(0)}+\frac{I_H(L)-I_H(0)}{I_{Hsat}}=-\alpha_{H0}L \tag{4.9}$$

where we have assumed the propagation loss of the waveguide is negligible. L is the length of the active waveguide. α_{H0} is the background absorption coefficient of the waveguide at the optical wavelength λ_H. With the substitution of the transmission parameter $T=\frac{I_H(L)}{I_H(0)}$, Eqn. (4.9) becomes

$$lnT+\frac{I_H(0)}{I_{Hsat}}(T-1)=-\alpha_{H0}L \tag{9.1}$$

As we can see, the transmission T is a function of incident intensity of light $I_H(0)$ and the waveguide length L, related with the material property parameter I_{Hsat} and α_{H0}. In other words, I_{Hsat} and α_{H0} could be deduced from the optical transmission of the waveguide at varied $I_H(0)$ and L.

However, in the actual experiment, we also have to take into account of the propagation loss of the waveguide due to the sidewall roughness caused by the etching process. Thus, the propagation equation in Eqn. (4.9) is modified as

$$\frac{dI_H(z)}{dz} = -\left[\frac{\alpha_{H0}}{1 + {I_H(z)}/{I_{Hsat}}} + \alpha_p\right] I_H(z) \tag{9.2}$$

where $\alpha_p$denotes the propagation loss coefficient. The solution of Eqn. (9.2) is given by

$$ln\frac{I_H(L)}{I_H(0)} + \frac{\alpha_{H0}}{\alpha_p} ln\frac{I_H(L) + \left(1 + \frac{\alpha_{H0}}{\alpha_p}\right) I_{Hsat}}{I_H(0) + \left(1 + \frac{\alpha_{H0}}{\alpha_p}\right) I_{Hsat}} = -(\alpha_{H0} + \alpha_p)L \tag{9.3}$$

α_p can be experimentally determined using Fabry-Perot technique [67-68] at a wavelength longer than the bandgap wavelength of the QW. The measurement details will be presented later. With α_p known, α_{H0} and I_{Hsat} can be subsequently determined based on curve fitting at varied $I_H(0)$ and L.

9.1.2 Waveguide structure and experimental set up

Fig. 9.1a shows the SEM image of QW-on-SOI waveguide for saturation intensity measurement, where the inserted figure shows the sidewall of the hybrid waveguide. The strained InGaAsP QW is directly bonded on SOI waveguide, forming the self-aligned QW-on-SOI waveguide. The waveguide length L varies from 10μm to 50μm in the following measurement. The cross-sectional structure of the waveguide and the quantum well layer structure are shown in Fig. 9.1b. The designed InGaAsP strained QW thin filmed ensures that the optical mode centers at the QW region as illustrated in Fig. 9.1c as 1342nm light propagates through the device structure. Note that 1342nm is the pump supply wavelength for I_{Hsat} and α_{H0} measurement, as well as for the all-optical switching operation to be presented in the later section.

There are two tapering structure designed at the waveguide ends for optical coupling between passive SOI waveguide and active QW-on-SOI waveguide. Optimization of the tapering structure will not be discussed in this dissertation. Two 100μm-length and 350nm-width SOI waveguides are introduced before and after the QW-on-SOI hybrid waveguide for higher-order mode filtering purpose. The passive SOI waveguide is tapered to 4μm wide at the cleaved wafer edge to increase free-space coupling efficiency, as shown in Fig. 9.1d.

The experimental set up for saturation intensity measurement is shown in Fig. 9.2. The measurement is carried out using a continuous wave (CW) solid state laser operating at a wavelength of 1342nm. The laser output beam is sent to an acousto-optic modulator (AOM), which is controlled by a Tektronix function generator to select a single 400ns pulse at a 2kHz repetition rate. The low repetition rate and short pulses were used to minimize thermal effects [69]. The 1342nm pulse sequence is

subsequently transmitted through a half-wave plate ($\lambda/2$ plate) at 1340nm, followed by a polarization beam splitter (PBS), where the TE-polarized (the polarization is parallel to the wafer surface) component is transmitted and the amount of transmission can be varied by rotating the polarization of light using of the half wave plate without changing the optical alignment. Next, the TE-polarized 1342nm pulse string is launched into the 4μm-width SOI waveguide through free-space coupling,

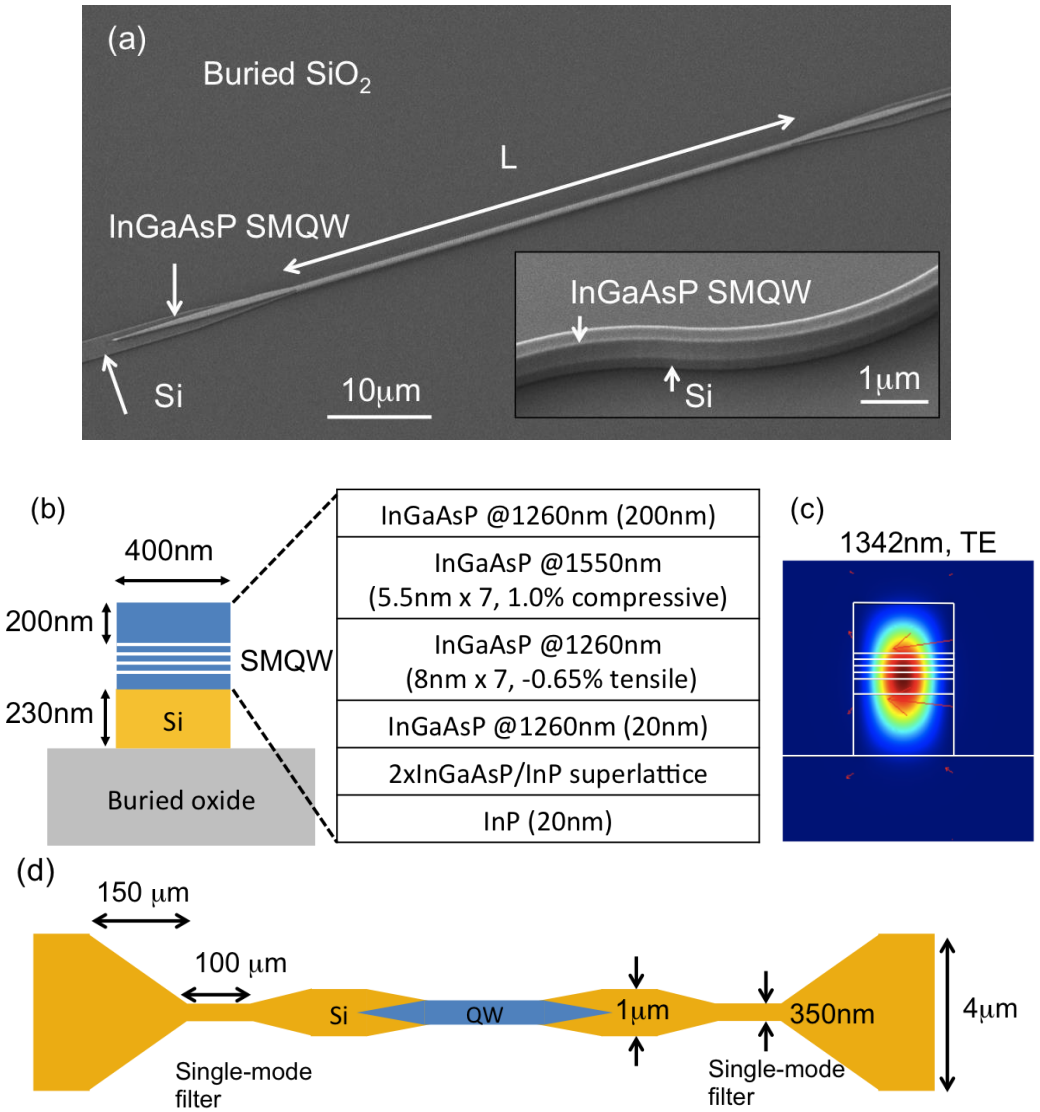

Figure 9.1: (a) SEM image of self-aligned QW-on-SOI waveguide with tapers for optical top-down coupling. (b) Cross section of the QW-on-SOI waveguide and the wafer structure of the QW thin film. (c) The optical mode intensity distribution in the QW-on-SOI waveguide for TE polarized 1342nm optical mode. (d) The full structure of QW-on-SOI hybrid waveguide with single-mode filters. The waveguide is not drawn to scale.

by using a x60 microscope objective lens to focus the free-space optical beam at the waveguide end facet. The transmitted light is collected by the second x60 objective lens and sent to the Thorlabs InGaAs-based photo-detector (PD). The generated photo-current signal is measured by the Stanford Research System lock-in amplifier, which is able to effectively remove the background noise out of the weak signal.

The blue solid line in Fig. 9.2 shows the optical path of 532nm alignment beam, which splits into two paths at a 50/50 beam splitter and propagates at opposite directions at the sample station. This beam is utilized to align the waveguide and two objective lenses. The dichroic mirror at right-bottom combines the alignment beam and the measurement beam by transmitting 1342nm light and partially reflecting 532nm light. The left-bottom mirror in dash line is removed during the measurement and put back when doing the alignment.

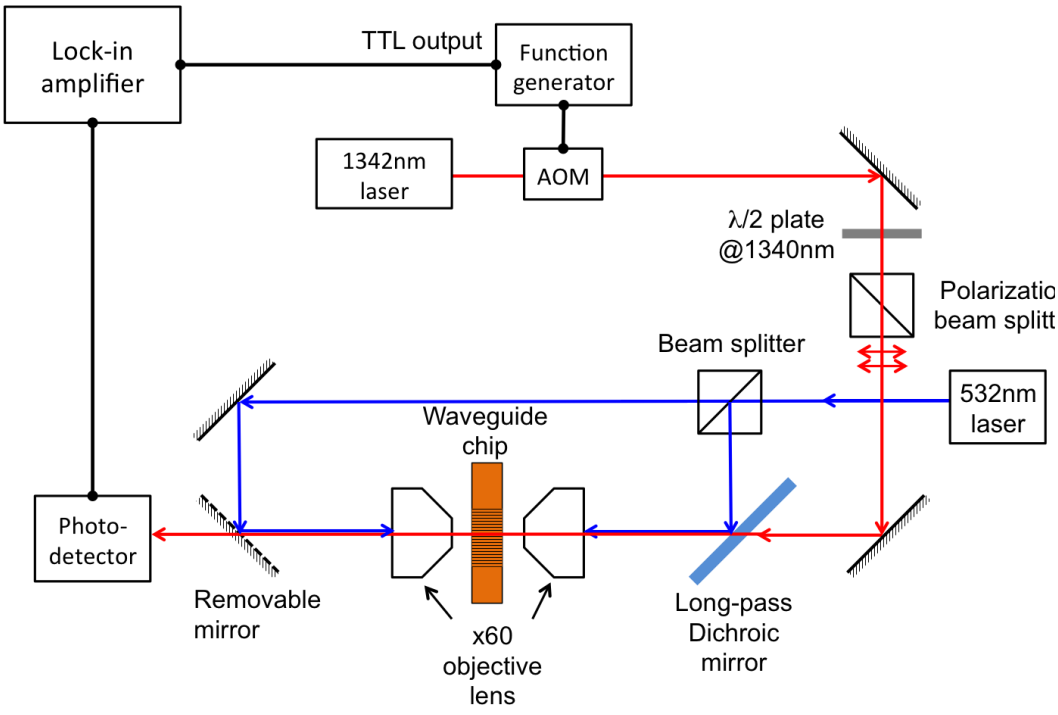

Figure 9.2: Experimental setup for saturation intensity measurement.

Fig. 9.3 shows the photo of the free-space coupling station with the input and

output objective lens aligned with the nano-waveguide on the sample chip. Multi-dimensional translational and angular adjustments with sub-micrometer accuracy are integrated to the sample stage and the objective lens mounts, in order to achieve fine control of optical coupling efficiency. Above the coupling station is an optical microscope integrated with visible and infrared vision systems.

The models of the instruments involved in our experiments are provided in Table 9.1.

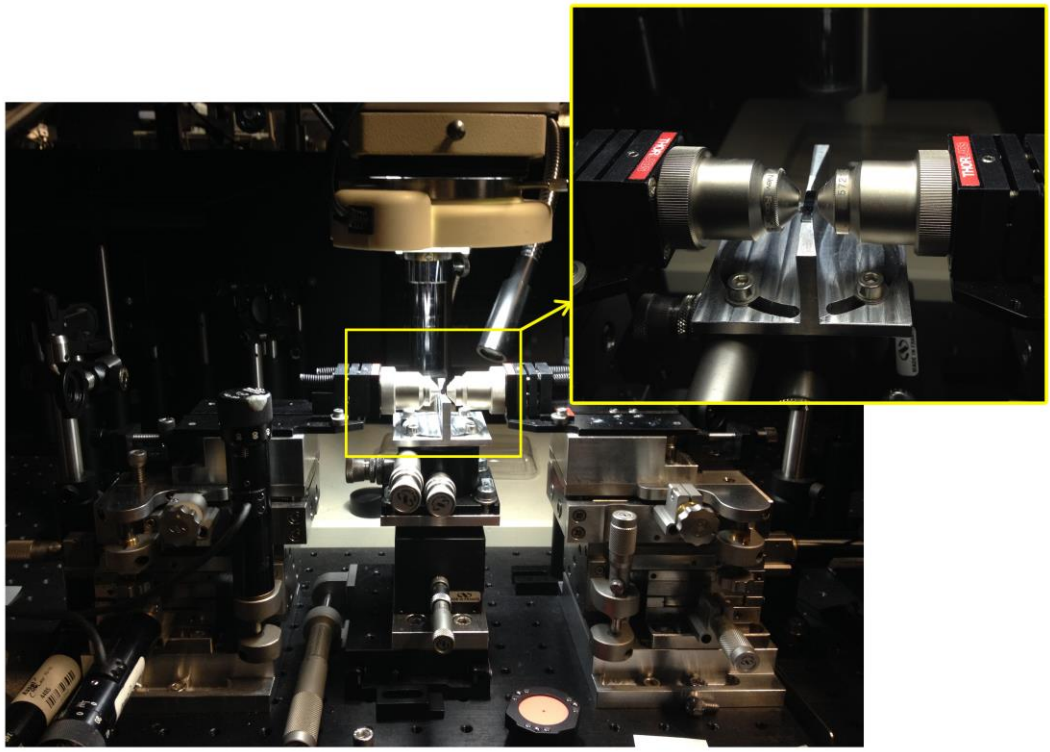

Figure 9.3: The free-space coupling station with input and output objective lens aligned with the nano-waveguide on the sample chip.

Table 9.1: Instrument model list

Instruments	Model
1342nm CW laser	Sintec Optronics LD pumped all-solid state laser
Acousto-optic modulator (AOM)	ISOMET 1206C
Function generator 1	Tektronix PFG 5105
Function generator 2	Tektronix AFG 3251
Lock in amplifier	Stanford Research System SR850
Oscilloscope	Agilent DSO-X 3054A (4GSa/s)
Photodetector (PD1 and PD2)	Thorlabs DET10C
Tunable laser (1460nm-1580nm)	Agilent 8164A
Tunable laser (1390nm - 1530nm)	Yenista Tunics Reference
Optical power meter	Thorlabs S112, S145C

9.1.3 Measurement procedure and results

From the measurement set up and device structure in Fig. 9.2 and Fig. 9.1, we can see Eqn. (9.3) is not sufficient to describe the actual measurement condition. In the experiment, the optical power are measured before and after the input and output objective lens, while $I_H(0)$ and $I_H(L)$ in Eqn. (9.3) refer to the optical intensities, or equivalently optical power, in the active QW-on-SOI waveguide. Thus input and output free-space coupling efficiency and Si-to-QW top-down coupling efficiency should be taken into account of our formulation. As a result, Eqn. (9.3) is modified as follows

$$ln\left(\frac{P_{out}}{P_{in}}\frac{1}{c_1c_2}\right)+\frac{\alpha_{H0}}{\alpha_p}ln\frac{P_{out}+\left(1+\frac{\alpha_{H0}}{\alpha_p}\right)c_2P_{Hsat}}{P_{in}c_1c_2+\left(1+\frac{\alpha_{H0}}{\alpha_p}\right)c_2P_{Hsat}}=-(\alpha_{H0}+\alpha_p)L \quad (9.4)$$

where P_{in} and P_{out} are the input and output optical power before and after the objective lens respectively. The variable P_{Hsat} denotes the saturation power, which determines the saturation intensity I_{Hsat}. The relationship between P_{Hsat} and I_{Hsat} is dependent on the cross-sectional structure of the waveguide, which will be discussed

later. The variable c_1 represents the total input coupling efficiency, i.e. the percentage of the incident laser power (before the first objective lens) being coupled into the QW-on-SOI waveguide, and c_2 represents the total output coupling efficiency, i.e. the percentage of the exited power (before coupled out of the QW-on-SOI waveguide) being detected by the photodetector.

As discussed in section 9.1.1, we can vary P_{in} and L to deduce the two unknown parameters P_{Hsat} and α_{H0} based on curve fitting technique. However, in order to use Eqn. (9.4) to fit the experimental data, we need to first know the values of α_p and c_1, c_2.

Section 9.1.3.1 will present the Fabry-Perot measurement of the propagation loss coefficient α_p of QW-on-SOI waveguide, from which c_1 and c_2 can be determined. After that, the transmission response of QW-on-SOI waveguides with varied input intensity is obtained. With the substitution of α_p, the theoretical calculation is fitted to the experimental results to get the saturation intensity value I_{Hsat} and the small-signal absorption coefficient α_{H0}.

9.1.3.1 Measurement of propagation loss coefficient and coupling coefficients

i. Introduction to Fabry-Perot technique

The propagation loss coefficient α_p of the QW-on-SOI waveguide is measured using the Fabry-Perot technique at a wavelength below the bandgap energy of the QW [67-68]. A brief introduction of FP technique will be presented here first.

Due to the presence of two reflective end facets of the waveguide, the light entering the waveguide experiences multiple reflections and thus exhibits self-

interference effect along the waveguide. The total transmission of the light can be derived analytically, which is given by

$$T_{FP} = C_{fw}\frac{\left(1-R_f\right)^2 A_t}{1+{R_f}^2{A_t}^2-2R_f A_t\cos(2\varphi)} \tag{9.5}$$

where C_{fw} represents the free-space-to-waveguide coupling coefficient, including the input and output coupling efficiencies. R_f is end-facet reflectivity of the waveguide. Due to the adoption of mode filtering structure along our waveguide (Fig. 9.1d), only the fundamental mode will propagate through and play roles in the FP response. Therefore, R_f measures the percentage of the incident fundamental-mode light reflected back to the fundamental mode from the waveguide end facet. A_t is the single-pass optical power loss of the waveguide. φ represents the single-pass phase shift of light, which can vary with the wavelength of light.

For the FP-loss measurement, the light source in Fig. 9.2 is replaced by the Agilent 8164A tunable laser (TL) source and AOM is removed. During the measurement, the incident light wavelength is varied from 1580nm to 1581nm and simultaneously the transmitted light power is measured as the photocurrent of PD.

Due to the wavelength change, $\cos(2\varphi)$ oscillates between -1 to 1, resulting in the oscillation of the transmission between $T_{FP-max} = C_{fw}\frac{\left(1-R_f\right)^2 A_t}{\left(1-R_f A_t\right)^2}$ and $T_{FP-min} = C_{fw}\frac{\left(1-R_f\right)^2 A_t}{\left(1+R_f A_t\right)^2}$. Therefore, A_t can be deduced from the contrast of transmission spectrum, i.e. $\frac{T_{FP-max}}{T_{FP-min}} = \left(\frac{1+R_f A_t}{1-R_f A_t}\right)^2$, where $R_f = 0.39$, which can be either analytically or numerically calculated [70]. Assuming the output power of the TL and coupling efficiency C_{fw} are constant over the 1nm wavelength span, the transmission spectrum contrast $\frac{T_{FP-max}}{T_{FP-min}}$ is equal to the photocurrent spectrum contrast measured at

the output PD. In other words, the single-pass optical loss A_t of the waveguide can be determined from the output photocurrent spectral contrast.

It is important to note that, for the QW-integrated hybrid waveguide, A_t includes the single-pass propagation loss of the QW-on-SOI waveguide and the SOI passive waveguide, as well as the top-down coupling loss between the QW-on-SOI waveguide and the SOI passive waveguide. The subscript *t* stands for the total loss. The procedures to separate the different types of loss above will be presented next.

ii. Fabry-Perot measurement of α_p

We first performed the FP measurement for the passive SOI waveguide to determine the single-pass propagation loss of SOI waveguide. The SOI waveguide has the same structure as the QW-integrated hybrid waveguide in Fig. 9.1d, except that the QW-on-SOI waveguide segment with tapering structure is replaced by a straight 1μm-wdith SOI waveguide. We get the single-pass propagation loss of SOI waveguide $A_S = 0.52$, where the subscript *S* stands for the SOI.

Subsequently, single-pass propagation loss A_t for the hybrid waveguides are determined at different QW-on-SOI waveguides lengths *L* (from 10 μm to 120 μm). A_t divided by A_S gives the loss within the QW-on-SOI region, which is denoted as A_{QS} and the subscript QS stands for QW-on-SOI. We can see A_{QS} includes the top-down coupling loss and propagation loss along the QW-on-SOI waveguide, thus can be written as $A_{QS} = C_{td}e^{-\alpha_p L}$. The variable C_{td} stands for the top-down coupling coefficient between the SOI waveguide and QW-on-SOI waveguide.

At the end, as shown in Fig. 9.4, $\ln(A_{QS})$ is plotted against *L*, and the slope of the linear interpolation gives the value of α_p, which is equal to $0.019\,\mu m^{-1}$. Meanwhile, we also obtain the total top-down coupling coefficient $C_{td} = 0.81$.

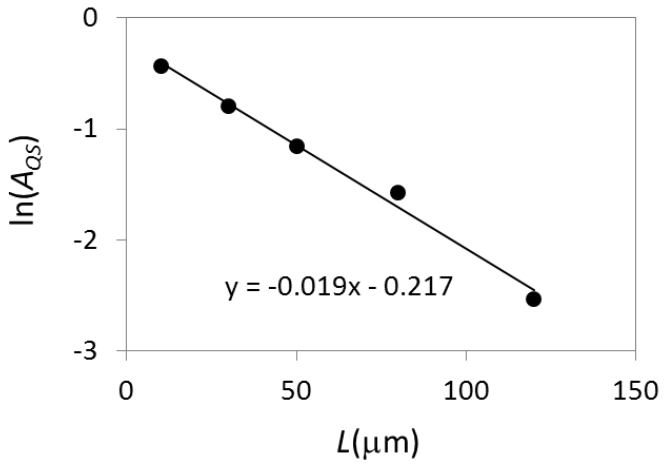

Figure 9.4: The experimentally determined $\ln(A_{QS})$ versus the QW-on-SOI waveguide length *L* (dots) and the linear interpolation (solid line) with the trend line's equation.

iii. Determination of c_1 and c_2

The variable c_1 and c_2 represent the total input and output coupling efficiencies, as defined in Eqn. (9.4). Thus we can write $c_1 c_2 \sim A_S C_{fw} C_{td}$, where A_S is the single-pass propagation loss of SOI waveguide, C_{fw} is the free-space coupling coefficient and C_{td} is the top down coupling coefficient. By measuring the transmission of the passive SOI waveguide at 1342nm, we have $A_S C_{fw} \sim 0.029$. With the substitution of C_{td} =0.81, we have $c_1 c_2 \sim 0.023$. Since the input and output coupling features in our set up are generally symmetric, we assume $c_2 \sim c_1$, which gives $c_1 = c_2 \sim 0.15$.

9.1.3.2 Transmission response of QW-on-SOI hybrid waveguide and curve fitting

With α_p, c_1 and c_2 determined, P_{Hsat} and α_{H0} are the only two unknown parameters in Eqn. (9.4), which can be experimentally deduced from the transmission response of the QW-integrated hybrid waveguide at varied length *L* and varied input

pump power P_{in}.

i. Measurement procedures

The transmission response measurement is carried out for the QW-on-SOI waveguides with $L = 10\,\mu m, 30\,\mu m$ and $50\mu m$. Using the measurement set up in Fig. 9.2, the input 1432nm beam is modulated at 2kHz repetition rate and 400ns pulse width. At each waveguide length L, the input optical power P_{in} is varied and measured before the first objective lens with an optical power meter. At each P_{in}, the transmitted optical power is detected by a PD, the photocurrent of which is measured by the Stanford Research System SR850 digital lock-in amplifier. Assuming the lock-in's reading is proportional to the average optical power detected at the PD, the proportionality is obtained based on a single measurement, which is subsequently used to convert the lock-in's reading to the optical power reading P_{out}.

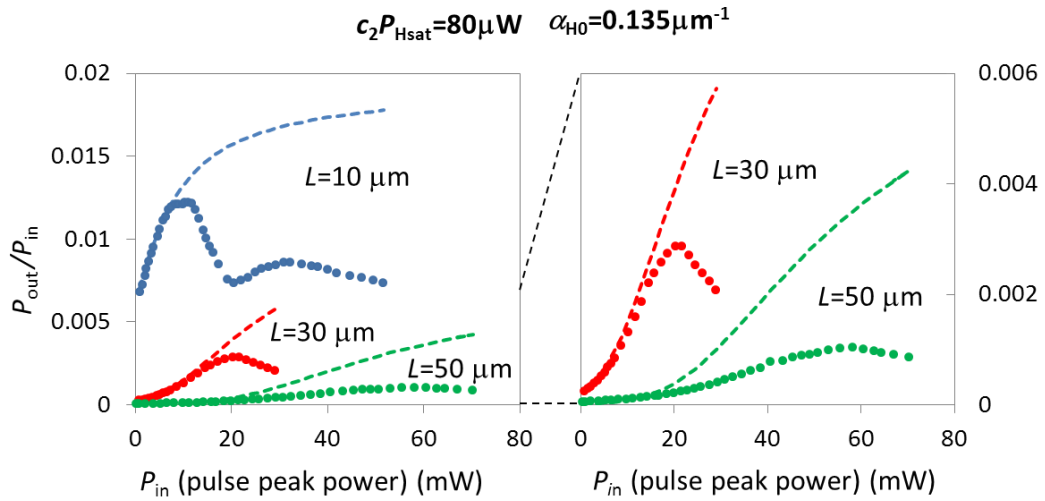

Figure 9.5: The transmission response of QW-on-SOI waveguide at length L=10μm (blue), 30 μm (red) and 50 μm (green) with respect to the peak pulse power of the pump supply beam at 1342nm. The input pulse at 1342nm is modulated at 2kHz repetition rate and 400ns pulse width. The dot plots correspond to the experimental measurement and the dash lines show the curve fitting using Eqn. (9.4).

The experimentally determined transmission response (P_{out}/P_{in} versus P_{in}) at different L is simultaneously fitted with Eqn. (9.4) using universal P_{Hsat} and α_{H0} values. The experimental data (dots) and best fitting curves (dash lines) are shown in Fig. 9.5, where the x axis shows the peak power of the input pump pulse. The blue, red and green plots correspond to the cases of $L = 10\,\mu m,\ 30\,\mu m$ and $50\mu m$ respectively.

ii. FP-assisted spontaneous emission amplification

One can see that, the transmission of the QW-integrated waveguide does not follow the saturation behavior expected, i.e. the transmission of the waveguide increases with the input optical power and gradually becomes constant when the input power is sufficiently high. Instead, with the increase of input optical power, the transmission of the waveguide increases at first, followed by a decrease. More importantly, the measurement results are repeatable, implying the transmission drop is not due to the thermal damage of the waveguide. Furthermore, we vary the pump pulse width from 100ns to 5μs without changing the pulse repetition rate, and find this increase-followed-by-decrease trend is consistently observed, which therefore excludes the possibility of local carrier heating. We then checked the transmitted spectrum of $L = 50\mu m$ QW-on-SOI waveguide, which is shown in Fig. 9.6. A strong amplification at 1537nm is observed as the input pump power increases. This phenomenon suggests at the high pumping strength, the spontaneously emitted light could sees high enough gain to compensate the propagation loss and end-facet loss to achieve optical power amplification. As a consequence, the carrier depletion rate got enhanced around 1537nm, which thus increases the absorption seen by the pump beam and induces the transmission drop phenomenon.

iii. Curve fitting and data analysis

The enhanced carrier depletion due to the FP-assisted spontaneous emission amplification deviates in the saturation behavior from our analytical model at high input power. Thus, the curve fitting in Fig. 9.5 aims at achieving theoretical-experimental matching at low input power. For future measurement studies, antireflection coating is needed at the waveguide end facets to remove the FP effect. Based on the low-input-power fitting, we obtain $\alpha_{H0} = 0.135\mu m^{-1} \pm 0.005\mu m^{-1}$ and $P_{Hsat} = 0.53mW \mp 0.03mW$.

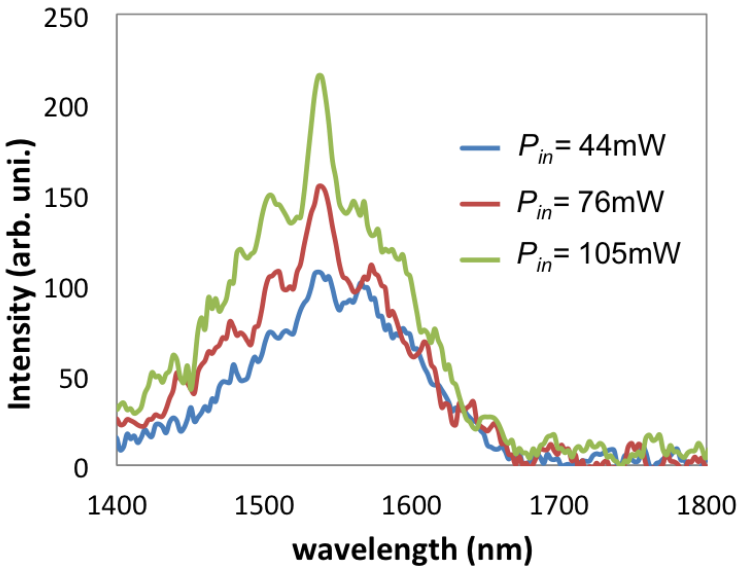

Figure 9.6: The transmitted spectrum of L=50μm QW-on-SOI waveguide with input pump pulse peak power at 44mW (blue), 76mW (red) and 105mW (green). The input pulse at 1342nm is modulated at 2kHz repetition rate and 400ns pulse width.

Next, mode simulation by COMSOL is carried out to analyze the intensity profile of the optical mode in our QW-on-SOI waveguide (Fig. 9.1c), to subsequently find the relationship between P_{Hsat} and I_{Hsat}. Let the refractive index of QW be 3.45, n(Si)=3.5 and n(SiO_2)=1.45. Let us denote the simulated mode power as P_{sim} and the

simulated mode intensity within the QW layer region as I_{sim}, we have $\frac{I_{sim}}{P_{sim}} = \frac{I_{Hsat}}{P_{Hsat}}$. As a result, it gives $I_{Hsat} \sim 65kW/cm^2 \pm 5kW/cm^2$, which is about 2.5 times of the theoretically calculated value for QW InGaAsP, i.e. $\sim 25.5kW/cm^2$ (Fig. 6.3). Furthermore, the mode simulation shows the optical power confinement in InGaAsP well layers is 10%, thus the material α_{H0} of well InGaAsP is $\sim 1.35\mu m^{-1} \pm 0.05\mu m^{-1}$, which is close to the other reported values [71-72].

9.1.4 More concerns with the actual EUPT device design

Based on the I_{Hsat} and α_{H0} values we obtained, several new concerns with the actual EUPT device design are highlighted here.

First of all, according to the previous studies in section 4.3.1, to pump our QW-on-SOI waveguide to 95% transparency state, it requires the incident pump power to be higher than $20\alpha_{H0}LP_{Hsat}$, which is equal to $10.6\alpha_{H0}L(mW)$ with $P_{Hsat} = 0.53mW$. That means if we want $\alpha_{H0}L = 22$ to promise switching gain>1, up to 230mW pump power is required, which is impractically high. To reduce the pump power requirement, we need to further optimize the waveguide design to enhance the mode intensity in the quantum well region, e.g. center the mode peak at the QW layers and reduce the mode size. In that case, if we want to reduce the pump power requirement to a practical value, say 10mW, the mode size needs to be reduced to $0.035\mu m^2$, which is equivalent to the mode size of 1550nm light in a 300nm x 300nm SOI waveguide. If we continue to use QW as the active medium, only the T-structure QW-on-SOI waveguide can give desired optical confinement. If so, we need to come out with a new fabrication process to eliminate the EBL misalignment issue as we highlighted in section 7.2.3.

Secondly, the small-signal absorption coefficient of our QW-on-SOI waveguide is ~0.135μm^{-1}. If we consider the $\alpha_{H0}L > 22$ criteria to achieve switching gain>1 with 2-WG EUPT, it would require $L_{C2} > 163\mu m$. As shown in Fig. 7.17, the effective modal refractive index change Δn_{eff} upon 10nm fabrication error in the QW-on-SOI waveguide width is around 0.02. At the pump wavelength 1342nm, the corresponding $\Delta\beta L_{C0}$ with $L_{C0} = 163\mu m$ is as high as 15.4, which will reduce the coupling efficiency to only 4%. Therefore, the self-aligned QW-on-SOI architecture is too sensitive to the fabrication error for practical implementation of 2-WG EUPT. It is necessary to increase the optical mode overlapping with the QW region to increase the small-signal absorption coefficient α_{H0} of the waveguide, and to subsequently reduce the required device length. Let's assume we can increase α_{H0} by 5 times, the required L_{C2} can be correspondingly reduced by 5 times and the fabrication error induced $\Delta\beta L_{C0}$ becomes ~3, giving a coupling efficiency ~50%. The situation will become more controllable. However, for our case, increasing α_{H0} by 5 times means increasing the modal confinement in the InGaAsP well layers to 50%, which is practically difficult to realize, since the occupation of well layers in entire MQW structure is only 5.5nm/(5.5nm+ 8nm)=40%. Therefore, the quantum well design has to be further optimized in the following two aspects: 1) increasing the gain of the QW to reduce the $\alpha_{H0}L$ requirement, 2) minimizing the barrier size without affecting the quantum confinement performance to increase the mode overlapping with the well layers thus to increase α_{H0}.

As for the 3-WG EUPT, which allows operation in the presence of index mismatch, it is still not practical to have very high $\Delta\beta L_{C0}$ value, as we discussed in section 8.3.1. Given $\Delta\beta L_{C0} < 8$ as a comfortable regime for 3-WG EUPT operation, and with $\Delta n_{eff} = 0.02$ as the fabrication error induced index mismatch, it requires

$L_{C0} < 85\mu m$. In other words, it is practical to design a 3-WG EUPT with L_{C0} less than $85\mu m$, so that the fabrication error induced effective-model-refractive-index mismatch would not compromise the power consumption of the 3-WG EUPT significantly. Then we look at the index matching case, in which the device length L_{C3} is equal to $\sqrt{2}L_{C0} = 121\mu m$. With $\alpha_{H0} = 0.135\mu m^{-1}$, we have $\alpha_{H0}L_{C3}$~16, which could be marginal for achieving the switching gain. Hence for the 3-WG EUPT, we still need a larger α_{H0}.

9.2 All-optical Switching with Switching Gain in a Hybrid III-V/Silicon Single Nano-waveguide

9.2.1 Introduction

As we highlighted in the first chapter, all-optical switching devices are of substantial interests for increasing the speed and reducing the power consumption of optical communication network through eliminating the OEO (optical-electrical-optical) conversion. In particular, with intense interests in large-scale photonic integration on silicon platform, signal gain (switching gain) in the high-speed all-optical switching operation would be desired [1-4]. Switching gain describes the ability of using small signal beam power to switch a much larger beam power, which is an important device requirement to achieve cascadability and high fan-out for the switches.

Demonstrations to date of all-optical switching gain on chip have relied on

post-amplifications of the switched signal, e.g. semiconductor optical amplifier (SOA), which result in higher power overhead and undesired spontaneous emission noise. The only reported on-chip architecture that exhibits internal switching gain without the need for post-stage amplifier is based on a silicon dual ring-resonator structure [8]. It utilized the slow thermo-optic effect, giving nanosecond-scale speed and narrow operational bandwidth of < 0.1nm. Such dual-ring resonant structures are also highly sensitive to the fabrication error, which limits the implementation practicality.

In this section, we report the first experimental demonstration of a non-resonator-based all-optical switch that exhibits internal switching gain on a hybrid III-V/silicon nanophotonic integration platform. The architecture is simply the self-aligned QW-on-SOI hybrid waveguide that we used for the material parameter characterization in the last section. The single-waveguide switch operates based on a dual-wavelength pump-versus-control (PvC) beam switching scheme as we described in Chapter 4. In addition, it features broadband operation, small device footprint and low sensitivity to fabrication error, making itself a viable candidate for large-scale photonic circuit integration.

More importantly, the realization of all-optical switching gain in the single-waveguide switch experimentally proves the self-enhanced carrier-depletion-induced absorption effect. This effect is known as the basic physics that induces the switching gain in the photonic transistor operation, thus the key that differentiates our photonic transistor from the previous all-optical switching devices reported.

9.2.2 Working principle of pump-versus-control (PvC) beam switching

Here we first give a brief review on the dual-wavelength pump-versus-control

(PvC) beam switching scheme for the single-waveguide switch.

As illustrated in Fig. 4.1, the single-waveguide switch consists of a nano-waveguide structure with an optically-active semiconductor medium of length L. The switching operation involves a strong continuous wave (CW) pump beam at wavelength λ_H and a weak control pulse (input signal) at wavelength λ_L, where $\lambda_H < \lambda_L < \lambda_g$ and λ_g is the band gap wavelength of the active medium. Under the OFF-state, the CW pump beam with input intensity I_{H-in} is launched into the waveguide to pump the active region to transparency, leading to a high transmitted pump beam intensity I_{H-out}. Under the ON-state, the counter-propagating control beam (input signal) with pulse peak intensity I_{L-in} is launched into the waveguide device, which depletes the carriers and induces absorption seen by the pump beam. The carrier dynamics is illustrated in Fig. 2.1b. This effect leads to a rapid cut-off of the transmitted pump beam power, generating an inverted output signal. The amount of change (i.e downward transition $\Delta P_{H-out} = \Delta I_{H-out} A_{eff}$) in the transmitted pump power is viewed as the "output signal". The pulse height of the control beam power $\Delta P_{L-in} = I_{L-in} A_{eff}$ is viewed as the "input signal". The switching gain factor is defined as $G_{sw} = \frac{\Delta P_{H-out}}{\Delta P_{L-in}} = \frac{\Delta I_{H-out}}{I_{L-in}}$. $G_{sw} > 1$ represents the case of switching gain.

It is worthwhile to note that the control beam would be amplified as it propagates through the strongly pumped active waveguide. Correspondingly, the carrier-depletion-induced absorption change in the medium enhances for the pump beam as the control beam continues propagating through. Hence, a weak control beam (input signal) (i.e. $I_{L-in} << I_{H-in}$) can gain the optical energy from the pump beam and effectuate large induced absorption to the pump beam. This effect differentiates our PvC switching scheme from the well-known cross-gain switching scheme in the semiconductor optical amplifier.

Parametric study and numerical simulation of PvC switching have been presented in Chapter 4. Experimental demonstration of PvC switching operation will be presented next.

9.2.3 Experimental set up for PvC switching operation

The measurement set up for PvC switching operation is shown in Fig. 9.7, where the green and red arrows represent the optical paths of pump beam and control beam respectively, and the visible alignment beam is not shown explicitly.

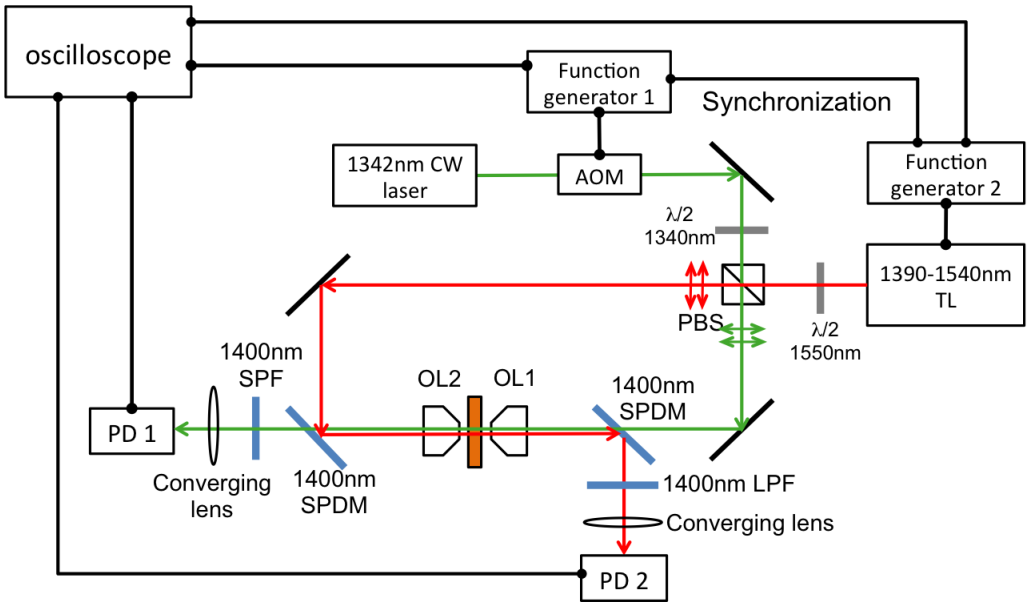

Figure 9.7: Measurement set up for dual-wavelength pump-control switching operation.

The pump beam is generated by a continuous wave (CW) solid state laser operating at a wavelength of 1342nm. It subsequently passes through an acousto-optic modulator, controlled by a function generator to choose 400ns single pulse with 5kHz. Then the pump pulse travels through a half-wave plate, followed by a polarization beam splitter, which is the same as the set up in Fig. 9.1. Two short-pass

dichroic mirrors (SPDM) at 1400nm are placed before the objective lens 1 (OL1) and after the objective lens 2 (OL2) to combine/separate the pump and control beams. 1342nm will transmit through the SPDM with little reflection. At the end, 1342nm pump beam is detected by a Thorlabs biased photodetector (PD1) with rising time ~10ns, before which is a converging lens to maximize the light detection and a short-pass filter (SPF) at 1400nm to remove any control light going into PD1.

The control pulse modulated at 200kHz with 400ns pulse width is generated by a Yenista tunable laser (TL) controlled by Tektronix function generator. The wavelength of light can be tuned from 1390nm to 1540nm. The control beam first transmits through a half-wave plate ($\lambda/2$ plate) at 1550nm and the polarization beam splitter (PBS), so that the amount of transmission can be varied by rotating the polarization of light without changing the optical alignment and the polarization entering the waveguide is kept at TE polarization. The control beam is subsequently guided to the second SPDM and reflected into the OL2, propagating in the opposite direction of the pump beam. The transmitted control beam through OL1 is then reflected by the other SPDM and towards another Thorlabs biased photodetector (PD2). PD1 and PD2 are of the same model. Same as the pump beam detection, a long pass filter (LPF) at 1400nm and a converging lens are placed in front of PD2 to remove any pump beam going into PD2 and maximize the detection of control beam.

At the end, PD1 and PD2 are connected to the Agilent digital storage oscilloscope through the 50Ω BNC cable to instantaneously monitor the transmitted pump pulse and control pulse.

9.2.4 Switching gain characterization

9.2.4.1 Switching gain versus control wavelength

The switching gain of pump-control switching is first examined in the L=30μm QW-on-SOI waveguide with control wavelength varying from 1520nm to 1540nm. The pump and control pulses are modulated at 5kHz and 200kHz respectively with the same pulse width at 400ns. The peak power of the input pump pulse is fixed at 180mW, and the control pulse peak power from TL varies around 9mW, depending on the emission wavelength. Note that, with input coupling efficiency c_1~0.15, the pump power coupled into the QW-on-SOI waveguide is $\sim 27mW$, which can only pump the waveguide to 90% transparency ($10\alpha_{H0}LP_{Hsat} = 21.5mW$).

At each control wavelength, the transmitted pump pulse is detected by PD1, and the photocurrent of which is measured by the oscilloscope. The pulse amplitude read at the oscilloscope is subsequently converted to the optical power by examining the responsivity of the photodetector. The average power of input control beam is directly measured using a power meter before OL2. Subsequently, the switching gain is determined using the following equation,

$$G_{sw} = \frac{\Delta P_{H-out}/c_2}{P_{L-in}c_1} = \frac{1}{c_1 c_2}\frac{\Delta P_{H-out}}{P_{L-in}} \tag{9.6}$$

where P_{H-out} is the peak power of transmitted pump pulse detected by PD1 and P_{L-in} is the peak power of the incident control pulse detected before OL2. c_1 and c_2 are the total input and output coupling coefficient, giving $c_1 c_2 = 0.023$ based on the previous measurement.

The switching gain versus the control wavelength is plotted in Fig. 9.8a. As we

see, the maximum switching gain is achieved at ~1537nm, which coincides with the peak of the transmitted spectrum of our QW-on-SOI waveguide in Fig. 9.6. The secondary peak at 1524nm could be due to the Fabry-Perot effect experienced by the pump. Exemplary switching with control wavelength at 1537nm is shown in Fig. 9.8b. The peak power of the control pulse is 8.4mW. The transmitted pump profiles detected at PD1 are shown in the upper set of plots. With the incidence of control pulse (green dash), the amplitude of the transmitted pump pulse is decreased. On the other hand, the transmitted control beam detected at PD2 (lower set of plots) is amplified with the presence of pumping (red dash).

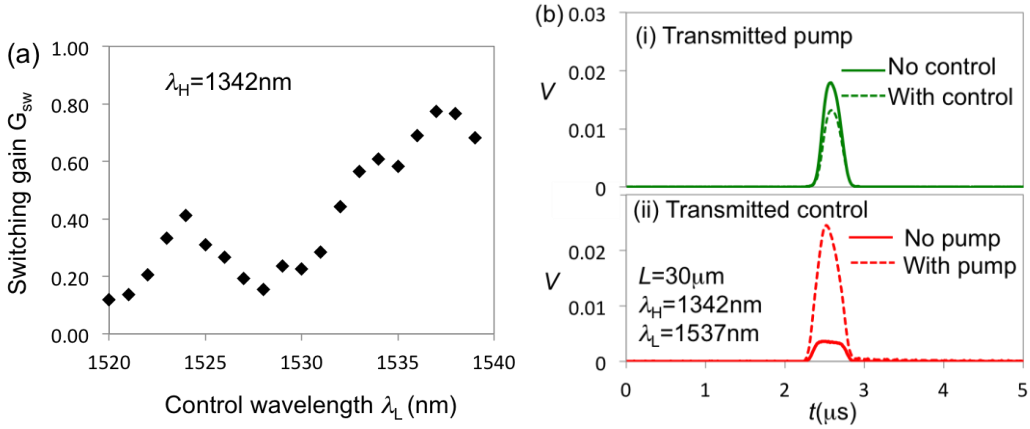

Figure 9.8: (a) Switching gain of L=30μm QW-on-SOI waveguide at different control wavelength. λ_H=1342nm. (b) Transmitted pump (upper set) with (red) and without (blue) the incidence of control pulse, and the transmitted control (lower set) with (red) and without (blue) the incidence of the pump. λ_L =1537nm.

9.2.4.2 Switching gain versus control power

Next, with fixed control wavelength at 1537nm, the switching gain is examined at varied incident control power. Fig. 9.8a shows the drop of the transmitted pump pulse peak power, i.e. ΔP_{H-out}, versus the incident control pulse peak power P_{L-in}. A quasi-linear increase of ΔP_{H-out} is observed, as P_{L-in} <4mW. When the input control power further increases, the transmission drop of the pump beam starts to saturate. The corresponding switching gain is calculated and plotted versus the control peak

power P_{L-in} in Fig. 9.8b, showing the maximum switching gain is achieved as the control power <4mW. Meanwhile, we noticed a small switching gain of ~1.2 is achieved with L=30μm QW-on-SOI waveguide.

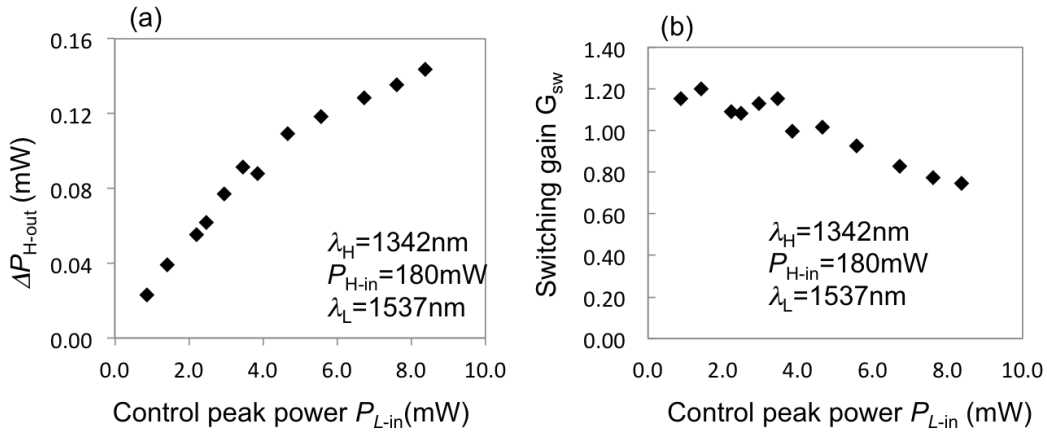

Figure 9.9: (a) the drop of transmitted pump pulse peak power and (b) the switching gain at varied input control pulse peak power.

9.2.4.3 Determination of g_{L0}/α_{H0}

We can also deduce the value of g_{L0}/α_{H0} from the PvC switching experiment based on the small-control measurement with $P_{L-in} = 0.875mW$. The length of QW-on-SOI waveguide is $L = 30\mu m$. The pump and control wavelengths are 1342nm and 1537nm. First of all, the amplification of the transmitted control pulse with the presence of 180mW 1342nm pump pulse is measured, which is equal to 9.1. Since the control pulse experiences material absorption when pump is not present, "9.1 times amplification" is not the actual gain it sees. Here we use $\alpha_{L0} \sim \sqrt{\lambda_L^{-1} - \lambda_g^{-1}}$ to estimate the absorption coefficient at the control wavelength α_{L0}, where $\lambda_g = 1.55\mu m$ is the band gap wavelength. It gives $\alpha_{L0} = \alpha_{H0}\sqrt{\lambda_L^{-1} - \lambda_g^{-1}} \Big/ \sqrt{\lambda_H^{-1} - \lambda_g^{-1}} = 0.032\mu m^{-1}$. As a result, the actual gain

coefficient seen by the control beam with the presence of optical pumping at 1342nm is g_{L0}~$0.04\mu m^{-1}$. Thus we have $\frac{g_{L0}}{\alpha_{H0}}$~0.3, which is as expected higher than the bulk InGaAsP semiconductor with $\frac{g_{L0}}{\alpha_{H0}}$~0.22.

9.2.4.4 Pump-control switching in longer QW-on-SOI waveguide

It is worthwhile to note that higher switching gain and lower operational power are possible by simply increasing the device length [29] and reducing the optical mode area (e.g. adopting the T-structure QW-on-SOI waveguide). However, the measurement carried out for $L = 50\mu m$ QW-on-SOI waveguide under the same pump beam condition and the optimized control beam condition gives a switching gain of 0.67. The failure of observing higher switching gain in the longer waveguide could be due to that 1) the longer waveguide requires higher incident pump power to excite the carriers. The input pump power is not high enough to provide equivalent transparency state as in the $L = 30\mu m$ case; 2) the FP-assisted spontaneous emission amplification effect as observed in Fig. 9.6 further suppresses the carrier excitation and thus the gain at the control wavelength. Therefore, future work should include 1) optimizing the tapering structure to increase the top-down coupling efficiency; 2) adopting anti-reflection coating to eliminate the FP resonance and suppress the spontaneous amplification effect.

9.3 2-WG EUPT 3-WG EUPT and MZI-EUPT Fabrication and Measurement

The 2-WG EUPT, 3-WG EUPT and MZI EUPT based on self-aligned QW-on-SOI integration are fabricated. The first batch of EUPT devices are designed to fulfill the $\alpha_{H0}L$ requirement for switching gain. Therefore, with $\alpha_{H0} = 0.135\mu m^{-1}$, the device lengths for 2-WG and 3-WG EUPT are generally longer than 200 μm and the active waveguide length in MZI-EUPT is chosen at 100μm. However, as we highlighted in section 9.1.4, the maximum pump supply power that can be delivered in our set up is not sufficient to pump up such long QW-on-SOI waveguides. Therefore, the desired OFF-state pumping characteristics in 2-WG, 3-WG and MZI-EUPT are not achieved.

In this section, the device design strategy, the varied device dimensions, and the SEM images of the three types of EUPT devices fabricated will be presented.

9.3.1 2-WG, 3-WG EUPT: design, fabrication and measurement

The general strategy of device design to achieve effective model refractive index matching in the 2-WG EUPT based on self-aligned QW-on-SOI structure has been presented in section 7.3.3. Among the 2-WG EUPT devices fabricated on the same sample chip, the self-aligned QW-on-SOI waveguide width is designed at a fixed value of 380nm, and the passive SOI waveguide width varies from 650nm to 900nm with an increment of 25nm to match the effective model index of the QW-on-

SOI waveguide. Introducing such wide range of width variation is to take into account of the QW-on-SOI waveguide width error in the fabrication process and the uncertainty of InGaAsP QW material refractive index. Furthermore, to meet the minimum $\alpha_{H0}L$ requirement for switching gain, without exacerbating the sensitivity of the coupler structure, the 2-WG EUPT device length is chosen around 200μm. Correspondingly, the gap size between the active and passive waveguide is fixed at 200nm in our design. The same strategy is adopted for the 3-WG EUPT testing sample design. The cross-sectional dimension of the designed 2-WG and 3-WG EUPT are shown in Fig. 9.10.

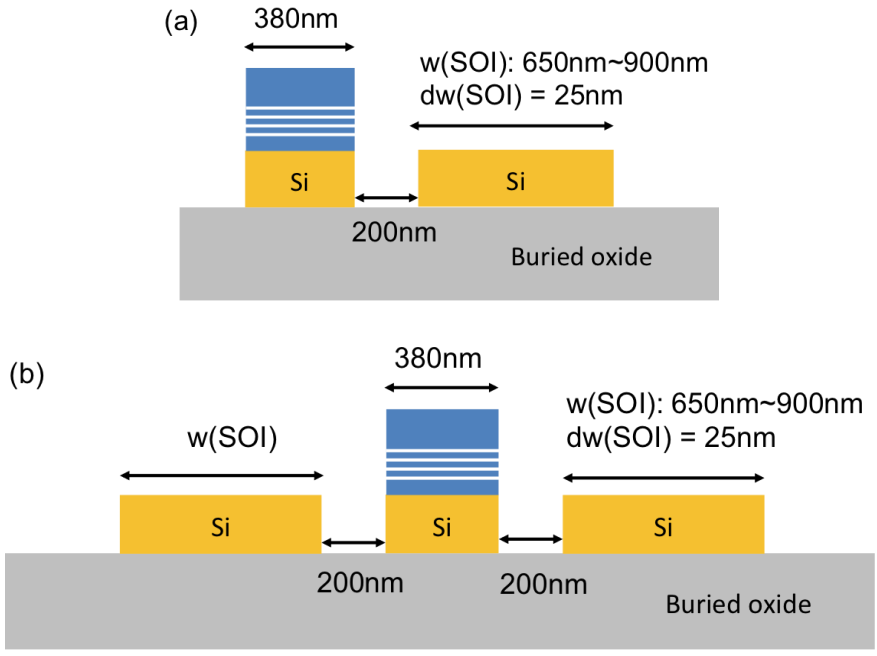

Figure 9.10: (a) 2-WG EUPT and (b) 3-WG EUTP design for effective model index matching test.

In addition to the SOI waveguide width variation, the device length variation is also required to match the actual coupling length. Consider the 2-WG EUPT first. Depending on the resultant QW-on-SOI waveguide width (370nm-390nm) and the

actual refractive index of QW (3.4-3.5), the complete coupling length in the index-matching condition varies in a wide range. Simulation shows, at 200nm gap size, the complete coupling length could be in the range of 150μm to 350μm. However, in practice, it is not necessary to introduce such wide variation of device length for each SOI waveguide width tested. We performed the model simulation for 2-WG EUPT under different parametric conditions of QW-on-SOI waveguide, as shown in Fig. 9.11a. At different QW-on-SOI width, i.e. $w(QW)$=370nm, 380nm and 390nm, the refractive index of QW is varied from 3.4 to 3.5, and the corresponding index-matched SOI waveguide width $w(SOI)$ and the complete coupling lengths L_{C2} are obtained. Subsequently, L_{C2} is plotted against $w(SOI)$ for each $w(QW)$. It is found L_{C2} is a function of $w(SOI)$ with little dependency on the QW-on-SOI waveguide width, as shown in Fig. 9.11b. In other words, regardless of how much error is introduced to the QW-on-SOI waveguide dimension, once the correct $w(SOI)$ is found, the device length is determined. Therefore, theoretically, we can assign one particular device length to each $w(SOI)$ tested. However, in real application, we still need to introduce device length variation in our design, since the coupling length may change due to deviation of gap size during the fabrication. Here we let the 2-WG EUPT device length vary by +/-50% around the L_{C2} value in Fig. 9.11b at the corresponding $w(SOI)$. On the other hand, since the complete coupling length of 3-WG directional coupler at index-matching condition is equal to $\sqrt{2}$ of 2-WG complete coupling length, the device length variation range for each $w(SOI)$ tested in 3-WG EUPT is set to be $\sqrt{2}$ of that for the corresponding 2-WG EUPT.

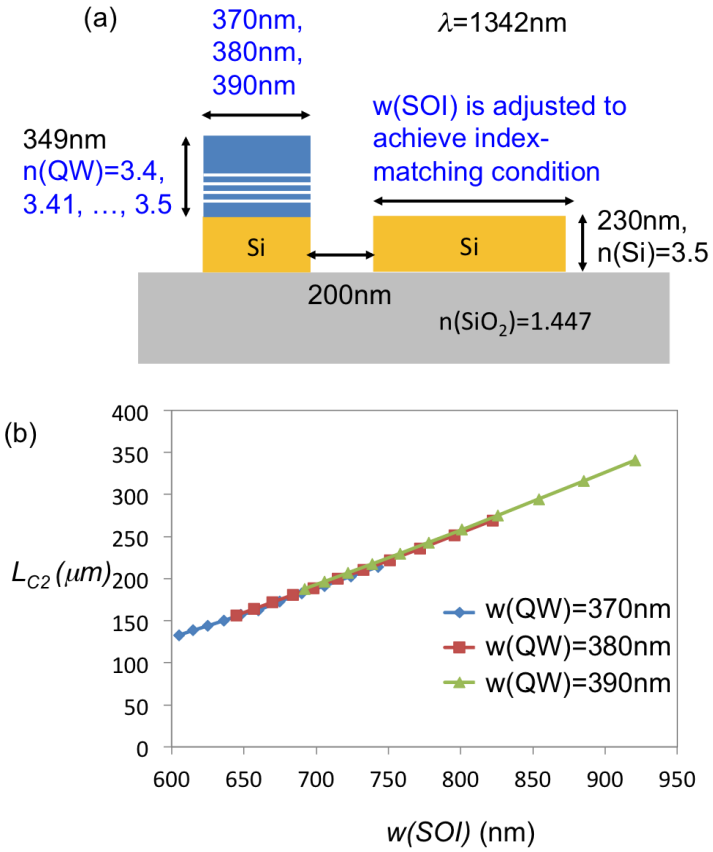

Figure 9.11: (a) Parametric variation for mode simulation in 2-WG EUPT. (b) Complete coupling length L_{C2} versus the corresponding index-matched SOI waveguide width at different QW-on-SOI width.

Fig. 9.12a and Fig. 9.12c show the SEM image of the SIG-IN and SIG-OUT ports of the 2-WG EUPT and 3-WG EUPT fabricated. The propagation directions of the signal and pump beams are indicated by the red and yellow arrows respectively. Fig. 9.12b and Fig. 9.12d show the coupler region of the 2-WG and 3-WG EUPT with the passive SOI waveguides and active QW-on-SOI waveguide lying in proximity. The optical pumping measurement is carried out on the free-space coupling station in Fig. 9.7. The pump beam at 1342nm is modulated to generate 400ns pulses at 5kHz repetition rate and the input pump pulse peak power is set at the maximum value of 180mW. The pump beam is launched into the passive waveguide, and the transmitted light spots from the passive and active waveguides are monitored

using an infrared IR camera. Unfortunately, we did not observe successful coupling in any of the 2-WG EUPTs or 3-WG EUPTs fabricated. Most of light exists from the passive waveguide.

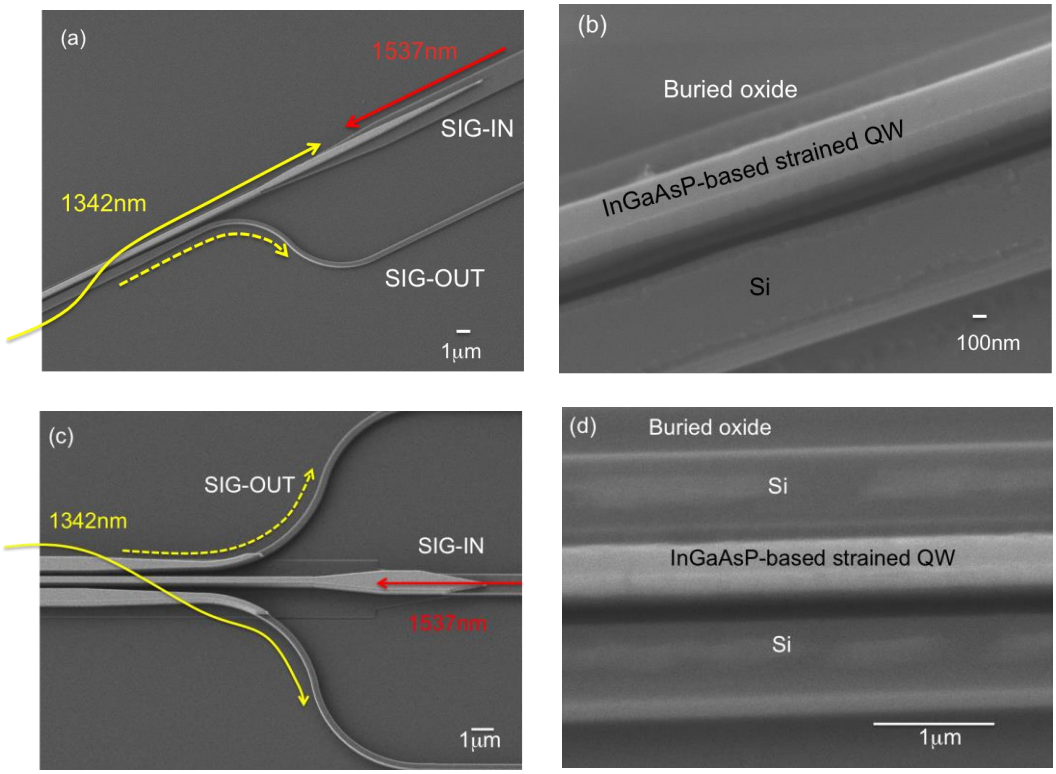

Figure 9.12: (a) SEM images of 2-WG EUPT fabricated with the SIG-IN and SIG-OUT ports and the propagation directions of pump supply and signal beams (b) the coupler region of 2-WG EUPT with the QW-on-SOI waveguide and SOI waveguide lying in proximity. (c) SEM image of 3-WG EUPT fabricated with the SIG-IN and SIG-OUT ports and the propagation directions of pump supply and signal beams. The QW on passive waveguides hasn't been removed. (d) the coupler region of 3-WG EUPT with the QW-on-SOI waveguide and SOI waveguide lying in proximity.

The failure of demonstrating the significant coupling phenomenon should be due to the lack of sufficient pump power for such long device structure, as we highlighted in the single-waveguide PvC switching experiment. If the active waveguide cannot be pumped into transparency state, the large absorption coefficient of it seen by the pump beam will prevent the efficient optical coupling, even in the

index-matching condition. In the future work, efforts should be devoted into further increasing the pump power coupled into the EUPT devices, e.g. increasing the free-space-to-waveguide coupling efficiency and the top-down coupling efficiency at the QW tapering structure, adopting the more proper AOM for the higher beam deflection efficiency.

9.3.2 MZI-EUPT: design, fabrication and measurement

Effective-model-refractive-index-matching constraint between SOI and QWI-on-SOI waveguide is avoided in the MZI-based EUPT. However, additional passive interferometric structures are required for optical beam splitting and combining. Theoretical demonstration of MZI-EUPT in section 8.2 utilized two 3-dB directional couplers. Alternatively, we can also adopt two 50/50 Multimode interferometers (MMI) to achieve the same effect with the smaller footprint size.

3D Lumerical FDTD simulation is performed to design the MMI structure, the optimized design is shown in Fig. 9.13. Fig. 9.14a shows the simulation structure with two 50/50 MMI joint together. The input light is launched from one port of the MMI. The dimensions of the constituent MMI is shown in Fig. 9.14b, where the refractive indices of the MMI and cladding medium are 3.5 and 1.5 respectively, and the wavelength of incident light is 1342nm. The resultant beam propagation characteristics is shown in Fig. 9.14c. We can see the input light equally splits to two paths at the first MMI, which are then combined and transmits out of one port.

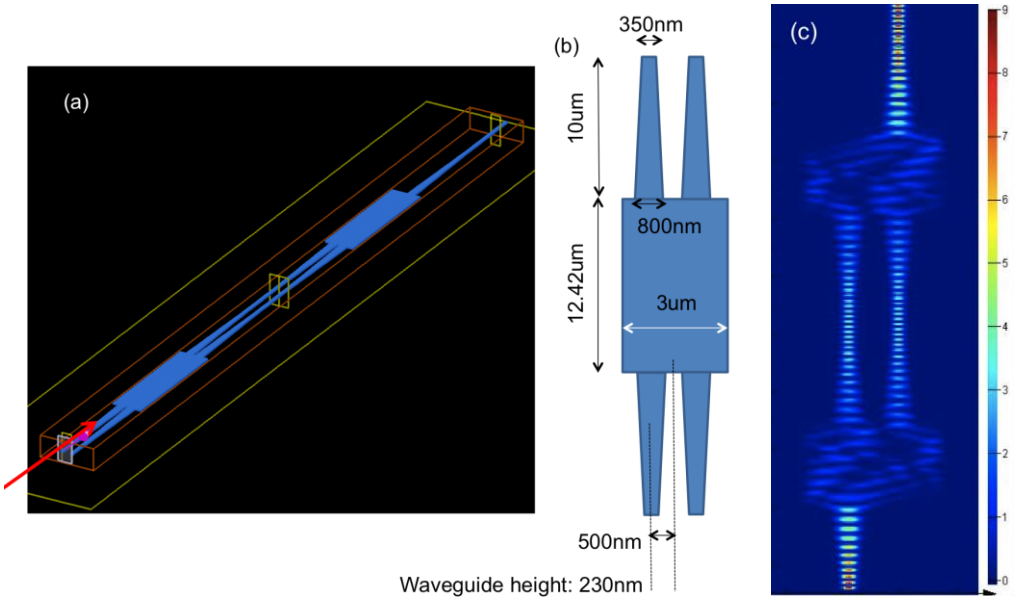

Figure 9.13: 50/50 MMI design for MZI EUPT application. (a) Lumerical FDTD simulation structure with two MMI joint together. The 1342nm light is launched from one port of the first MMI (b) dimension of the constituent MMI. Refractive indices of MMI and cladding are 3.5 and 1.5 respectively. (c) beam propagation simulated by FDTD.

The designed MMI is fabricated on the SOI substrate with 230nm thick Si and the measurement shows 50/50 power splitting can be achieved. However, the transmission characteristics as simulated in Fig. 9.13b are not observed in the joint MMI structure. This is because the beam-combining effect at the second MMI is sensitive to the relative phase difference between the two incoming beams. Fabrication error may induce slight difference in the waveguide widths between the two waveguides connecting the MMIs, which deviates the phase difference between the two optical paths. Thus for future MZI EUPT device design, additional phased tuning mechanism, e.g. thermal tuning mechanism, is required along at least one active arm to adjust the relative phase of light to optimize the interference performance at the output MMI.

MMI-based MZI-EUPT devices with 100μm-length QW-on-SOI waveguide are fabricated for testing. Since additional fabrication steps are required and the

fabrication process flow needs to be re-developed, the phased tuning component is not introduced in these devices. Fig. 9.14a shows the input part of the MMI-based MZI structure fabricated. The output part of MZI EUPT is shown in Fig. 9.14b, where the input signal beam is coupled into the active arm through a passive symmetric directional coupler. The same directional coupler is used to couple the pump supply beam to the output port of the device. Since the longer wavelength experiences the shorter coupling length, the signal beam will propagates over more than one coupling length and will be coupled back to the incident waveguide (the active arm), while the pump supply beam will experience significant power transfer to the output waveguide. The same design is included at the other arm to make the structure symmetric. At the output of MZI EUPT is another identical MMI to combine two beams.

Launching the 1342nm 400ns pulsed pump beam at the maximum power into these MZI-EUPT, we did not observe any output light from the device. It could be due to that the pump power is not sufficiently high to pump through the whole device or the series of interferometric structures along the MZI-EUPT device are not optimized. The future work for MZI-EUPT device development should start with the purely passive configuration to optimize the interferometric structures first.

As we can see, despite of eliminating the difficult index-matching constraint between QW-on-SOI and SOI waveguides, the MZI-EUPT involves multiple interferometric structures and requires additional phase tuning mechanism. It not only increases the total device footprint, but also increases the fabrication challenges, which therefore limits its feasibility for large-scale device integration.

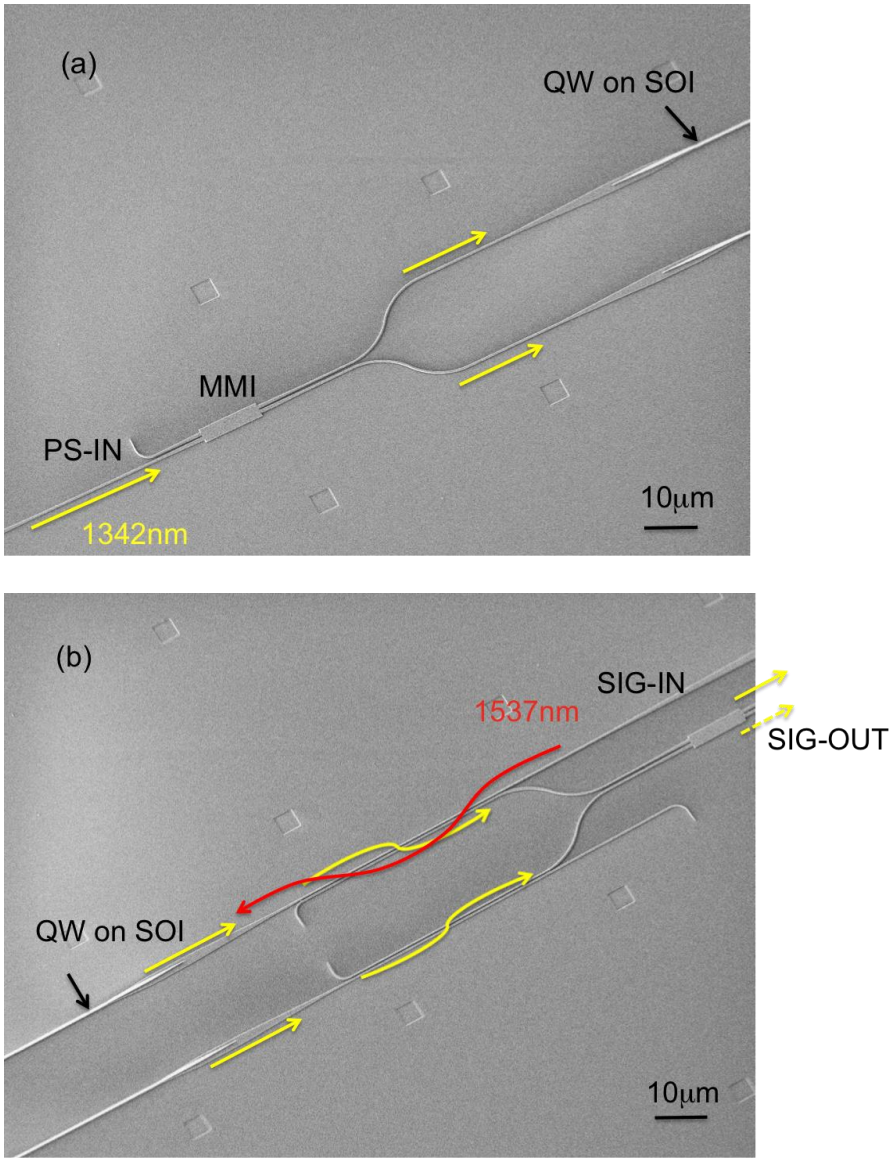

Figure 9.14: SEM images of MZI EUPT fabricated (a) the PS-IN port with 50/50 MMI for pump supply splitting (b) the SIG-IN and SIG-OUT ports with symmetric directional coupler for signal input and pump output.

9.4 Conclusion

In this chapter, the saturation intensity and small-signal absorption measurements is carried out for our self-aligned QW-on-SOI waveguide, which gives $I_{Hsat} = 65kW/cm^2$ and $\alpha_{H0} = 0.135\mu m^{-1}$. Pump-control switching with switching gain of 1.2 is demonstrated in a $30\mu m$-length QW-on-SOI waveguide, from which

we also deduced $\frac{g_{L0}}{\alpha_{H0}} = 0.3$.

The measurement results highlighted several new device design aspects that need to be taken into consideration in the future, including 1) the waveguide mode size should be further reduced to increase the power efficiency; 2) the quantum well layer design needs further optimization to increase the optical mode overlapping thus to increase the small-signal absorption coefficient of the waveguide, which can consequently reduces the device size and the device tolerance to the fabrication error; 3) anti-reflection has to be included to prevent the spontaneous emission amplification that causes the strong self-depletion of carriers and the gain reduction.

CHAPTER X DISCUSSION AND FUTURE PLAN

10.1 Summary of Achievements

The main achievements of the thesis can be summarized as follows:

Firstly, we report a novel analytical approach for analyzing the performance of EUPT systematically. An analytical formulation for the absorption and gain coefficients seen by two monochromatic waves at different wavelengths interacting with a semiconductor medium is developed for the first time, based on which the optical field propagation and light-matter interaction in a semiconductor medium can be self-consistently dealt with without the need of iterative calculation or numerical computation. The switching gain, switching speed and switching energy are subsequently formulated analytically, from which important device design aspects are highlighted. It shows $\frac{g_{L0}}{\alpha_{H0}}$, $\frac{I_{Lsat}}{I_{Hsat}}$, I_{Hsat} and $\alpha_{H0}L$ are the four key parameters that effectively determine the switching gain of 2-WG EUPT. Increasing $\frac{g_{L0}}{\alpha_{H0}}$, $\alpha_{H0}L$ and I_{Hsat}, or effectively reducing $\frac{I_{Lsat}}{I_{Hsat}}$ will lead to the higher switching gain. On the other hand, increasing $\alpha_{H0}LI_{Hsat}$ will compromise the power efficiency of EUPT in the way that more pump power is required to pump the active waveguide to transparency. With the employment of the InGaAsP's energy band parameters, we obtained the minimum $\alpha_{H0}L$ values for achieving switching gain in the bulk-InGaAsP-based EUPT and QW-InGaAsP-based EUPT, which are equal to 30 and 22 respectively, and the minimum energy consumption is ~250fJ/bit. The resultant Figure of Merit is one order worse than the FOM obtained from the 4-level 2-electron FDTD simulation presented with the initial proposal of PT. Furthermore, numerical simulation via a MLME-FDTD program, which is capable of addressing complex carrier dynamics in

the realistic semiconductor band structure, is adopted to verify our analytical calculation. At the end, 20Gbps switching operation with switching gain of ~2 and switching energy of 0.4pJ/bit is demonstrated with MLME-FDTD simulation in a bulk-InGaAsP-based EUPT.

Secondly, a new architecture based on a three-waveguide (3-WG) directional coupler is proposed to achieve the switching merits of a 2-WG EUPT without stringent effective modal index matching requirement between the coupled waveguides. The symmetric nature of the structure promises efficient coupling, thus high extinction ratio switching, despite index mismatch between the active and passive waveguides. The absorption manipulation-based switching performance is not compromised by the presence of index mismatch and thus enhances the device tolerance to fabrication errors. Meanwhile, an alternative device architecture to alleviate the index matching constraint is proposed, which is based on the symmetric Mach Zehnder Interferometer consisting of two identical active arms. Amplitude modulation induced by absorption change in one of the arm is utilized for the switching operation. Without the direct coupling between the passive and active waveguides, the fabrication challenge is greatly reduced. Our analytical method provides a systematic comparison between the original 2-WG EUPT and our new EUPT architectures. The calculation results show 3-WG EUPT is generally slower but has higher switching gain than 2-WG EUPT under the same operational conditions. The switching gain of MZI EUPT ranks between the 3-WG EUPT and 2-WG EUPT when they have the same $\alpha_{H0}L$, but the switching speed of MZI EUPT is slower than 2-WG EUPT since the incident pump power splits into half before it pumps the active arms. The Figure of Merit for 3-WG EUPT is shown higher than the 2-WG EUPT and the MZI EUPT with the same $\alpha_{H0}L$. Increasing the index

mismatching factor $\Delta\beta L_{L0}$ in 3-WG EUPT can further improve the FOM due to the increase of switching gain. However, the pump supply power coupled into the central waveguide decreases with the increase of $\Delta\beta L_{L0}$, which poses the higher pump power requirement for achieving the transparency state at the switch-off state. Thus $\Delta\beta L_{L0} < 8$ is suggested for high-performance operation with 3-WG EUPT.

Thirdly, different fabrication approaches are proposed for the realization of EUPT, including quantum-well-intermixing (QWI) approach on InP-based substrate, and III-V-on-silicon integration approach assisted by direct wafer bonding technique. For the QWI approach, a diffusion-stop gap technique is proposed to achieve sub-micron spatial resolution of local band gap shift induced by ion-implantation assisted quantum well intermixing. With adoption of BCB bonding technique, thin-film QW nano-waveguide with high index contrast is realized. For the III-V-on-silicon approach, two different QW-on-SOI waveguide architectures, i.e. T-structure and self-aligned structure, are proposed for the active waveguide in EUPT. The corresponding fabrication procedures and individual process steps are developed. Since the EBL alignment error will cause sever repeatability issue with the T-structure EUPT, self-aligned QW-on-SOI architecture is adopted for the EUPT realization. Single-waveguide switch, 2-WG EUPT, 3-WG EUPT and MZI EUPT are successfully fabricated based on the QW-on-SOI integration approach.

Lastly, the optical measurement station for the waveguide-based dual-wavelength switching operation is designed and constructed based on the free-space coupling scheme. The saturation intensity and small-signal absorption for our self-aligned QW-on-SOI waveguide are experimentally determined, giving $I_{Hsat} = 65kW/cm^2$ and $\alpha_{H0} = 0.135\mu m^{-1}$. Pump-control switching with switching gain of 1.2 is demonstrated in a $30\mu m$-length QW-on-SOI waveguide, from which we also

deduced $\frac{g_{L0}}{\alpha_{H0}} = 0.3$. Furthermore, spontaneous emission amplification is observed in the strongly pumped active waveguide due to the Fabry-Perot resonance formed by the waveguide end facets, which induces significant carrier depletion, thus increased absorption seen by the pump beam and reduced gain seen by the control beam. As a result, the switching gain performance is greatly compromised. To alleviate the spontaneous emission amplification effect in the actual device application or the integrated photonic circuit, novel anti-reflection design is proposed for the EUPT operation.

Apart from photonic transistor studies, there are some other theoretical and experimental works on the optical nano-waveguides having been carried out, which were not presented in this dissertation.

First of all, we derived an exact analytical solution for the facet reflection of a strongly-guided wave propagating in a planar waveguide with high-refractive-index contrast between the waveguide core and cladding layers. Facet reflections at the waveguide-air interface for strongly-guiding waveguides with sub-wavelength scale dimensions do not follow the usual Snell's law. Significant amount of reflected power can be channeled into higher order modes as well as radiation modes. Our work shows for the first time how the exact analytical solution of the facet reflection can be obtained by using a new technique based on Fourier analysis and perturbative series summation without the need for approximation or iteration. The proposed analysis enables the distribution of power reflected into various guided and radiation modes to be readily computed. Through this technique, a spectral overlapping criterion and a coupling matrix are derived that analyze effectively the power distribution among all the strongly and weakly-coupled radiation modes in an end-facet reflection. Accurate pre-determination of the number of radiation modes for

efficient computation without compromising resultant accuracy is achieved. More importantly, the anomalous wave reflection behaviors at the facet of a strongly-guiding waveguide are presented. These include anomalous high radiation modes coupling as a function of cladding refractive index not reported before [70].

Secondly, we reported the first realization of sub-200 nm wide AlN-GaN-AlN (AGA) ridge waveguide with height-to-width ratio of ~6:1, fabricated via inductively-coupled plasma (ICP) etching with Cl_2/Ar gas chemistry. RIE power and ICP power were varied in the ranges of 100 W-450 W and 200 W-600 W respectively. An optimized RIE power and ICP power at 100 W and 400 W respectively, reduced the density of nano-rods formed in the etched trenches. Further optimization of the gas flow rate of Cl_2/Ar to 40 sccm/10 sccm improved the slope of the etched waveguide. In addition, we also developed a simple and novel dice-and-cleave technique to achieve cleaved end facet of AGA waveguide [73]. The same technique is utilized to cleave the thick SOI substrate of our EUPT device.

10.2 Future Works

The main works to be carried out in the future include:

First of all, the anti-reflection coating will be applied to the new batch of single-waveguide switch and 2-WG EUPT to repeat the saturation intensity measurement, single-waveguide PvC switching measurement and the index-matching test for the 2-WG EUPT.

After that, the integrated anti-reflection structure will be tested. In an actual photonic integration circuit, un-desired back-reflection of light can exist everywhere, which may compromise the active photonic device performance significantly. Integrated anti-reflection structure is thus necessary to prevent the back-reflected

light from entering the active devices. An exemplary design for 2-WG EUPT is shown in Fig. 10.1. The pump supply beam is coupled into the EUPT through a narrow-band ring resonator at the pump wavelength. This can prevent the spontaneous emitted light and the transmitted input signal entering the photonic circuit. Secondly, to prevent the back reflection of pump supply beam, we may place an absorptive ring resonator with the resonance wavelength at the pump supply wavelength at the SIG-IN port. The transmitted pump beam sees effective coupling thus will be absorbed by the ring, while the input signal sees little coupling and will be propagating into the EUPT. Lastly, at the terminations of the two non-functional ports, we put a small-radius bending structure joint to an absorptive sharp tapering structure to effectively scatter and absorb the light propagating towards there.

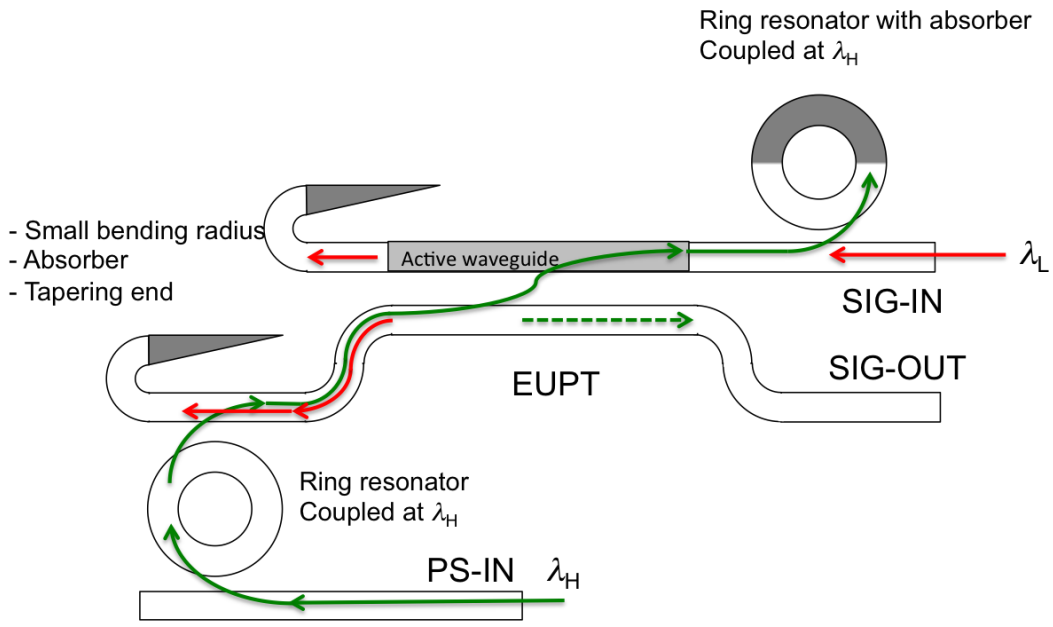

Figure 10.1: EUPT design with anti-reflection structures.

Furthermore, measure the dynamic response of the single-waveguide switch,

and eventually demonstrate the switching operation in 2-WG EUPT or 3-WG EUPT. The quantum well wafer design will be further optimized to increase the mode-overlapping factor with the well layers to increase the small signal absorption coefficient of the QW-on-SOI waveguide. The waveguide design and fabrication process need the further optimization as well to enhance the optical confinement and mode intensity in the QW region and reduce the device tolerance to the fabrication error.

For the theoretical work, we may evaluate the potential application of quantum dots in our EUPT, since studies have shown that this class of material could have substantially low saturation intensity and ultrafast carrier transition response. The co-directional pumping rate of waveguide also requires further verification and studies, since it plays the key role in determining the energy consumption per bit of our photonic transistor. Systematic analysis for the GMOI-based EDPT will be carried out in the future.

APPENDIX:

The fabrication process and process parameters for self-aligned QW-on-SOI based EUPT are tabulated as follows.

	Steps	sample	equipment model	parameters
1	Cleaning	SOI	-	1. Acetone + ultrasnoic for 5min 2. IPA + ultrasnic for 5min 3. DI water + ultrasonic for 5min
2	PECVD deposition of 280nm SiO_2	SOI	PECVD System, Nextral ND200 (Unaxis)	H_2: 184sccm N_2O: 400sccm Pressure: 729mTorr Temperature: 279.2ºC RF: 100W DC: 44.2V Time 150s
3	Spin coating of 300nm PMMA950_5A and E-spacer	SOI	Spin coater	1. Spin coat PMMA950_5A at 3000rpm for 90s 2. Baked on hot plate at 170 ºC for 15min 3. Spin coat E-spacer at 2000rpm for 90s 4. Baked on hot plate at 95 ºC for 1min
4	EBL patterning of alignment marker and de-gassing channel	SOI	Electron Beam Lithography System (Elionix 100 kV)	Current: 1nA Dosage: 1100μC/cm^2 Dot map: 600μm, 60000 dot
5	Develop EBL pattern	SOI	-	1. DI water rinse for 5s and N_2 blow 2. Immersion in MIBK:IPA (1:3) for 70s 3. IPA rinse for 5s and N_2 blow dry
6	RIE etching of SiO_2	SOI	RIE Etcher, Plasmalab 80plus (Oxford)	CHF_3: 45sccm Ar: 15sccm Pressure: 50mTorr RF: 150W DC: 353V time: 15min
7	Remove PMMA	SOI	RIE Etcher, SIRUS (Trion)	1. O_2 plasma etching: - O_2: 10sccm - Pressure: 250mTorr - RF:100W 2. Acetone + ultrasnoic for 5min 3. IPA + ultrasnoic for 3min 4. DI water + ultrasnoic for 3min
8	ICP etching of Si	SOI	ICP System, Shuttle Lock Reactor SLR-7701-8R (Unaxis)	HBr: 48sccm Cl_2: 40sccm ICP: 400W RIE: 80W Pressure: 10mTorr Temperature: 20 ºC Time: 119s

9	Direct wafer bonding of QW on SOI	SOI, strained QW	Table 7.1, Step 3-13	
10	Spin coating of 200nm HSQ	QW on SOI	spin coater and hot plate	1. Baked on hot plate at 120 ºC for 10min for dehydration 2. Spin coat HSQ006 at 3000rpm for 90s 3. Baked on hot plate at 120 ºC for 2min 4. Baked on hot plate at 180 ºC for 2min
11	EBL patterning of device structure	QW on SOI	Electron Beam Lithography System (Elionix 100 kV)	Current: 500pA Dosage: 2800μC/cm^2 Dot map: 300μm, 60000 dot
12	Develop EBL pattern	QW on SOI	-	1. Immersion in TMAH for 28s 2. DI water rinse for 5s and use N_2 gun to blow dry
13	ICP etching of QW	QW on SOI	ICP etcher (Plasmalab System 100)	Cl_2: 15sccm N_2: 60sccm RF: 70W ICP: 400W Temperature: 250 ºC DC bias: 239V Time: 45s
14	ICP etching of Si	QW on SOI	ICP etcher (Plasmalab System 100)	CHF_3: 50sccm SF_6: 9sccm ICP: 1000W RF: 33W Pressure: 15mTorr Temperature: -20 ºC DC: 93-113V Time: 25s
15	HF remove HSQ mask	QW on SOI	-	Immersion in BHF (1:7) for 10s
16	Spin coating of 800nm HSQ	QW on SOI	Spin coater and hot plate	1. Spin coat HSQ (FOX 24) at 3000rpm for 90s 2. Baked on hot plate at 120 ºC for 2min 3. Baked on hot plate at 180 ºC for 2min
17	EBL patterning of active waveguides	QW on SOI	Electron Beam Lithography System (Elionix 100 kV)	Current: 500pA Dosage: 2900μC/cm^2 Dot map: 300μm, 60000 dot
18	Develop EBL pattern	QW on SOI	-	1. Immersion in TMAH for 28s 2. DI water rinse for 5s and use N_2 gun to blow dry

19	ICP etching of QW	QW on SOI	ICP etcher (Plasmalab System 100)	Cl_2: 15sccm N_2: 60sccm RF: 70W ICP: 400W Temperature: 250 ºC DC bias: 239V Time: 45s
20	HF remove HSQ mask	QW on SOI	-	Immersion in BHF (1:7) for 20s
21	ALD deposition of 30nm Al_2O_3 to improve heat dissipation	QW on SOI	ALD R200 Advanced, Picosun	H20 Precursor pulse Time : 0.1s, purge Time : 10s TMA Precursor Pulse Time : 0.1s, Purge Time : 6s Process cycle : 500 Carrier gas: Ar Temperature : 300degC
22	ICP-CVD deposition of 1μm SiO_2 protection layer	QW on SOI	ICP - Chemical Vapor Depostion (Plasmalab System 380)	SiH_4: 7.5sccm N_2O: 14sccm RF: 20W ICP: 1000W Temperature: 250 ºC DC: 100-146V Time: 70min
23	Dice and Cleave	QW on SOI	Disco dicing and cleaning system DAD321	1. Dice from the backside of wafer to 200μm away from the wafer top surface - 150μm thick DSICO diamond blade - 30000 rpm - Feed speed: 5mm/s 2. Apply a force from the side of the substrate to cleave the wafer [73]

REFERENCE

[1] A. A. M. Saleh, and J. M. Simmons, “All-optical networking-evolution, benefits, challenges, and future vision”, Proc. IEEE **100**, 1105 (2012).

[2] D. F. Welch, F. A. Kish, R. Nagarajan, C. H. Joyner, R. P. Schneider, Jr., V. G. Dominic, M. L. Mitchell, S. G. Grubb, T.-K. Chiang, D. D. Perkins, and A. C. Nilsson, “The realization of large-scale photonic integrated circuits and the associated impact on fiber-optic communication systems”, J. Lightwave. Technol. **24**, 4674 (2006).

[3] O. Wada, “Recent Progress in Semiconductor-Based Photonic Signal-Processing Devices”, J. Sel. Top. Quantum Electronics. **17**, 309 (2011).

[4] K. Ohashi, K. Nishi, T. Shimizu, M. Nakada, J. Fujikata, J. Ushida, S. Torii, K. Nose, M. Mizuno, H. Yukawa, M. Kinoshita, N. Suzuki, A. Gomyo, T. Ishi, D. Okamoto, K. Furue, T. Ueno, T. Tsuchizawa, T. Watanabe, K. Yamada, S. Itabashi and J. Akedo, “On-chip optical interconnects”, Proc. IEEE **97**, 1186 (2009).

[5] R. Dekker, N. Usechak, M. Forst and A. Driessen, “Ultrafast nonlinear all-optical processes in silicon-on-insulator waveguides”, J. Phys. D: Appl. Phys. **40**, R249 (2007).

[6] H. Uenohara, “Recent advances in SOA-based optical signal processing”, Photonics in Switching, pp. 1 (2012).

[7] D. Fitsios, T. Alexoudi, G. T. Kanellos, K. Vyrsokinos, N. Pleros, T. Tekin, M. Cherchi, S. Ylinen, M. Harjanne, M. Kapulainen and T. Aalto, “Dual SOA-MZI wavelength converters based on III-V hybrid integration on a μm-scale Si platform”, Photonics Technology Letter **PP,** 1 (2014).

[8] L. T. Varghese, L. Fan, J. Wang, F. Gan, B. Niu, Y. Xuan, A. M. Weiner and M.

Qi, “A silicon optical transistor,” Frontiers in Optics, FW6C.6 (2012).

[9] Y. Huang and S. -T. Ho, "High-speed low-power photonic transistor devices based on optically-controlled gain or absorption to affect optical interference," Opt. Express **16,** 16806 (2008).

[10] Y. Huang, “Simulation of Semiconductor Material Using FDTD Method”, Master Thesis, Northwestern University, June 2002. https://depot.northwestern.edu/yhu234/publish/YYHMS.pdf.

[11] S. Chang, Y. Huang, G. Chang, and S. T. Ho, “THz All-Optical Shutter based on Semiconductor transparency switching by two Optical π-pulses”, OSA Annual Meeting, TuY3, Long Beach, CA, (2001).

[12] S. Chang, and A. Taflove, “Finite-difference time-domain model of lasing action in a four-level two-electron atomic system”, Opt. Express **12**, 3827 (2004)

[13] V. Krishnamurthy, Y. Chen and S. T. Ho, “Photonic transistor design principles for switching gain >=2,” J. Lightwave Tech. **31**, 2086 (2013)

[14] Y. Huang, “Simulation and Experimental Realization of Novel High Efficiency All-Optical and Electrically Pumped Nanophotonic Devices”, PhD Thesis, Northwestern University, June 2007. http://gradworks.umi.com/32/56/3256025.html

[15]. W. W. Chow, S. Koch, and M. Sargent III, Semiconductor-Laser Physics, Springer Verlag, Berlin, 1994.

[16]. J. Piprek, Optoelectronic Devices: Advanced Simulation and Analysis, Springer Verlag, New York, 2005.

[17]. S. Park, "Development of InGaAsP/InP Single-mode Lasers Using Microring Resonators for Photonic Integrated Circuits", PhD Thesis, Northwestern University, Dec. 2000, and references therein.

[18] Y. Huang and S.-T. Ho, “Computational model of solid-state, molecular or

atomic media for FDTD simulation based on a multi-level, multi-electron system governed by Pauli exclusion and Fermi-Dirac thermalization with application to semiconductor photonics," Opt. Express **14**, 3569 (2006).

[19] K. Ravi, Y. Huang and S.-T Ho, "A highly efficient computational model for FDTD simulations of ultrafast electromagnetic interactions with semiconductor media with carrier heating/cooling dynamics", J. Lightwave Technol**. 30**, 772 (2012).

[20] K. Mistry, et al., "A 45nm Logic Technology with High-k+Metal Gate Transistors, Strained Silicon, 9 Cu Interconnect Layers, 193nm Dry Patterning, and 100% Pb-free Packaging," Electron Devices Meeting, 2007. IEDM 2007.

[21]. S. T. Ho, C. E. Soccolich, W. S. Hobson, A. F. J. Levi, M. N. Islam, and R. E. Slusher, "Large Nonlinear Phase Shifts in Low-Loss AlXGa1-XAs Waveguides Near Half-Gap," App. Phys. Lett. **59,** 2558-2560 (1991).

[22] R. P. Espindola, M. K. Udo, D. Y. Chu, S. L. Wu, R. C. Tiberio, P. F. Chapman, D. Cohen, and S. T. Ho, "All-Optical Switching with Low-Peak Power in Microfabricated AlGaAs Waveguides," IEEE Photon. Tech. Lett., **7**, 641-643 (1995).

[23] Y.-H. Kao, T. J. Xia, M. N. Islam, and G. Raybon, "Limitations on ultrafast optical switching in a semiconductor laser amplifier operating at transparency current," J. Appl. Phys. **86,** 4740-4747 (1999).

[24] B. Dagens, C. Janz, D. Leclerc, V. Verdrager, F. Poingt, I. Guillemot, F. Gaborit, and D. Ottenw¨alder, "Design Optimization of All-Active Mach–Zehnder Wavelength Converters," IEEE Photon. Tech. Lett. **11**, 424-426 (1999).

[25] M.L. Ma˘sanovic´, V. Lal, J. S. Barton, E. J. Skogen, L. A. Coldren, and D. J. Blumenthal, "Monolithically Integrated Mach–Zehnder Interferometer Wavelength Converter and Widely Tunable Laser in InP," IEEE Photon. Tech. Lett. **15,** 1117-1119 (2003).

[26] Y. Chen, S.-T. Ho and V. Krishnamurthy, “All-optical switching in a symmetric three-waveguide coupler with phase-mismatched absorptive central waveguide”, Applied Optics **52**, 8845 (2013)

[27] V. Krishnamurthy, K. Ravi, and S.-T. Ho, ‘Analytical Framework for the stead state analysis of wavelength-dependent and intensity-dependent interaction of multiple monochromatic beams in semiconductor photonic structures with multiple active and passive sections’, J. Quant. Electron. **4**, 1282 (2012).

[28] W. W. Chow, and S. W. Koh, “Free-Carrier Theory,” in Semiconducdtor-Laser Fundamentals. New York: Springer, 1999, ch. 2, sec. 2, pp. 45-48

[29] Y. Chen, V. Krishnamurthy, Y. Lai, and S.-T. Ho, “Realization of Ultrafast All-optical Switching with Switching Gain in a Single Semiconductor Waveguide”, Optics Letters **39**, 3567 (2014)

[30] D. A. B. Miller, “Device requirement for optical interconnects to silicon chips”, Proc. IEEE **97**, 1166 (2009)

[31] D. A. Miller, “Optical Physics of Quantum Wells”, https://www.google.com.sg/?gws_rd=ssl#q=Optical+Physics+of+Quantum+Wells

[32] D. S. Chemla and D. A. B. Miller, “Room-temperature excitonic nonlinear optical effects in semiconductor quantum well structures”, J. Opt. Soc. Am. B **2**, 1155 (1985).

[33] P. M. Smith, Y. Silberberg, and D. A. B. Miller, “Mode locking of semiconductor diode laser using saturable excitonic nonlinearities”, J. Opt. Soc. Am. B **2,** 1228 (1985).

[34] M. Baldo, and V. Stojanović, “Optical switching: Excitonic interconnects”, Nature Photonics **3**, 558 (2009).

[35] Y. H. Lee, A. Chavez-Pirson, S. W. Koch, H. M. Gibbs, S. H. Park, J.

Morhange, A. Jeffrey, N. Peyghambarian, L. Banyai, A. C. Gossard and W. Wiegmann, “Room-temperature optical nonlinearities in GaAs,” Phys. Rev. Lett., vol. 57, pp. 2446-2449, 1986.

[36] P. S. Zory, “TE polarization Enhancement of the Matrix element” in Quantum well lasers. Academic Press, 1993, sec. 2.2.3, pp. 153.

[37] M. Silver, and E. P. O’Leilly, “Optimization of long wavelength InGaAsP Strained Quantum-Well Lasers”, J. Quantum Electron. **31**, 1193 (1995)

[38] P. J. A. Thijs, “Progress in quantum well lasers: application of strain”, Semiconductor Laser Conference, pp. 2-5 (1992).

[39] M. Nido, K. Naniwae, J. Shimizu, S. Murata, and A. Suzuki, “Analysis of Differential Gain in InGaAs-InGaAsP Compressive and Tensile Strained Quantum-Well Lasers and Its Application for Estimation of High-speed Modulation Limit”, J. Quantum Electron. **29**, 885 (1993).

[40] M. T. Furtado, E. J. T. Manganote, A. C. G. Bordeaux-Rego, F. Steinhagen, H. Janning, and H. Burkhard, “InGaAs/AlGaInAs/InP Laser with Compressively Strained Multiquantum Well Layers for High Speed Modulation Bandwidth”, Brazilian Journal of Physics **27**, 411 (1997).

[41] J. Minch, S. H. Park, T. Keating, and S. L. Chuang, “Theory and experiment of $In_{1-x}Ga_xAs_yP_{1-y}$ and $In_{1-x-y}Ga_xAl_yAs$ long-wavelength strained quantum-well lasers”, J. Quantum Electron. **35**, 771 (1999).

[42] Y. Zou, J. S. Osinski, P. Grodzinski, P. D. Dapkus, W. C. Rideout, W. F. Sharfin, J. Sharfin, and F. D. Crawford, “Experimental study of Auger recombination, gain and temperature sensitivity of 1.5um compressively strained semiconductor laser”, J. Quant. Electron. **29**, 1565 (1993).

[43] D. Ahn, and S.-L. Chuang, “Optical gain in a strained-layer quantum-well laser”,

J. Quant. Electron. **24**, 2400 (1988).

[44] C. H. Joyner, M. Zirngibl, and J. P. Meester, “A multifrequency waveguide grating laser byselective area epitaxy”, Photonics Technology Letters, IEEE **6**, 1277 (1994).

[45] A. Talneau, N. Bouadma, Y. Lebellego, S. Slempkes, A. Ougazzaden, G. Patriarche, and B. Sermage, “Low-damage dry-etched grating on an MQW active layer and dislocation-free InP regrowth for 1.55-μm complex-coupled DFB lasers fabrication”, IEEE Photonics Technology Letters **10**, 1070 (1998).

[46] V. Aimez, J. Beauvais, J. Beerens, D. Morris, H. S. Lim, and B. S. Ooi, “Low-energy ion-implantation-induced quantum-well intermixing”, IEEE J. Sel. Topics in Quantum Electron. **8**, 870 (2002).

[47] D. Y. Chu, M. K. Chin, S. Z. Xu, T. Y. Chang, and S. T. Ho, "1.5 μm InGaAs/InAlGaAs Quantum-Well Microdisk Lasers," IEEE Photonics Technol. Lett. **5**, 1353 (1993).

[48] W. Fang, J. Y. Xu, A. Yamilov, H. Cao, Y. Ma, S. T. Ho, and G. S. Solomon, "Large Enhancement of Spontaneous Emission Rates of InAs Quantum Dots in GaAs Microdisks," Opt. Lett. **27**, 948 (2002).

[49] K. Inoue, K. Ohtaka, Photonic Crystals: Physics, Fabrication and Applications, Springer.

[50] Y. Ma, G. Chang, S. J. Park, L. W. Wang, and S.T. Ho, "InGaAsP Thin Film Microdisk Resonators Fabricated by Polymer Wafer Bonding for Wavelength Add-drop Filters"," IEEE Photonics Technology Letters **12**, 1495 (2000).

[51] Tong Q-Y and Gösele U 1999 Semiconductor Wafer Bonding (New York: Wiley Inter-Science).

[52] H. Moriceau, F. Rieutord, F. Fournel, Y. L. Tiec, L. D. Cioccio, C. Morales, A.

M. Charvet and C. Deguet, “Overview of recent wafer bonding advances and applications”, Adv. Nat. Sci.: Nanosci. Nanotechnol. **1**, 043004 (2010)

[53] G. Roelkens, L. Liu, D. Liang, R. Jones, A. Fang, B. Koch and J. Bowers, “III-V/Silicon photonics for on-chip and intra-chip optical interconnects”, Laser & Photon. Rev. 1-29 (2010)

[54] D. Liang, A. W. Fang, J. E. Bowers, D. C. Oakley, A. Napoleone, D. C. Chapman, C.-L. Chen, P. W. Juodawlkis and Omri Raday, “150mm InP-to-Silicon direct wafer bonding for silicon photonic integrated circuit”, 214th Electrochemical Society Meeting, paper 2220, (2008)

[55] D. Liang and J. E. Bowers, “Highly efficient vertical outgassing channels for low-temperature InP-to-silicon direct wafer bonding on the silicon-on-insulator substrate”, J. Vac. Sci. Technology B **26**, 1560 (2008)

[56] T.-A. Ma, Z.-M. Li, T. Makino, and M. S. Wartak, “Approximate Optical Gain Formulas for 1.55-mm strained Quaternary Quantum Well Lasers”, J. Quant. Electron**. 31**, 29 (1995).

[57] M. Nido, K. Naniwae, J. Shimizu, S. Murata, and A. Suzuki, “Analysis of Differential Gain in InGaAs-InGaAsP Compressive and Tensile Strained Quantum-Well Lasers and Its Application for Estimation of High-Speed Modulation Limit”, J. Quant. Electron**. 29**, 885 (1993).

[58] D. Liang, D. C. Chapman, Y. Li, D. C. Oakley, T. Napoleone, P. W. Juodawlkis, C. Brubaker, C. Mann, H. Bar, O. Raday, and J. E. Bower, “Uniformity study of wafer-scale InP-to-Silicon hybrid integration”, Appl. Phys. A **103**, 213 (2011).

[59] F. Fiedler and A. Schlachetzki, “Optical parameters of InP-based waveguides”, Solid-State Electronics **30**, 73-83 (1987)

[60] H. Burkhard, H. W. Dinges and E. Kuphal, “Optical properties of In1-xGaxPAs,

InP, GaAs and GaP determined by ellipsometry", J. Appl. Phys. **53**, 655 (1982)

[61] M. A. Afromowitz, Solid State Commun. **15**, 59 (1974)

[62] S. Adachi, "Refractive indices of III-V compounds: Key properties of InGaAsP relevant to device design", J. Appl. Phys. **53**, 5863 (1982)

[63] C. H. Henry, L. F. Johnson, R. A. Logan and D. P. Clarke, "Determination of the refractive index of InGaAsP epitaxial layers by mode line luminescence spectroscopy", J. Quantum Electron. **QE-21**, 1887 (1985)

[64] Govind P. Agarwal, Fiber-Optic Communication Systems (Wiley 1997)

[65] K. Tsutsui and K. Sakuda, "Analysis of a phase mismatched three-waveguide coupler with an optical amplifier", J. Lightwave Tech. **LT-5**, 1763 (1987)

[66] V. Krishnamurthy, Y. Chen, and Q. Wang, " MZI-Semiconductor-Based All-optical Switch With Switching Gain", J. Lightwave Technol. **32,** 2433 (2014).

[67] S. Taebi, M. Khorasaninejad, and S. S. Saini, "Modified Fabry–Perot interferometric method for waveguide loss measurement", Applied Optics **47**, 6625 (2008).

[68] K. H. Park, M. W. Kim, Y. T. Byun, D. Woo, S. H. Kim, S. S. Choi, Y. Chung, W. R. Cho, S. H. Park, and U. Kim, "Nondestructive propagation loss and facet reflectance measurements of GaAs/AlGaAs strip-loaded waveguides," J. Appl. Phys**. 78,** 6318–6320 (1995).

[69] T. Sizer II, R. E. LaMarche, and T. K. Woodward, " Point source heating effects in multiple quantum well modulators", Appl. Phys. Lett. **61**, 420 (1992)

[70] Y. Chen, Y. Lai, T. C. Chong, and S.-T. Ho, "Exact Solution of Facet Reflections for Guided Modes in High-Refractive-Index-Contrast Sub-Wavelength Waveguide Via a Fourier Analysis and Perturbative Series Summation: Derivation and Application", J. Lightwave Technol. **30**, 2455 (2012).

[71] H. Burkhard, H. W. Dinges, and E. Kuphal, "Optical properties of $In_{1-x}Ga_xP_{1-y}As_y$, InP, GaAs, and GaP determined by ellipsometry", J. Appl. Phys. **53**, 665 (1982).

[72] S. Adachi, "Optical dispersion relations for GaP, GaAs, GaSb, InP, InAs, InSb, $Al_xGa_{1-x}As$ and $In_{1-x}Ga_xAs_yP_{1-y}$", J. Appl. Phys. **66**, 6030 (1989).

[73] Y. Chen, V. Krishnamurthy, Y. Lai, Y. Luo, Z. Hao, L. Wang, and S.-T. Ho, "Fabrication of sub-300nm AlN-GaN-AlN waveguide with cleaved end facet", J. Vac. Sci. Technol. B **32**, 041207 (2014)

[74] Y. Chen, Y. Lai, T.-C. Chong, and S.-T. Ho, "All-optical switching with switching gain in a hybrid III-V/silicon single nano-waveguide", Asia Communication and Photonics Conference, Postdeadline I, AF4A.1 (2014)